

**Genetic and ultrastructural analysis of
magnetosome membrane biogenesis
and biomineralization in
*Magnetospirillum gryphiswaldense***

Dissertation

zur Erlangung des Doktorgrades der Naturwissenschaften

(Dr. rer. nat.)

an der Fakultät für Biologie der

Ludwig-Maximilians-Universität München



vorgelegt von

Dipl.-Biol. Oliver Raschdorf

aus Ludwigsburg

München im November 2015

**Genetic and ultrastructural analysis of
magnetosome membrane biogenesis
and biomineralization in
*Magnetospirillum gryphiswaldense***

Dissertation

zur Erlangung des Doktorgrades der Naturwissenschaften

(Dr. rer. nat.)

an der Fakultät für Biologie der

Ludwig-Maximilians-Universität München



vorgelegt von

Dipl.-Biol. Oliver Raschdorf

aus Ludwigsburg

München im November 2015

Die vorliegende Doktorarbeit wurde im Zeitraum von Dezember 2011 bis November 2015 an der Ludwig-Maximilians-Universität München und dem Max-Planck-Institut für Biochemie in Martinsried durchgeführt.

Gutachter:

1. Prof. Dr. Dirk Schüler (Universität Bayreuth)
2. Prof. Dr. Marc Bramkamp (Ludwig-Maximilians-Universität München)

Datum der Abgabe: 23. November 2015

Datum der mündlichen Prüfung: 29. Januar 2016

‘Whether you can observe a thing or not depends on the theory which you use. It is the theory which decides what can be observed’

Albert Einstein (1879 – 1955)

Eidesstattliche Erklärung

Ich versichere hiermit an Eides statt, dass die vorgelegte Dissertation von mir selbstständig und ohne unerlaubte Hilfe angefertigt ist. Des Weiteren erkläre ich, dass ich nicht anderweitig ohne Erfolg versucht habe eine Dissertation einzureichen oder mich der Doktorprüfung zu unterziehen. Die vorliegende Dissertation liegt weder ganz, noch in wesentlichen Teilen einer anderen Prüfungskommission vor.

I hereby confirm that I have written the accompanying thesis by myself, without contribution from any sources other than those cited in the text. Moreover, I declare that I have not submitted or defended a dissertation previously without success. This thesis has not been presented to any other examining board.

Oliver Raschdorf

München, 23. November 2015

Index

Eidesstattliche Erklärung	IV
Index.....	V
List of publications.....	VIII
Manuscripts included in this thesis	VIII
Further co-authored manuscripts.....	VIII
Contributions to publications	IX
Abbreviations	XI
Abstract	1
Zusammenfassung.....	3
1 Introduction	5
1.1 Bacterial organelles and intracytoplasmic membranes.....	5
1.2 Magnetosomes and magnetotactic bacteria	6
1.3 Characteristics of the magnetosome membrane	9
1.4 Magnetite biomineralization	11
1.5 Genetic manipulation of <i>Magnetospirillum gryphiswaldense</i>	12
1.6 Genetic control over magnetosome biosynthesis.....	12
1.6.1 The <i>mamGFDC</i> , <i>mms6</i> and <i>mamXY</i> operons encode accessory functions for magnetosome formation	14
1.6.2 The <i>mamAB</i> operon encodes the core functions for magnetosome formation	16
1.7 General and bacteria-specific mechanisms of internal membrane formation	18
1.8 Scope of this work	22
2 Discussion	23
2.1 An efficient genetic tool for tailored chromosomal manipulations in <i>M. gryphiswaldense</i>	23

2.2	Proteins encoded within the <i>mamXY</i> operon play an important role in magnetosomal redox control systems	25
2.3	Genetic control over magnetosome membrane formation - MamB is most important, but not sufficient for the process	29
2.4	Insights into structure and formation dynamics of magnetosome membranes	32
2.5	The magnetosome membrane is tightly packed with integral Mam and Mms proteins.....	34
2.6	New hypothetical models for magnetosome membrane formation	36
2.7	Further directions	39
3	References	42
4	Appendices	55
4.1	Publication A: A tailored <i>galK</i> counterselection system for efficient markerless gene deletion and chromosomal tagging in <i>Magnetospirillum gryphiswaldense</i>	55
	Publication A: Supplementary Information	65
4.2	Publication B: The magnetosome proteins MamX, MamZ, and MamH are involved in redox control of magnetite biomineralization in <i>Magnetospirillum gryphiswaldense</i>	75
	Publication B: Supplementary Information.....	91
4.3	Manuscript C: Genetic and ultrastructural analysis reveals the key players and initial steps of bacterial magnetosome membrane biogenesis	101
	Manuscript C: Supplementary Information.....	137
4.4	Manuscript D: Semi-quantitative analysis of the integral magnetosome membrane sub-proteome	165
	Acknowledgement.....	199
	Curriculum Vitae.....	200

Digital (CD) content

Movies to chapter 4.3:

Cryo-electron tomography

- Movie S1: Tomogram of *Magnetospirillum gryphiswaldense* wild type cell
- Movie S2: Segmented tomogram of *M. gryphiswaldense* wild type cell
- Movie S3: Segmented tomogram of *M. gryphiswaldense* cell, cultivated under aerobic conditions
- Movie S4: Segmented tomogram of *M. gryphiswaldense* $\Delta mamI$ mutant cell
- Movie S5: Segmented tomogram of *M. gryphiswaldense* $\Delta mamN$ mutant cell
- Movie S6: Segmented tomogram of *M. gryphiswaldense* $\Delta mamL$ mutant cell
- Movie S7: Segmented tomogram of *M. gryphiswaldense* $\Delta mamQ$ mutant cell
- Movie S8: Segmented tomogram of *M. gryphiswaldense* $\Delta mamM$ mutant cell
- Movie S9: Segmented tomogram of *M. gryphiswaldense* $\Delta mamB$ mutant cell

Time-lapse fluorescence microscopy

- Movie S10: Induction of MamB-GFP, 24h, frame every 15 min, GFP channel
- Movie S11: Induction of MamB-GFP, 24h, frame every 15 min, selected detail, GFP channel
- Movie S12: Induction of MamB-GFP, 24h, frame every 15 min, selected detail, DIC channel [number of cell divisions]

Tables to chapter 4.4:

- Interactive table to analyze semi-quantitative magnetosome membrane proteome data.xlsx

List of publications

Manuscripts included in this thesis

- I. **Raschdorf, O., J.M. Plitzko, D. Schüler and F.D. Müller.** 2014. A tailored *galK* counterselection system for efficient markerless gene deletion and chromosomal tagging in *Magnetospirillum gryphiswaldense*. *Applied and Environmental Microbiology* **80**(14):4323-4330
- II. **Raschdorf, O., F.D. Müller, M. Pósfai, J.M. Plitzko and D. Schüler.** 2013. The magnetosome proteins MamX, MamZ, and MamH are involved in redox control of magnetite biomineralization in *Magnetospirillum gryphiswaldense*. *Molecular Microbiology* **89**(5):872-886
– On cover of *Molecular Microbiology* 2013, **89**(5)
- III. **Raschdorf, O., Y. Forstner, I. Kolinko, R. Uebe, J.M. Plitzko and D. Schüler.** Biogenesis of a bacterial organelle: Genetic and ultrastructural analysis of magnetosome membrane formation. In preparation.
- IV. **Raschdorf, O., F. Bonn, N. Zeytuni, R. Zarivach, D. Becher and D. Schüler.** Semi-quantitative analysis of the integral magnetosome membrane sub-proteome. In preparation.

Further co-authored manuscripts

- V. **Lohße, A., S. Borg, O. Raschdorf, I. Kolinko, E. Tompa, M. Pósfai, D. Faivre, J. Baumgartner and D. Schüler.** 2014. Genetic dissection of the *mamAB* and *mms6* operons reveals a gene set essential for magnetosome biogenesis in *Magnetospirillum gryphiswaldense*. *Journal of Bacteriology* **196**(14):2658-2669
- VI. **Li, Y., O. Raschdorf, K.T. Silva and D. Schüler.** 2014. The terminal oxidase *cbb3* functions in redox control of magnetite biomineralization in *Magnetospirillum gryphiswaldense*. *Journal of Bacteriology* **196**(14):2552-2562
- VII. **Zeytuni, N., R. Uebe, M. Maes, G. Davidov, M. Baram, O. Raschdorf, A. Friedler, Y. Miller, D. Schüler and R. Zarivach.** 2014. Bacterial magnetosome biomineralization - a novel platform to study molecular

- mechanisms of human CDF-related Type-II diabetes. PLoS ONE **9**(5): e97154.
- VIII. **Kolinko, I., A. Lohße, S. Borg, O. Raschdorf, C. Jogler, Q. Tu, M. Pósfai, É. Tompa, J. M. Plitzko, A. Brachmann, G. Wanner, R. Müller, Y. Zhang and D. Schüler.** 2014. Biosynthesis of magnetic nanostructures in a foreign organism by transfer of bacterial magnetosome gene clusters. *Nature Nanotechnology* **9**:193–197.
- IX. **Zeytuni, N., R. Uebe, M. Maes, G. Davidov, M. Baram, O. Raschdorf, M. Nadav-Tsubery, S. Kolusheva, R. Bitton, G. Goobes, A. Friedler, Y. Miller, D. Schüler and R. Zarivach.** 2014. Cation Diffusion Facilitators transport initiation and regulation is mediated by cation induced conformational changes of the cytoplasmic domain. PLoS ONE **9**(3): e92141.
- X. **Müller, F.D., O. Raschdorf, H. Nudelman, M. Messerer, E. Katzmann, J.M. Plitzko, R. Zarivach and D. Schüler.** 2014. The FtsZ-like protein FtsZm of *M. gryphiswaldense* likely interacts with its generic FtsZ homolog and is required for biomineralization under nitrate deprivation. *Journal of Bacteriology* **196**(3):650-659.
- XI. **Lohße, A., I. Kolinko, O. Raschdorf, R. Uebe, S. Borg, A. Brachmann, J. Plitzko, R. Müller, Y. Zhang and D. Schüler.** Genomic amplification of biosynthetic gene clusters in *Magnetospirillum gryphiswaldense* causes magnetosome overproduction. In preparation.
- XII. **Raschdorf, O., R. Uebe and D. Schüler.** Preparation of bacterial magnetosomes for proteome analysis. Book chapter in *Microbial Proteomics (Methods in Molecular Biology)*, D. Becher and R. Westermeier (Ed.), Springer. In preparation.

Contributions to publications

- I. O.R., D.S. and F.D.M. designed the study and wrote the manuscript. O.R. planned, constructed and validated the counterselection vector and the mutagenesis strategy. F.D.M. modified vector for experiments, constructed the mutants and analyzed mutants by transmission-electron microscopy and fluorescence microscopy. O.R. and J.M.P. performed cryo-electron tomography experiments.

- II. O.R., F.D.M and D.S. designed the study. O.R. designed the experiments and constructed all plasmids and mutants O.R. performed transmission electron and fluorescence microscopy and analyzed the data. M.P. took high-resolution transmission electron micrographs. O.R. and J.M.P. performed cryo-electron tomography experiments. O.R. and D.S. wrote the manuscript.
- III. O.R. and D.S. designed the study and wrote the manuscript. O.R. planned and created most plasmids and strains used in this study, some with the assistance of Y.F and R.U. I.K. designed fully synthetic magnetosome gene construct. R.U. designed pre-plasmid for Tn7 based transposition. O.R. performed transmission-electron-microscopy and together with J.M.P. cryo-electron tomography. O.R. and Y.F. performed fluorescence microscopy. O.R. analyzed and integrated all the data.
- IV. O.R., F.B., D.B. and D.S. designed the study. O.R. created all plasmids and strains and performed fluorescence microscopy. O.R. prepared all samples for proteomic analysis, while F.B. separated proteins and performed mass spectrometry. O.R. developed evaluation model and analyzed the data, with the help of F.B. and D.B. N.Z. and R.Z. initiated integral membrane protein coverage model. O.R. wrote the manuscript.
- V. O.R. created and complemented $\Delta mamL$ mutant, created some plasmids and performed some of the electron and fluorescent microscopy experiments
- VI. O.R. performed transmission-electron microscopy.
- VII. O.R. performed transmission-electron microscopy.
- VIII. O.R. performed transmission-electron microscopy and cryo-electron tomography with isolated magnetosomes and analyzed the respective data.
- IX. O.R. performed transmission-electron microscopy.
- X. O.R. constructed $\Delta ftsZm$ mutant, performed overexpression and induction experiment, analyzed the respective data and wrote parts of the manuscript.
- XI. O.R. performed cryo-electron tomography and analyzed the respective data.
- XII. O.R., R.U. and D.S. conceived the book chapter and wrote the manuscript.

I hereby confirm these statements

Oliver Raschdorf

Prof. Dr. Dirk Schüler

Abbreviations

BAR	Bin–Amphiphysin–Rvs (protein domain)
CDF	Cation diffusion facilitator
CET	Cryo-electron tomography
CM	Cytoplasmic membrane
COP	Coat protein complex
DMM	Dense magnetosome membrane-like structure
DNA	Deoxyribonucleic acid
ENTH	Epsin N-terminal homology (protein domain)
GFP	Green fluorescent protein
GTP	Guanosine triphosphate
ICM	Intracellular membrane
LH	Light harvesting
<i>mad</i>	magnetosome associated deltaproteobacterial (gene)
MAI	Genomic magnetosome island
<i>mam</i>	magnetosome membrane (gene)
<i>man</i>	putative magnetosome genes in Nitrospirae
MFS	Major facilitator superfamily
MM	Magnetosome membrane
MTB	Magnetotactic bacteria
<i>mms</i>	magnetosome membrane specific (gene)
OMP	Outer membrane protein
PDZ	PSD95-Dlg1-zo-1 (protein domain)
pH	Negative decimal logarithm of proton concentration
PHB	Polyhydroxybutyrate
RC	Reaction Center
TEM	Transmission electron microscopy
TRP	Tetratricopeptide (protein domain)

Abstract

Magnetosomes are membrane-bounded organelles that contain magnetic nanocrystals and enable magnetotactic bacteria to orient in magnetic fields. Magnetosomes have emerged as excellent model systems to study biomineralization, and lately also organelle formation in prokaryotes. In the Alphaproteobacterium *Magnetospirillum gryphiswaldense*, magnetosome biogenesis proceeds by invagination of the cytoplasmic membrane, followed by controlled biomineralization of regular magnetite crystals within the confined environment of the magnetosome membrane compartment.

Magnetosome formation in *M. gryphiswaldense* is controlled by approximately 30 genes that are organized in four operons within a genomic island. The *mamAB* operon comprises 17 genes that are essential and sufficient for magnetite formation and are partially conserved in all known magnetotactic bacteria, while the other three operons, including *mamXY*, encode accessory functions that are required for the formation of monocrystalline and regularly sized and shaped particles. However, the functions of the individual genes have not been completely elucidated, yet.

Until recently, the lack of methods for efficient and accurate genomic modifications was the major obstacle for elaborate genetic studies. In this thesis, a genetic tool based on the counterselection marker *galK* was developed, which now enabled the construction of markerless gene deletions or fusions with high efficiency and has become the state-of-the-art method for targeted chromosomal modifications in *M. gryphiswaldense*. This tool was successfully employed to investigate the function of the *mamXY* operon-encoded MamX and MamZ proteins, whose roles in magnetite biogenesis have remained entirely unknown so far. The study revealed that MamX and MamZ functionally co-operate and are both important players in the complex magnetosomal iron-redox control system for the formation of well-ordered magnetite crystals.

While the process of magnetite biomineralization has recently become increasingly well understood, almost nothing is known about the first step of magnetosome biogenesis, the invagination of the magnetosome membrane. To reveal the genetic determinants for magnetosome membrane formation, the ultrastructure of

M. gryphiswaldense and several gene deletion mutants was therefore comprehensively studied by cryo-electron tomography. The magnetosomal iron transporter MamB was found to be most important for the formation of magnetosome membrane-like structures and might act as a hub for the organization of other magnetosome proteins. On the other hand, expression of a synthetic cluster of seven magnetosome genes was required to re-enable internal membrane formation in the absence of other genes from the *mamAB* operon. These results indicated that magnetosome membrane biogenesis is a multi-determined, but not tightly controlled process that relies on the action of certain key magnetosome proteins. Furthermore, a new genetic system allowed the synchronous induction of *de novo* magnetosome formation and suggested that magnetosome membrane invagination proceeds from confined magnetosome protein clusters at random positions in the cytoplasmic membrane.

Finally, a comparative and semi-quantitative proteomic study showed that the protein composition of the magnetosome membrane of *M. gryphiswaldense* is dominated by a subset of only 20-25 integral membrane proteins that are specifically and highly enriched. These magnetosome membrane proteins seem to exhibit a tightly packed confirmation, which also indicates an important role of local membrane protein crowding in the differentiation and origination of the organelle from the cytoplasmic membrane.

In summary, the genetic, ultrastructural and proteomic studies that are presented in this thesis provided new insights into the function of several magnetosome proteins and enabled to refine the models for magnetosome membrane formation and biomineralization.

Zusammenfassung

Magnetosomen sind bakterielle Organellen, die aus membranumgebenen Nanomagnetkristallen bestehen und mit deren Hilfe sich magnetotaktische Bakterien im Erdmagnetfeld orientieren. Magnetosomen haben sich als ausgezeichnete Modellsysteme zur Untersuchung von Biomineralisationsprozessen erwiesen und dienen seit einiger Zeit auch zur Erforschung der Organellbiogenese in Prokaryoten. Die Entstehung von Magnetosomen läuft im Alphaproteobakterium *Magnetospirillum gryphiswaldense* in zwei Schritten ab: Zuerst bildet sich durch Invagination der Zytoplasmamembran die Magnetosomenmembran aus; anschließend erfolgt in diesem Kompartiment unter kontrollierten Bedingungen die Biomineralization von stöchiometrischen Magnetitkristallen. Die Ausbildung von Magnetosomen wird in *M. gryphiswaldense* von ca. 30 Genen kontrolliert, die hauptsächlich in vier Operons einer genomischen Magnetosomeninsel angeordnet sind. Das *mamAB* Operon beinhaltet alle essentiellen Gene der Magnetitbiosynthese und liegt in Teilen konserviert in allen magnetotaktischen Bakterien vor. Die anderen drei Operons, unter ihnen das *mamXY* Operon, kodieren hingegen für zusätzliche Funktionen, die zur Bildung von regulären, monokristallinen Partikeln der richtigen Form und Größe benötigt werden. Jedoch wurden die genauen Funktionen aller Gene noch nicht komplett aufgeklärt.

Tiefgreifende genetische Studien wurden bislang durch das Fehlen von effizienten und genauen Methoden zur Genommodifikation verhindert. In dieser Arbeit wurde daher ein genetisches Werkzeug entwickelt, das auf dem Gegenselektionsmarker *galK* basiert und effizientes, markerfreies Deletieren und Fusionieren von Genen in *M. gryphiswaldense* ermöglicht. Die Methode wurde unter anderem dazu eingesetzt um die Funktionen der vom *mamXY* Operon kodierten Proteine MamX und MamZ aufzuklären, deren Rolle bei der Magnetosomenbiogenese bisher noch nicht analysiert worden ist. Es stellte sich dabei heraus, dass beide Proteine funktionell zusammenwirken und eine wichtige Rolle im ausgedehnten magnetosomalen Redox-Kontrollsystem spielen, das zur Ausbildung von regulären und intrinsisch geordneten Magnetitkristallen in diesem Kompartiments benötigt wird.

Während die Biomineralisationsprozesse innerhalb der Magnetosomen in letzter Zeit immer besser erforscht wurden, ist derzeit nur sehr wenig bekannt über den ersten

Schritt der Magnetosomenbiogenese, die Ausbildung der Magnetosomen-membran. Durch die Anwendung von Kryoelektronentomographie wurde in dieser Arbeit daher eine umfassende ultrastrukturelle Studie zur Untersuchung der Magnetosomenmembranbildung in *M. gryphiswaldense* und verschiedenen Deletionsmutanten durchgeführt. Der magnetosomale Eisentransporter MamB, konnte als wichtigstes Protein für die Ausbildung von Magnetosomenmembranen identifiziert werden und dient möglicherweise der zentralen Anordnung von anderen Magnetosomenproteinen. Hingegen ermöglichte die Expression von sieben Magnetosomengeneten die Neubildung von internen Membranstrukturen in der Abwesenheit anderer Bestandteile des *mamAB* Operons. Diese Daten weisen darauf hin, dass die Biogenese von Magnetosomenmembranen zwar nicht besonders genau reguliert wird und von mehreren redundanten Faktoren abhängt, aber die Anwesenheit mehrerer Schlüsselproteine voraussetzt. Die Entwicklung eines induzierbaren genetischen Systems ermöglichte weiterhin die Beobachtung der synchronen Neuausbildung von Magnetosomenmembranen. Die Analyse deutete darauf hin, dass die Bildung von Magnetosomenmembranen über die Assemblierung von Magnetosomenproteinclustern an mehreren zufälligen Stellen innerhalb der Zytoplasmamembran abläuft.

Zum Abschluss der Arbeit wurde eine vergleichende, halbquantitative Bestimmung der Membranproteinzusammensetzung der Magnetosomen von *M. gryphiswaldense* durchgeführt. Die Studie zeigte, dass die Magnetosomenmembran spezifisch nur mit 25 bis 30 hochabundanten, integralen Transmembranproteinen angereichert ist. Diese Proteine scheinen dicht gepackt in der Magnetosomenmembran vorzuliegen, was einen Hinweis auf die Entstehung des Organells durch kompakte lokale Membranproteinakkumulation in der Zytoplasmamembran gibt.

Zusammenfassend betrachtet konnten durch die genetischen, ultrastrukturellen und proteomischen Studien in dieser Arbeit neue Einblicke in die Funktion von mehreren Magnetosomenproteinen gewonnen werden und die bestehenden Modelle zur Biogenese und Biomineralisation von Magnetosomen aktualisiert und verbessert werden.

1 Introduction

1.1 Bacterial organelles and intracytoplasmic membranes

Internal spatial organization on a molecular level is inevitable to accomplish crucial cellular functions of all living organisms [1]. On a subcellular level, functional compartments, like organelles, concentrate enzymatic activities and substrates in a diffusion-confined space with a specific physio-chemical environment and sequester toxic (by-)products of the reactions [2]. Nevertheless, despite acknowledgement of the periplasmic space in Gram negative bacteria, intracellular compartmentalization was for a long time not attributed to prokaryotes, but only seen as a unique eukaryotic feature [3]. However, over the last decades, it became increasingly clear that even prokaryotes, such as bacteria, possess a variety of structures that facilitate internal spatial organization. For instance, bacteria contain a huge diversity of cytoskeletal elements that are involved in cell wall synthesis, cytokinesis, polarity determination, cell shape regulation, chromosome segregation and several other tasks in defining subcellular localization [4–6]. Membrane microdomains organize the cell membrane in functional entities [7], and although prokaryotic cells lack a membrane-enveloped nucleus, the DNA is still highly condensed and organized within a nucleoid that is associated with specific proteins and can be considered as a compartment [8].

Furthermore, a variety of protein-encapsulated or membrane-enveloped intracellular compartments or organelles were described in specific bacteria [9,10]. Bacterial micro-compartments are organelles that compartmentalize various metabolic functions in polyhedral protein shells [11]. The most well studied examples are carboxysomes that facilitate CO₂-fixation in Cyanobacteria and some Proteobacteria [12]. Gas vesicles confer buoyancy to several photosynthetic bacteria and some halophilic archaea and are another class of proteinaceous compartments [13]. Intracytoplasmic membranes (ICM), on the other hand, are a diverse group of membranous compartments in prokaryotes that are either continuous with cytoplasmic membrane or detached from the to form intracellular organelles [14]. Most types of ICM fulfill metabolic functions. Some of the most widespread and thoroughly studied examples are photosynthetic membranes that occur in *Cyanobacteria*, purple bacteria and green bacteria [9]. They exhibit different

morphologies that range from simple membrane invaginations or vesicular structures (chromatophores) and oblong bodies (chlorosomes) to extended ribbon or sheet-like structures which can be detached (thylakoids) or continuous (chromatophores) with the cytoplasmic membrane [15–18]. Despite their different morphologies, they all fulfill the same function by increasing the membrane surface area and by providing the ideal subcellular environment for photosynthetic reactions [9]. Lamellar and tubular membrane invaginations also occur in a number of polyphyletic chemoautotrophic bacteria in which they as well increase the membrane surface to accommodate membrane bound metabolic enzyme complexes [19]. Many species of the *Planctomycetes-Verrucomicrobia-Chlamydiae* (PVC) superphylum show very complex ICM systems that were compared to the eukaryotic cell plan [20], but recently turned out to likely be sophisticated invaginations of the cytoplasmic membrane [21]. Additionally, some special planctomycetes contain a well characterized metabolic membranous organelle, called the anammoxosome, which bounds an energy-yielding aerobic ammonium oxidation processes [22,23]. Additionally, some planctomycetes also display the ability for membrane internalization processes that are reminiscent of eukaryotic endocytosis [24]. Specific storage compartments like polyphosphate granule, polyhydroxyalkanoates, or sulfur globules could also be considered as intracellular organelles, since they compartmentalize special metabolic functions and are reported to be enclosed by phospholipids [14,25]. Despite their widespread occurrence, only little is known about the formation mechanisms of ICM and membranous organelles in bacteria.

1.2 Magnetosomes and magnetotactic bacteria

Magnetosomes are one of the most sophisticated examples for non-metabolic ICM in prokaryotes and have emerged as model systems to study biomineralization and lately also organelle formation. Magnetosomes comprise membrane-enveloped magnetic crystals of greigite or magnetite and are utilized by magnetotactic bacteria (MTB) to navigate along the Earth's magnetic field lines [26–29]. MTB generally arrange their magnetosomes in single or multiple linear chains (Figure 1 and Figure 2). This arrangement lines up the individual magnetic dipole moments of the concatenated particles in one direction to create a moment that is large enough to align cells with the weak magnetic field of the Earth [30,31] (Figure 2c-ii). MTB combine their passive magnetic alignment with an active flagella-mediated

swimming motility to orient along oxygen gradients in their natural habitat, the anoxic-oxic transition zone in salt- or freshwater sediments [32–34]. In contrast to classical chemotactic motility, magneto-aerotaxis of MTB thereby reduces the effective maneuvering space from three dimensions to one, facilitating faster search for favorable microoxic environments [35,36].

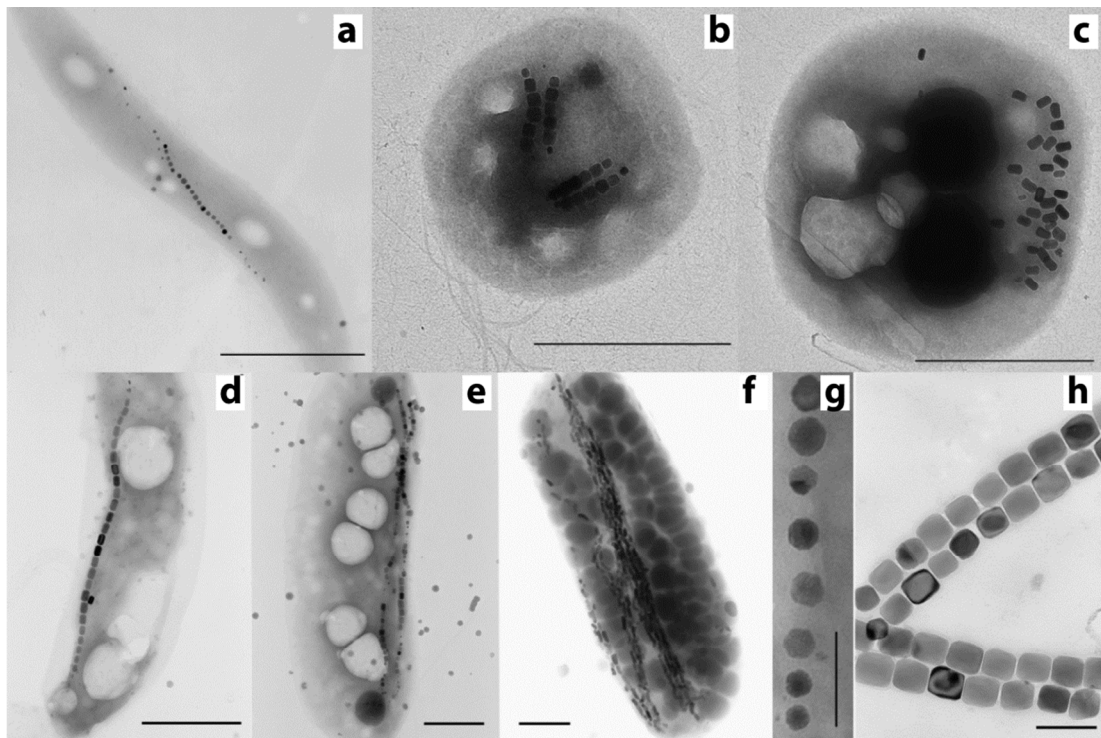


Figure 1: Examples for the diversity of magnetite producing magnetotactic bacteria and crystal morphologies. Transmission electron micrographs. Scale bars: a-f: 1 μm , g-h: 100 nm.

(a) Spirillum with one chain of cubo-octahedral magnetosome crystals. (b) Coccus with two double chains of elongated prismatic magnetosome crystals. (c) Coccus with clustered elongated magnetosome crystal. (d) Vibrioid cell with one chain of elongated prismatic or elongated octahedral magnetosome crystals. (e) Vibrioid cell with two chains of crystals. (f) Rod shaped bacterium with several chains of bullet shaped magnetosome crystals. (g) Higher magnification micrograph of cubo-octahedral magnetosome crystals. (h) Higher magnification micrograph of elongated prismatic or elongated octahedral magnetosome crystals. The figure is modified and adapted from [37].

MTB species are grouped within the Alpha-, Delta- and Gammaproteobacteria as well as Nitrospirae, the candidate phylum Omnitrophica (PVC superphylum associated) and the Fibrobacteres-Chlorobi-Bacteroidetes superphylum [38–44]. The polyphyletic MTB display high morphological and physiological heterogeneity: So far, magnetotactic rods, cocci, spirilla, vibrioid cells, ovoid cells and even multicellular magnetotactic bacteria were described [38–40,45–47] (Figure 1). MTB also produce a variety of different crystal morphologies: magnetite crystals in

different organisms are cuboctahedral, elongated prismatic, elongated octahedral or bullet-shaped elongated while greigite crystals more often show an equidimensional and irregular appearance [48] (Figure 1). Depending on the organism, magnetosome crystals usually have a long axis diameter of 30-120 nm and are found in numbers from 10 to up to 1000 particles per cell [49]. An actin-like magnetosome filament assists the organization of the particles in coherent chains and helps to equally segregate the magnetosome chains during cell division [50–53] (Figure 2a+d).

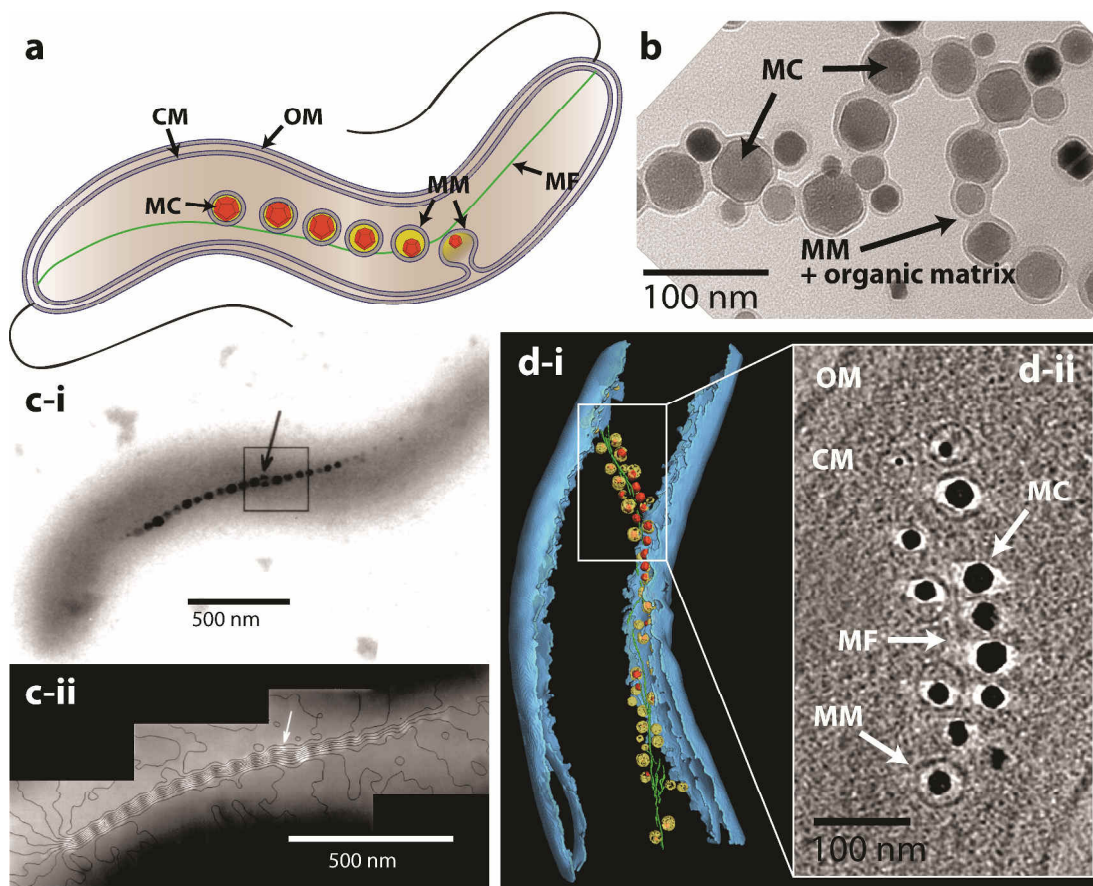


Figure 2: Ultrastructure of *Magnetospirillum gryphiswaldense* and related MTB.

(a) Model of magnetosome chain organization in *Magnetospirillum gryphiswaldense*. (b) Transmission electron micrograph of unstained purified magnetosomes from *M. gryphiswaldense*. The magnetite crystals exhibit different sizes and are surrounded by an organic matrix. (c) (c-i) shows transmission electron micrograph of single *Magnetospirillum magnetotacticum* cell comprising one linear magnetosome chain. (c-ii) shows magnetic induction map from off-axis electron holography of the same cell. All magnetic moments of the individual crystals are lined up in one direction. The arrow indicates an imperfect magnetite crystal. Figure c is modified and adapted from [31]. (d) Segmented cryo-electron tomogram of *M. gryphiswaldense* cell (d-i). The cell membranes are segmented in blue, magnetosome membranes in yellow, magnetite crystals in red and the magnetosome filament in green. (d-ii) shows a x-y slice detail of tomogram. Abbreviation: OM: outer membrane, CM: cytoplasmic membrane, MC: magnetite crystal, MM: magnetosome membrane, MF: magnetosome filament

Although MTB display a huge phylogenetical diversity and natural abundance, most strains are very fastidious and therefore only a very limited number of suitable laboratory strains are available. The magnetite producing Alphaproteobacteria *Magnetospirillum gryphiswaldense* and *Magnetospirillum magneticum* were among the first MTB that could be isolated in pure culture and are the best genetically tractable strains [54–57]. A number of methods for the genetic manipulation of both organisms were adapted and applied, and therefore most of the functional genetic and cell biological studies were conducted with these two MTB species. Consequently, *M. gryphiswaldense* was also utilized as model organism for all studies conducted in this thesis. Cells of this strain are spiral-shaped, bipolar monotrichously flagellated, typically 2-3 μm long and 0.5-0.6 μm in diameter (Figure 2). They on average contain 30-40, but sometimes >60 magnetosomes, in a size range of 15-50 nm, wherein most crystals are found in the 35-45 nm range [56,58,59]. In *M. gryphiswaldense*, magnetosomes are usually organized in one single chain, but closely spaced parallel chains were also frequently observed (Figure 2) [51].

1.3 Characteristics of the magnetosome membrane

Very early after their description, thin-sectioning and transmission electron microscopy (TEM) revealed that the magnetite crystals in *Magnetospirilla* species were surrounded by a visible electron dense matrix [26]. This matrix was later identified as a lipid bilayer by biochemical studies and called magnetosome membrane (MM) [27]. Also then, it was suggested that the magnetosome membrane might originate from the cytoplasmic membrane, on the basis of a similar lipid composition [27]. This hypothesis was finally confirmed by cryo-electron tomography (CET) and the visualization of magnetosome membrane invaginations that were still continuous with the cytoplasmic membrane [51,52] (Figure 2d and Figure 3). Additionally, the enveloping magnetosome membrane was visualized in a number of different MTB by means of different electron microscopy techniques [33,60–64], therefore indicating that, independent of the morphology, all magnetosome minerals of MTB are surrounded by a biological membrane [65]. This is also supported by the fact that most conserved magnetosome-associated proteins are predicted, and in many cases demonstrated, to be integral membrane proteins (see section 1.6 and Figure 4b). Although magnetosome membranes have not yet been observed in EM studies with the bullet-shaped magnetite producer *Desulfovibrio*

magneticus [66], transmembrane magnetosome proteins were detected in isolated magnetosomes of this organism [67], which strongly suggested that the particles are at least transiently surrounded by a membrane or originate within a membranous compartment [68].

Based on observations made by CET in *M. magneticum*, Komeili *et al.* suggested that invaginated magnetosome membranes are permanently continuous with the cytoplasmic membrane (Figure 3) [52]. Using the same technique with *M. gryphiswaldense* cells, Katzmann *et al.* however confirmed the previously assumed theory that the magnetosome membrane completely surrounds the magnetite particle as a detached magnetosome membrane vesicle and is only transiently connected with the cytoplasmic membrane in early development stages [50,51] (see also Figure 2d).

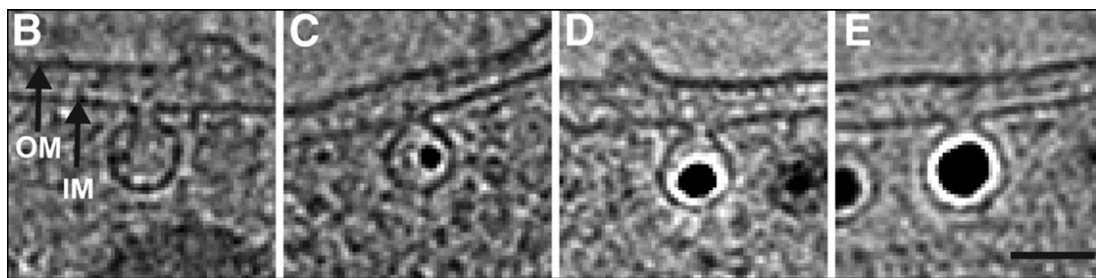


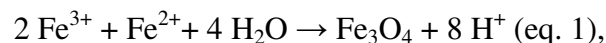
Figure 3: Cryo-electron tomography slices showing magnetosome membranes from *M. magneticum* that are continuous with the cytoplasmic membrane.

The magnetosome membranes contain crystals of different sizes. Outer (OM) and inner (cytoplasmic) membrane (IM) are indicated. Scale bar: 50 nm. The figure is adapted from [52].

The underlying bio- and physiochemical principles of magnetosome formation are not completely understood until now. The current model suggest a stepwise assembly: First, the magnetosome membrane differentiates and invaginates from the cytoplasmic membrane and extracellular iron is taken up and transported into this compartment, which provides a controlled environment for nucleation and growth of magnetic crystals. Finally, or already during an earlier step, magnetosomes are attached to the magnetosome filament and concatenated into a stable linear chain [52,60,65,69].

1.4 Magnetite biomineralization

M. gryphiswaldense biomineralizes well-ordered magnetite crystals within the magnetosome compartment [70]. Magnetite is a mixed-valence iron oxide [Fe(II)Fe(III)₂O₄] and has stable ferrimagnetic properties once crystal grains reach a size range of approximately 15-30 and up to 200 nm. Below that size, the crystals are super-paramagnetic, which means that they can be magnetized but do not exhibit a stable single magnetic domain state [71]. The composition of biologically formed minerals strongly depend on environmental conditions (e.g., pH, oxygen concentration, redox potential, temperature) and requires local supersaturation of the involved ions [72,73]. Magnetite biomineralization in MTB occurs only under microoxic or anoxic conditions and is inhibited by atmospheric oxygen concentrations [74,75]. The complete pathway of magnetite biomineralization is so far not fully understood. The two most supported models for magnetosomal magnetite formation are the fast co-precipitation of ferrous and ferric iron, or the transient formation of ferrihydrite, possibly with the participation of bacterioferritin [37,76–80]. Independent of the model, it is definitely clear that controlled redox processes have to take place within the magnetosome compartment to achieve the mineralization of ordered, stoichiometric magnetite [70]. Additionally, a stable, most likely alkaline pH range has to be maintained within the magnetosomes since magnetite biomineralization is expected to dynamically release protons according to the following, very simplified equation 1 [37].



Furthermore, crystal nucleation and growth has to be controlled in order to mineralize single monocrystalline particles. The magnetosome membrane compartment provides the necessary environment and houses specific proteins that most probably control all of these processes [65].

1.5 Genetic manipulation of *Magnetospirillum gryphiswaldense*

A very important breakthrough in magnetosome biosynthesis research was the development of tools for targeted genomic manipulations of MTB [54,55]. Since that time, various methods for genetic engineering of MTB and especially *M. gryphiswaldense* were adapted. Genomic manipulations were first performed by RecA-mediated homologous single crossover recombination and interruption of the target gene by a plasmid [81], which however is very prone to cause polar effects. Simultaneous double crossover recombination, on the other hand, is very inefficient in *M. gryphiswaldense* and relies on a high screening effort [82]. Later, Cre/lox mediated systems were developed that were more efficient, less prone for causing polar effects and could be applied for creating large or multiple deletions [58,83–86]. Although efficient, the implementation of Cre/lox modifications is very time-consuming and due to the remaining scar lox sequence, not suitable for tailored in-frame genomic modifications.

Highly efficient sequential double crossover recombination techniques, on the other hand, rely on the action of chromogenic or conditionally lethal counterselection markers [87]. The counterselection marker gene *sacB* confers sensitivity to sucrose and was used for mutagenesis in *M. magneticum* [88]. However, the application of *sacB*, as well as the chromogenic marker *gusA* was limited to only a few studies in *M. gryphiswaldense* so far, since random inactivation of the marker genes causes high numbers of false-negative colonies [51,58,69,81]. Identification and application of an efficient counterselection marker could overcome the current limitations that are associated with genomic engineering of the fastidious *M. gryphiswaldense*.

1.6 Genetic control over magnetosome biosynthesis

Although magnetosome membranes exhibited a similar lipid and fatty acid composition than the cytoplasmic membrane [27,89], biochemical analysis of purified magnetosomes from *M. gryphiswaldense* revealed the presence of over 30 proteins that were specifically enriched in the membrane of this compartment [90,91]. The genes encoding these proteins were termed *mam*¹ or *mms*² and found to

¹ magnetosome membrane

be organized within a 115-kb hypervariable genomic region, called the magnetosome island (MAI) (Figure 4a). A large deletion within a spontaneous non-magnetic mutant of *M. gryphiswaldense* could be mapped within the MAI, indeed proving that this region is essential for functional magnetosome formation [92]. In *M. gryphiswaldense*, 29 known magnetosome-associated *mam* and *mms* genes are clustered within four operons in the MAI, namely *mamAB*, *mamGFDC*, *mms6* and *mamXY* (Figure 4), of which each are monocistronically transcribed [93–95]. This organization and gene content is grossly conserved within closely related MTB of the genus *Magnetospirillum*, but varies in other MTB from the Alphaproteobacteria class and all other phyla [39,95].

Some magnetosome genes are conserved throughout all MTB, while others are restricted to certain phylogenetic groups. The genes of the accessory *mamGFDC*, *mms6* and *mamXY* operons, for instance, are often encoded in a different genomic context, but are generally only conserved in Alphaproteobacteria, while a recently discovered and so far uncharacterized class of *mad*³ genes was found in magnetotactic Deltaproteobacteria, Nitrospirae and in the only known MTB species of the Omnitrophica phylum (PVC-associated). Additionally, another novel class of *man*⁴ genes is present only in the latter two phyla [43,96,97]. However, a set of *mam* gene orthologs is conserved in all known MTB from which sufficient genomic information is available. These genes are all organized in *mamAB*-like operons of magnetotactic Alphaproteobacteria and in MAI-like genomic regions in other phyla. Nine genes, namely *mamABEIKMOPQ* are conserved in all MTB, while magnetite-producers also comprise a homolog of *mamL* as the tenth conserved gene [96] (potentially with the exception of species from the ‘*Candidatus Magnetobacterium*’ genus [97]). Numerous deletion studies revealed that the magnetosome proteins are controlling all steps of magnetosome biogenesis. Due to challenges in genome modifications of most other MTB, almost all genetic studies were conducted in *M. magneticum* and *M. gryphiswaldense*.

² magnetosome membrane specific

³ magnetosome associated deltaproteobacterial

⁴ putative magnetosome genes in Nitrospirae

1.6.1 The *mamGFDC*, *mms6* and *mamXY* operons encode accessory functions for magnetosome formation

Deletion of the *mamGFDC* and *mms6* operons in *M. gryphiswaldense* caused the formation of smaller and fewer magnetite crystals [58,85]. The four genes of the *mamGFDC* operon individually have a significant role in controlling crystal size [58]. Same is true for *mms6* and *mmsF* of the *mms6* operon, whose deletion additionally influences the shape of magnetite particles [98–101]. *In vitro* studies showed that purified MamC, Mms6 and MmsF supported mineralization of large magnetite crystals under ambient conditions from mixed-valence iron salts, implying that the proteins *in vivo* also are involved in the initial steps of magnetite nucleation [102]. Additional studies suggested that these proteins could influence the surface structure of magnetite by templating the formation of the species specific cuboctahedral crystals in Magnetospirilla [98,100], while other recent experiments indicated that some of these proteins have a function in recruiting other magnetosome proteins to the organelle [R. Uebe unpublished].

In contrast to *mamGFDC* and *mms6*, the functions of the proteins encoded within the *mamXY* operon are not very well investigated yet. Deletion of the whole operon in *M. gryphiswaldense* caused a distinctive phenotype with regular wild type-like magnetosomes, flanked by a variable number of irregular poorly-crystalline particles at the end of magnetosome chains. A similar phenotype was associated with the deletion of *ftsZm*, the last gene of this operon [103]. MamY was implicated in magnetosome membrane formation in *M. magneticum* since purified MamY protein could tubulate liposomes *in vitro* [104]. Although no clear magnetosome-associated phenotype of the deletion mutant was reported, the authors suggested that MamY might also play an important role in membrane remodeling for magnetosome biogenesis *in vivo* [104]. However, an ongoing study in *M. gryphiswaldense* rather indicates that MamY oligomerizes in a filamentous structure and helps to position the magnetosome chain in the inner curvature of the cell [O. Raschdorf, M. Toro-Nahuelpan, F.D. Müller, unpublished].

Notably, some other genes within the MAI, but outside of the four well defined operons, were recently implicated in magnetosome formation. *M. gryphiswaldense* and *M. magneticum* contain additional genes similar to *mamD*, *mamF* and *mmsF* [98,105,106], which were called MamF2 (Mms5) and MamD2 (MmxF) in

M. gryphiswaldense [R. Uebe, unpublished]. Additionally, one homolog of the common bacterial ferrous iron uptake system FeoAB [107] is encoded within the MAI of *M. gryphiswaldense* (FeoAB1). In contrast to the generic FeoAB system of *M. gryphiswaldense*, FeoAB1 seems to be specifically involved in iron uptake for the magnetosomal pathway [108] [R. Uebe, unpublished].

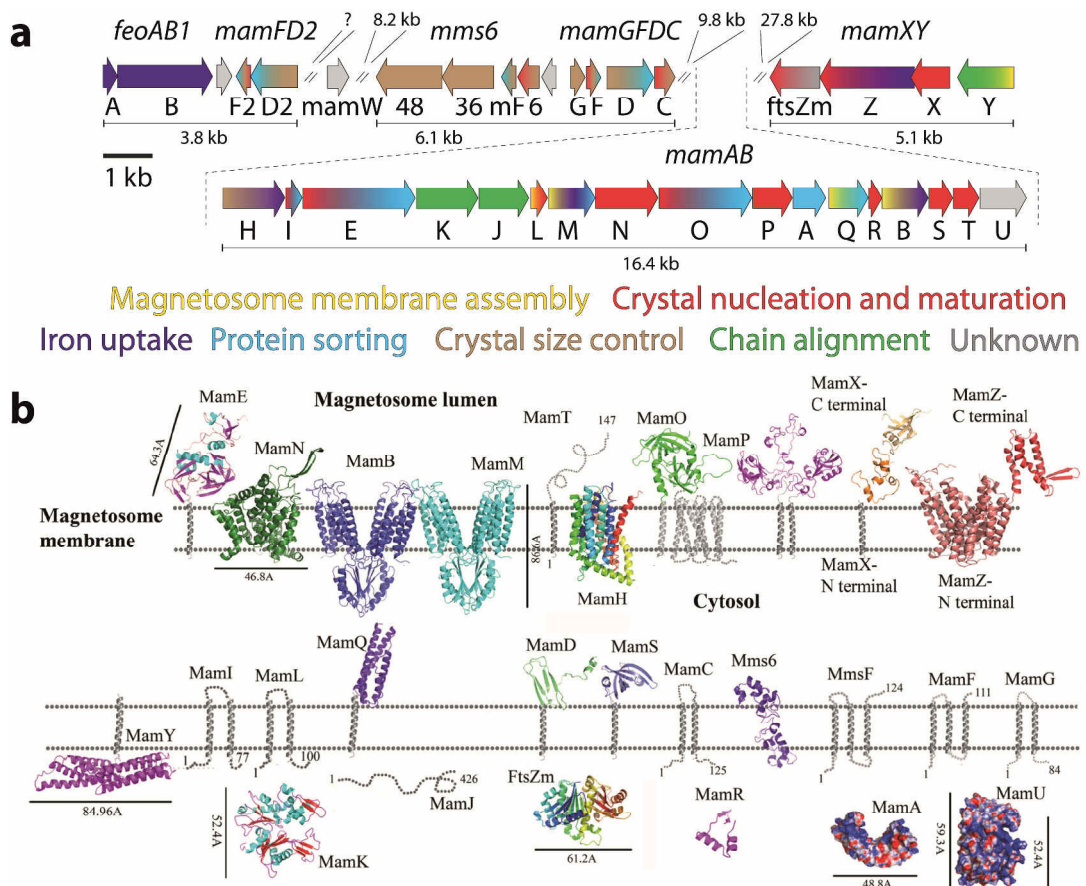


Figure 4: Molecular organization of magnetosome associated genes in the genomic magnetosome island (MAI) and prediction of structure and topology of magnetosome proteins.

(a) Organization of relevant magnetosome-associated genes within the MAI of *M. gryphiswaldense*. The distances between the operons are indicated. The genes are colored due to their experimentally proven or evidence-based predicted function for the magnetosome formation process (see caption). Findings of this thesis are already incorporated. Due to the lack of data, no specific function can yet be associated to grey-colored genes. Some genes show multi-color labeling, indicating that they are involved in several processes.

(b) Homology modelled structures of most proteins from the major four operons. MamA and MamU structures are represented in stick-and-ball model, while all other protein structures are represented in ribbon model. Fully grey proteins are only represented in secondary structure due to the absence of valid templates for modelling. Predicted transmembrane helices are indicated. The magnetosome lumen/periplasmic space in both layers is predicted to be above the model membrane, the cytosolic space below. MamB, MamM and MamP are visualized as dimers. Figure 1B is modified and adapted from [109].

1.6.2 The *mamAB* operon encodes the core functions for magnetosome formation

In contrast to *mms6*, *mamGFDC* and *mamXY*, deletion of the whole *mamAB* operon completely abrogated magnetosome formation in *M. gryphiswaldense* and *M. magneticum* [85,110]. Since deletion of all other parts of the MAI, but *mamAB*, still allowed the two organisms to form rudimentary magnetosomes, the 17-18 gene comprising *mamAB* operon was found essential and sufficient for magnetosome formation [85,100]. The functions of the proteins encoded within the *mamAB* operon are variably well investigated: Deletion of *mamH* and *mamU* did not notably influence magnetosome formation [110,111]. While *mamH*, the first gene of the *mamAB* operon, encodes a homolog of the major facilitator superfamily (MFS) transporter, the last gene *mamU* codes for a protein with similarities to diacylglycerol kinases. Their roles in magnetosome formations are so far unclear. [38]. Deletion of *mamR*, *mamP*, *mamS* and *mamT* drastically decreased magnetic properties of *M. gryphiswaldense* and *M. magneticum* cells and led to the formation of significantly smaller and sometimes irregular magnetite particles. These findings indicated that all four proteins play a role in magnetite biomineralization or maturation. These proteins are MTB-specific and do not show any large homologies to described protein families. MamP and MamT, however, contain putative CXXCH heme binding motifs [109,110]. Deletion of *mamN* and *mamI* in *M. gryphiswaldense* led to the formation of very tiny magnetite crystals and amorphous, partially hematite containing particles, respectively [85]. While MamI is a small (7 kDa) MTB-specific transmembrane protein of unknown function, MamN shows weak similarities to a Na⁺/H⁺ antiporter family. It was therefore speculated that the protein functions as a proton extruder to control the pH within magnetosomes [110,112].

Other *mamAB*-encoded proteins are better investigated: MamK is an actin-like protein that polymerizes *in vitro/vivo* and forms the magnetosome filament. The filament assists magnetosome chain organization and positioning [51–53,60,113]. In *M. gryphiswaldense*, the acidic MamJ acts as an intermediary to connect the magnetosomes to the magnetosome filament and also stabilizes individual magnetosomes from clustering [60,114,115]. Deletion of *mamA* caused a slight reduction in magnetite particle numbers and led to the formation of some empty magnetosome compartments [88,111]. The soluble MamA seems to oligomerize and

co-interact with integral magnetosome membrane proteins to form a magnetosome-surrounding matrix [116,117]. Although this feature seems to be reminiscent of eukaryotic vesicle coat proteins, MamA is most likely not involved in magnetosome membrane formation, since the mutant contains regular vesicles. It was rather suggested that the protein is implicated in activating magnetosomes for magnetite biomineralization [88].

Deletion of either *mamL*, *mamQ*, *mamB*, *mamM*, *mamE* or *mamO*, on the other hand, completely abrogated magnetite formation in *M. gryphiswaldense* [69,111,118]. MamB and MamM are homologs of the ubiquitous cation diffusion facilitator (CDF) family and show highest similarity to Fe²⁺/Zn²⁺-transporters [69,90,119]. MamB and MamM were therefore suggested to transport ferrous iron into the magnetosome lumen [69]. CDF proteins usually contain six conserved transmembrane helices and form homodimers [119], biochemical studies suggest that MamM and MamB together might additionally form heterodimers [69]. The cytoplasmic C-terminal domain in MamB contains a tetratricopeptide repeat (TPR) recognition sequence and was shown to interact with the PDZ⁵ domain of MamE [69]. MamE and MamO are integral membrane proteins and putative serine proteases of the HtrA/DegP family. Amino acid substitutions in the catalytic triad of both predicted protease domains highly decreased magnetite crystal size in *M. magneticum* [120]. Similar to MamP and MamT, MamE additionally contains two putative heme-binding CXXCH motifs that are crucial for the formation of regular magnetite crystals [120]. Furthermore, deletion of *mamE* led to the mislocalization of several GFP-labeled magnetosome associated proteins (MamJ, MamA, MamI, MamC) [110,120]. It was therefore suggested that MamE has a bi-functional role in protein sorting after magnetosome membrane invagination and in controlling biomineralization [120]. Similar to MamI, MamL is a small (9 kDa) MTB-specific protein without any described functional domain, but two predicted transmembrane helices [109]. The only distinguishable feature of MamL is the high abundance of positively charged amino acids in its C-terminal region, which are absent in MamI. MamQ is a member of the LemA protein family, typified by LemA from *Listeria monocytogenes* [90,121]. Although proteins

⁵ PSD95/Dlg1/zo-1, structural protein domain that is associated with protein-protein interactions [171]

of this family are found widespread in prokaryotes, their biological functions are so far totally unclear [122]. All proteins from this family comprise a short N-terminal unstructured region with a predicted transmembrane helix, followed by a larger soluble C-terminal domain. The C-terminal domain of LemA from *Thermotoga maritima* was crystallized and showed a coiled-coil bundle formed by four α helices (compare with Figure 4b).

Altogether, only the six genes *mamBELMOQ* were found essential for biomineralization in *M. gryphiswaldense*. The ability of the mutants for magnetosome membrane formation was however so far not comprehensively analyzed. It is known that $\Delta mamE$ and $\Delta mamO$ still produce chains of empty magnetosome membranes and $\Delta mamM$ produced single empty magnetosome vesicles. However, none of these structures were found in $\Delta mamB$ [69,118].

Notably, slightly different observations were made in *M. magneticum*: Here, *mamN* and *mamI* were also essential for magnetite biomineralization and their deletion completely abrogated crystal formation [110]. Only deletion of *mamI*, *mamL*, *mamQ* and *mamB* led to the complete absence of magnetosome membranes and it was therefore suggested that these four genes are essential for magnetosome membrane formation [110].

1.7 General and bacteria-specific mechanisms of internal membrane formation

Until now, it was totally unclear how magnetosome proteins induce the invagination of the cytoplasmic membrane to form the boundary of the magnetosome organelle. In general, internal membrane formation and invagination must be preceded by the creation of local curvature within the cell membrane. Mechanistic models for this process were mostly derived from eukaryotic systems [123]: Five distinct mechanisms were described for the introduction of membrane curvature (Figure 5): (1) *Lipid heterogeneity*: Theoretically, membrane curvature can be created ‘spontaneously’ by a heterogeneous lipid distribution. This might proceed by the enrichment of lipids with bulky polar head groups in one leaflet of the membrane and lipids with small head groups in the other, a mechanism that is however highly unlikely to self-organize and requires protein mediated energy input, e.g. by flippases [124] (2) *Cytoskeletal elements*: actin filaments can cause membrane tubulation by exerting a force (‘pushing’) against the membrane, as seen in filopodia. However,

when a pulling force would be required, e.g. for invaginating the plasma membrane from the cytoplasmic side, motor proteins would have to transmit the polymerization force onto the membrane [125]. (3) *Protein scaffolding and crowding*: Asymmetrically bound peripheral membrane proteins can effectively introduce curvature by imposing their own curved surface structure onto the membrane. Huge clusters of curved proteins can accordingly invaginate and stabilize the membrane, e.g. prior to vesicle formation. Very well documented examples of multimeric spherical scaffolds are protein coats such as clathrin, COPI⁶ and COPII that interact with cargo receptors. Cylindrical scaffolds can be created by polymeric dynamin and proteins containing BAR⁷ domains [123]. The mechanoenzyme dynamin is majorly known to participate in neck constriction and scission of invaginated buds to form vesicles. Recently, it was shown that local tethering and crowding of unspecific soluble proteins on one side of a model membrane *in vitro* also can create curvature, even when the proteins are usually not associated with invagination processes, like GFP⁸. This might be driven by lateral pressure from steric protein congestion on one side of the membrane and might generally also explain the high efficiency of scaffolds [126]. (4) *Shallow membrane insertion*: Amphipathic helices insert only into one leaflet of the lipid-bilayer membrane. This imposed asymmetry can also very efficiently invaginate the underlying membrane. Examples for this mechanism are given by Arf, Arl and caveolin proteins, as well as N-BAR and ENTH⁹ domains, which all are involved in membrane invagination processes and combine shallow membrane insertion with scaffolding, either by itself or additional factors [123,127,128]. (5) *Insertion of integral membrane proteins*: It is known that membrane-integral voltage-dependent K⁺-channels and acetylcholine receptors localize preferentially in curved membranes, but clusters of these proteins can likely also transmit their conical shape into the membrane to create curvature [125,129,130]. This also seems to be the case for non-funnel shaped transmembrane domains of clustered proteins that exhibit bulky soluble domains on one side of the

⁶ Coat protein complex

⁷ Bin–Amphiphysin–Rvs, curved structural dimerization domains that often occur in proteins associated with membrane remodeling/dynamics [172]

⁸ Green fluorescent protein

⁹ Epsin N-terminal homology, alpha-helical, globular protein domain that is associated with lipid and protein interactions [173]

membrane [125]. Despite these findings, insertion of integral membrane proteins remains the least best described mechanism for curvature formation [130].

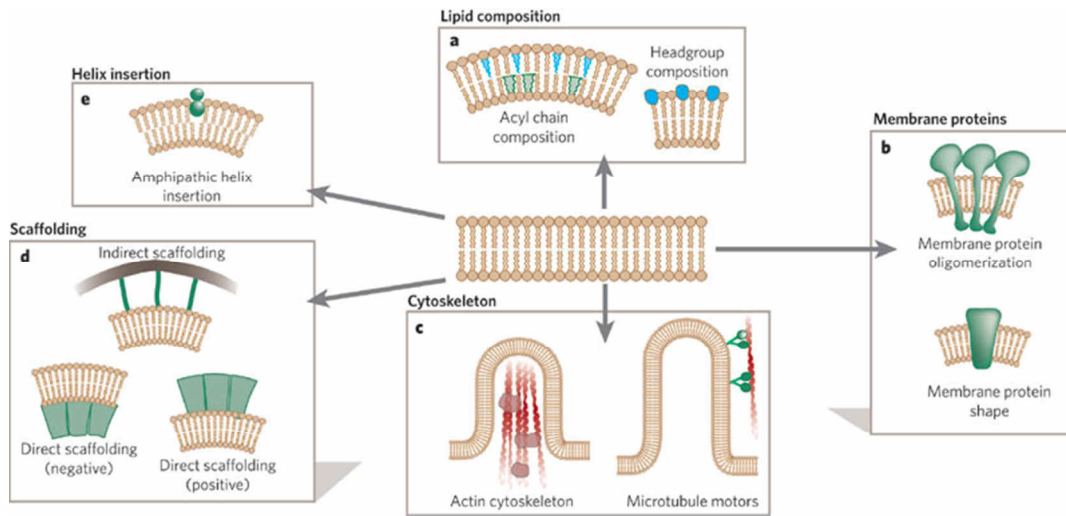


Figure 5: Suggested mechanisms for membrane curvature formation. For detailed explanations, see main text. Adapted from [125]

Although a variety of ICM were described in bacteria, very little is known about the underlying formation mechanisms. Orthologs to eukaryotic coat-like and other endocytosis-related proteins are present in genomes of some members of the PVC superphylum [131], but no other bacteria. Dynamin-like proteins are more widely conserved in a number of bacterial strains and showed the ability for membrane remodeling and fusion *in vitro* [132,133]. However, so far no conclusive *in vivo* evidence for a role in ICM formation exists for any of these proteins and no ortholog of them is encoded within the genome of *M. gryphiswaldense*.

One of the very few bacterial model organisms for ICM formation is *Rhodobacter sphaeroides*. This phototrophic Alphaproteobacterium forms several 100 intracellular membrane vesicles per cell that house the photosynthesis machinery. These vesicles contain large dimers of the photosynthetic RC-LH1-PufX¹⁰ “core” complex that have dimensions of 20.4 x 12.8 nm and exhibit a 146° angle bend shape between both subunits. *In vitro*, the protein indeed causes formation of regular tubular structures in the presence of lipids. Furthermore, vesicles are densely populated with regular clusters of ring-shaped LH2 complexes. Computer simulations predicted that

¹⁰ Photosynthetic reaction center (RC) & light harvesting (LH) complex associated with protein PufX

insertion of both types of complexes into a model membrane can introduce local curvature, suggesting that both contribute to photosynthetic vesicle formation in *R. sphaeroides* [17,134–136]. Otherwise, it is known that the formation of ICM can be nonspecifically induced by the overproduction of integral [137,138] or monotopic membrane proteins [139] in strain that normally lack the ability to form ICM, such as *Escherichia coli*. Furthermore, by heterologous expression of caveolin in *E. coli*, the formation of ICM was presumably also specifically induced by the action of an eukaryotic membrane-remodeling factor [140].

Magnetosomes have emerged as an interesting model system to study the formation of a prokaryotic ICM system. Yet, many of the more basic questions about magnetosome membrane formation are unanswered or were never examined. Finding answers to the following questions might not only significantly advance magnetosome research, but might also improve the current understanding of ICM formation in prokaryotes.

- (I) Does the magnetosome membrane form a continuous structure with the cytoplasmic membrane or does it become detached to form free vesicles?
- (II) What are the essential and sufficient genetic determinants for magnetosome membrane formation?
- (III) What is the exact protein composition and protein abundance in the magnetosome membrane?
- (IV) How are magnetosome proteins organized in the cytoplasmic membrane prior to invagination of the magnetosome membrane?
- (V) What is the structure-function relationship of magnetosome proteins in magnetosome membrane formation?
- (VI) How do magnetosome proteins initiate membrane invagination? Are there intermediary formation stages and can the process be visualized?

1.8 Scope of this work

This thesis had four main objectives. First, to overcome the limitations of the currently available genomic manipulation techniques in *M. gryphiswaldense*, a genetic tool based on *galK* counter-selection was developed and subsequently adapted for precise genome tailoring.

The genes *mamX* and *mamZ*, encoded in the *mamXY* operon, remain the last genes of the major MAI operons, whose function was not yet assessed. The second project therefore aimed to understand the function of the two proteins in the magnetosome formation process.

The third and main goal of this thesis was to improve the currently small knowledge about the control of magnetosome membrane biogenesis. To this end, the ultrastructure of *M. gryphiswaldense* wild type and several mutants was intensively studied using cryo-electron tomography. Open questions about the magnetosome membrane formation biogenesis were addressed and the essential and sufficient genes for the process were elucidated. Additionally, the possibility to enable *de novo* magnetosome formation by means of an inducible expression system was investigated.

Finally, to refine the protein composition of the magnetosome membrane and to assess the relative abundancies of the integral membrane proteins, a semi-quantitative and comparative proteomic approach with different cellular fractions of *M. gryphiswaldense* was developed and evaluated.

2 Discussion

2.1 An efficient genetic tool for tailored chromosomal manipulations in *M. gryphiswaldense*

Established methods for targeted genomic manipulation in *M. gryphiswaldense* were so far cumbersome and time-consuming. In search for a more reliable counterselection marker for double crossover recombination, we tested the gene *galK*, which was already successfully applied for this purpose in other bacteria [141,142]. The conserved galactokinase GalK phosphorylates galactose in the first step of the galactose metabolizing pathway. In the absence of the downstream enzymes, the action of GalK accumulates galactose-phosphate to cytotoxic levels [143]. We found that the genes of the *gal* operon are absent from the genome of *M. gryphiswaldense* and that the strain could tolerate growth on medium containing galactose. Despite the lack of known active galactose uptake systems, the strain was efficiently killed by heterologous *galK* expression in the presence of the sugar. Based on these findings, we subsequently developed a suicide vector that contained an antibiotic marker, a multiple cloning site for homologous regions and inducible *galK* as the counterselection marker. The plasmid and the whole workflow for gene deletion are shown in Figure 6. By deleting a gene of the polyhydroxybutyrate (PHB) metabolism, we proved that the system can be efficiently utilized for markerless genomic in-frame deletions with minimal screening effort. Previously, the creation of deletion mutants within the genome of *M. gryphiswaldense* typically took several months. The *galK* counterselection method significantly decreased the required time to construct a deletion to three to four weeks. The system not only enabled the high-throughput and repetitive markerless deletion of single genes and genomic regions, but also allowed the introduction of new genetic sequences of variable length to respectively create gene fusions or point-mutations at the native chromosomal locus of the target gene. We proved this by constructing strains with in-frame fluorescent protein fusions at the native chromosomal position of *mamC* and *mamK*. The strains exhibited almost wild type like magnetosome formation properties and showed very stable and consistent fluorescence, unmatched by all previously applied plasmid systems. The here developed system is therefore in most cases advantageous over all previous methods for genomic modifications. It was applied in subsequent projects

of this thesis and in several other studies [36,111,144–146] and now is the state of the art genome engineering tool for *M. gryphiswaldense*.

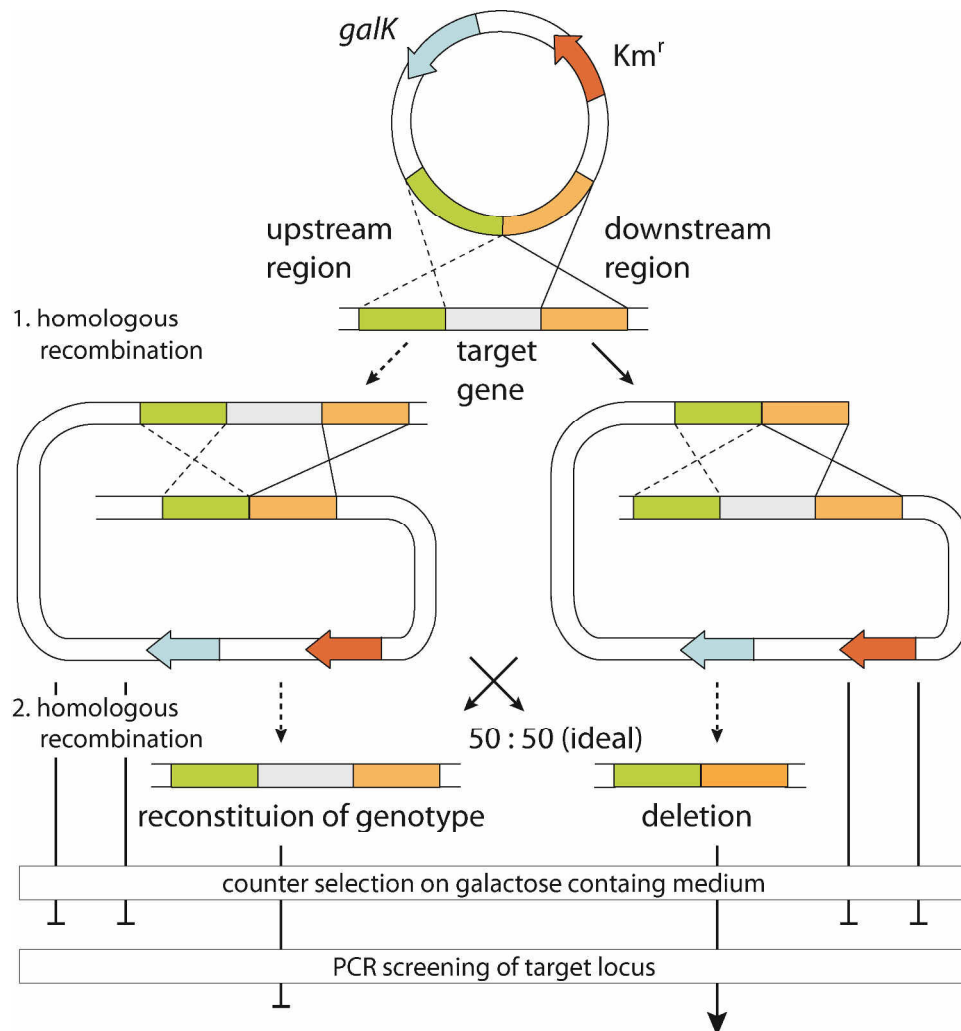


Figure 6: Scheme for markerless in-frame gene deletion using *galK* counterselection vector. The vector contains a kanamycin resistance marker gene (*Km^r*) and the counterselection gene *galK*, as well as DNA fragments that are homologous to regions upstream (green) and downstream (orange) of the target gene. The first homologous recombination inserts the plasmid via one or the other homologous region into the genome of the host. Insertion mutants can be selected by kanamycin resistance. Random secondary homologous recombination events in passaged cultures will excise plasmid and either reconstitute the genotype of the mother strain (via the same homologous region as in first recombination) or will cause the desired gene deletion (via the other region). Counterselection with galactose medium will discriminate and kill clones that did not undergo secondary recombination event and still contain *galK* gene. Remaining clones have to be screened by PCR to discriminate desired (here: deletion) genotype from reconstituted mother strain genotype. Modified and adapted from [147].

2.2 Proteins encoded within the *mamXY* operon play an important role in magnetosomal redox control systems

Formation of stoichiometric magnetite crystals requires specific control over the physicochemical parameters within the magnetosome compartment, including control of the redox-environment. Deletion of the *mamXY* operon caused the formation of poorly crystalline particles at the magnetosome chain ends, which hinted towards an unbalanced magnetite redox control in the mutant [85]. Along with the previously mentioned *mamY*, the *mamXY* operon comprises the genes *mamX*, *mamZ* and *ftsZm* (Figure 4) [148]. The last gene of the operon, *ftsZm*, intriguingly encodes a homolog of the cell division protein FtsZ [149]. Although FtsZm was shown to polymerize and co-polymerize with FtsZ *in vitro* and *in vivo*, deletion of *ftsZm* in *M. gryphiswaldense* did unexpectedly not affect cell division or magnetosome chain segregation, but caused the formation of prevailing poorly crystalline and small magnetosome particles in the absence of nitrate from the medium [103,149]. FtsZm therefore rather is involved in the process of magnetite biomineralization than any other process unusually associated with cytoskeletal proteins [149].

The remaining two genes of the operon, *mamX* and *mamZ* were not investigated so far and therefore subjected to a detailed mutagenesis analysis in this thesis. We found that MamX, similar to MamP, MamT and MamE, contains a paired CXXCH motif, which is known to mediate covalent heme binding in *c*-type cytochromes [150]. Deletion of *mamX* caused a magnetite mineralization phenotype that phenocopied deletion of the whole operon. Although wild type-sized and frequently twinned magnetite particles were observed in the center of the mutant's magnetosome chain, the outer particles were of flake-like and poorly crystalline consistency, but housed in regular magnetosome membrane vesicles. Surprisingly, some of the flake-like particles could be identified as hematite (α -Fe₂O₃) by high-resolution TEM, indicating a major redox imbalance in the formed mineral. Amino acid substitution within the CXXCH motifs of MamX caused the same phenotype as was observed for deletion of the whole gene and revealed that this motif is crucial for the protein's function. In another recent study, the CXXCH domains from purified protein fragments of MamP and MamE were functionally characterized and shown to be redox active. Siponen *et al.* therefore termed this new motif 'magnetochrome'

domain. [151]. Additionally, the crystal structure of MamP from the magnetotactic ovoid bacterium MO-1 was determined [152]: MamP dimerized and showed a di-iron binding pocket, formed by both subunits. The magnetochrome domains exhibited a distinct new fold and each coordinated a covalently bound heme. Furthermore, purified MamP homologs from *Magnetospirillum marine* and *M. magneticum* were shown to have a cytochrome c-like redox activity [151]. Although no biochemical experiments were so far performed with MamX, the occurrence of two magnetochrome domains highly suggests that the protein is also redox active and might be a dimer in its active form.

In the *mamXY* operon, *mamX* is followed by the overlapping *mamZ* gene, suggesting translational coupling (Figure 4a). MamZ has a unique domain composition, comprising a full-length MFS transporter domain fused to a YedZ-like ferric reductase domain (Figure 4b) [153] and suggesting that the protein is involved in redox coupled transport processes. The genuine YedZ protein is associated with a heme group and part of an oxidoreductase [154], which, as shown here, is not involved in magnetite formation in *M. gryphiswaldense*. Deletion of the whole *mamZ* gene or only of its *yedZ*-like domain also did phenocopy deletion of *mamX* and the *mamXY* operon. This not only highlighted the importance of the YedZ-like domain for the function of MamZ, but also strongly suggested that MamX and MamZ are both constituents of the same functional process. Both proteins hence have potential redox active domains which are essential for their function and the absence of the proteins affected the mineralization state of the magnetosome particles.

The MFS domain of MamZ shows high sequence similarity to MamH, which is a predicted MFS transporter without additional domains and encoded as the first gene of the *mamAB* operon. Although *mamH* deletion alone did not cause a strong magnetosome phenotype, co-deletion with *mamZ* further impaired magnetite formation and magnetic orientation of *M. gryphiswaldense*. MamZ and MamH therefore seem to partly complement the function of each other. Since both proteins are predicted transporters, they might be involved in (ferrous) iron(-chelate) transport, and in the case of MamX/MamZ combine this function with iron oxidoreductase activity.

Proteins with magnetochrome domains are redundant in *M. gryphiswaldense* and found in every magnetotactic bacterium. The magnetochrome domains of MamE,

MamT and MamP were also shown to be involved in magnetite biomineralization control *in vivo* [120,155,156]. *In vitro*, MamP from MO-1 and *M. magneticum* could efficiently oxidize ferrous sulfate to ferrihydrite and later magnetite [152,156]. Although none of the magnetochrome proteins is individually essential for magnetite formation, together they might be essential for the process. The redundancy of magnetochromes in some MTB might be explained by different electron transfer partners and pathways. MamX and MamZ could for example play a role in iron uptake and coupled oxidoreduction, while MamP, MamT and MamE oxidize soluble ferrous iron.

Interestingly, magnetosome redox control and metabolic respiration seem to be linked, since deletion of the periplasmic nitrate reductase Nap, the cytochrome *cd*₁ nitrite reductase NirS, as well as the terminal oxidase *cbb*₃ also impaired magnetite biomineralization in *M. gryphiswaldense* [75,146,157]. Nap and NirS perform the first steps of respiratory nitrate reduction by subsequently reducing nitrate to nitrite and nitrite to nitric oxide. It is rather unlikely that the respiratory enzymes are directly involved in magnetite biomineralization. However, these findings indicate that some specific respiratory enzymes can directly or indirectly re-oxidize other fully reduced enzymes, presumably magnetochromes, and so reactivate them for their function in magnetosomal iron redox control (Figure 7b). The pathway of this reaction is currently unclear. Strikingly, when we cultivated Δ *mamX* or Δ *mamZ* in medium without nitrate, the phenotypes were further aggravated, almost causing the total absence of wild type-like magnetite crystals and the prevalent occurrence of poorly crystalline flakes. The same was true when *nap* and *mamX* were co-deleted. The removal of Nap function or its substrate nitrate most likely caused an additive effect on the already imbalanced redox control due to *mamX* deletion, forcing the whole redox control system to collapse in certain magnetosomes. Intriguingly, the adverse effect of *ftsZm* deletion could also only be triggered by depriving the cells from nitrate [149]. Although the connection between a potential cytoskeleton protein and redox control is very unexpected, it might be explained by a function of FtsZm in organizing other redox active proteins [149]. Altogether, the results indicate that the *mamXY* encoded MamX, MamZ and FtsZm play an important role in the complex redox control system of *M. gryphiswaldense* and most likely also in other magnetotactic Alphaproteobacteria. A model to illustrate magnetite biomineralization is shown in Figure 7b.

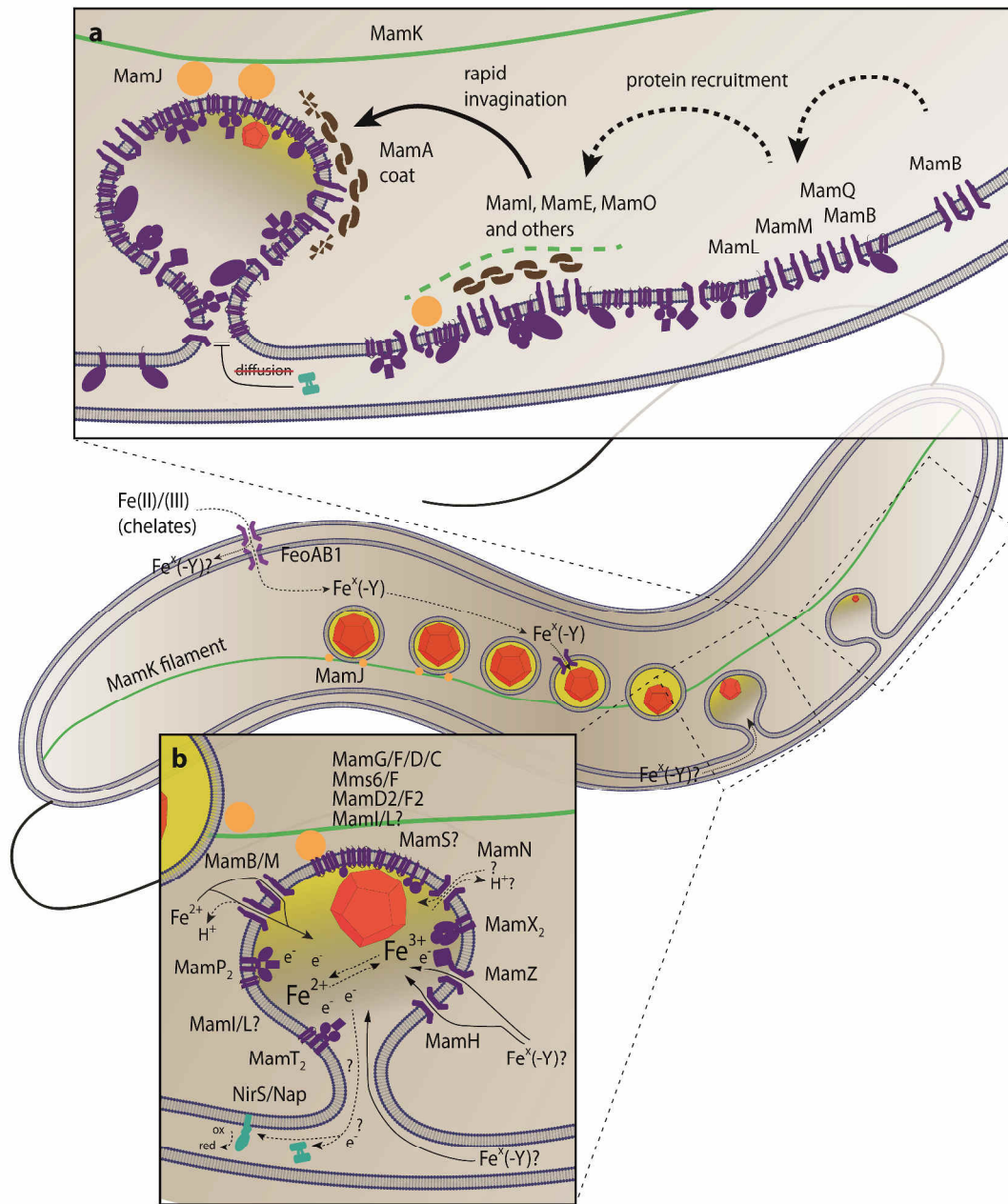


Figure 7: Model for magnetosome membrane formation and magnetite biomineralization in *M. gryphiswaldense*. The background shows a general model of iron import and magnetosome organization. Detail (a) shows a hypothetical model for magnetosome membrane (MM) formation and invagination. MamB primes the nucleus for magnetosome protein (MMP) accumulation in the cytoplasmic membrane (CM). After assembly of MamMQLIEO, other MMP are recruited to form a dense cluster. Protein crowding and the structure of the transmembrane proteins introduce curvature into the CM and causes rapid invagination of the MM. For more schematic representation, see also Figure 8. Detail (b) shows a model for magnetite biomineralization. MMPs putatively involved in redox control, iron import, proton export and crystal nucleation are shown. Iron is transported in the magnetosome lumen via cytoplasm (MamB/M) and/or periplasm (unknown mechanism). MamPTX(E) adjust Fe²⁺ and Fe³⁺ ratio for magnetite nucleation and growth, MamZX forms a putative iron uptake/redox control complex. NirS/Nap/(ccb₃) remove excess electrons. Magnetite nucleation is supported by the action of Mms6 and MamGFDC-like proteins and probably by MamI/MamL.

2.3 Genetic control over magnetosome membrane formation - MamB is most important, but not sufficient for the process

While the biomineralization of magnetosomes and their subsequent assembly into linear chains recently have become increasingly well understood, very little is known about the molecular mechanisms of magnetosome membrane biogenesis. In order to investigate the essential gene set for magnetosome membrane formation, we analyzed the ultrastructure of several key deletion mutants that were previously found to be impaired in magnetite formation [69,111]. The cryo-tomography data (see chapter 2.4 for more detailed information about this technique) presented in this thesis showed that in *M. gryphiswaldense* single gene deletion of *mamN*, *mamI* and *mamL* does not cause the elimination of magnetosome vesicles. Compared to the wild type, vesicles in Δ *mamL* however appeared smaller and reduced in number, indicating an accessory role for the protein in magnetosome membrane formation. While Δ *mamL* was previously considered to be devoid of iron-minerals [111], even magnetite particles were unexpectedly found in some of the magnetosome vesicles of the mutant. Besides the impact of MamL in magnetosome membrane formation, the phenotype of Δ *mamL* therefore strongly suggests a dedicated role of the protein in the biomineralization process. We further could pinpoint this function down to the carboxy-terminal region of MamL, which is particularly rich in basic, potentially positively charged amino acids. Substitution of these residues in groups to similar but neutral amino acids had a gradual effect on the biomineralization properties of the mutants and substitution of all basic residues completely phenocopied the whole-gene deletion mutant. It is not clear if the protein is directly involved in biomineralization or indirectly by the ability to recruit other proteins. The latter is supported by localization experiments which suggested that MamL might be involved in the proper localization of MamC-GFP and to a lesser degree also seems to influence positioning of MamI-GFP.

In addition to generally smaller magnetosome vesicles, some of the empty magnetosome membranes in the Δ *mamL* mutant exhibited an aberrant appearance with an electron denser lumen and poorer contrast in cryo-electron tomograms, as compared to wild type-like magnetosome vesicles. These vesicles were called dense magnetosome membrane-like structures (DMMs). DMMs were also found in tomograms of both Δ *mamQ* and Δ *mamM*, which showed comparable phenotypes to

each other: Although some cells displayed few scattered empty wild type-like magnetosome membranes, they predominantly comprised the described DMM structures. In some $\Delta mamQ$ and $\Delta mamM$ cells, these DMMs were very abundant and then also organized along a linear cytoskeletal structure, most probably the magnetosome filament. The magnetosome marker protein MamI-GFP showed linear fluorescent signal in some of the $\Delta mamM$ and $\Delta mamQ$ cells, indicating that the protein still became recruited into DMMs. MamI-GFP recruitment and magnetosome filament-association therefore suggests that the structures represent abnormal magnetosome membranes. It is not totally clear how these structures are formed and what is the nature of their electron-dense lumen. One possibility might be that soluble iron is accumulated, but does not precipitate as magnetite.

Interestingly, N-terminally fluorescently labeled MamQ formed patches in the cytoplasmic membrane rather than accumulations in the chain aligned magnetosomes. If this localization pattern was not artificially caused by presence of the fluorophore, it might indicate a function for MamQ in orchestrating magnetosome proteins within the cytoplasmic membrane.

Nevertheless, the results indicated that both *mamM* and *mamQ* are not essential for the formation of magnetosome membrane-like structures, but might somehow be involved in controlling their correct assembly. Tomograms of $\Delta mamB$ cells, on the other hand, were found to be devoid of any wild type-like magnetosome membranes and only a few cells showed low-abberant structures that resembled DMMs, albeit never organized in coherent chains. While magnetosome membrane formation is therefore most severely inhibited in that strain, MamB also does not seem to be absolutely essential for the formation of internal membranes.

M. gryphiswaldense $\Delta mamE$ and $\Delta mamO$ are the only magnetite-devoid mutants that were not analyzed in this study, but were already previously shown to still contain empty magnetosome compartments [118]. Hence, *mamB* remained the most crucial gene for magnetosome membrane formation in *M. gryphiswaldense*.

In contrast, individual deletion of either *mamB*, *mamQ*, *mamI* and *mamL* could already completely abrogate magnetosome membrane formation in the closely related organism *M. magneticum*, as assayed by cryo-ultramicrotomy and TEM [110]. Therefore, these four genes were found to be absolutely essential for the process in this strain [110]. If the phenotypical divergence in some mutants of the two strains

was not caused by the different electron microscopy techniques used in the studies or by simply failing to notice these structures, this would hint towards significant differences in magnetosome membrane formation in both strains.

In order to analyze if *mamB*, *mamM*, *mamQ*, *mamL*, the most influential genes for vesicle formation in *M. gryphiswaldense*, are altogether also sufficient for re-enabling magnetosome membrane formation, they were expressed in a mutant background lacking major parts of the magnetosome island, but failed to induce notable internal membrane formation. Even co-expression of a synthetic construct, comprising all individually essential genes for the formation of regular magnetite containing magnetosomes (*mamL*, *mamQ*, *mamB*, *mamE*, *mamI*, *mamM* and *mamO* [111]), could not clearly restore magnetite biomineralization. However, while the expression of the same *mamLQBEIMO*-construct in a strain that lacks the *mamAB*, *mamGFDC* and *mms6* operons did also not notably cause the formation of magnetosome membranes, some scattered and sometimes enlarged vesicular structures were detected when the genes were expressed in a Δ *mamAB* operon strain (i.e. in the absence of all other 11 genes of the *mamAB* operon, but in the presence of 12 genes from *mamGFDC*, *mms6* and *mamXY* operons). This was particularly surprising since the complete *mamAB* operon was also sufficient for the formation of rudimentary magnetosomes [85,100]. Thus, the seven conserved proteins MamLQBEIMO are together not sufficient to induce magnetosome membrane formation, but might constitute the core unit for the process. Only if supplemented by some additional magnetosome proteins encoded either within the *mamAB*, or within the *mms6*, *mamGFDC* and *mamXY* operons, the protein composition allowed for the invagination of magnetosome membrane-like structures.

Interestingly, a very recent study by Kolinko *et al.* succeeded in transferring magnetosome genes from *M. gryphiswaldense* into the non-magnetotactic host *Rhodospirillum rubrum* and with that the ability for magnetosome biogenesis [158]. In contrast to its sufficiency in *M. gryphiswaldense*, the sole transfer of the *mamAB* operon was not sufficient for the formation of detectable magnetite particles in *R. rubrum*, which only succeeded at least in the presence of *mms6* and *mamGFDC* operons [158]. This also indicated that, depending on the genetic context, the *mamAB* operon is not always sufficient to initiate the process of magnetosome formation.

2.4 Insights into structure and formation dynamics of magnetosome membranes

Until now, it was totally unclear how the cytoplasmic membrane is transformed into the magnetosome membrane and if transient membrane invagination stages exist. In order to visualize magnetosome formation and to promote a better understanding of the process, cryo-electron tomography was performed on *M. gryphiswaldense* cells. The fast vitrification of unstained and living cells within amorphous ice ideally preserves the sample in a near-native state [159]. Cryo-TEM images obtained from different angles are used to computationally calculate a three-dimensional tomogram of a cell and enclosed structures. For data interpretation, it is important to note that due to missing information caused by limitations in the angular tilt range, some parts of the tomogram, and of every object within, cannot be reconstructed, causing the so called missing wedge [159].

In previous CET studies with *M. magneticum*, it was claimed that invaginated magnetosome membranes are permanently continuous with the cytoplasmic membrane and do not become detached [52]. Our study confirmed that magnetosome chains are always positioned in close proximity to the cytoplasmic membrane in *M. gryphiswaldense*. Although some invaginated magnetosome membranes were observed to be continuous with the cytoplasmic membrane, other magnetosomes appeared detached and therefore as real vesicles. Due to the missing wedge, only a very limited area of each tomogram shows sufficient information to interpret the continuity of the membranes. While it remained ambiguous in many cases, the presence of clearly disconnected vesicles suggested that magnetosome membrane invaginations eventually become pinched-off. Detached magnetosome vesicles therefore most likely represent the mature development stage, widely confirming a previous model in which magnetosome membranes are only transiently continuous with the cytoplasmic membrane in *M. gryphiswaldense* [51,60].

Another experiment showed that diffusion of GFP and the small fluorescent molecule 5(6) Carboxyfluorescein from the periplasm over the transiently connecting neck into the magnetosome lumen is likely inhibited. Hence, diffusion into the compartment seems to be blocked or tightly controlled at all times, even while magnetosomes membranes are still continuous with the cytoplasmic membrane.

Since magnetosomes are constantly formed in the wild type, which is also not prevented by environmental conditions that inhibit proper magnetite biomineralization, exclusive analysis of *de novo* magnetosome formation was challenging so far. We therefore developed a system for synchronous genetic induction of magnetosome membrane formation based on the most influential gene: *mamB*. The system allowed for time-resolved studies of *de novo* magnetosome formation using CET and fluorescence microscopy. In tomograms, magnetite-containing magnetosome membranes did occur at different and separated positions within the cell after induction of *mamB* expression, but became organized in (multiple) short concatenated chains at an early time point. In time-lapse fluorescence microscopy experiments with inducible, GFP-tagged MamB, the fluorescence also first developed in scattered but defined patches all over the cell membrane that after some time transformed into linear signals. The membrane patches might be interpreted as local protein accumulations or nascent magnetosomes, also indicating that magnetosome membrane formation initiates at random positions from distinct MamB clusters in the cytoplasmic membrane. In tomograms, magnetite crystals were only observed in invaginated membranes or vesicles, indicating that magnetite biomineralization does indeed only initiate after formation of the magnetosome compartment. Before crystals could reach the stable ferrimagnetic size range, magnetosomes were already recruited into magnetosome chains, presumably by the action of the MamK filament, similarly to previous observations by iron-induction of iron starved cells [60].

Interestingly, *mamB* induction also caused the formation of dense chains of DMMs, similar as seen in $\Delta mamM$ and $\Delta mamQ$ (see chapter 2.3), potentially as an artefact of the genetic induction. However, as an alternative explanation, DMMs might be precursor structures of regular magnetosome membranes, lacking certain factors that enable the transition to mature magnetosome membranes. In this case, they should transiently also occur in wild type cells. Although DMM could not be unambiguously detected in tomograms of the wild type, conspicuous structures coexisted with regular magnetosomes in some of the analyzed cells and the precursor theory might thus still be a valid alternative for the appearance of DMMs.

Otherwise, no putative intermediate states of early magnetosome membrane development (e.g. bulges in cytoplasmic membrane) were found in tomograms,

sampled at all time points after induction of MamB expression, indicating that the process of membrane invagination is relatively fast and putative intermediate invagination states must be very transient.

In the course of this thesis, an attempt was made to isolate and purify empty magnetosome membranes of regular and DMM-type from different mutant backgrounds for structural and proteomic analysis. The very abundant MamC and MamA proteins were C-terminally conjugated with a hexa-histidine-tag (6-His) or GFP and expressed in the wild type, $\Delta mamM$, $\Delta mamN$ and $\Delta mamI$ mutants. MamC was chosen for its abundance in the magnetosome membrane and MamA for its likely localization as the outermost protein layer. According to dot blots, the tags were accessible on both proteins to antibodies applied to purified magnetosomes. To isolate magnetosome membrane vesicles by affinity-purification, agarose beads conjugated with GFP-antibodies or Ni-NTA¹¹ were used in batch preparation, gravity flow or pressure flow assemblies. Despite efforts in optimizing binding, washing and elution of the beads, the purification of empty or crystal-filled magnetosomes from cell lysates repetitively failed. Even magnetically separated wild type MamC-6-His magnetosomes did not efficiently bind to the Ni-NTA bead material, indicating that not only purification of vesicles out of cell lysates was impeded, but that the binding strength of the system or accessibility of the tag generally was too low to allow a sufficient strong interaction of the large organelle and the beads.

2.5 The magnetosome membrane is tightly packed with integral Mam and Mms proteins

Previous proteomic studies with isolated magnetosomes revealed the presence of a great number of proteins that are not encoded within the major MAI operons [91,160,161]. Until now it was not completely clear if some of these factors are genuinely anchored within the magnetosome membrane or if they represent contaminants. Many of these proteins were also abundantly found in the cytoplasmic membrane fraction, like ATPase subunits, or were obvious contaminants, like outer membrane proteins (OMPs) [91,160,161]. For most other proteins found in the

¹¹ Nitrilotriacetic acid coordinated nickel ions

magnetosome membrane, it was less obvious. For example, an abundant magnetosome-enriched GTPase that early evoked interest for being possibly involved in magnetosome membrane remodeling and therefore named Mms16 was later found to be directly involved only in PHB metabolism, and therefore to likely be a contamination in purified magnetosomes [81,162].

The comparative semi-quantitative proteomic approach developed and conducted in this thesis aimed to discriminate contaminants from genuine integral magnetosome membrane proteins and also tried to reveal unrecognized *bona fide* magnetosome membrane proteins. Furthermore, it was designed to estimate the abundance of individual magnetosome proteins within the compartment.

To achieve this goal, the protein compositions of magnetically separated magnetosomes, ultra-pure magnetosomes after high-salt and alkaline buffer treatment, total membrane fraction and total nonmagnetic cell lysate fraction were analyzed by gel electrophoresis and liquid chromatography tandem-mass spectrometry. The obtained peptide spectra data were normalized, cross-correlated and interpreted by the criteria that genuine (*bona fide*) integral magnetosome membrane proteins have to be highly enriched in the magnetosome membrane, be true integral membrane proteins, and do not become diluted by stringent magnetosome washing. Our results indicated that, by far, most of the >1000 individual proteins found in magnetosome preparations are contaminations from the isolation procedure. Almost all proteins that fulfilled the specified criteria were annotated Mam or Mms magnetosome proteins. On the other hand, all known contaminants, like Mms16 and OMPs, as well as all of the known non-integral (only magnetosome membrane-associated) Mam proteins, like MamK and MamA, were excluded, confirming the high efficiency of the applied methodology.

MamB/C/D/E/F/G/H/I/M/N/O/P/S/T/W/X/Y/Z/F2 and Mms6/F were found to be *bona fide* magnetosome membrane proteins, while Mms36, Mms48, MamA/Q/J/K/R/U/D2 and FtsZm did not meet the criteria and are most likely only magnetosome associated or active in other cellular fractions. Although MamL is a confirmed magnetosome protein (fluorescent microscopy results), it was not at all detected in the experiments, indicating that technical limitations of the method can result in a slight underrepresentation of peptides from specific proteins. The recently magnetosome-implicated MamF2 was found to be an integral magnetosome membrane protein, while we could not reliably confirm this for FeoB1 and MamD2.

Only 5 to 9 of the confirmed integral magnetosome proteins were not annotated as Mam or Mms proteins. However, the calculated abundance for all of these proteins was comparably low and their putative magnetosome localization needs to be confirmed by more direct techniques, for example fluorescence microscopy. Only one of these proteins (MGR_4114) is encoded within the MAI, its deletion did however not cause a magnetosome-related phenotype. The 21 identified Mam and Mms proteins therefore seem to constitute almost the whole mass of integral magnetosome membrane proteins. In combination with recently published quantitative western-blot data that estimated the copy number of the magnetosome membrane protein MamC to be around 100 per magnetosome [163], our semi-quantitative data allowed us to estimate the copy number of all other proteins. The copy number showed a wide distribution and ranged from approximately 120 (Mms6) to 2 (MamX and MamZ). According to the data, Mms6, MamC, MamD, MamE, MamF2, MmsF, MamB, MamM and MamF, in this order, are the most abundant integral magnetosome membrane proteins. Very intriguingly, taking into account the average membrane surface area calculated from cellular cryo-tomograms and the predicted topology of the involved magnetosome proteins, approximately 20% of the magnetosome membrane already seems to be occupied by trans-membrane helices of integral proteins. Assuming that these hydrophobic protein moieties are coordinated by rings of boundary lipids in the membrane, the surface coverage increases to approximately 63-97%, only counting the first order boundary lipid. This hints towards a densely protein-packed membrane and a very rigid organization with a limited number of free lipids. Initial native gel electrophoresis data obtained in this work also implies that magnetosome proteins after detergent extraction form several high-molecular weight clusters and remain in complexes, also indicating a dense and stable magnetosome membrane protein organization.

2.6 New hypothetical models for magnetosome membrane formation

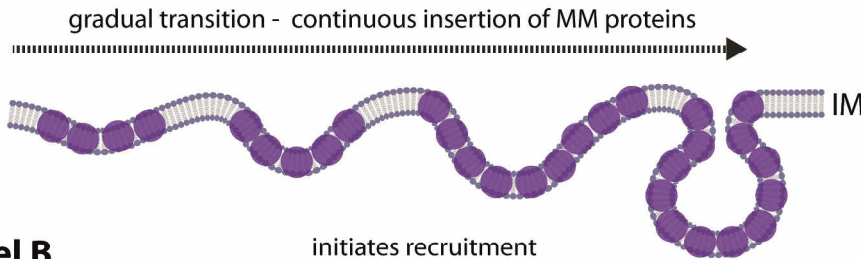
So far, it was mainly assumed that single magnetosome proteins have a direct function in membrane remodeling. For example, it was suggested that the positively charged residues of MamL could intercalate into the membrane to create curvature in a wedge-like manner [65]. It however was shown here that these residues are mainly involved in biomineralization related processes. Likewise, MamQ was implicated in membrane-bending since its coiled-coil helix domain is very remotely reminiscent of

the curvature sensor F-BAR [65]. Our data however also suggests that the protein is not absolutely essential for membrane formation and therefore most likely not directly involved in membrane remodeling. Also MamY, which was linked with membrane tubulation in *M. magneticum*, is most likely not involved in magnetosome membrane formation, since its elimination does not majorly change the appearance of magnetosomes in *M. magneticum* [104] and *M. gryphiswaldense* [O. Raschdorf, M. Toro-Nahuelpan, F. D. Müller, unpublished].

The results presented in this thesis rather suggest that the initial steps of magnetosome formation are more complex in terms of the numbers of participating proteins, but less structurally controlled than expected earlier. As already suggested in a recent review [164], magnetosome membrane formation seems to rather proceed by local protein accumulation in the cytoplasmic membrane, which after a critical protein composition and concentration is reached, causes the newly formed magnetosome membrane rapidly to invaginate. The organization of magnetosome membrane proteins within the cytoplasmic membrane is most likely orchestrated by certain key proteins. Since MamB is the most important protein for the process, it could act as the initial landmark factor in the cytoplasmic membrane (Figure 7a and Figure 8). Considering that aberrant magnetosome membranes are formed in the absence of MamM, MamQ and less dominantly also in the absence of MamL, the proteins most probably also are recruited at an early stage and might in turn be involved in targeting other proteins to the nucleation area in the cytoplasmic membrane (Figure 7a and Figure 8). If one of these proteins is missing, the composition of the recruited proteins might drastically change and only allow for the formation of smaller DMM invaginations with an aberrant protein composition (Figure 8). Next, MamI, MamE, and MamO are recruited to complete the core protein set that attracts and organizes further redundant magnetosome proteins. Membrane invagination might then proceed by a scaffold that is formed by the interaction and oligomerization of all recruited magnetosome proteins and which overall bends and remodels the membrane analogous to the classical scaffolding and integral transmembrane protein mechanisms [124,125]. This might be similar to chromatophore membrane invagination in *R. sphaeroides*, which also seems to proceed via curved transmembrane protein complexes and clusters (see chapter 1.7) [135]. Alternatively, an inhomogeneous membrane protein composition created by

the local crowding of integral magnetosome proteins in the cytoplasmic membrane of *M. gryphiswaldense* might introduce curvature and lead to invagination of these areas (Figure 7a).

model A (alternative)



model B (preferred)

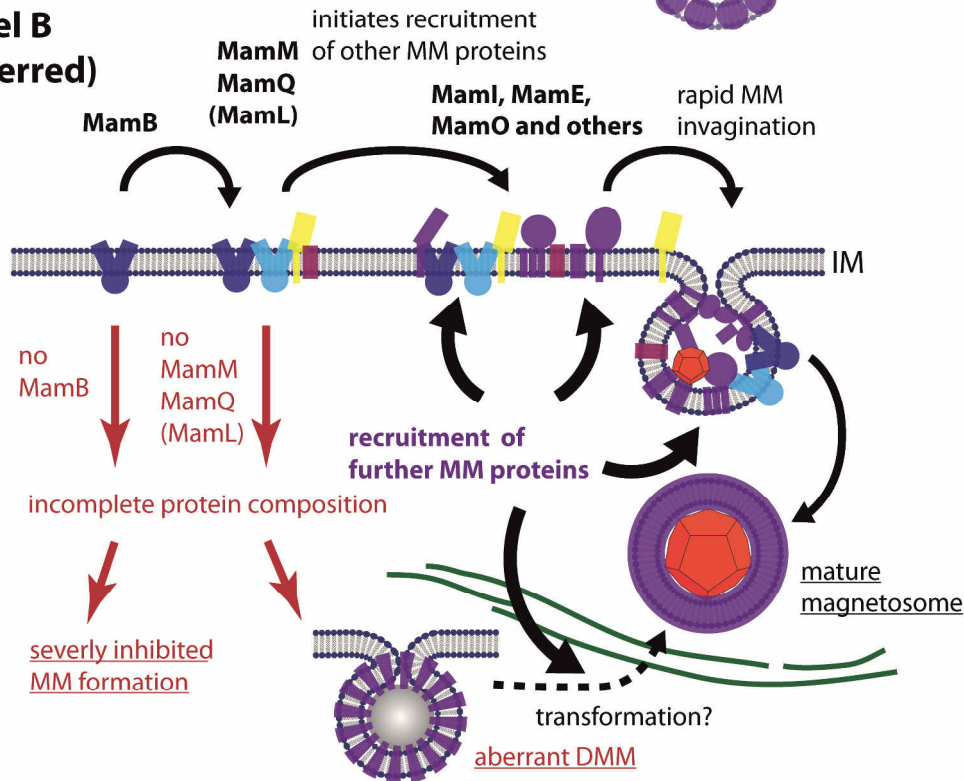


Figure 8: Models for magnetosome membrane formation in *M. gryphiswaldense*. Two different models are presented. Model A suggests a gradual transition of the cytoplasmic membrane into the magnetosome membrane (MM) by a continuous recruitment of magnetosome membrane proteins (pink circles), which causes the membrane to bulb and finally to invaginate. Model B suggests that MM proteins are recruited into the cytoplasmic membrane in a hierarchical manner, with the key proteins MamB, MamM, MamQ and MamL (labeled in shades of blue, yellow and red) acting as nucleating factors. MamI, MamE, MamO are also recruited and in turn help the orchestration of additional magnetosome proteins. After a critical protein concentration/composition is reached, the MM domain invaginates rapidly to form the magnetosome lumen. The membrane finally becomes detached to form magnetosome vesicles. Before or after detachment, several further proteins are recruited into the magnetosome membrane. The absence of the nucleating factor MamB severely inhibits magnetosome formation, while the absence of either MamM, MamQ or MamL might cause a disturbed protein composition, which leads to the formation of defective dense magnetosome membrane-like structures (DMMs) or blocks MM formation at an immature state.

The lack of observable stable intermediary membrane transformation stages in induction experiments rather suggest a very quick (seconds) formation of magnetosome membrane invaginations from assembled protein complexes in the cytoplasmic membrane (model B in Figure 8), than a slow, gradual transformation of the membrane (model A). It still needs to be elucidated if DMMs rather are precursor forms of mature magnetosome membranes, or only stalled and defective end-products. In both cases, an aberrant or immature magnetosome protein composition prior to or after invagination might distinguish DMMs from regular magnetosome membranes and also prevent nucleation of magnetite in these structures (Figure 8).

Since magnetosomes seem to eventually pinch off from the cytoplasmic membrane, the mechanism of scission for invaginated magnetosome membranes is another open question. Although this might as well be a stochastic process, spontaneous scission of vesicles in the size range of magnetosomes membranes is energetically unfavorable [130]. Dynamin-like proteins are absent from *M. gryphiswaldense*, but it might be possible that the actin-like MamK (magnetosome) filament can exert forces on the magnetosomes that are strong enough to cause scission. Alternatively, the strong magnetic attraction forces in between the magnetosomes might also create membrane fission.

Magnetotactic bacteria and other prokaryotes generally lack orthologs of eukaryotic proteins with well described function in introducing curvature for membrane invaginations. Similar as in the *M. gryphiswaldense* magnetosome model, local crowding and complex formation of specific integral membrane proteins might therefore be a common mechanism for internal membrane formation in other bacteria.

2.7 Further directions

Magnetosomes are fascinating prokaryotic organelles whose complex biogenesis is controlled by the action of several magnetosome membrane proteins. In this thesis, the magnetosome proteins MamX and MamZ were e.g. shown to be involved in the magnetosomal redox system and the biomineralization of regularly shaped crystals within the magnetosome compartment. While biomineralization in MTBs recently became increasingly well understood, research on structural aspects of magnetosome biogenesis is at very early stage. Although this thesis comprises the so far most

comprehensive study of magnetosome membrane formation and could address or answer some questions regarding the first steps of magnetosome formation, a multitude of open issues remained or arose in that study and might be pursued in follow-up research:

- The nature of DMMs: These electron denser and smaller magnetosome membrane structures were described here in some of the analyzed mutants, but require more intensive characterization in the future. For example, the nature of their apparently electron denser lumen, as well as their protein composition are yet completely unclear. Isolation and (proteomic) characterization would allow investigating their origin.
- Deeper insights into the function of key magnetosome proteins and their complexes: Although all genes associated with magnetosome formation now have been analyzed in deletion mutagenesis studies in *M. gryphiswaldense*, the mutant phenotypes only allowed a superficial characterization of the functions of the encoded proteins. Towards deciphering the hierarchies and interactions of the complex magnetosomal protein network as well as the molecular functions of all involved proteins in magnetosome formation, three strategies have to be followed in consecutive research:
 - a. Co-deletions: Many magnetosome proteins share similar features and might be functionally redundant. Additionally, since some magnetosome proteins were shown to be important in recruiting other proteins to the magnetosome membrane [9,111,120], deletion of one gene might not always reveal the true function of the encoded protein, but could also cause secondary effects that influence the phenotype. More co-deletion studies have to be established to gain a better understanding of these gene/protein classes. The chromosome modification method developed in this thesis will help to facilitate these studies in the future.
 - b. Comprehensive (co-)localization studies: The induction strain developed in this thesis might be ideal for further (co-)localization studies with fluorescently labeled magnetosomes proteins. Time-lapse experiments could reveal their hierarchy in the recruiting process and might help to understand the stepwise assembly of the magnetosome protein network, similar to recent study of carboxysome biogenesis [165]. These assays

could be further complemented by using high-resolution fluorescence microscopy techniques, which in theory should be able to resolve single magnetosomes.

- c. Direct biochemical studies: Only the purification of key magnetosome proteins and biochemical *in vitro* characterization can undoubtedly give detailed insights into their molecular function, whether in redox processes, templating of bio-mineralization, membrane remodeling or protein-recruiting and -processing
- The minimal gene set for magnetite magnetosome formation: Besides the implications for prokaryotic cell biology research, there is considerable interest in magnetosomes for biotechnological or biomedical applications [166–169]. Based on the findings of this thesis, the seven utilized genes should be gradually extended to find the minimal gene set for magnetite magnetosome formation. This might not only help to better understand the biogenesis process, but also could be the basis for heterologous gene transfer and rudimentary magnetosome formation in other bacterial hosts [170]. Genes encoding for magnetochromes, like MamP, MamT and MamX, whose redox control properties are likely vital for magnetite formation, would be appropriate next candidates [152,155,156].
 - Universality of the process: All experiments of this thesis were performed in *M. gryphiswaldense*. The closely related *M. magneticum* is the only other well-established MTB model organism and differences regarding magnetosome formation in between both strains were already found. For a more comprehensive picture, magnetosome biogenesis should in the future also be analyzed in several other MTB that produce magnetosomes of different shapes and sizes. Ultimately this might also be done by magnetosome gene transfer in heterologous hosts: Although so far only one foreign bacterium could be transformed with a full set of magnetosome genes to artificially produce magnetite magnetosomes [158,170], it is currently unclear if other hosts are able to assemble magnetosome compartments that just lack the iron-mineral core and might act as accommodating hosts for further studies.

3 References

1. Harold FM. Molecules into Cells: Specifying Spatial Architecture. *Microbiol Mol Biol Rev.* 2005;69: 544–564
2. Cornejo E, Abreu N, Komeili A. Compartmentalization and organelle formation in bacteria. *Curr Opin Cell Biol.* 2014;26C: 132–138.
3. Saier MH, Bogdanov M V. Membranous organelles in bacteria. *J Mol Microbiol Biotechnol.* 2013;23: 5–12.
4. Carballido-López R. The bacterial actin-like cytoskeleton. *Microbiol Mol Biol Rev.* 2006;70: 888–909.
5. Cabeen MT, Jacobs-Wagner C. The Bacterial Cytoskeleton. *Annu Rev Genet.* 2010;44: 365–92.
6. Adams DW, Errington J. Bacterial cell division: assembly, maintenance and disassembly of the Z ring. *Nat Rev Microbiol.* Nature Publishing Group; 2009;7: 642–653.
7. Bramkamp M, Lopez D. Exploring the Existence of Lipid Rafts in Bacteria. *Microbiol Mol Biol Rev.* 2015;79: 81–100.
8. Thanbichler M, Wang SC, Shapiro L. The Bacterial Nucleoid: A Highly Organized and Dynamic Structure. *J Cell Biochem.* 2005;96: 506–521.
9. Murat D, Byrne M, Komeili A. Cell biology of prokaryotic organelles. *Cold Spring Harb Perspect Biol.* 2010;2: a000422.
10. Diekmann Y, Pereira-Leal JB. Evolution of intracellular compartmentalization. *Biochem J.* 2013;449: 319–331.
11. Kerfeld CA, Erbilgin O. Bacterial microcompartments and the modular construction of microbial metabolism. *Trends Microbiol.* 2015;23: 22–34.
12. Rae BD, Long BM, Badger MR, Price GD. Functions, compositions, and evolution of the two types of carboxysomes: polyhedral microcompartments that facilitate CO₂ fixation in cyanobacteria and some proteobacteria. *Microbiol Mol Biol Rev.* 2013;77: 357–379
13. Pfeifer F. Distribution, formation and regulation of gas vesicles. *Nat Rev Microbiol.* Nature Publishing Group; 2012;10: 705–715.
14. Shively JM, Cannon GC, Heinhorst S, Fuerst A, Bryant DA, Gantt E, et al. Intracellular Structures of Prokaryotes: Inclusions, Compartments and Assemblages. *Encyclopedia of Microbiology.* Moselio Sc. Oxford: Elsevier; 2009.
15. Konorty M, Kahana N, Linaroudis A, Minsky A, Medalia O. Structural analysis of photosynthetic membranes by cryo-electron tomography of intact *Rhodospirillum rubrum* cells. *J Struct Biol.* 2008;161: 393–400.

16. Liberton M, Pakarasi HB. Membrane Systems in Cyanobacteria. In: Herrero A, Flores E, editors. *The Cyanobacteria: Molecular Biology, Genomics, and Evolution*. Caister Academic Press; 2008. pp. 217–287.
17. Tucker JD, Siebert CA, Escalante M, Adams PG, Olsen JD, Otto C, et al. Membrane invagination in *Rhodobacter sphaeroides* is initiated at curved regions of the cytoplasmic membrane, then forms both budded and fully detached spherical vesicles. *Mol Microbiol*. 2010;76: 833–47.
18. Psencik J, Collins AM, Liljeroos L, Torkkeli M, Laurinma P, Ansink HM, et al. Structure of Chlorosomes from the Green Filamentous Bacterium. *J Bacteriol*. 2009;191: 6701–6708.
19. Stolz JF. Bacterial Intracellular Membranes. *Encycl Life Sci*. 2007;
20. Fuerst JA, Sagulenko E. Beyond the bacterium: planctomycetes challenge our concepts of microbial structure and function. *Nat Rev Microbiol*. 2011;9: 403–413.
21. Devos DP. PVC bacteria: variation of, but not exception to, the Gram-negative cell plan. *Trends Microbiol*. Elsevier Ltd; 2014;22: 14–20.
22. Strous M, Fuerst J a, Kramer EH, Logemann S, Muyzer G, van de Pas-Schoonen KT, et al. Missing lithotroph identified as new planctomycete. *Nature*. 1999;400: 446–449
23. van Niftrik L, Geerts WJC, van Donselaar EG, Humbel BM, Yakushevskaya A, Verkleij AJ, et al. Combined structural and chemical analysis of the anammoxosome: A membrane-bounded intracytoplasmic compartment in anammox bacteria. *J Struct Biol*. 2008;161: 401–410.
24. Lonhienne TGA, Sagulenko E, Webb RI, Lee K-C, Franke J, Devos DP, et al. Endocytosis-like protein uptake in the bacterium *Gemmata obscuriglobus*. *PNAS*. 2010;107: 12883–8.
25. Jendrossek D. Polyhydroxyalkanoate Granules Are Complex Subcellular Organelles (Carbonosomes). *J Bacteriol*. 2009;191: 3195–3202.
26. Balkwill DL, Maratea D, Blakemore RP. Ultrastructure of a magnetotactic spirillum. *J Bacteriol*. 1980;141: 1399–1408.
27. Gorby YA, Beveridge TJ, Blakemore RP. Characterization of the bacterial magnetosome membrane. *J Bacteriol*. 1988;170: 834–41.
28. Frankel RB, Blakemore RP, Wolfe RS. Magnetite in freshwater magnetotactic bacteria. *Science*. 1979;203: 1355–1356.
29. Heywood BR, Bazylinski D a., Garratt-Reed a., Mann S, Frankel RB. Controlled biosynthesis of greigite (Fe₃S₄) in magnetotactic bacteria. *Naturwissenschaften*. 1990;77: 536–538
30. Klumpp S, Faivre D. Interplay of magnetic interactions and active movements in the formation of magnetosome chains. *PLoS ONE*. 2012;7: e33562.
31. Dunin-Borkowski RE, McCartney MR, Frankel RB, Pósfai M, Buseck PR. Magnetic Microstructure of Magnetotactic Bacteria by Electron Holography. *Science*. 1998;282: 1868–1870.

32. Bellini S. On a unique behavior of freshwater bacteria. *Chinese J Oceanol Limnol.* 2009;27: 3–5.
33. Blakemore RP. Magnetotactic bacteria. *Science.* 1975;190: 377–379.
34. Spormann AM, Wolfe RS. Chemotactic, magnetotactic and tactile behaviour in a magnetic spirillum. *FEMS Microbiol Lett.* 1984;22: 171–177.
35. Frankel RB, Bazylinski DA, Johnson MS, Taylor BL. Magneto-aerotaxis in marine coccoid bacteria. *Biophys J.* 1997;73: 994–1000.
36. Popp F, Armitage JP, Schüler D. Polarity of bacterial magnetotaxis is controlled by aerotaxis through a common sensory pathway. *Nat Commun.* 2014;5.
37. Faivre D, Schüler D. Magnetotactic bacteria and magnetosomes. *Chem Rev.* 2008;108: 4875–98
38. Jogler C, Kube M, Schübbe S, Ullrich S, Teeling H, Bazylinski DA, et al. Comparative analysis of magnetosome gene clusters in magnetotactic bacteria provides further evidence for horizontal gene transfer. *Environ Microbiol.* 2009;11: 1267–77.
39. Lefèvre CT, Wu L-F. Evolution of the bacterial organelle responsible for magnetotaxis. *Trends Microbiol.* 2013; 1–10.
40. Spring S, Amann R, Ludwig W, Schleifer KH, Van Gemerden H, Petersen N. Dominating role of an unusual magnetotactic bacterium in the microaerobic zone of a freshwater sediment. *Appl Environ Microbiol.* 1993;59: 2397–2403.
41. Kolinko S, Jogler C, Katzmann E, Wanner G, Peplies J, Schüler D. Single-cell analysis reveals a novel uncultivated magnetotactic bacterium within the candidate division OP3. *Environ Microbiol.* 2012;14: 1709–1721.
42. Lefèvre CT, Menguy N, Abreu F, Lins U, Pósfai M, Prozorov T, et al. A cultured greigite-producing magnetotactic bacterium in a novel group of sulfate-reducing bacteria. *Science.* 2011;334: 1720–3.
43. Kolinko S, Richter M, Glöckner F-O, Brachmann A, Schüler D. Single-cell genomics of uncultivated deep-branching magnetotactic bacteria reveals a conserved set of magnetosome genes. *Environ Microbiol.* 2015; n/a–n/a.
44. Lin W, Pan Y. A putative greigite-type magnetosome gene cluster from the candidate phylum Latescibacteria. *Environ Microbiol Rep.* 2015;7: 237–242.
45. Delong EF, Frankel RB, Bazylinski DA. Multiple evolutionary origins of magnetotaxis in bacteria. *Science.* 1993;259: 803–6.
46. Flies CB, Peplies J, Schüler D. Combined approach for characterization of uncultivated magnetotactic bacteria from various aquatic environments. *Appl Environ Microbiol.* 2005;71: 2723–31.
47. Rodgers FG, Blakemore RP, Blakemore NA, Frankel RB, Bazylinski DA, Maratea D, et al. Intercellular structure in a many-celled magnetotactic prokaryote. *Arch Microbiol.* 1990;154: 18–22–22.

48. Pósfai M, Lefèvre CT, Trubitsyn D, Bazylinski DA, Frankel RB. Phylogenetic significance of composition and crystal morphology of magnetosome minerals. *Front Microbiol.* 2013;4: 344.
49. Schüler D. Genetics and cell biology of magnetosome formation in magnetotactic bacteria. *FEMS Microbiol Rev.* 2008;32: 654–672.
50. Katzmann E, Müller FD, Lang C, Messerer M, Winklhofer M, Plitzko JM, et al. Magnetosome chains are recruited to cellular division sites and split by asymmetric septation. *Mol Microbiol.* 2011;82: 1316–1329.
51. Katzmann E, Scheffel A, Gruska M, Plitzko JM, Schüler D. Loss of the actin-like protein MamK has pleiotropic effects on magnetosome formation and chain assembly in *Magnetospirillum gryphiswaldense*. *Mol Microbiol.* 2010;77: 208–224.
52. Komeili A, Li Z, Newman DK, Jensen GJ. Magnetosomes are cell membrane invaginations organized by the actin-like protein MamK. *Science.* 2006;311: 242–245.
53. Draper O, Byrne ME, Li Z, Keyhani S, Barrozo JC, Jensen G, et al. MamK, a bacterial actin, forms dynamic filaments in vivo that are regulated by the acidic proteins MamJ and LimJ. *Mol Microbiol.* 2011;82: 342–354.
54. Schultheiss D, Schüler D. Development of a genetic system for *Magnetospirillum gryphiswaldense*. *Arch Microbiol.* 2003;179: 89–94.
55. Matsunaga T, Nakamura C, Burgess JG, Sode K. Gene transfer in magnetic bacteria: transposon mutagenesis and cloning of genomic DNA fragments required for magnetosome synthesis. *J Bacteriol.* 1992;174: 2748–2753.
56. Schleifer KH, Schüler D, Spring S, Weizenegger M, Admann R, Ludwig W, et al. The genus *magnetospirillum* gen. nov. description of *Magnetospirillum gryphiswaldense* sp. nov. and transfer of *Aquaspirillum magnetotacticum* to *Magnetospirillum Magnetotacticum* comb. nov. *Syst Appl Microbiol.* 1991;14: 379–385.
57. Matsunaga T, Sakaguchi T, Tadakoro F. Magnetite formation by a magnetic bacterium capable of growing aerobically. *Appl Microbiol Biotechnol.* 1991;35: 651–655–655.
58. Scheffel A, Gärdes A, Grünberg K, Wanner G, Schüler D. The major magnetosome proteins MamGFDC are not essential for magnetite biomineralization in *Magnetospirillum gryphiswaldense* but regulate the size of magnetosome crystals. *J Bacteriol.* 2008;190: 377–86.
59. Schüler D. Molecular analysis of a subcellular compartment: The magnetosome membrane in *Magnetospirillum gryphiswaldense*. *Arch Microbiol.* 2004;181: 1–7.
60. Scheffel A, Gruska M, Faivre D, Linaroudis A, Graumann PL, Plitzko JM, et al. An acidic protein aligns magnetosomes along a filamentous structure in magnetotactic bacteria. *Nature.* 2006;440: 110–4.

61. Abreu F, Sousa AA, Aronova MA, Kim Y, Cox D, Leapman RD, et al. Cryo-electron tomography of the magnetotactic vibrio *Magnetovibrio blakemorei*: Insights into the biomineralization of prismatic magnetosomes. *J Struct Biol.* 2013;181: 162–168
62. Abreu F, Silva KT, Farina M, Keim CN, Lins U. Greigite magnetosome membrane ultrastructure in “*Candidatus Magnetoglobus multicellularis*.” *Int Microbiol.* 2008;11: 75–80.
63. Kolinko S, Wanner G, Katzmann E, Kiemer F, M. Fuchs B, Schüler D. Clone libraries and single cell genome amplification reveal extended diversity of uncultivated magnetotactic bacteria from marine and freshwater environments. *Environ Microbiol.* 2013;15: 1290–1301.
64. Williams TJ, Lefèvre CT, Zhao W, Beveridge TJ, Bazylinski DA. *Magnetospira thiophila* gen. nov., sp. nov., a marine magnetotactic bacterium that represents a novel lineage within the Rhodospirillaceae (Alphaproteobacteria). *Int J Syst Evol Microbiol.* 2012;62: 2443–2450.
65. Komeili A. Molecular Mechanisms of Compartmentalization and Biomineralization in Magnetotactic Bacteria. *FEMS Microbiol Rev.* 2012;36:
66. Byrne ME, Ball DA, Guerquin-Kern J-L, Rouiller I, Wu T-D, Downing KH, et al. *Desulfovibrio magneticus* RS-1 contains an iron- and phosphorus-rich organelle distinct from its bullet-shaped magnetosomes. *PNAS.* 2010;107:
67. Nakazawa H, Arakaki A, Narita-Yamada S, Yashiro I, Jinno K, Aoki N, et al. Whole genome sequence of *Desulfovibrio magneticus* strain RS-1 revealed common gene clusters in magnetotactic bacteria. *Genome Res.* 2009;19:
68. Rahn-Lee L, Byrne ME, Zhang M, Le Sage D, Glenn DR, Milbourne T, et al. A genetic strategy for probing the functional diversity of magnetosome formation. *PLoS Genet.* 2015;11.
69. Uebe R, Junge K, Henn V, Poxleitner G, Katzmann E, Plitzko JM, et al. The cation diffusion facilitator proteins MamB and MamM of *Magnetospirillum gryphiswaldense* have distinct and complex functions, and are involved in magnetite biomineralization and magnetosome membrane assembly. *Mol Microbiol.* 2011;84: 818–835.
70. Fischer A, Schmitz M, Aichmayer B, Fratzl P, Faivre D. Structural purity of magnetite nanoparticles in magnetotactic bacteria. *J R Soc Interface.* 2011;6,8: 1011–1018.
71. Muxworthy AR, Williams W. Critical superparamagnetic/single-domain grain sizes in interacting magnetite particles: implications for magnetosome crystals. *J R Soc Interface.* 2009;6: 1207–1212.
72. Bell PE, Mills AL, Herman JS. Biogeochemical Conditions Favoring Magnetite Formation during Anaerobic Iron Reduction. *Appl Environ Microbiol.* 1987;53: 2610–2616.
73. Bazylinski DA, Frankel RB, Konhauser KO. Modes of Biomineralization of Magnetite by Microbes Modes of Biomineralization of Magnetite by Microbes. *Geomicrobiol J.* 2007;24: 465–475.

74. Mandernack KW, Bazylinski DA, Shanks WCI, Bullen TD. Oxygen and Iron Isotope Studies of Magnetite Produced by Magnetotactic Bacteria. *Science*. 1999;285: 1892–1896. doi:
75. Li Y, Katzmann E, Borg S, Schüler D. The Periplasmic Nitrate Reductase Nap Is Required for Anaerobic Growth and Involved in Redox Control of Magnetite Biomineralization in *Magnetospirillum gryphiswaldense*. *J Bacteriol*. 2012;194: 4847–56.
76. Frankel RB, Papaefthymiou GC, Blakemore RP, O'Brien W. Fe₃O₄ Preceipitation in Magnetotactic Bacteria. *Biochim Biophys Acta*. 1983;763: 147–159.
77. Mann S, Frankel RB, Blakemore RP. Structure, morphology and crystal growth of bacterial magnetite. *Nature*. 1984;310: 405–407.
78. Faivre D, Böttger LH, Matzanke BF, Schüler D. Intracellular magnetite biomineralization in bacteria proceeds by a distinct pathway involving membrane-bound ferritin and an iron(II) species. *Angew Chemie - Int Ed*. 2007;46: 8495–8499.
79. Fdez-Gubieda ML, Muela A, Alonso J, García-Prieto A, Olivi L, Fernández-Pacheco R, et al. Magnetite Biomineralization in *Magnetospirillum gryphiswaldense*: Time-Resolved Magnetic and Structural Studies. *ACS Nano*. 2013; 3297–3305.
80. Baumgartner J, Morin G, Menguy N, Perez Gonzalez T, Widdrat M, Cosmidis J, et al. Magnetotactic bacteria form magnetite from a phosphate-rich ferric hydroxide via nanometric ferric (oxyhydr)oxide intermediates. *PNAS*. 2013;1. doi:10.1073/pnas.1307119110
81. Schultheiss D, Handrick R, Jendrossek D, Hanzlik M, Schüler D. The Presumptive Magnetosome Protein Mms16 Is a Poly(3-Hydroxybutyrate) Granule-Bound Protein (Phasin) in *Magnetospirillum gryphiswaldense*. *J Bacteriol*. 2005;187: 2416–2425.
82. Schultheiss D, Kube M, Schüler D. Inactivation of the flagellin gene *flaA* in *Magnetospirillum gryphiswaldense* results in nonmagnetotactic mutants lacking flagellar filaments. *Appl Environ Microbiol*. 2004;70: 3624–31.
83. Sternberg N, Hamilton D. Bacteriophage P1 site-specific recombination. I. Recombination between *loxP* sites. *J Mol Biol*. 1981;150: 467–86.
84. Ullrich S, Schüler D. Cre-*lox*-based method for generation of large deletions within the genomic magnetosome island of *Magnetospirillum gryphiswaldense*. *Appl Environ Microbiol*. 2010;76: 2439–44.
85. Lohße A, Ullrich S, Katzmann E, Borg S, Wanner G, Richter M, et al. Functional Analysis of the Magnetosome Island in *Magnetospirillum gryphiswaldense*: The *mamAB* Operon Is Sufficient for Magnetite Biomineralization. Battista JR, editor. *PLoS ONE*. 2011;6: e25561.
86. Suzuki N, Tsuge Y, Inui M, Yukawa H. Cre/*loxP*-mediated deletion system for large genome rearrangements in *Corynebacterium glutamicum*. *Appl Microbiol Biotechnol*. 2005;67: 225–33.

87. Metcalf WW, Jiang W, Daniels LL, Kim SK, Haldimann A, Wanner BL. Conditionally replicative and conjugative plasmids carrying lacZ alpha for cloning, mutagenesis, and allele replacement in bacteria. *Plasmid*. 1996;35: 1–13.
88. Komeili A, Vali H, Beveridge TJ, Newman DK. Magnetosome vesicles are present before magnetite formation, and MamA is required for their activation. *PNAS*. 2004;101: 3839–44.
89. Ardelean II, Moisescu C, Ignat M, Constantin M, Virgolici M. *Magnetospirillum gryphiswaldense*: Fundamentals and Applications. *Biotechnol Biotechnol Equip*. 2009; 751–754.
90. Grünberg K, Wawer C, Tebo BM, Schüler D. A Large Gene Cluster Encoding Several Magnetosome Proteins Is Conserved in Different Species of Magnetotactic Bacteria. *Appl Environ Microbiol*. 2001;67: 4573–4582.
91. Grünberg K, Müller E-C, Otto A, Reszka R, Linder D, Kube M, et al. Biochemical and Proteomic Analysis of the Magnetosome Membrane in *Magnetospirillum gryphiswaldense*. *Appl Environ Microbiol*. 2004;70: 1040–1050.
92. Schübbe S, Kube M, Scheffel A, Wawer C, Heyen U, Meyerdierks A, et al. Characterization of a Spontaneous Nonmagnetic Mutant of *Magnetospirillum gryphiswaldense* Reveals a Large Deletion Comprising a Putative Magnetosome Island. *J Bacteriol*. 2003;185: 5779–5790.
93. Ullrich S, Kube M, Schübbe S, Reinhardt R, Schüler D. A Hypervariable 130-Kilobase Genomic Region of *Magnetospirillum gryphiswaldense* Comprises a Magnetosome Island Which Undergoes Frequent Rearrangements during Stationary Growth. *J Bacteriol*. 2005;187: 7176–7184.
94. Schübbe S, Würdemann C, Peplies J, Heyen U, Wawer C, Glöckner FO, et al. Transcriptional organization and regulation of magnetosome operons in *Magnetospirillum gryphiswaldense*. *Appl Environ Microbiol*. 2006;72: 5757–65.
95. Richter M, Kube M, Bazylnski DA, Lombardot T, Glöckner FO, Reinhardt R, et al. Comparative genome analysis of four magnetotactic bacteria reveals a complex set of group-specific genes implicated in magnetosome biomineralization and function. *J Bacteriol*. 2007;189: 4899–910.
96. Lefèvre CT, Trubitsyn D, Abreu F, Kolinko S, Jogler C, de Almeida LGP, et al. Comparative Genomic Analysis of Magnetotactic Bacteria from the Deltaproteobacteria Provides New Insights into Magnetite and Greigite Magnetosome Genes Required for Magnetotaxis. *Environ Microbiol*. 2013;15: 2712–2735.
97. Lin W, Deng A, Wang Z, Li Y, Wen T, Wu L, et al. Genomic insights into the uncultured genus “*Candidatus Magnetobacterium*” in the phylum Nitrospirae. *ISME J. Nature Publishing Group*; 2014;8: 2463–2477.
98. Arakaki A, Yamagishi A, Fukuyo A, Tanaka M, Matsunaga T. Co-ordinated functions of Mms proteins define the surface structure of cubo-octahedral magnetite crystals in magnetotactic bacteria. *Mol Microbiol*. 2014;93: 554–7.

99. Tanaka M, Mazuyama E, Arakaki A, Matsunaga T. MMS6 protein regulates crystal morphology during nano-sized magnetite biomineralization in vivo. *J Biol Chem.* 2011;286: 6386–92.
100. Murat D, Falahati V, Bertinetti L, Csencsits R, Körnig A, Downing K, et al. The magnetosome membrane protein, MmsF, is a major regulator of magnetite biomineralization in *Magnetospirillum magneticum* AMB-1. *Mol Microbiol.* 2012;85: 684–699.
101. Lohße A, Borg S, Raschdorf O, Kolinko I, Tompa É, Pósfai M, et al. Supplement - Genetic dissection of the mamAB and mms6 operons reveals a gene set essential for magnetosome biogenesis in *magnetospirillum gryphiswaldense*. *J Bacteriol.* 2014;
102. Amemiya Y, Arakaki A, Staniland SS, Tanaka T, Matsunaga T. Controlled formation of magnetite crystal by partial oxidation of ferrous hydroxide in the presence of recombinant magnetotactic bacterial protein Mms6. *Biomaterials.* 2007;28: 5381–9.
103. Ding Y, Li J, Liu J, Yang J, Jiang W, Tian J, et al. Deletion of the ftsZ-like gene results in the production of superparamagnetic magnetite magnetosomes in *Magnetospirillum gryphiswaldense*. *J Bacteriol.* 2010;192: 1097–105.
104. Tanaka M, Arakaki A, Matsunaga T. Identification and functional characterization of liposome tubulation protein from magnetotactic bacteria. *Mol Microbiol.* 2010;76: 480–8.
105. Rioux J-B, Philippe N, Pereira S, Pignol D, Wu L-F, Ginet N. A second actin-like MamK protein in *Magnetospirillum magneticum* AMB-1 encoded outside the genomic magnetosome island. *PLoS ONE.* 2010;5: e9151.
106. Rawlings AE, Bramble JP, Walker R, Bain J, Galloway JM, Staniland SS. Self-assembled MmsF proteinosomes control magnetite nanoparticle formation in vitro. *PNAS.* 2014;111: 16094–16099.
107. Kammler M, Schön C, Hantke K. Characterization of the ferrous iron uptake system of *Escherichia coli*. *J Bacteriol.* 1993;175: 6212–6219.
108. Rong C, Zhang C, Zhang Y, Qi L, Yang J, Guan G, et al. FeoB2 Functions in Magnetosome Formation and Oxidative Stress Protection in *Magnetospirillum gryphiswaldense* Strain MSR-1. *J Bacteriol.* 2012;194: 3972–6.
109. Nudelman H, Zarivach R. Structure prediction of magnetosome-associated proteins. *Front Microbiol.* 2014;5: 1–17.
110. Murat D, Quinlan A, Vali H, Komeili A. Comprehensive genetic dissection of the magnetosome gene island reveals the step-wise assembly of a prokaryotic organelle. *PNAS.* 2010;107: 5593–5598.
111. Lohße A, Borg S, Raschdorf O, Kolinko I, Tompa É, Pósfai M, et al. Genetic dissection of the mamAB and mms6 operons reveals a gene set essential for magnetosome biogenesis in *magnetospirillum gryphiswaldense*. *J Bacteriol.* 2014;196: 2658–2669.
112. Jogler C, Schüler D. Genetic Analysis of Magnetosome Biomineralization. In: Schüler D, editor. *Magnetoreception and Magnetosomes in Bacteria.* 2007. pp. 133–161.

113. Pradel N, Santini C-L, Bernadac A, Fukumori Y, Wu L-F. Biogenesis of actin-like bacterial cytoskeletal filaments destined for positioning prokaryotic magnetic organelles. *PNAS*. 2006;103: 17485–9.
114. Scheffel A, Schüler D. The acidic repetitive domain of the *Magnetospirillum gryphiswaldense* MamJ protein displays hypervariability but is not required for magnetosome chain assembly. *J Bacteriol*. 2007;189: 6437–46.
115. Carillo MA, Bennet M, Faivre D. Interaction of Proteins Associated with the Magnetosome Assembly in Magnetotactic Bacteria As Revealed by Two-Hybrid Two-Photon Excitation Fluorescence Lifetime Imaging Microscopy Förster Resonance Energy Transfer. *J Phys Chem*. 2013;117: 14648.
116. Yamamoto D, Taoka A, Uchihashi T, Sasaki H, Watanabe H, Ando T, et al. Visualization and structural analysis of the bacterial magnetic organelle magnetosome using atomic force microscopy. *PNAS*. 2010;107: 9382–7.
117. Zeytuni N, Ozyamak E, Harush K Ben, Davidov G, Levin M, Gat Y, et al. Self-recognition mechanism of MamA, a magnetosome-associated TPR-containing protein, promotes complex assembly. *PNAS*. 2011;
118. Yang W, Li R, Peng T, Zhang Y, Jiang W, Li Y, et al. mamO and mamE genes are essential for magnetosome crystal biomineralization in *Magnetospirillum gryphiswaldense* MSR-1. *Res Microbiol*. 2010;161: 701–5.
119. Paulsen IT, Saier MH. A novel family of ubiquitous heavy metal ion transport proteins. *J Membr Biol*. 1997;156: 99–103.
120. Quinlan A, Murat D, Vali H, Komeili A. The HtrA/DegP family protease MamE is a bifunctional protein with roles in magnetosome protein localization and magnetite biomineralization. *Mol Microbiol*. 2011;80: 1075–1087.
121. Lenz LL, Dere B, Bevan MJ. Identification of an H2-M3-Restricted *Listeria* Epitope: Implications for Antigen Presentation by M3. *Immunity*. 1996;5: 63–72.
122. D’Orazio SEF, Velasquez M, Roan NR, Naveiras-Torres O, Starnbach MN. The *Listeria monocytogenes* lemA Gene Product Is Not Required for Intracellular Infection or to Activate fMIGWII-Specific T Cells. *Infect Immun*. 2003;71: 6721–6727.
123. Kozlov MM, Campelo F, Liska N, Chernomordik L V, Marrink SJ, McMahon HT. Mechanisms shaping cell membranes. *Curr Opin Cell Biol*. 2014;29C: 53–60.
124. Zimmerberg J, Kozlov MM. How proteins produce cellular membrane curvature. *Nat Rev Mol Cell Biol*. 2006;7: 9–19.
125. McMahon HT, Gallop JL. Membrane curvature and mechanisms of dynamic cell membrane remodelling. *Nature*. 2005;438: 590–596.
126. Stachowiak JC, Schmid EM, Ryan CJ, Ann HS, Sasaki DY, Sherman MB, et al. Membrane bending by protein-protein crowding. *Nat Cell Biol*. Nature Publishing Group; 2012;14: 944–949.

127. Ariotti N, Rae J, Leneva N, Ferguson C, Loo D, Okano S, et al. Molecular Characterization of Caveolin-Induced Membrane Curvature. *J Biol Chem.* 2015; 1–26.
128. Kirchhausen T. Bending membranes. *Nat Cell Biol.* 2012;14: 906–908.
129. Aimon S, Callan-jones A, Berthaud A, Pinot M, Toombes GES. Membrane Shape Modulates Transmembrane Protein Distribution. *Dev Cell. Elsevier Inc.;* 2014;28: 212–218.
130. Johannes L, Wunder C, Bassereau P. Bending “ On the Rocks ”— A Cocktail of Biophysical Modules to Build Endocytic Pathways. *Cold Spring Harb Perspect Biol.* 2014;6: :a016741.
131. Santarella-Mellwig R, Franke J, Jaedicke A, Gorjanacz M, Bauer U, Budd A, et al. The compartmentalized bacteria of the planctomycetes-verrucomicrobia-chlamydiae superphylum have membrane coat-like proteins. *PLoS Biol.* 2010;8: e1000281.
132. Low HH, Sachse C, Amos L a, Löwe J. Structure of a bacterial dynamin-like protein lipid tube provides a mechanism for assembly and membrane curving. *Cell.* 2009;139: 1342–52.
133. Bramkamp M. Structure and function of bacterial dynamin-like proteins. *Biol Chem.* 2012;393: 1203–1214.
134. Qian P, Bullough PA, Hunter CN. Three-dimensional reconstruction of a membrane-bending complex: the RC-LH1-PufX core dimer of *Rhodobacter sphaeroides*. *J Biol Chem.* 2008;283: 14002–11.
135. Chandler DE, Gumbart J, Stack JD, Chipot C, Schulten K. Membrane curvature induced by aggregates of LH2s and monomeric LH1s. *Biophys J. Biophysical Society;* 2009;97: 2978–84.
136. Hsin J, Gumbart J, Trabuco LG, Villa E, Qian P, Hunter CN, et al. Protein-induced membrane curvature investigated through molecular dynamics flexible fitting. *Biophys J.* 2009;97: 321–9.
137. Arechaga I, Miroux B, Karrasch S, Huijbregts R, De Kruijff B, Runswick MJ, et al. Characterisation of new intracellular membranes in *Escherichia coli* accompanying large scale over-production of the b subunit of F1F(o) ATP synthase. *FEBS Lett.* 2000;482: 215–219.
138. Lefman J, Zhang P, Hirai T, Weis RM, Juliani J, Bliss D, et al. Three-dimensional electron microscopic imaging of membrane invaginations in *Escherichia coli* overproducing the chemotaxis receptor Tsr. *J Bacteriol.* 2004;186: 5052–5061.
139. Eriksson HM, Wessman P, Ge C, Edwards K, Wieslander A. Massive formation of intracellular membrane vesicles in *Escherichia coli* by a monotopic membrane-bound lipid glycosyltransferase. *J Biol Chem.* 2009;284: 33904–14
140. Walser PJ, Ariotti N, Howes M, Ferguson C, Webb R, Schwudke D, et al. Constitutive Formation of Caveolae in a Bacterium. *Cell.* 2012;150: 752–763.

141. Ueki T, Inouye S, Inouye M. Positive-negative KG cassettes for construction of multi-gene deletions using a single drug marker. *Gene*. 1996;183: 153–157.
142. McKenney K, Shimatake H, Court D, Schmeissner U, Brady C, Rosenberg M. A system to study promoter and terminator signals recognized by *Escherichia coli* RNA polymerase. *Gene Amplif Anal.*; 1981;2: 383–415.
143. Slepak T, Tang M, Addo F, Lai K. Intracellular galactose-1-phosphate accumulation leads to environmental stress response in yeast model. *Mol Genet Metab. Elsevier*; 2015;86: 360–371.
144. Borg S, Popp F, Hofmann J, Leonhardt H, Rothbauer U, Schüler D. An Intracellular Nanotrap Redirects Proteins and Organelles in Live Bacteria. *MBio*. 2015;6: e02117–14.
145. Davidov G, Müller FD, Baumgartner J, Bitton R, Faivre D, Schüler D, et al. Crystal structure of the magnetobacterial protein MtxA C-terminal domain reveals a new sequence-structure relationship, *Frontiers in Molecular Bioscience*, 2015.
146. Li Y, Raschdorf O, Silva KT, Schüler D. The terminal oxidase *cbb3* functions in redox control of magnetite biomineralization in magnetospirillum gryphiswaldense. *J Bacteriol*. 2014;196: 2552–2562.
147. Raschdorf O. Untersuchung der Funktion des *mamXY* Operons bei der Magnetosomenformation in *Magnetospirillum gryphiswaldense*. Ludwig-Maximilians-Universität München. 2011.
148. Yang J, Li S, Huang X, Li J, Li L, Pan Y, et al. MamX encoded by the *mamXY* operon is involved in control of magnetosome maturation in *Magnetospirillum gryphiswaldense* MSR-1. *BMC Microbiol*. 2013;13: 203.
149. Müller FD, Raschdorf O, Nudelman H, Messerer M, Katzmann E, Plitzko JM, et al. The FtsZ-Like Protein FtsZm of *Magnetospirillum gryphiswaldense* Likely Interacts with Its Generic Homolog and Is Required for Biomineralization under Nitrate Deprivation. *J Bacteriol*. 2014;196: 650–9.
150. Bowman SEJ, Bren KL. The chemistry and biochemistry of heme c: functional bases for covalent attachment. *Nat Prod Rep*. 2008;25: 1118–30.
151. Siponen MI, Adryanczyk G, Ginet N, Arnoux P, Pignol D. Magnetochrome: a c-type cytochrome domain specific to magnetotactic bacteria. *Biochem Soc Trans*. 2012;40: 1319–23.
152. Siponen MI, Legrand P, Widdrat M, Jones SR, Zhang W-J, Chang MCY, et al. Structural insight into magnetochrome-mediated magnetite biomineralization. *Nature*. Nature Publishing Group; 2013;502: 681–4.
153. von Rozycki T, Yen M-R, Lende EE, Saier MH. The YedZ family: possible heme binding proteins that can be fused to transporters and electron carriers. *J Mol Microbiol Biotechnol*. 2005;8: 129–40.
154. Brokx SJ, Rothery RA, Zhang G, Ng DP, Weiner JH. Characterization of an *Escherichia coli* sulfite oxidase homologue reveals the role of a conserved active site cysteine in assembly and function. *Biochemistry*. 2005;44: 10339–48.

155. Taoka A, Eguchi Y, Mise S, Oestreicher Z, Uno F, Fukumori Y. A magnetosome-associated cytochrome MamP is critical for magnetite crystal growth during the exponential growth phase. *FEMS Microbiol Lett.* 2014;358: 21–29.
156. Jones SR, Wilson TD, Brown ME, Rahn-Lee L, Yu Y, Fredriksen LL, et al. Genetic and biochemical investigations of the role of MamP in redox control of iron biomineralization in *Magnetospirillum magneticum*. *PNAS.* 2015; 201417614.
157. Li Y, Bali S, Borg S, Katzmann E, Ferguson SJ, Schüler D. Cytochrome cd1 nitrite reductase NirS is involved in anaerobic magnetite biomineralization in *magnetospirillum gryphiswaldense* and requires nirn for proper d1 heme assembly. *J Bacteriol.* 2013;195: 4297–4309.
158. Kolinko I, Lohße A, Borg S, Raschdorf O, Jogler C, Tu Q, et al. Biosynthesis of magnetic nanostructures in a foreign organism by transfer of bacterial magnetosome gene clusters. *Nat Nanotechnol.* 2014;9: 193–7.
159. Vanhecke D, Asano S, Kochovski Z, Fernandez-Busnadiego R, Schrod N, Baumeister W, et al. Cryo-electron tomography: methodology, developments and biological applications. *J Microsc.* 2011;242: 221–7.
160. Tanaka M, Okamura Y, Arakaki A, Tanaka T, Takeyama H, Matsunaga T. Origin of magnetosome membrane: proteomic analysis of magnetosome membrane and comparison with cytoplasmic membrane. *Proteomics.* 2006;6: 5234–47.
161. Matsunaga T, Nemoto M, Arakaki A, Tanaka M. Proteomic analysis of irregular, bullet-shaped magnetosomes in the sulphate-reducing magnetotactic bacterium *Desulfovibrio magneticus* RS-1. *Proteomics.* 2009;9: 3341–3352.
162. Okamura Y, Takeyama H, Matsunaga T. A Magnetosome-specific GTPase from the Magnetic Bacterium *Magnetospirillum magneticum* AMB-1. *J Biol Chem.* 2001;276: 48183–48188.
163. Borg S, Hofmann J, Pollithy A, Lang C, Schüler D. New Vectors for Chromosomal Integration Enable High-Level Constitutive or Inducible Magnetosome Expression of Fusion Proteins in *Magnetospirillum gryphiswaldense*. *Appl Environ Microbiol.* 2014;80: 2609–16.
164. Murat D. Magnetosomes: how do they stay in shape? *J Mol Microbiol Biotechnol.* 2013;23: 81–94.
165. Cameron JC, Wilson SC, Bernstein SL, Kerfeld CA. Biogenesis of a Bacterial Organelle: The Carboxysome Assembly Pathway. *Cell.* 2013;155: 1131–1140.
166. Goldhawk DE, Rohani R, Sengupta A, Gelman N, Prato FS. Using the magnetosome to model effective gene-based contrast for magnetic resonance imaging. *Wiley Interdisciplinary Rev Nanomedicine nanobiotechnology.* 2012;4: 378–88.
167. Yoshino T, Maeda Y, Matsunaga T. Bioengineering of bacterial magnetic particles and their applications in biotechnology. *Recent Pat Biotechnol. United Arab Emirates;* 2010;4: 214–225.

168. Lang C, Schüler D, Faivre D. Synthesis of magnetite nanoparticles for bio- and nanotechnology: genetic engineering and biomimetics of bacterial magnetosomes. *Macromol Biosci.* 2007;7: 144–51.
169. Wang H, Yu Y, Sun Y, Chen Q. Magnetic Nanochains: a Review. *Nano.* 2011;06: 1–17.
170. Kolinko I. Homologous and heterologous expression of magnetosome operons from *Magnetospirillum gryphiswaldense*. Ludwig-Maximilians-Universität München. 2014.
171. Songyang Z, Fanning AS, Fu C, Xu J, Marfatia SM, Chishti AH, et al. Recognition of unique carboxyl-terminal motifs by distinct PDZ domains. *Science.* 1997;275: 73–77.
172. Peter BJ, Kent HM, Mills IG, Vallis Y, Butler PJG, Evans PR, et al. BAR Domains as Sensors of Membrane Curvature: The Amphiphysin BAR Structure. *Science.* 2004;303: 495–499.
173. Itoh T, De Camilli P. BAR, F-BAR (EFC) and ENTH/ANTH domains in the regulation of membrane–cytosol interfaces and membrane curvature. *Biochim Biophys Acta - Mol Cell Biol Lipids.* 2006;1761: 897–912.

4 Appendices

4.1 Publication A:

A tailored *galK* counterselection system for efficient markerless gene deletion and chromosomal tagging in *Magnetospirillum gryphiswaldense*

Oliver Raschdorf^{1,2}, Jürgen M. Plitzko², Dirk Schüler^{1,3} and Frank D. Müller^{1,3}.

Affiliations:

1: Ludwig Maximilian University Munich, Department of Microbiology

2: Max-Planck-Institute of Biochemistry, Department of Molecular Structural Biology

3: University of Bayreuth, Department of Microbiology

Applied and Environmental Microbiology (2014) **80**(14):4323-4330

A Tailored *galk* Counterselection System for Efficient Markerless Gene Deletion and Chromosomal Tagging in *Magnetospirillum gryphiswaldense*

Oliver Raschdorf,^{a,b} Jürgen M. Plitzko,^{b,c} Dirk Schüler,^{a*} Frank D. Müller^{a*}

Ludwig Maximilian University Munich, Department Biology I, Biocenter, Planegg-Martinsried, Germany^a; Max Planck Institute of Biochemistry, Department of Molecular Structural Biology, Planegg-Martinsried, Germany^b; Bijvoet Center for Biomolecular Research, Utrecht University, Utrecht, the Netherlands^c

Magnetotactic bacteria have emerged as excellent model systems to study bacterial cell biology, biomineralization, vesicle formation, and protein targeting because of their ability to synthesize single-domain magnetite crystals within unique organelles (magnetosomes). However, only few species are amenable to genetic manipulation, and the limited methods for site-specific mutagenesis are tedious and time-consuming. Here, we report the adaptation and application of a fast and convenient technique for markerless chromosomal manipulation of *Magnetospirillum gryphiswaldense* using a single antibiotic resistance cassette and *galk*-based counterselection for marker recycling. We demonstrate the potential of this technique by genomic excision of the *phbCAB* operon, encoding enzymes for polyhydroxyalkanoate (PHA) synthesis, followed by chromosomal fusion of magnetosome-associated proteins to fluorescent proteins. Because of the absence of interfering PHA particles, these engineered strains are particularly suitable for microscopic analyses of cell biology and magnetosome biosynthesis.

Magnetotactic bacteria (MTB) are exceptional in their ability to synthesize unique organelles (magnetosomes) that consist of membrane-enveloped, nanometer-sized, single-domain magnetite crystals. Magnetosomes are associated with a specific set of proteins (1) and are attached to a filamentous cytoskeletal structure (2, 3), which enables them to assemble into a cohesive chain positioned at midcell (4). Therefore, MTB have emerged as excellent model organisms to study the biogenesis of bacterial organelles, biomineralization, protein targeting, and bacterial cell biology. In addition, magnetosomes have been genetically engineered with respect to both their magnetite core as well their enveloping membrane, and numerous applications of functionalized magnetosomes have been demonstrated (5–8). However, the progress in exploring the biology of MTB and in engineering magnetosomes has been impeded by the limited genetic tools available for these fastidious bacteria.

To date, genetic systems are available for only two *Magnetospirillum* species from the alphaproteobacteria, but their genetic manipulation has remained rather inefficient, laborious, and time-consuming (2, 9). In *Magnetospirillum gryphiswaldense* (MSR-1), for example, the genome has been routinely mutated by Cre-*lox* recombination (10–12), which relies on the integration of 34-bp *loxP* sequences directly up- and downstream of the genomic target by one double homologous (thereby replacing the target DNA by a resistance marker) or two single homologous recombination events. Because of the low frequency of double recombination in MSR-1, two distinct integrating vectors have been used, each one providing a specific resistance marker for clonal selection. After integration of both *loxP*-carrying vectors, Cre recombinase becomes expressed from a third, nonintegrating plasmid. The recombinase specifically recognizes the integrated *loxP* sites, and when their sequences are parallel, enclosed nucleotides become excised. Since one *loxP* sequence remains after excision, the system had to be advanced for repeated deletions in the same host (13). This advanced system has proven useful to delete single

genes, entire operons, and even larger genomic loci in MSR-1 (14).

However, the Cre-*lox* technology exhibits several practical disadvantages. First, two different vectors for genome integration need to be constructed. To positively select for double integration, two antibiotics have to be applied, which impedes cell growth. Second, three consecutive cycles of transformation, each accompanied by clonal selection and screening, are necessary. These procedures are particularly time-consuming for slow-growing magnetospirilla. Third, *lox* nucleotides remain in the genomic target region and complicate the design of in-frame deletion vectors. More importantly, these scar sequences render the introduction of targeted single-base exchanges nearly impossible.

An alternative technique to manipulate bacterial genomes relies on RecA-mediated chromosomal integration and excision of a nonreplicating vector that carries the mutated allele, an antibiotic resistance cassette for positive selection, and a conditionally lethal gene as essential components for counterselection.

In magnetospirilla, counterselection can be mediated by SacB, which confers sensitivity to sucrose (15, 16). This selection marker is commonly used to mutate *Magnetospirillum magneticum* AMB-1 (17–20), but it has been applied to MSR-1 in only a few

Received 20 February 2014 Accepted 30 April 2014

Published ahead of print 9 May 2014

Editor: R. E. Parales

Address correspondence to Frank D. Müller, Frank.Mueller@biologie.uni-muenchen.de.

* Present address: Dirk Schüler and Frank D. Müller, University of Bayreuth, Department of Microbiology, Bayreuth, Germany.

Supplemental material for this article may be found at <http://dx.doi.org/10.1128/AEM.00588-14>.

Copyright © 2014, American Society for Microbiology. All Rights Reserved.
doi:10.1128/AEM.00588-14

TABLE 1 Bacterial strains and vectors

Strain or vector	Application and/or characteristic(s)	Reference and/or source
Strains		
<i>E. coli</i>		
DH5 α	Host for cloning; <i>fhuA2</i> Δ (<i>argF-lacZ</i>)U169 <i>phoA glnV44</i> ϕ 80 Δ (<i>lacZ</i>)M15 <i>gyrA96 recA1 relA1 endA1 thi-1 hsdR17</i>	47
BW29427	Donor for conjugation; <i>thrB1004 pro thi rpsL hsdSlacZ</i> Δ M15 <i>RP4-1360</i> Δ (<i>araBAD</i>)567 Δ <i>dapA1341::[erm pir]tra</i>	K. A. Datsenko and B. L. Wanner (Purdue University), unpublished
<i>M. gryphiswaldense</i>		
MSR-1 R/S	wt	21
FM019	<i>mamC-mCherry</i>	This work
FM021	<i>mamC-egfp</i>	This work
FM022	<i>mCherry-mamK</i>	This work
FM025	Δ <i>phbCAB</i>	This work
FM046	Δ <i>phbCAB mamC-egfp</i>	This work
FM047	Δ <i>phbCAB mamC-mCherry</i>	This work
FM048	Δ <i>phbCAB mCherry-mamK</i>	This work
Vectors		
pK19 mob GII	Backbone for pORFM suicide vectors; <i>npt mobRK2</i> pMB-1 replicon	36; GenBank accession no. AF012346
pJET 1.2/blunt	Cloning vector; <i>bla</i>	Thermo Scientific
pAPI60	Source of <i>tetR</i>	A. Pollithy, unpublished
pAP173	Source of P _{tet} and terminator sequences	A. Pollithy, unpublished
pOR014	Construction vector for pORFM GalK; <i>npt</i> terminator <i>mobRK2</i>	This work
pOR025a	Intermediate for pORFM GalK construction; <i>ter npt mobRK2 tetR</i>	This work
pORFM GalK	General backbone vector for GalK counterselection; <i>npt galK tetR mobRK2</i>	This work
pORFM blu	General backbone vector for GalK counterselection, blue-white screening; <i>lacZα npt galK tetR mobRK2</i>	This work
pFM234	<i>phbCAB</i> deletion; <i>npt galK tetR mobRK2</i>	This work
pFM236	<i>mamC-egfp</i> chromosomal fusion; <i>npt galK tetR mobRK2</i>	This work
pFM237	<i>mamC-mCherry</i> chromosomal fusion; <i>npt galK tetR mobRK2</i>	This work
pFM245	<i>mCherry-mamK</i> chromosomal fusion; <i>npt gal, tet, mobRK2</i>	This work

cases (21). The reason for this is that in our hands, *sacB* counterselection has proven not to be reliable, likely because of rapid spontaneous gene inactivation upon selective pressure leading to numerous false-positive colonies on counterselective plates (11; E. Katzmann, unpublished data), requiring laborious and cumbersome replica platings.

Thus, to enhance targeted mutagenesis techniques for MSR-1 and potentially other magnetospirilla, we tested alternative conditional marker genes, and as one promising candidate, we analyzed the galactokinase-encoding gene *galK*. Galactokinase confers sensitivity to galactose or 2-deoxygalactose in the absence of a galactose-metabolizing pathway (22, 23) and is utilized for counterselection in several Gram-positive and Gram-negative bacteria (24–26).

In our study, we found that GalK represents a reliable and robust marker for counterselection in MSR-1. Using *galK*, we constructed a universal vector for efficient and markerless genome manipulation. To prove its practical use, we abolished synthesis of intracellular polyhydroxyalkanoate (PHA) inclusions by deletion of the putative *phbCAB* operon in MSR-1, which resulted in cells with reduced autofluorescence and diminished distortion of magnetosome chains. We used this technique further for native-site genomic in-frame fluorescent tagging of magnetosome key proteins in the wild type (wt) and in the *phbCAB* mutant, and we found the fusion proteins to be functional. In summary, we developed an efficient and powerful tool for genome manipulation of

MSR-1 and generated strains particularly suitable for analysis of subcellular structures by light and electron microscopy.

MATERIALS AND METHODS

Bacterial strains, vectors, and culture conditions. Bacterial strains and vectors are listed in Table 1. *Escherichia coli* strains were cultivated in lysogeny broth (LB) medium as described previously (27). Kanamycin was added to 25 μ g/ml, and 5-bromo-4-chloro-3-indolyl- β -D-galactopyranoside (X-Gal) was added to 40 μ g/ml when necessary. *E. coli* BW29427 cultures (K. A. Datsenko and B. L. Wanner, unpublished data) were supplemented with 1 mM DL- α , ϵ -diaminopimelic acid (DAP). *M. gryphiswaldense* cultures were grown microaerobically in modified flask standard medium (FSM) at 30°C (28) with agitation at 120 rpm, unless otherwise stated. When appropriate, kanamycin was added to 5 μ g/ml; galactose was added to 0.5, 1, 2.5, or 5% (wt/vol); and anhydrotetracycline was added to 100 ng/ml after autoclaving. Media were solidified by the addition of 1.5% (wt/vol) agar. The optical density and magnetic response (C_{mag}) of exponentially growing MSR-1 cultures were measured photometrically at 565 nm, as reported previously (29).

Correlation of optical density and cell counts. To test whether the correlation of optical density (measured photometrically at 565 nm) and cell numbers per ml between the wt and the *phbCAB* mutant was identical, cultures of the wt and three mutant strains grown overnight were diluted to an optical density at 565 nm (OD₅₆₅) of 0.1 and fixed with formaldehyde (1% final concentration). Samples of each strain were applied to a hemocytometer, and cells per chamber ($n = 11$) were enumerated. Mean values were calculated from the cell counts, and the mean value of wt cells was set to 100%.

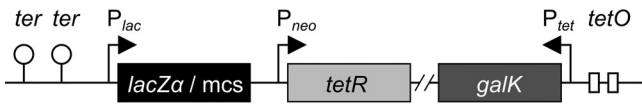


FIG 1 Vector design for *galK*-based counterselection in MSR-1 by pORFM blu. To repress *galK* expression under nonselective conditions, the gene is placed under the control of the *tet* promoter/operator ($P_{tet-tetO}$). The *tet* repressor (*tetR*) is constitutively expressed from a neomycin promoter (P_{neo}). Upon induction with anhydrotetracycline, the *tet* promoter becomes active, and *galK* expression increases. To enable blue-white screening in *E. coli*, the multiple-cloning site (*mcs*) was combined with a *lacZα* gene fragment.

Molecular and genetic techniques. Plasmids (Table 1) were constructed by standard recombinant techniques. Oligonucleotides that were used as primers for PCRs are listed in Table S1 in the supplemental material. PCR-amplified DNA fragments for cloning were routinely sequenced with BigDye Terminator v3.1 chemistry on an ABI 3700 capillary sequencer (Applied Biosystems).

Construction of integrative vectors for markerless gene deletion and chromosomal fluorescent fusion. To avoid transcriptional read-through from upstream regions in pK19mobGII, the bacteriophage lambda T0 and the *E. coli rrmB* T1 transcription terminators were amplified from plasmid pAP173 (A. Pollithy, unpublished data) by using primer pair oOR059/oOR060 and cloned upstream of the pK19mobGII multiple-cloning site (MCS) after HindIII and PstI restriction, yielding pOR014. To ensure *galK* transcription in MSR-1, a *tet* promoter-*galK* fusion was generated. Therefore, the *galK* gene was amplified from *E. coli* K-12 genomic DNA by using primer pair oOR063/oOR077 and ligated downstream of the *tet* promoter in pAP173 after NdeI and BamHI restriction. This $P_{tet-galK}$ cassette was intended to be cloned into pOR014. However, since no colonies grew after transformation in *E. coli*, the $P_{tet-galK}$ fusion was amplified from the ligation reaction by using primer pair oOR082/oOR083 and cloned into pJET 1.2/blunt (Fermentas), but again, no colonies grew after transformation. Thus, the *tet* repressor gene (*tetR*) under the control of the neomycin promoter ($P_{neo-tetR}$) was amplified from pAP160 (A. Pollithy, unpublished) by using primer pair tetRfWsaclI/tetRrevSaclI and cloned into pOR014, yielding pOR025a. Subsequently, to construct pORFM GalK (see Fig. S1A in the supplemental material), the $P_{tet-galK}$ PCR product was cloned into pOR025a by using MunI and Bsp119I restriction sites. To facilitate the design and cloning of homologous up- and downstream regions into pORFM GalK, the MCS of pORFM GalK was amended by a *lacZα* gene fragment containing EcoRV and SmaI/XmaI restriction sites, both suitable for blunt-end cloning, yielding pORFM blu (Fig. 1; see also Fig. S1B in the supplemental material).

For pFM234 construction, the ~1.6-kb regions up- and downstream of the putative *phbCAB* operon were PCR amplified by using a proofreading DNA polymerase and primer pairs oFM341/oFM342 and oFM343/oFM344. PCR products were fused in a second PCR (30) using primer pair oFM341/oFM344, thereby generating the mutated allele where the *phbCAB* operon is replaced by a truncated open reading frame (ORF) consisting of 5' *phbC* and 3' *phbB* codons. This DNA fragment was blunt-end ligated into the EcoRV-digested pORFM blu vector and transformed into *E. coli* DH5α, and transformed cells were plated onto LB medium supplemented with kanamycin and X-Gal. White colonies were selected from the plates, and the presence of the cloned fragment was confirmed by colony PCR using primer pair oFM280b/oFM281b.

To generate fluorescent chromosomal fusions to MamC and MamK, monomeric DsRed in its variant mCherry and enhanced green fluorescent protein (EGFP; Clontech) were used. MamC was C-terminally (31) fused to mCherry and EGFP, and MamK was N-terminally (32) fused to mCherry.

pFM236 (for the *mamC-egfp* fusion) was generated essentially as described above but with pORFM GalK as the vector backbone and without blue-white screening of *E. coli* colonies. Briefly, the ~1.6-kb regions up-

and downstream of the *mamC* 3' end were PCR amplified by using primer pairs oFM270/oFM271 and oFM274/oFM275, respectively. *egfp* was amplified with primer pair oFM272/oFM273. The upstream fragment was cloned into pORFM GalK after digestion with Sall and KpnI, followed by *egfp* after digestion with KpnI and EcoRI. The downstream fragment was cloned into the resulting vector after digestion with EcoRI and NheI.

For pFM237 (*mamC-mCherry*) construction, *mCherry* was PCR amplified with primer pair oFM276/oFM277. *egfp* was then cut out from pFM236 by KpnI and EcoRI digestion and replaced by *mCherry*.

To construct pFM245 (*mCherry-mamK* fusion), the ~1.4-kb regions up- and downstream of the *mamK* start codon were PCR amplified by using primer pairs oFM369/oFM370 and oFM373/oFM374, and *mCherry* was amplified with primer pair oFM371/oFM372, including a spacer sequence. The upstream fragment and *mCherry* were fused by a second PCR using primer pair oFM369/oFM372. The fused fragment was cloned into pORFM GalK after digestion with Sall and BamHI. The downstream fragment was cloned behind this insert after restriction with BamHI and SpeI.

Conjugation experiments. Plasmid transfer by biparental conjugation was performed with *E. coli* BW29427 as the donor strain and *M. gryphiswaldense* MSR-1 as the acceptor strain. The conjugation procedure was performed as described previously (9, 12).

Screening of MSR-1 insertion mutants. Kanamycin-resistant colonies were transferred into 100 μl FSM in 96-well plates and grown microaerobically overnight. The cultures were screened for up- or downstream integration of the vector by PCR (see Fig. S3 in the supplemental material) using a vector-specific oligonucleotide primer (oFM280a or -281 for pORFM GalK derivatives and oFM280b or -281b for pORFM blu derivatives) and one primer specific for a sequence adjacent to one homologous region (verification primer) (see Table S1 in the supplemental material). If possible, at least one insertion mutant strain with either up- or downstream integration was used for counterselection.

Galactose counterselection of insertion mutants. PCR-verified insertion mutants were transferred into 1 ml FSM in 24-well plates and grown overnight. Two hundred microliters of the culture grown overnight was plated onto FSM containing 0.5% (wt/vol) galactose and 100 ng/ml anhydrotetracycline. Plates were incubated at 30°C under microaerobic conditions for 5 days, as described previously (33).

Screen for in-frame deletion and fusion. To discriminate between reconstituted wt and mutated genotypes, colonies were transferred from counterselective plates into 100 μl FSM and incubated microaerobically overnight in 96-well plates. The genotype was determined by PCR using oligonucleotide primers specific to sequences adjacent to the cloned homologous regions (verification primers) (see Table S1 and Fig. S4 in the supplemental material). Loss of the vector was further confirmed by re-inoculating mutant strains into FSM with kanamycin, where no growth was observed, and in medium with galactose, where growth occurred.

Fluorescence microscopy. *M. gryphiswaldense* strains were grown in 15-ml polypropylene tubes with sealed screw caps and a culture volume of 11 ml to early log phase. To image fluorescent proteins, 10-μl samples were directly immobilized on 1% (wt/vol) agarose pads and covered with a coverslip. For Nile red staining, 1-ml samples were withdrawn, and 1 μl 0.5 mg/ml Nile red (in dimethyl sulfoxide [DMSO]) was added. Cells were incubated for 5 min, harvested by centrifugation, and washed with phosphate-buffered saline (PBS) before immobilization on agarose. The samples were imaged with an Olympus BX81 microscope equipped with a 100× UPLSAPO100XO objective and an Orca-ER camera (Hamamatsu).

Transmission electron microscopy. For transmission electron microscopy (TEM) analysis, cells were grown at 25°C under microaerobic conditions to an OD₅₆₅ of 0.1, fixed in formaldehyde (1%), concentrated, adsorbed onto carbon-coated copper mesh grids, and washed three times with particle-free water. Samples were viewed and recorded with a Morgagni 268 microscope (FEI, Eindhoven, the Netherlands) at an 80-kV accelerating tension.

Cryo-electron tomography. Cryo-electron tomography (CET) was performed on logarithmic MSR-1 cultures embedded in vitreous ice by plunge freezing into liquid ethane, as described previously (34).

Image acquisition and processing. Fluorescence images were recorded and processed (brightness and contrast adjustments) by using Olympus Excellence software, TEM images were acquired with the iTEM software program (5.0), and CET tilt series were recorded with Serial EM and FEI software. Three-dimensional (3D) reconstructions of the tomograms were performed with the weighted back-projection method using TOMtoolbox (35) and visualized with Amira 3D image processing software. Images were assembled with the GNU Image Manipulation Program (GIMP 2.8), and graphics were drawn by using Inkscape (0.48) software.

RESULTS AND DISCUSSION

Generation of a universal GalK-based counterselection vector for MSR-1. To investigate whether GalK may be a suitable counterselection marker, we first verified the absence of a potential galactose utilization pathway from the MSR-1 genome. To preclude adverse effects of increased galactose concentrations on MSR-1, we next tested growth on medium supplemented with 0, 0.5, 1, 2.5, and 5.0% (wt/vol) galactose. Similar numbers of colonies emerged under all conditions, although colonies on plates with 5.0% galactose were somewhat smaller, indicating a slight growth impairment at this high concentration (data not shown).

Based on these results, we pursued construction of a *galK*-containing suicide plasmid, and we selected the mobilizable broad-host-range vector pK19mobGII (conferring kanamycin resistance) (36) as the backbone. To introduce *galK*, we first amplified the gene from *E. coli* K-12 and cloned it under the control of the *tet* promoter (P_{tet}), which is constitutively active in MSR-1 and of intermediate strength (37). However, we failed to obtain *E. coli* colonies, suggesting that constitutive (over)expression of *galK* in *E. coli* was lethal. To prevent this effect, we first cloned the tetracycline repressor gene (*tetR*) into pK19mobGII and repeated the insertion of the P_{tet} -*galK* construct (see Materials and Methods for details). This yielded the counterselective vector with tetracycline-inducible *galK* expression, designated pORFM GalK.

In addition, to facilitate direct blunt-end cloning of PCR-amplified genomic sections for homologous recombination, we reintroduced a multiple-cloning site into the plasmid and combined it with a *lacZ α* gene fragment as a chromogenic marker for blue-white screening in *E. coli*, as outlined in Fig. 1. We designated this vector pORFM blu.

Deletion of the *phbCAB* operon eliminates PHA granules. In MSR-1 growing on standard FSM, large parts of the intracellular volume are frequently occupied by PHA granules. These inclusions tend to distort magnetosome chains (Fig. 2A and B) and interfere with fluorescence microscopy by autofluorescence or adsorption of lipophilic membrane stains (Fig. 2A and C, insets). To prove the function of pORFM blu and to generate a strain with enhanced properties for light and electron microscopy, we intended to abolish PHA granule formation by the deletion of genes essential for PHA synthesis. Inspection of the MSR-1 genome revealed a set of three genes (*Mgr_4240* to *Mgr_4242*), encoding a putative PHA polymerase, an acetyl coenzyme A (acetyl-CoA) acetyltransferase, and an acetyl-CoA reductase (organized in a presumed *phbCAB* operon), as the most promising target for deletion. We constructed the deletion vector as diagrammed in Fig. S2 in the supplemental material and transferred it into MSR-1 by biparental conjugation. Eight of the kanamycin-resistant colonies

were screened for vector insertion up- or downstream of the *phbCAB* operon by PCR. All strains contained a downstream insertion, suggesting that vector integration upstream of the *phbCAB* genes was lethal. Three of the downstream insertion mutants were processed further and transferred onto FSM plates supplemented with 0.5, 1, or 2.5% (wt/vol) galactose and 100 ng/ml anhydrotetracycline for counterselection. The numbers of colonies on all plates were similar, suggesting that the lowest galactose concentration of 0.5% was entirely sufficient to suppress growth of cells which did not recombine. We therefore set 0.5% (wt/vol) galactose as the default concentration and obtained 29 colonies from these counterselective plates. A PCR screen suggested that 15 of them converted back to the wt, whereas 13 contained the desired deletion and 1 was inconclusive (see Fig. S4 in the supplemental material). This result indicated an approximate 1:1 ratio between deletion and reconstitution, as expected for an unbiased loop-out of the plasmid.

Nile red staining (38) and fluorescence microscopy revealed the absence of PHA inclusions in all 13 putative deletion mutants, suggesting that the cells had become deficient in PHA granule formation. Transmission electron microscopy (TEM) and cryo-electron tomography (CET) corroborated this observation and further revealed wt-like magnetosome chains and crystals (Fig. 2). Consistently, the *phbCAB* mutant strains exhibited a wt-like magnetic response, although cultivation experiments suggested a slight growth impairment of the mutants (see Fig. S5 in the supplemental material). To distinguish whether this in fact relies on reduced cell density or may be caused by different light scattering properties of the PHA granule-free cells, we determined absolute cell numbers by counting. The results indeed suggested a difference in the correlation of optical density and cell counts between wt and mutant strains (about 126% of wt cells). However, this difference did not completely compensate for the lower optical density (see Fig. S5 in the supplemental material), which might indicate that deletion of the *phbCAB* genes interferes with other metabolic pathways. Diminished growth (depending on the carbon source) upon deletion of PHA polymerase genes has also been reported, for example, for *Rhodospirillum rubrum* (39).

The only further MSR-1 mutant for which perturbed PHA synthesis has been reported to date accumulated 71% less PHA but hydrolyzed more ATP and consumed more oxygen than the wt. In contrast to our targeted deletion, this strain originated from aberrant recombination of a suicide vector next to an ATPase gene, which likely caused increased transcription of the gene (40). Thus, the reduced PHA synthesis in this mutant was presumably due to higher energy consumption and, hence, a secondary effect.

Since there is growing evidence that the distribution and segregation of intracellular macromolecules, organelles, and storage inclusions in bacteria are nonrandom (4, 41–43), we compared the positionings of polyphosphate inclusions and magnetosome chains in the *phbCAB* mutant to those in the wt. We found that the formation and cellular distribution of polyphosphate were not affected (Fig. 2, black arrows) and that the formation and positioning of magnetosome chains in the *phbCAB* mutant were indistinguishable from those of the wt (Fig. 2C).

Construction of unmarked and functional MamC and MamK fluorescent fusions. Fluorescent fusions to magnetosome-associated proteins have been described previously and have proven useful for analyses of subcellular protein localization patterns and dynamics (2, 19, 31, 32, 44–46). However, these

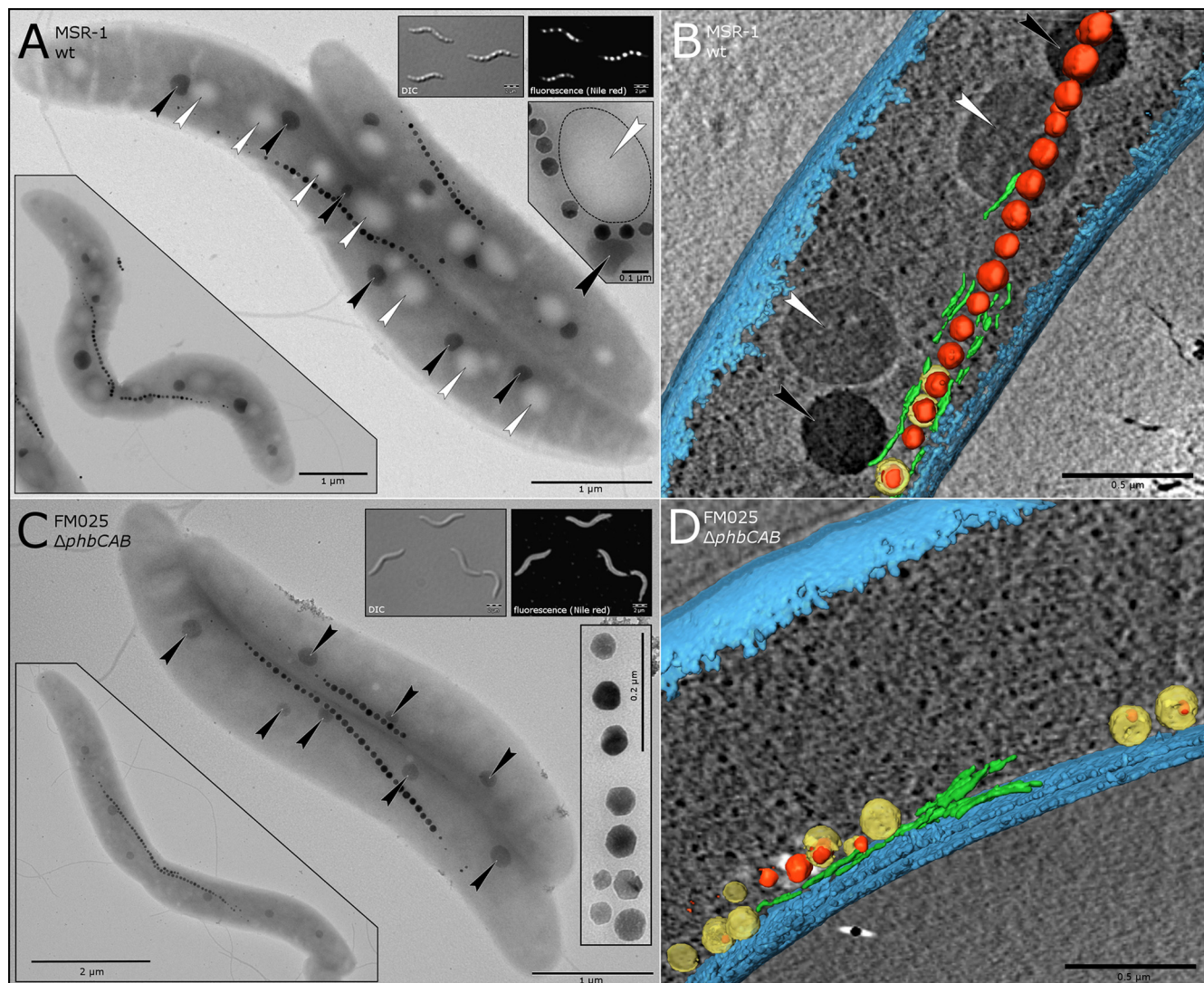


FIG 2 The *phbCAB* mutant is devoid of PHA granules but forms wt-like crystals, magnetosome chains, and polyphosphate inclusions. (A) TEM image of typical wt cells containing multiple PHA granules (indicated by white arrows) and attached polyphosphate inclusions (black arrows) beside a magnetosome chain (series of crystals). (Top insets) Differential interference contrast (DIC) and fluorescence images of Nile red-stained wt cells. PHA granules appear as three-dimensional globules by differential interference contrast and as brightly stained dots under fluorescence illumination. (Bottom right inset) Close-up view of a magnetosome chain entrapped by a PHA granule (white arrow, with the boundary marked by a dotted line) and a polyphosphate inclusion (black arrow). (Bottom left inset) Dividing wt cell with incipient division septum and buckling magnetosome chain, which is displaced by PHA granules. (B) Section of a segmented cryo-electron tomogram from a wt cell. PHA and polyphosphate inclusions are marked with white and black arrows, respectively. Magnetite crystals are depicted in red, magnetosome membranes are yellow, magnetosome filaments are in green, and the cell membrane is shown in blue. (C) TEM image of *phbCAB* mutant cells. Note the absence of PHA granules and the preserved regular spacing of polyphosphate inclusions (black arrows). (Top insets) Differential interference contrast and fluorescence images of Nile red-stained $\Delta phbCAB$ cells. The cells appear smooth by differential interference contrast. The fluorescence image suggests membrane-specific staining in the absence of PHA granules. (Bottom right inset) wt-like magnetite crystals of the *phbCAB* mutant. (Bottom left inset) Dividing cell with a characteristically buckling magnetosome chain opposite the asymmetrically inward growing division septum. (D) Segmented tomogram of a *phbCAB* mutant cell. The absence of PHA inclusions facilitates reconstruction of intracellular structures.

genes were expressed either from replicating vectors that cause cell-to-cell heterogeneity and overexpression of the fusion protein due to plasmid copy number variation or as additional variants from ectopic positions in the chromosome with the native, untagged gene present. However, we wished to demonstrate the functionality of fused key magnetosome marker proteins when expressed solely from their native chromosomal position. Therefore, we constructed markerless fluorescent fusions of *mamC* (carboxy terminal) or *mamK* (amino terminal) to *mCherry* or *egfp*

within the *mamGFDC* or *mamAB* operon, respectively, in both the wt and the *phbCAB* mutant using the newly established Galk counterselection technique. We selected MamC because of its abundance and specificity for the magnetosome membrane and the actin-like MamK for its function as a cytoskeletal element and its central role in magnetosome chain assembly and segregation (2, 4).

Fluorescence microscopy revealed filamentous fluorescence signals for both proteins, similar to previous reports (2, 4, 31, 44).

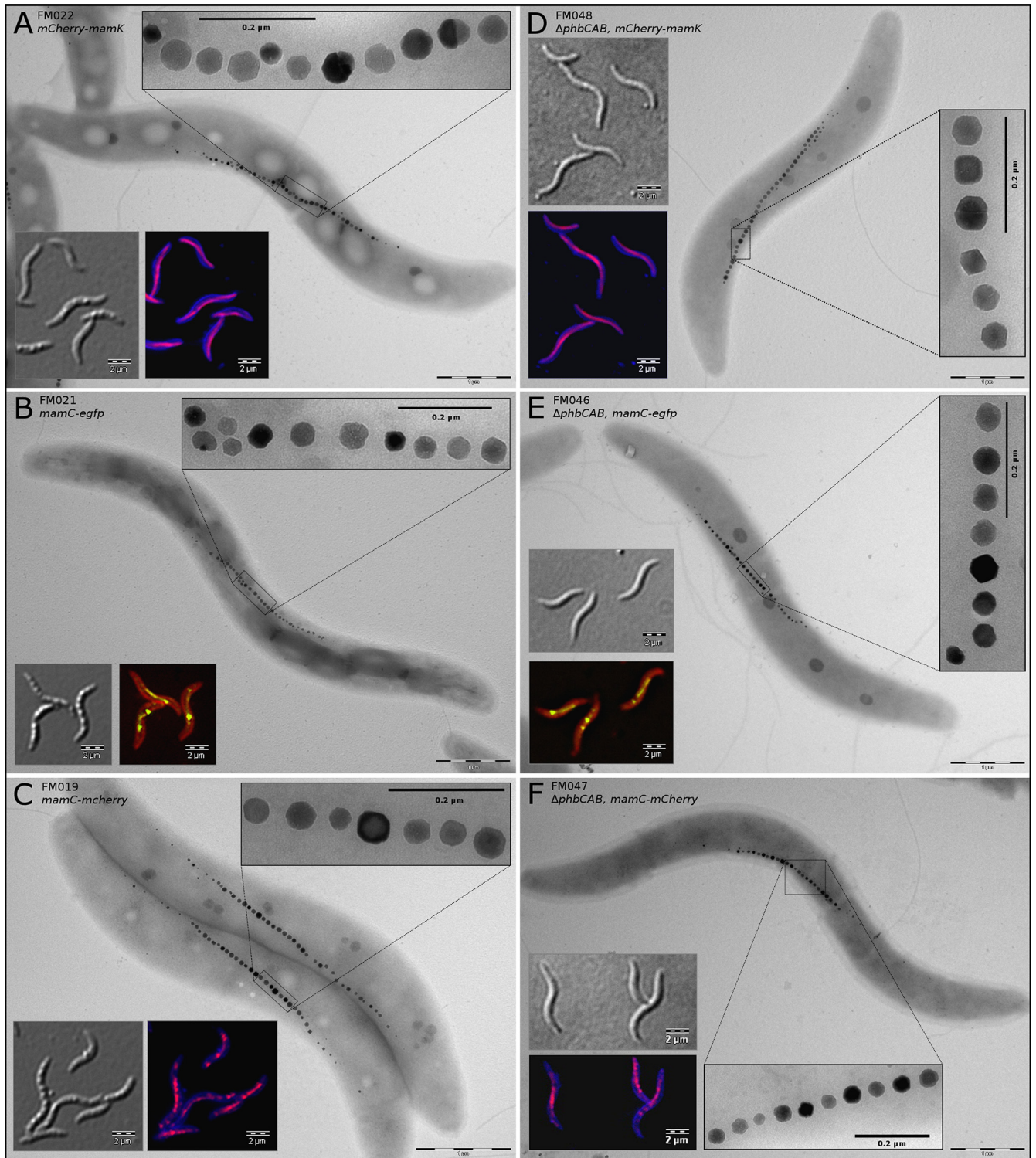


FIG 3 Differential interference contrast, fluorescence, and TEM images of MSR-1 wt (left column) and *phbCAB* mutant (right column) cells with markerless chromosomal fusions of *mamC* and *mamK* to *mCherry* (red) and *egfp* (green). The filamentous fluorescence signals are of even intensity throughout the cell populations (see also Fig. S5 and S6 in the supplemental material). All strains display wt-like magnetosome chains and crystals, indicating that the fusion proteins are functional and that there are no polar effects on downstream genes. (A and D) *mCherry-mamK*; (B and E) *mamC-egfp*; (C and F) *mamC-mCherry*. Membranes in panels B and E were stained with FM4-64 (red), and those in panels A, C, D, and F were stained with Cellbrite Blue cytoplasmic membrane stain.

MamC-EGFP and MamC-mCherry fluorescence was confined to intracellular spots, which concatenated into a nonresolvable string-like structure at midcell, corresponding to the magnetosome chain (Fig. 3B, C, E, and F). However, mCherry-MamK formed a filamentous structure of constant intensity reaching from pole to pole (Fig. 3A and B). Interestingly, the fluorescence signals were of uniform strength throughout the population (see Fig. S6 and S7 in the supplemental material), which is not observed when fluorescent protein fusions are expressed from plasmids. Electron microscopy showed wt-like magnetosome crystals and chains in all strains, indicating that the fusion proteins were functional as a sole copy in the chromosome and that no polar effects on downstream genes occurred (Fig. 3, insets). Markedly, in the *mCherry-mamK* strain, magnetosomes were organized into single or double chains at midcell, which is not observed in mutants with nonfunctional or missing MamK (4, 44). These characteristics of the mutant strains suggest that they are most favorable for microscopic and ultrastructural analyses as well as live-cell imaging.

Conclusions. In summary, we were able to enhance the toolbox for genetic manipulation of MSR-1 and potentially of other magnetospirilla by a quick, efficient, and reliable technique. Effort and time to generate mutants in MSR-1 could be reduced to less than one-third compared to the *Cre-lox* technology. These savings result mainly because only one deletion vector is constructed, only one conjugation procedure is necessary, and insertion mutants grow in the presence of only one antibiotic. In contrast to *sacB*-mediated counterselection, in our hands, the use of *galK* resulted in strict selection for recombination events and obviated the need for replica platings, reducing the time typically required for an unmarked mutation from several months to 3 to 5 weeks. Since no scar sequence is left in the chromosome, the introduction of tailored in-frame deletions, in-frame fusions, and site-specific point mutations is feasible. Recently, this technique was used to reliably introduce a number of single nucleotide exchanges into the MSR-1 chromosome and to precisely delete genome fragments of >19 kb (data not shown), illustrating that the adapted counterselection technique presented here is currently the most powerful tool for chromosomal manipulation of MSR-1.

ACKNOWLEDGMENTS

We are grateful to Isabelle Mai for technical assistance and to Günter Pfeifer for continuously supporting CET. We also thank A. Pollithy for providing vectors pAPI160 and pAPI173.

This research was supported by Deutsche Forschungsgemeinschaft grants Schu1080/9-1 and Schu1080/15-1 and by HFSP grant RGP0052/2012 to D.S.

REFERENCES

- Grünberg K, Müller EC, Otto A, Reszka R, Linder D, Kube M, Reinhardt R, Schüler D. 2004. Biochemical and proteomic analysis of the magnetosome membrane in *Magnetospirillum gryphiswaldense*. *Appl. Environ. Microbiol.* 70:1040–1050. <http://dx.doi.org/10.1128/AEM.70.2.1040-1050.2004>.
- Komeili A, Li Z, Newman DK, Jensen GJ. 2006. Magnetosomes are cell membrane invaginations organized by the actin-like protein MamK. *Science* 311:242–245. <http://dx.doi.org/10.1126/science.1123231>.
- Scheffel A, Gruska M, Faivre D, Linaroudis A, Pitzko JM, Schüler D. 2006. An acidic protein aligns magnetosomes along a filamentous structure in magnetotactic bacteria. *Nature* 440:110–114. <http://dx.doi.org/10.1038/nature04382>.
- Katzmann E, Müller FD, Lang C, Messerer M, Winkhofer M, Pitzko JM, Schüler D. 2011. Magnetosome chains are recruited to cellular division sites and split by asymmetric septation. *Mol. Microbiol.* 82:1316–1329. <http://dx.doi.org/10.1111/j.1365-2958.2011.07874.x>.
- Lang C, Schüler D, Faivre D. 2007. Synthesis of magnetite nanoparticles for bio- and nanotechnology: genetic engineering and biomimetics of bacterial magnetosomes. *Macromol. Biosci.* 7:144–151. <http://dx.doi.org/10.1002/mabi.200600235>.
- Ohuchi S, Schüler D. 2009. In vivo display of a multisubunit enzyme complex on biogenic magnetic nanoparticles. *Appl. Environ. Microbiol.* 75:7734–7738. <http://dx.doi.org/10.1128/AEM.01640-09>.
- Pollithy A, Romer T, Lang C, Müller FD, Helma J, Leonhardt H, Rothbauer U, Schüler D. 2011. Magnetosome expression of functional camelid antibody fragments (nanobodies) in *Magnetospirillum gryphiswaldense*. *Appl. Environ. Microbiol.* 77:6165–6171. <http://dx.doi.org/10.1128/AEM.05282-11>.
- Sugamata Y, Tanaka T, Matsunaga T, Yoshino T. 2014. Functional expression of an scFv on bacterial magnetic particles by in vitro docking. *Biochem. Biophys. Res. Commun.* 445:1–5. <http://dx.doi.org/10.1016/j.bbrc.2013.12.102>.
- Schultheiss D, Schüler D. 2003. Development of a genetic system for *Magnetospirillum gryphiswaldense*. *Arch. Microbiol.* 179:89–94. <http://magneticliquid.narod.ru/authority/573.pdf>.
- Marx C, Lidstrom M. 2002. Broad-host-range cre-lox system for antibiotic marker recycling in Gram-negative bacteria. *Biotechniques* 33:1062–1067. http://www.biotechniques.com/multimedia/archive/00010/02335rr01_10092a.pdf.
- Scheffel A, Gardes A, Grünberg K, Wanner G, Schüler D. 2008. The major magnetosome proteins MamGFDC are not essential for magnetite biomineralization in *Magnetospirillum gryphiswaldense* but regulate the size of magnetosome crystals. *J. Bacteriol.* 190:377–386. <http://dx.doi.org/10.1128/JB.01371-07>.
- Ullrich S, Schüler D. 2010. Cre-lox-based method for generation of large deletions within the genomic magnetosome island of *Magnetospirillum gryphiswaldense*. *Appl. Environ. Microbiol.* 76:2439–2444. <http://dx.doi.org/10.1128/AEM.02805-09>.
- Suzuki N, Nonaka H, Tsuge Y, Inui M, Yukawa H. 2005. New multiple-deletion method for the *Corynebacterium glutamicum* genome, using a mutant lox sequence. *Appl. Environ. Microbiol.* 71:8472–8480. <http://dx.doi.org/10.1128/AEM.71.12.8472-8480.2005>.
- Lohße A, Ullrich S, Katzmann E, Borg S, Wanner G, Richter M, Voigt B, Schweder T, Schüler D. 2011. Functional analysis of the magnetosome island in *Magnetospirillum gryphiswaldense*: the mamAB operon is sufficient for magnetite biomineralization. *PLoS One* 6:e25561. <http://dx.doi.org/10.1371/journal.pone.0025561>.
- Gay P, Le Coq D, Steinmetz M, Berkelman T, Kado CI. 1985. Positive selection procedure for entrapment of insertion sequence elements in gram-negative bacteria. *J. Bacteriol.* 164:918–921.
- Ried JL, Collmer A. 1987. An nptI-sacB-sacR cartridge for constructing directed, unmarked mutations in Gram-negative bacteria by marker exchange- eviction mutagenesis. *Gene* 57:239–246. [http://dx.doi.org/10.1016/0378-1119\(87\)90127-2](http://dx.doi.org/10.1016/0378-1119(87)90127-2).
- Kanetsuki Y, Tanaka M, Tanaka T, Matsunaga T, Yoshino T. 2012. Effective expression of human proteins on bacterial magnetic particles in an anchor gene deletion mutant of *Magnetospirillum magneticum* AMB-1. *Biochem. Biophys. Res. Commun.* 426:7–11. <http://dx.doi.org/10.1016/j.bbrc.2012.07.116>.
- Komeili A, Vali H, Beveridge TJ, Newman DK. 2004. Magnetosome vesicles are present before magnetite formation, and MamA is required for their activation. *Proc. Natl. Acad. Sci. U. S. A.* 101:3839–3844. <http://dx.doi.org/10.1073/pnas.0400391101>.
- Murat D, Quinlan A, Vali H, Komeili A. 2010. Comprehensive genetic dissection of the magnetosome gene island reveals the step-wise assembly of a prokaryotic organelle. *Proc. Natl. Acad. Sci. U. S. A.* 107:5593–5598. <http://dx.doi.org/10.1073/pnas.0914439107>.
- Tanaka M, Mazuyama E, Arakaki A, Matsunaga T. 2011. MMS6 protein regulates crystal morphology during nano-sized magnetite biomineralization in vivo. *J. Biol. Chem.* 286:6386–6392. <http://dx.doi.org/10.1074/jbc.M110.183434>.
- Schultheiss D, Kube M, Schüler D. 2004. Inactivation of the flagellin gene *flaA* in *Magnetospirillum gryphiswaldense* results in nonmagnetotactic mutants lacking flagellar filaments. *Appl. Environ. Microbiol.* 70:3624–3631. <http://dx.doi.org/10.1128/AEM.70.6.3624-3631.2004>.
- McKenney K, Shimatake H, Court D, Schmeissner U, Brady C, Rosen-

- berg M. 1981. A system to study promoter and terminator signals recognized by *Escherichia coli* RNA polymerase. *Gene Amplif. Anal.* 2:383–415.
23. Ueki T, Inouye S, Inouye M. 1996. Positive-negative KG cassettes for construction of multi-gene deletions using a single drug marker. *Gene* 183:153–157. [http://dx.doi.org/10.1016/S0378-1119\(96\)00546-X](http://dx.doi.org/10.1016/S0378-1119(96)00546-X).
 24. Barkan D, Stallings CL, Glickman MS. 2011. An improved counterselectable marker system for mycobacterial recombination using galK and 2-deoxy-galactose. *Gene* 470:31–36. <http://dx.doi.org/10.1016/j.gene.2010.09.005>.
 25. Merritt J, Tsang P, Zheng L, Shi W, Qi F. 2007. Construction of a counterselection-based in-frame deletion system for genetic studies of *Streptococcus mutans*. *Oral Microbiol. Immunol.* 22:95–102. <http://dx.doi.org/10.1111/j.1399-302X.2007.00329.x>.
 26. Müller FD, Schink CW, Hoiczky E, Cserti E, Higgs PI. 2012. Spore formation in *Myxococcus xanthus* is tied to cytoskeleton functions and polysaccharide spore coat deposition. *Mol. Microbiol.* 83:486–505. <http://dx.doi.org/10.1111/j.1365-2958.2011.07944.x>.
 27. Sambrook J, Russell DW. 2001. *Molecular cloning: a laboratory manual*, 3rd ed. Cold Spring Harbor Laboratory Press, Cold Spring Harbor, NY.
 28. Heyen U, Schüler D. 2003. Growth and magnetosome formation by microaerophilic *Magnetospirillum* strains in an oxygen-controlled fermentor. *App Microbiol. Biotechnol.* 61:536–544. <http://dx.doi.org/10.1007/s00253-002-1219-x>.
 29. Schüler D, Uhl R, Bäuerlein E. 1995. A simple light scattering method to assay magnetism in *Magnetospirillum gryphiswaldense*. *FEMS Microbiol. Lett.* 132:139–145. <http://dx.doi.org/10.1111/j.1574-6968.1995.tb07823.x>.
 30. Ho SN, Hunt HD, Horton RM, Pullen JK, Pease LR. 1989. Site-directed mutagenesis by overlap extension using the polymerase chain reaction. *Gene* 77:51–59. [http://dx.doi.org/10.1016/0378-1119\(89\)90358-2](http://dx.doi.org/10.1016/0378-1119(89)90358-2).
 31. Lang C, Schüler D. 2008. Expression of green fluorescent protein fused to magnetosome proteins in microaerophilic magnetotactic bacteria. *Appl. Environ. Microbiol.* 74:4944–4953. <http://dx.doi.org/10.1128/AEM.00231-08>.
 32. Scheffel A, Schüler D. 2007. The acidic repetitive domain of the *Magnetospirillum gryphiswaldense* MamJ protein displays hypervariability but is not required for magnetosome chain assembly. *J. Bacteriol.* 189:6437–6446. <http://dx.doi.org/10.1128/JB.00421-07>.
 33. Uebe R, Voigt B, Schweder T, Albrecht D, Katzmann E, Lang C, Bottger L, Matzanke B, Schüler D. 2010. Deletion of a fur-like gene affects iron homeostasis and magnetosome formation in *Magnetospirillum gryphiswaldense*. *J. Bacteriol.* 192:4192–4204. <http://dx.doi.org/10.1128/JB.00319-10>.
 34. Raschdorf O, Müller FD, Posfai M, Pitzko JM, Schüler D. 2013. The magnetosome proteins MamX, MamZ and MamH are involved in redox control of magnetite biomineralization in *Magnetospirillum gryphiswaldense*. *Mol. Microbiol.* 89:872–886. <http://dx.doi.org/10.1111/mmi.12317>.
 35. Nickell S, Forster F, Linaroudis A, Net WD, Beck F, Hegerl R, Baumeister W, Pitzko JM. 2005. TOM software toolbox: acquisition and analysis for electron tomography. *J. Struct. Biol.* 149:227–234. <http://dx.doi.org/10.1016/j.jsb.2004.10.006>.
 36. Katzen F, Becker A, Ielmini MV, Oddo CG, Ielpi L. 1999. New mobilizable vectors suitable for gene replacement in Gram-negative bacteria and their use in mapping of the 3' end of the *Xanthomonas campestris* pv. *campestris* gum operon. *Appl. Environ. Microbiol.* 65:278–282.
 37. Borg S, Hofmann J, Pollithy A, Lang C, Schüler D. 2014. New vectors for chromosomal integration enable high-level constitutive or inducible magnetosome expression of fusion proteins in *Magnetospirillum gryphiswaldense*. *Appl. Environ. Microbiol.* 80:2609–2616. <http://dx.doi.org/10.1128/AEM.00192-14>.
 38. Spiekermann P, Rehm BHA, Kalscheuer R, Baumeister D, Steinbüchel A. 1999. A sensitive, viable-colony staining method using Nile red for direct screening of bacteria that accumulate polyhydroxyalkanoic acids and other lipid storage compounds. *Arch. Microbiol.* 171:73–80. <http://dx.doi.org/10.1007/s002030050681>.
 39. Jin H, Nikolau BJ. 2012. Role of genetic redundancy in polyhydroxyalkanoate (PHA) polymerases in PHA biosynthesis in *Rhodospirillum rubrum*. *J. Bacteriol.* 194:5522–5529. <http://dx.doi.org/10.1128/JB.01111-12>.
 40. Liu J, Ding Y, Jiang W, Tian J, Li Y, Li J. 2008. A mutation upstream of an ATPase gene significantly increases magnetosome production in *Magnetospirillum gryphiswaldense*. *Appl. Microbiol. Biotechnol.* 81:551–558. <http://dx.doi.org/10.1007/s00253-008-1665-1>.
 41. Galán B, Dinjaski N, Maestro B, de Eugenio LI, Escapa IF, Sanz JM, Garcia JL, Prieto MA. 2011. Nucleoid-associated PhaF phasin drives intracellular location and segregation of polyhydroxyalkanoate granules in *Pseudomonas putida* KT2442. *Mol. Microbiol.* 79:402–418. <http://dx.doi.org/10.1111/j.1365-2958.2010.07450.x>.
 42. Jendrossek D, Pfeiffer D. 21 January 2014. New insights in the formation of polyhydroxyalkanoate granules (carbonosomes) and novel functions of poly(3-hydroxybutyrate). *Environ. Microbiol.* <http://dx.doi.org/10.1111/1462-2920.12356>.
 43. Pfeiffer D, Wahl A, Jendrossek D. 2011. Identification of a multifunctional protein, PhaM, that determines number, surface to volume ratio, subcellular localization and distribution to daughter cells of poly(3-hydroxybutyrate), PHB, granules in *Ralstonia eutropha* H16. *Mol. Microbiol.* 82:936–951. <http://dx.doi.org/10.1111/j.1365-2958.2011.07869.x>.
 44. Draper O, Byrne ME, Li Z, Keyhani S, Barrozo JC, Jensen G, Komeili A. 2011. MamK, a bacterial actin, forms dynamic filaments in vivo that are regulated by the acidic proteins MamJ and LimJ. *Mol. Microbiol.* 82:342–354. <http://dx.doi.org/10.1111/j.1365-2958.2011.07815.x>.
 45. Schultheiss D, Handrick R, Jendrossek D, Hanzlik M, Schüler D. 2005. The presumptive magnetosome protein Mms16 is a poly(3-hydroxybutyrate) granule-bound protein (phasin) in *Magnetospirillum gryphiswaldense*. *J. Bacteriol.* 187:2416–2425. <http://dx.doi.org/10.1128/JB.187.7.2416-2425.2005>.
 46. Zeytuni N, Ozyamak E, Ben-Harush K, Davidov G, Levin M, Gat Y, Moyal T, Brik A, Komeili A, Zarivach R. 2011. Self-recognition mechanism of MamA, a magnetosome-associated TPR-containing protein, promotes complex assembly. *Proc. Natl. Acad. Sci. U. S. A.* 108:E480–E487. <http://dx.doi.org/10.1073/pnas.1103367108>.
 47. Hanahan D. 1983. Studies on transformation of *Escherichia coli* with plasmids. *J. Mol. Biol.* 166:557–580. [http://dx.doi.org/10.1016/S0022-2836\(83\)80284-8](http://dx.doi.org/10.1016/S0022-2836(83)80284-8).

Publication A: Supplementary Information

A tailored *galK* counterselection system for efficient markerless
gene deletion and chromosomal tagging in
Magnetospirillum gryphiswaldense

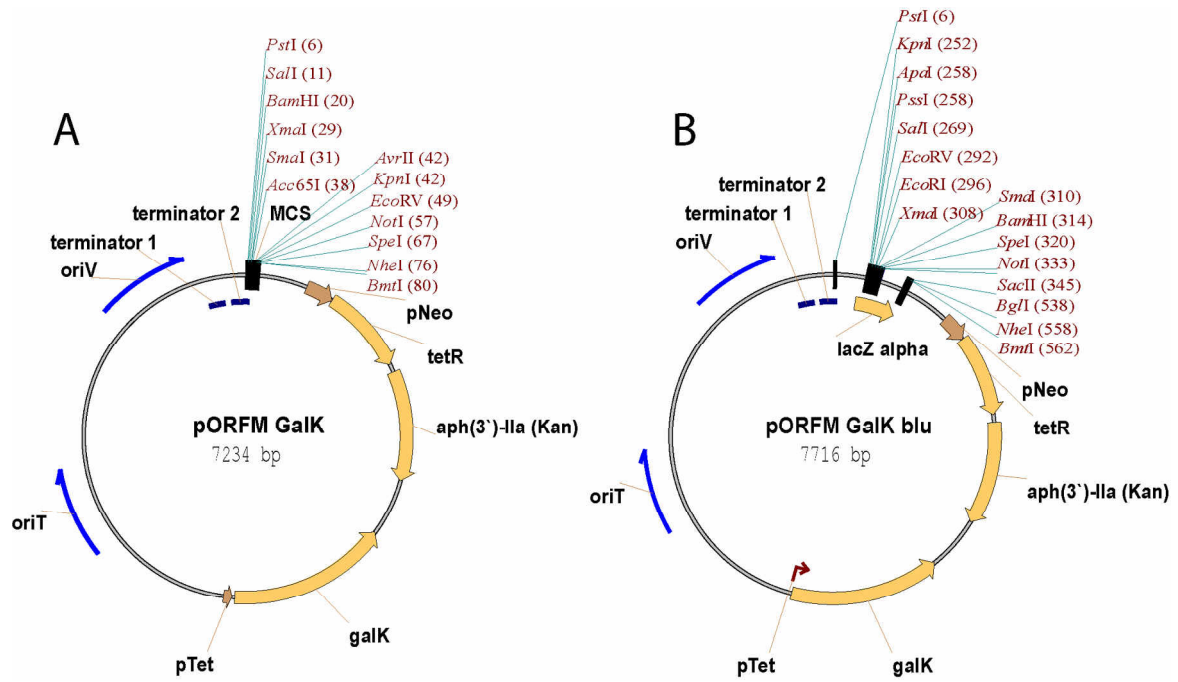


Figure S1. Vector maps of (A) pORFM GalK and (B) pORFM GalK blu. All relevant plasmid features are indicated. Unique restriction sites located in the multiple cloning site (MCS) or the lacZ gene fragment, respectively are labelled in red.

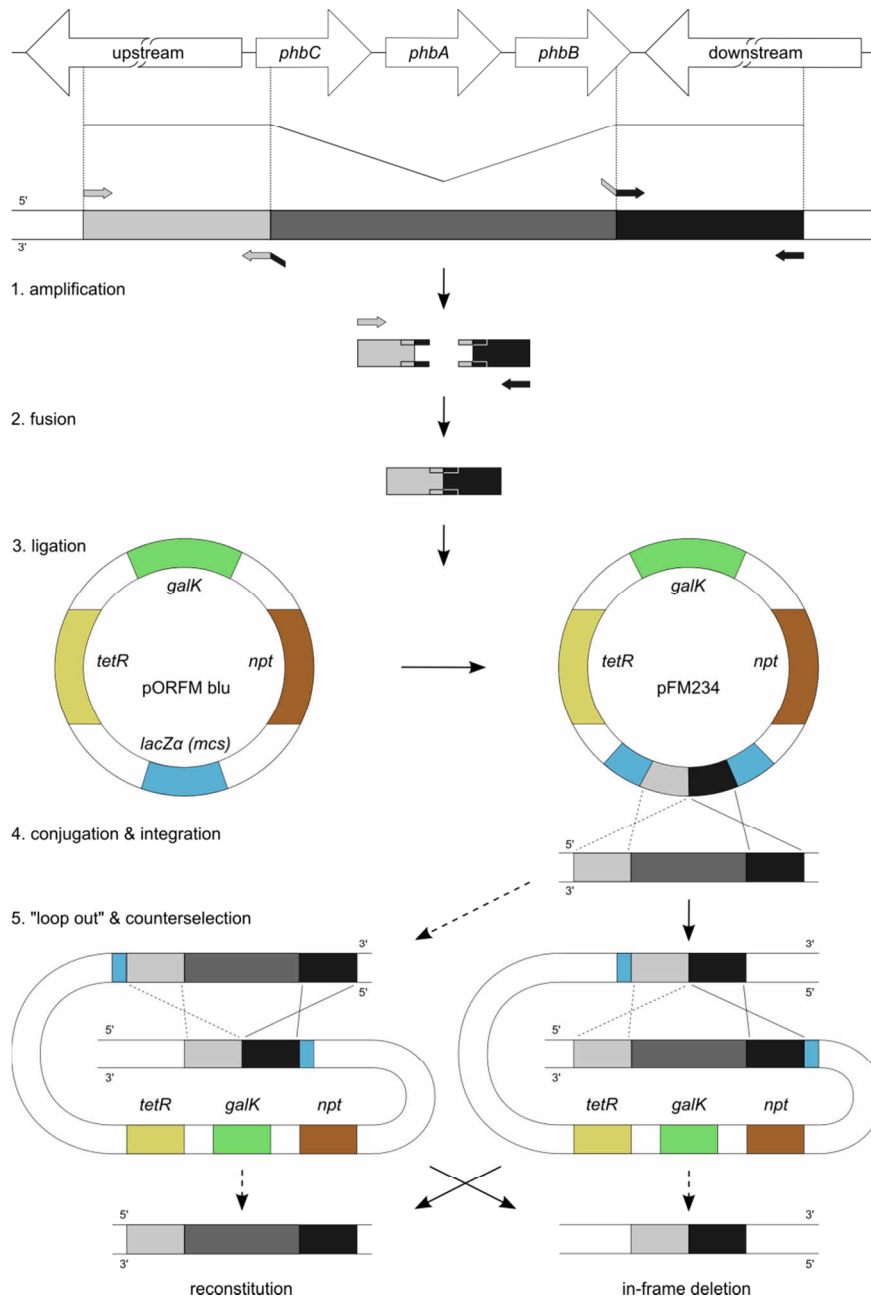


Figure S2. Scheme of in-frame gene deletion in MSR-1 with pORFM *blu* exemplified by the *phbCAB* operon. First, homologous regions up- and downstream of the target are amplified by PCR and fused by a second, overlap-extension PCR. This generates the mutated in-frame allele *in vitro* where the first and last codons of the target coding region are fused in-frame generating a short nonsense ORF. The PCR product becomes blunt-end ligated into pORFM *blu* and transformed into *E. coli* DH5α. White, kanamycin resistant clones are selected and the inserts of their plasmids are sequenced with vector specific primers oFM280b and oFM281b to verify absence of mutations within the homologous regions (not shown). Subsequently, the vector is transformed into *E. coli* BW29427 and conjugated into MSR-1. Recombinant, merodiploid clones are isolated from kanamycin supplemented FSM plates and screened for up or downstream integration of the plasmid (step 4, dashed or solid lines, respectively and illustrated in Figure S2 for the fusion of *mamC* to *egfp* and *mCherry*). At least one of each integration type is used for counterselection with galactose which results either in reconstitution of the wt genotype or in-frame deletion of the target sequence (step 5).

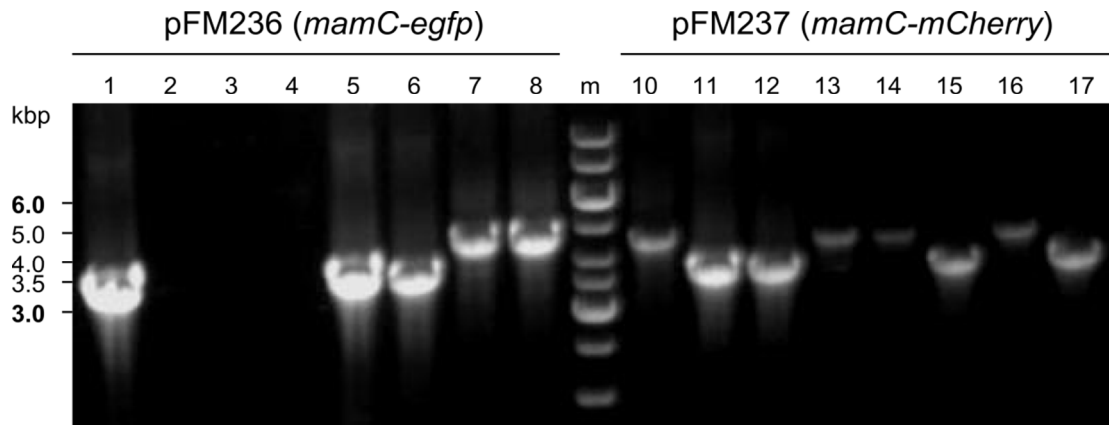


Figure S3. Result of up- or downstream vector insertion diagnosis after pFM236 (*mamC-egfp*, lanes 1-8) and pFM237 (*mamC-mCherry*, lanes 10-17) conjugation. Larger fragments represent vector insertions upstream of *mamC*, smaller fragments represent downstream insertions. The size difference of the DNA fragments corresponds to *egfp* and *mCherry* (approximately 720 bp) respectively. m: DNA size standard (marker). Cells were picked from FSM plates with kanamycin and grown in 96-well plates over night prior to colony-PCR with oligonucleotide primers oFM281/oFM289a. One strain of each insertion type was used for counterselection on galactose plates.

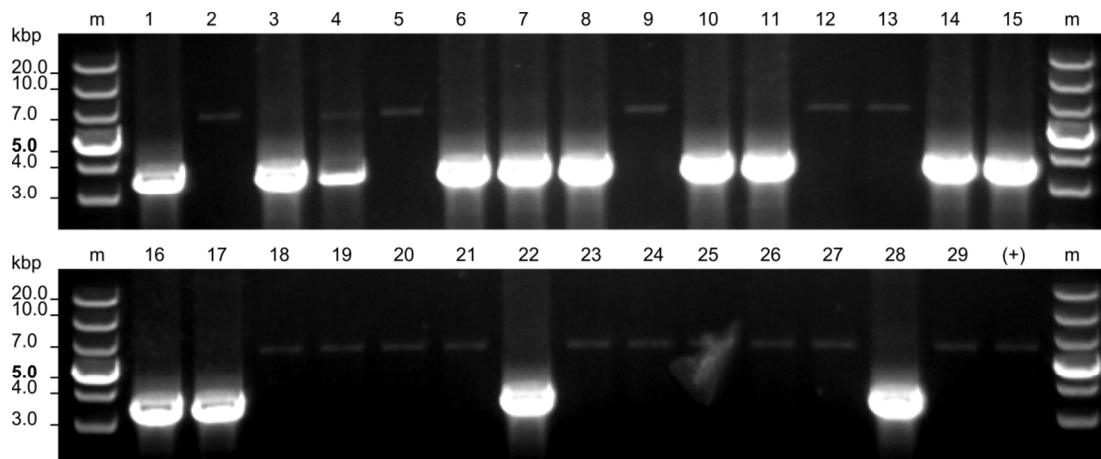


Figure S4. Result of colony-PCR diagnosis for *phbCAB* deletion after galactose counterselection. Of the 29 colonies tested, 13 likely contain the deletion (as suggest by the lower ~ 3.5 kb band), 15 converted back to wt (~7 kb band) and one was inconclusive (lane 4). (+) = wt control, m = DNA size standard (marker).

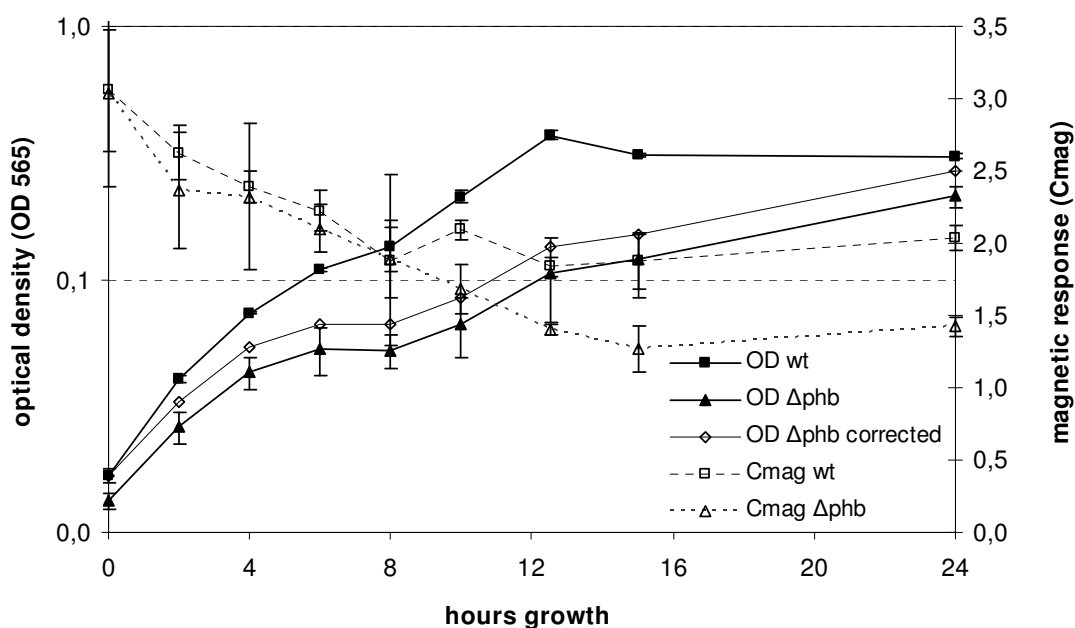


Figure S5. Growth and magnetic response of phbCAB mutant and wt cultures as determined by light scattering and cell counts. OD measurements of the Δ phbCAB mutant (filled triangles) suggest slight growth impairment compared to wt (filled squares). Open diamonds: Calculated OD values of the phbCAB mutant according to the difference in cell counts. 100 ml FSM medium in sealed glass bottles (pre-flushed with 2% oxygen and 98% nitrogen as described (41)) were inoculated from overnight cultures to a calculated optical density of 0.01 and incubated at 30°C and 120 rpm agitation. 1 ml samples were withdrawn at the indicated time points and measured photometrically for optical density and magnetic response as described in the Experimental Procedures section.

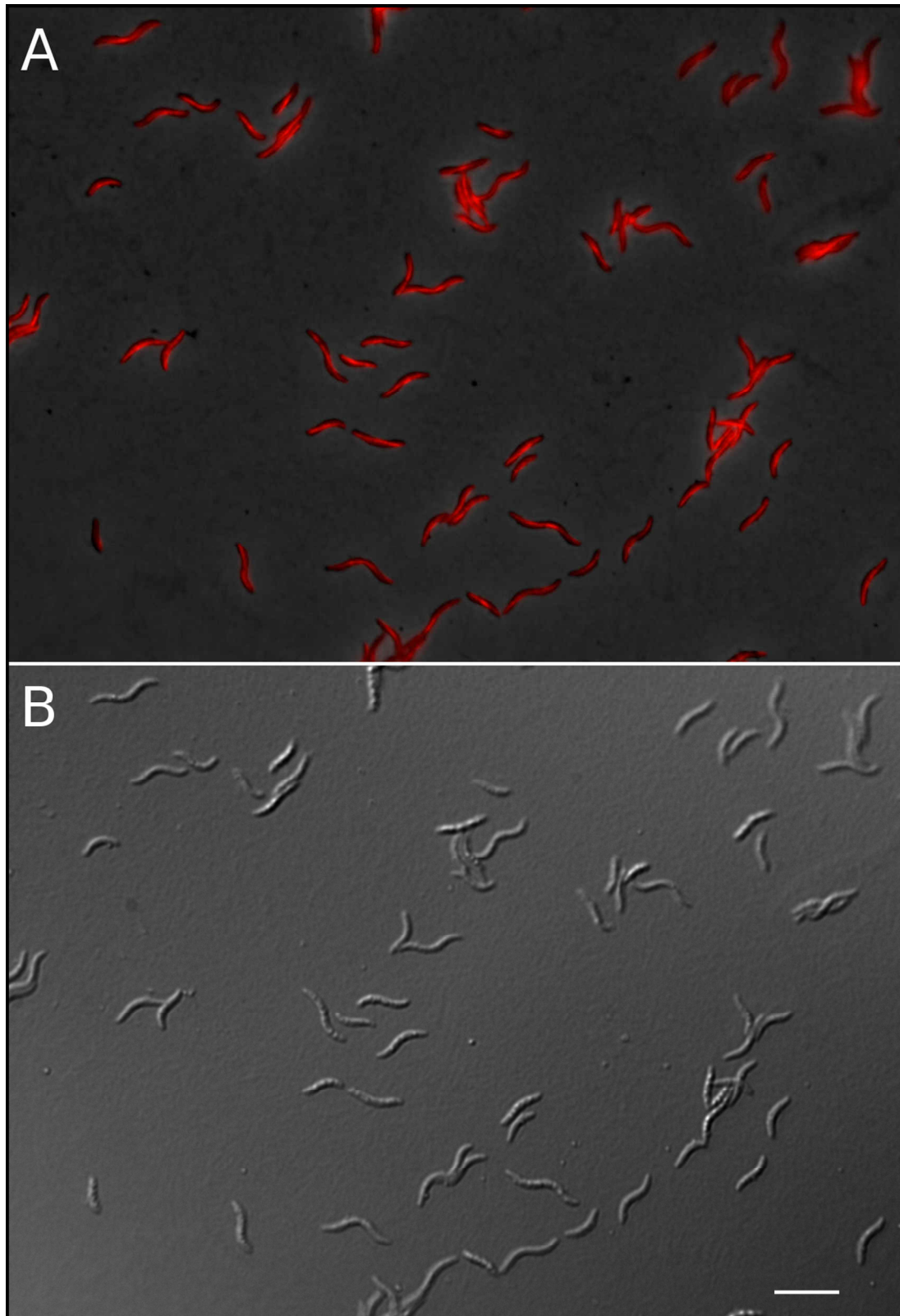


Figure S6. Chromosomal tagging of the actin-like *mamK* with *mCherry* results in a cell population with filamentous pole-to-pole fluorescence signals of uniform intensity and distribution. (A) Fluorescence and phase contrast overlay image of strain FM022 (*mcherry-mamK*). (B) DIC image of the same section. Bar: 5 μm .

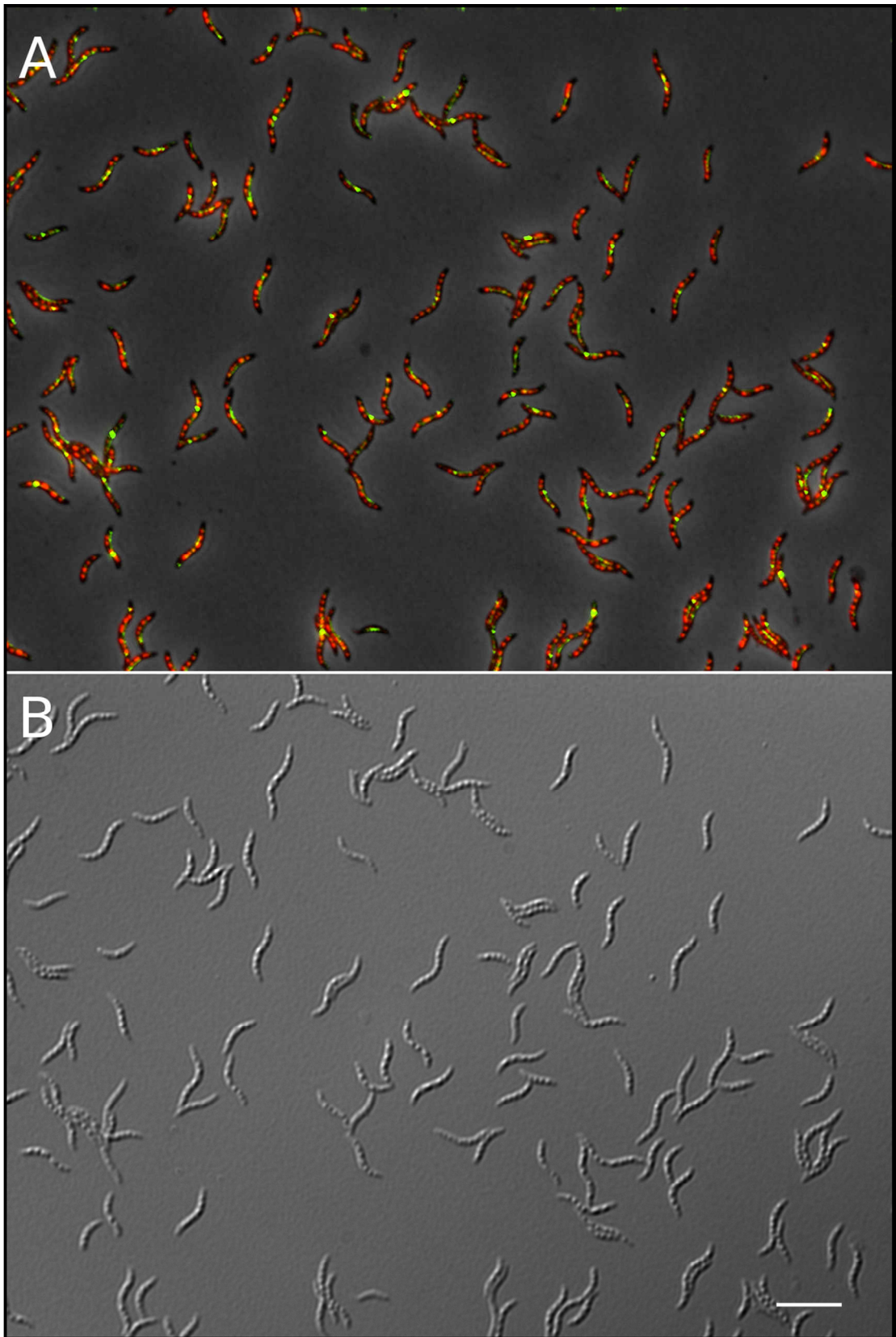


Figure S7. (A) Fluorescence and phase contrast overlay image of strain FM021 harbouring a chromosomally encoded fusion of the magnetosome membrane-specific MamC protein to EGFP. PHA inclusions were stained with Nile red. (B) DIC image of the same section. Bar: 5 μm.

Table S1: DNA oligonucleotides

Name	Sequence (5' → 3')¹	Description
Primers for pORFM GalK / blu construction		
oOR059	gatgaagctggcggattgtcctactcagg	terminator amplification forward
oOR060	gactctgcaggactcctgttgatagatccagtaatgac	terminator amplification reverse
oOR063	cgagcatatgagtctgaaagaaaaacacaatctc	<i>galk</i> forward
oOR077	acttggatcccgttcagcactgtcctgtctcc	<i>galk</i> reverse
oOR082	atgagtcgacaattttgtgacactctatcattgatag	<i>P_{ter}</i> - <i>galk</i> forward
oOR083	gttccaattgcgttcagcactgtcctgtctcc	<i>P_{ter}</i> - <i>galk</i> reverse
tetRfwSacI	gcagagctcctccggctggctggtttattg	<i>tetR</i> forward
tetRrevSacI	gctgagctcctttaagaccctttcac	<i>tetR</i> reverse
General pORFM screening and sequencing primers		
oFM280a	ctgccactcatcgcagcttagcttgg	pORFM GalK sequencing forward
oFM281	ggctttctacgtgtccgcttcttagc	pORFM GalK sequencing reverse
oFM280b	aaacagctatgaccatgattacgccaagcg	pORFM blu sequencing forward
oFM281b	cgcgtaatacgcactcactatagggcg	pORFM blu sequencing reverse
<i>phbCAB</i> deletion with pORFM blu		
oFM341	ggccggcgcgatcctcgacc	upstream fragment forward
oFM342	acggcccacatggcggtaaagggcgacgccg	upstream fragment reverse
oFM343	taccgcatgtgggctgtggccg	downstream fragment forward
oFM344	tggggcgggcccacgtgctgc	downstream fragment reverse
oFM207g	gccaggggaatcacccgtaaagccg	sequencing (upstream fragment)
oFM207h	gtcccggatgccccatcggc	sequencing (upstream fragment)
oFM207i	tcgggcgcggtattcagccg	sequencing (downstream fragment)
oFM207k	ccatggcccaggccaatgccg	sequencing (downstream fragment)
oFM207l	ctgggtgaagatcttgcgaggaaattgg	verify deletion (upstream)
oFM207m	gccaggatcaaggcttgagtaccg	verify deletion (downstream)
<i>mamC-egfp</i> and <i>mamC-mCherry</i> in-frame fusion with pORFM GalK		
oFM270	gtcgacctagctatctgggcatcctctgctcg	upstream fragment forward

oFM271	<u>gg</u> taccggccaattctccctcagaatgtctctcgtcg	upstream fragment reverse
oFM272	<u>gg</u> taccgaacgttacgcgtcaccggtcggccacctgt gcctgcagggcgag <u>ctcg</u> aggtagcaagggcgag gagctgttc	<i>egfp</i> forward
oFM273	<u>ga</u> attctatcactgttacagctcgtccatgccgagag	<i>egfp</i> reverse
oFM274	<u>ga</u> attcaatattgggctgggtcacggcattcagacacc	downstream fragment forward
oFM275	<u>g</u> ctagccgacgaaggtggtcatttccaatgaccg	downstream fragment reverse
oFM276	<u>gg</u> taccgaacgttacgcgtcaccggtcggccacctgt gcctgcagggcgag <u>ctcg</u> aggtagcaagggcgag gaggataacatgg	<i>mCherry</i> forward
oFM277	<u>ga</u> attctcattactgttacagctcgtccatgccgcc	<i>mCherry</i> reverse
oFM278	atcggcggcatcggaaactggattgc	upstream fragment sequencing forward
oFM278a	ttcgtctcaggaaggccaataaccatgc	upstream fragment sequencing forward
oFM279	aatgacctcagggggaatcctctaccg	downstream fragment sequencing reverse
oFM279a	ggcctgggcctttagatgtacg	downstream fragment sequencing reverse
oFM289a	gagcctgctaagcgagggcacaagc	verify fusion (upstream)
oFM290	cgccattcatgccttgcgatgacg	verify fusion (downstream)
<hr/> <i>mCherry-mamK</i> in-frame fusion with pORFM GalK <hr/>		
oFM369	<u>gtc</u> gacggggctcaggccaatgatcttatcatcg	<i>mamK-mCherry</i> fusion upstream fragment forward
oFM370	<i>ctg</i> ctcatttgtcactccgttcgctgctaacagatc	<i>mamK-mCherry</i> fusion upstream fragment reverse
oFM371	<i>agt</i> gacaaaatgagcaagggcgaggaggataacat gg	<i>mCherry</i> forward
oFM372	<u>gg</u> atccgcgccgccgaattctccggagctcgagatc ttaaggtagcctgttacagctcgtccatgccgcc	<i>mCherry</i> reverse
oFM373	<u>gg</u> atcctatgagtgaaggtgaaggccaggccaag	<i>mCherry-mamK</i> fusion downstream fragment forward
oFM374	<u>act</u> agtgaacgccttcatcaccatgagcacgg	<i>mCherry-mamK</i> fusion downstream fragment reverse
oFM375	atgtccagccggaacggatgccg	upstream fragment sequencing
oFM376	ggctatggcttgacaagctgaacaatacc	downstream fragment sequencing
oFM377	ctgggatggagatcgagacttttatggc	verify fusion (upstream)
oFM378	cccaataatcaccatcagggcggttcagc	verify fusion (downstream)

¹Reverse complementary sequences are *italicised*, restriction sites are underlined.

4.2 Publication B:

The magnetosome proteins MamX, MamZ, and MamH are involved in redox control of magnetite biomineralization in *Magnetospirillum gryphiswaldense*

Oliver Raschdorf^{1,2}, Frank D. Müller^{1,3}, Mihály Pósfai⁴, Jürgen M. Plitzko²
and Dirk Schüler^{1,3}.

Affiliations:

1: Ludwig Maximilian University Munich, Department of Microbiology

2: Max-Planck-Institute of Biochemistry, Department of Molecular Structural Biology

3: University of Bayreuth, Department of Microbiology

4: University of Pannonia, Veszprém, Department of Department of Earth and Environmental Science

Molecular Microbiology (2013) **89**(5):872-886

The magnetosome proteins MamX, MamZ and MamH are involved in redox control of magnetite biomineralization in *Magnetospirillum gryphiswaldense*

Oliver Raschdorf,^{1,2} Frank D. Müller,¹ Mihály Pósfai,³ Jürgen M. Plitzko^{2,4} and Dirk Schüler^{1*}

¹Ludwig Maximilian University Munich, Dept. Biology I, Microbiology, D-82152 Planegg-Martinsried, Germany.

²Max Planck Institute of Biochemistry, Dept. of Molecular Structural Biology, D-82152 Planegg-Martinsried, Germany.

³University of Pannonia, Dept. of Earth and Environmental Sciences, POB 158, 8200 Veszprém, Hungary.

⁴Bijvoet Center for Biomolecular Research, Utrecht University, 3584 CH Utrecht, the Netherlands.

Summary

***Magnetospirillum gryphiswaldense* uses intracellular chains of membrane-enveloped magnetite crystals, the magnetosomes, to navigate within magnetic fields. The biomineralization of magnetite nanocrystals requires several magnetosome-associated proteins, whose precise functions so far have remained mostly unknown. Here, we analysed the functions of MamX and the Major Facilitator Superfamily (MFS) proteins MamZ and MamH. Deletion of either the entire *mamX* gene or elimination of its putative haem c-binding magnetochrome domains, and deletion of either *mamZ* or its C-terminal ferric reductase-like component resulted in an identical phenotype. All mutants displayed WT-like magnetite crystals, flanked within the magnetosome chains by poorly crystalline flake-like particles partly consisting of haematite. Double deletions of both *mamZ* and its homologue *mamH* further impaired magnetite crystallization in an additive manner, indicating that the two MFS proteins have partially redundant functions. Deprivation of Δ *mamX* and Δ *mamZ* cells from nitrate, or additional loss of the respiratory nitrate reductase Nap from Δ *mamX* severely exacerbated the magnetosome defects and entirely inhibited the formation of regular crystals,**

suggesting that MamXZ and Nap have similar, but independent roles in redox control of biomineralization. We propose a model in which MamX, MamZ and MamH functionally interact to balance the redox state of iron within the magnetosome compartment.

Introduction

Magnetotactic bacteria (MTB) use unique intracellular organelles, the magnetosomes, to orient along magnetic fields (Jogler and Schüler, 2009). In *Magnetospirillum gryphiswaldense* (MSR-1) and other MTB, magnetosomes consist of membrane-enveloped, single-magnetic domain magnetite (Fe₃O₄) crystals that are aligned in regular chains (Jogler and Schüler, 2009). Biomineralization of functional magnetite crystals proceeds in sequential steps and starts with the invagination of the cytoplasmic membrane to form the magnetosome membrane (MM) (Scheffel *et al.*, 2006; Katzmann *et al.*, 2010), which is associated with a set of > 20 specific proteins. This is followed by the uptake and transport of iron into MM vesicles (Uebe *et al.*, 2010, 2011) and the synthesis of magnetite nanoparticles within them (Faivre *et al.*, 2007). It is assumed that biomineralization of the mixed-valence iron oxide magnetite depends on reducing and slightly alkaline conditions and proceeds by co-precipitation of balanced amounts of ferric and ferrous iron (Faivre *et al.*, 2004; Faivre and Schüler, 2008; Fischer *et al.*, 2011). Thus, the process requires a precise biological control of redox conditions (Faivre and Schüler, 2008). Recently it was shown that magnetosome biomineralization in MSR-1 is closely linked with the activity of the respiratory nitrate reductase Nap, and that deletion of the multi-gene *nap* operon resulted in severe defects in magnetosome crystals (Li *et al.*, 2012).

Besides several accessory and general metabolic functions such as cellular iron uptake and regulation (Uebe *et al.*, 2010; Rong *et al.*, 2012), all specialized functions for magnetosome synthesis in magnetospirilla are encoded by the four operons *mms6*, *mamGFDC*, *mamAB* and *mamXY* that are part of a larger (~ 115 kb) genomic region, the magnetosome island (MAI) (Schübbe *et al.*, 2003; Ullrich *et al.*, 2005). The 16.3 kb *mamAB* cluster encodes functions essential for magnetosome biogenesis (*mamB*, *I*,

Accepted 29 June, 2013. *For correspondence. E-mail dirk.schueler@lrz.uni-muenchen.de; Tel. (+49) 89218074502; Fax (+49) 89218074515.

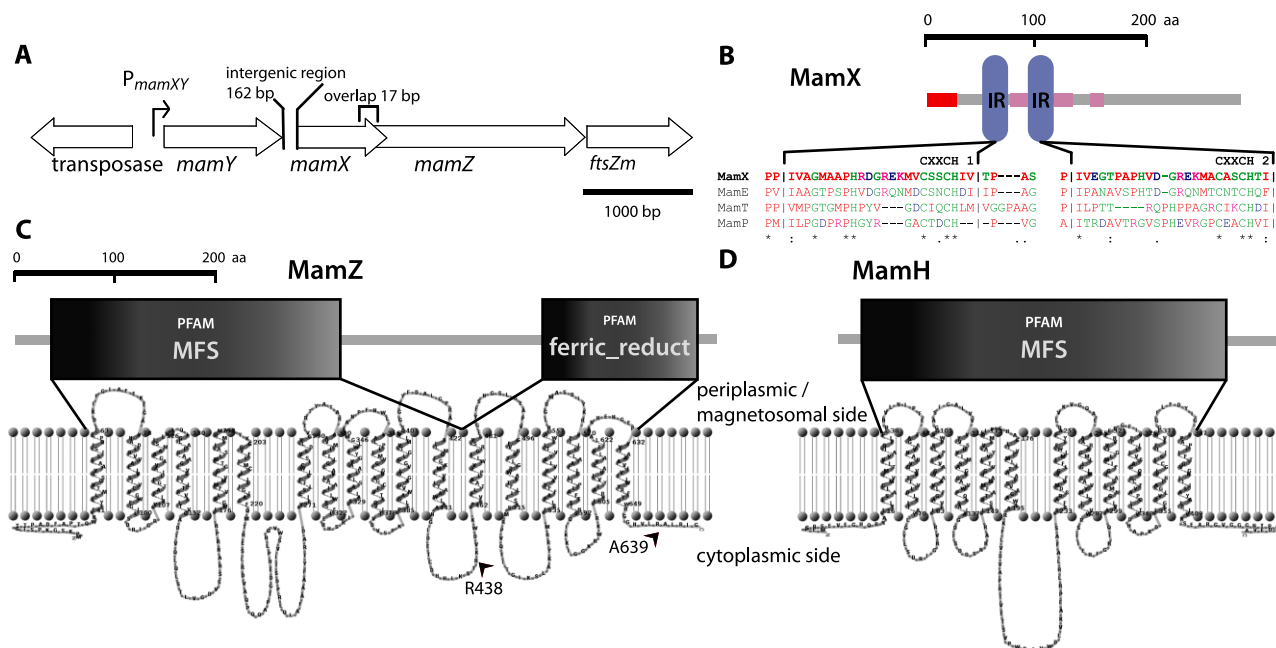


Fig. 1. Molecular characteristics of MamX, MamZ and MamH.

A. Organization of the *mamXY* operon. The putative P_{mamXY} and the intergenic region between *mamY* and *mamX* are indicated. The coding regions of *mamX* and *mamZ* overlap by 17 bp.

B. Predicted domain structure of MamX. The protein has a C-terminal signal peptide or a transmembrane helix (red), followed by two internal repeats (IR), containing the putative magnetochrome motifs, and three low complexity regions (magenta). Alignment of MamX, MamE, MamT and MamP of MSR-1 (colour code: red = small and hydrophobic and aromatic aa, w/o Y, green = hydroxyl, sulphhydryl and amine aa incl. G, blue = acidic aa, magenta = basic w/o H) reveals the conserved paired CXXCH motif.

C. Predicted domain structure of MamZ. The protein consists of a C-terminal MFS domain, comprising the first 12 TMD and an N-terminal ferric reductase like transmembrane component, comprising the last six TMD. Marked R438 and A639 residues represent the predicted boundaries of the ferric reductase domain.

D. Predicted domain structure of MamH.

A high-resolution image of the predicted membrane topologies of MamZ and MamH can be found in Fig. S2.

L, *Q*), magnetosomal iron transport (*mamB*, *M*) and magnetite biomineralization (*mamE*, *O*, *T*, *P*, *S*, *R*) (Murat *et al.*, 2010; Yang *et al.*, 2010; Quinlan *et al.*, 2011; Uebe *et al.*, 2011) in addition to functions controlling magnetosome chain assembly and segregation encoded by *mamK* and *mamJ* (Komeili *et al.*, 2006; Scheffel *et al.*, 2006; Katzmann *et al.*, 2010; Draper *et al.*, 2011). The *mamGFDC* (2.1 kb) and *mms6* (3.6 kb) operons are not essential for biomineralization but encode accessory functions for size and shape control of magnetite particles (Scheffel *et al.*, 2008; Murat *et al.*, 2010; 2012; Lohße *et al.*, 2011; Tanaka *et al.*, 2011).

The *mamXY* operon is conserved in all magnetospirilla and encodes MamY, MamX, MamZ [previously also referred to as MamH-like (Richter *et al.*, 2007)] and the tubulin-like FtsZm protein [previously also referred to as FtsZ-like (Ding *et al.*, 2010)] (Fig. 1). Independent studies in MSR-1 and *Magnetospirillum magneticum* (AMB-1) revealed that all proteins are associated with the MM (Grünberg *et al.*, 2004; Tanaka *et al.*, 2006; Lohße *et al.*, 2011). Deletion of the entire 5.0 kb *mamXY* operon of

MSR-1 resulted in cells that formed two distinct types of magnetosome particles: short chains of nearly regularly shaped, cubo-octahedral crystals were flanked by small particles with poorly defined morphologies (Lohße *et al.*, 2011). MamY of AMB-1 was implicated in membrane tubulation and MM vesicle formation, but has no function in biomineralization as a $\Delta mamY$ mutant still produced WT-like magnetosomes (Tanaka *et al.*, 2010). However, loss of FtsZm caused the formation of small, irregular and superparamagnetic particles (Ding *et al.*, 2010).

MamX and MamZ were identified as magnetosome signature genes by genome comparisons of magnetotactic alphaproteobacteria, but so far were not found in other MTB (Richter *et al.*, 2007). MamX displays weak and local sequence similarity to the other magnetosome proteins MamS and MamE. Whereas the C-terminal domain of MamZ exhibits similarities to a ferric reductase-like transmembrane component (Richter *et al.*, 2007) its N-terminal domain is homologous to the Major Facilitator Superfamily (MFS) transporter MamH (64% similarity) which is encoded within the *mamAB* operon. A *mamH* deletion

mutant in AMB-1 was able to produce WT-like magnetosomes and only showed a slightly reduced magnetic response (C_{mag}) (Murat *et al.*, 2010). However, the functions of MamX, MamZ and MamH and their significance for magnetosome formation have remained unknown.

In this study we genetically dissected the functions of *mamX*, *mamZ* and *mamH* in MSR-1. Our data indicate that all three genes have key roles in magnetite biomineralization. We demonstrate that MamX and MamZ are likely involved in redox control to poise optimal conditions for magnetite formation, and that these functions rely on the presence of two putative haem *c* binding 'magnetochrome' domains in MamX and the ferric reductase-like transmembrane component of MamZ. Furthermore, our data suggest that the redox pathway mediated by MamX and MamZ is likely to act independently from nitrate reduction. We present a model, in which MamZ, MamX and MamH functionally interact in the MM to form an iron oxidoreductase and transport complex for magnetite biomineralization.

Results

Transcriptional organization of the mamXY operon

After correction of a mispredicted N-terminus we found *mamX* and *mamZ* of MSR-1 to overlap by 17 bp as in other magnetospirilla (Fig. 1A and Fig. S1), suggesting a close functional association and translational coupling of both genes. *mamX* is always followed by *mamZ* in all other magnetospirilla and also in *Magnetococcus marinus* (MC-1) and *Magnetovibrio blakemorii* (MV-1), despite the different genomic context of *mamXZ* in these strains (Jogler and Schüler, 2007; Richter *et al.*, 2007). It was shown in a previous study that all four genes of the polycistronic *mamXY* operon are likely driven from a single, yet unidentified promoter (Ding *et al.*, 2010), which we predicted within the region 285 bp upstream of the first transcribed gene *mamY* and downstream of an adjacent transposase gene (Fig. 1A). In addition, a conspicuously large (162 bp) intergenic region between *mamY* and *mamX* might contain an alternative internal promoter (Fig. 1A). To assess activity and strength of the putative promoters, we transcriptionally fused *egfp* and *gusA* as reporter genes behind the 285 bp and the 162 bp fragment respectively. Except for the positive control (*egfp* fused to the strong *mamDC* promoter) (C. Lang *et al.*, unpublished), fluorescence intensities of all tested EGFP fusions were below detection in plate reader assays. By fluorescence microscopy we only detected a faint signal for the $P_{\text{mamXY}}\text{-egfp}$ fusion, indicating that the 285 bp region is active as a promoter, but relatively weak (Fig. S3). No fluorescence was detectable for the intergenic sequence between *mamY* and *mamX* by microscopy (Fig. S3). Although this

region may contain other regulatory elements, we therefore conclude that P_{mamXY} is the only promoter which drives transcription of the polycistronic *mamXY* operon. Using the more sensitive GusA reporter, we estimated the relative strength of P_{mamXY} as approximately 22.5% of the P_{mamDC} activity (Fig. S3).

Deletion of mamX and mamZ cause similar impairments of magnetosome biomineralization

To analyse their function in magnetosome formation, we constructed non-polar in-frame deletions of *mamX* and *mamZ*. Both mutants exhibited very similar phenotypes: when grown under standard conditions (microoxic, FSM medium), both ΔmamX and ΔmamZ strains showed a slightly reduced magnetic response ($C_{\text{mag}} = 88 \pm 5\%$ and $77 \pm 7\%$ of WT respectively) and still produced chains of electron-dense particles. However, two types of crystals could be clearly distinguished by TEM: in addition to apparently regularly shaped and -sized, WT-like particles (in the following referred to as 'regular'), cells contained variable numbers of small, irregularly shaped particles that appeared to be thin, i.e. flake-like, sometimes needle-shaped (in the following referred to as 'flakes') (Fig. 2A and B). All particles were still aligned in a single chain, in which regular particles were found at the centre and sandwiched by flakes at both ends. Among cells from the same culture, appearance of particles varied from individuals with either almost all-regular or all-flake particles, whereas most cells typically had several regular crystals (Fig. 2A and B). While particles were still clearly aligned in chains even in those cells in which flakes were predominant, in places scattered flakes could also be observed. The distributions of the diameters of ΔmamX (26.1 ± 9.3 nm) and ΔmamZ particles (30.1 ± 15.0 nm) did not differ significantly ($P = 0.0767$ in Mann-Whitney *U*-test), but particles were significantly ($P < 0.0001$) smaller than the magnetosomes of the WT (39.2 ± 9.3 nm) (Fig. 2E).

High-resolution transmission electron microscopy (HRTEM) and electron diffraction revealed that regular particles of both mutants were fully crystalline and consisted of magnetite as in the WT. However, flake-like, irregularly shaped particles were poorly crystalline, and if they displayed any periodic lattice fringes in HRTEM micrographs, the spacings of those fringes (as measured from the Fourier transforms of the HRTEM images) were consistent with the d-spacings in the structure of haematite ($\alpha\text{-Fe}_2\text{O}_3$) (Fig. 3). Although regular particles superficially resembled magnetosome crystals of the WT, TEM of isolated ΔmamZ crystals at higher magnification revealed a higher proportion of the crystals (42%, $n = 233$) to be twinned than in the WT, and an additional 12% of polycrystalline particles (WT: 22% twinned, 1% polycrystalline, $n = 218$) (Fig. 2D). This observation suggests that

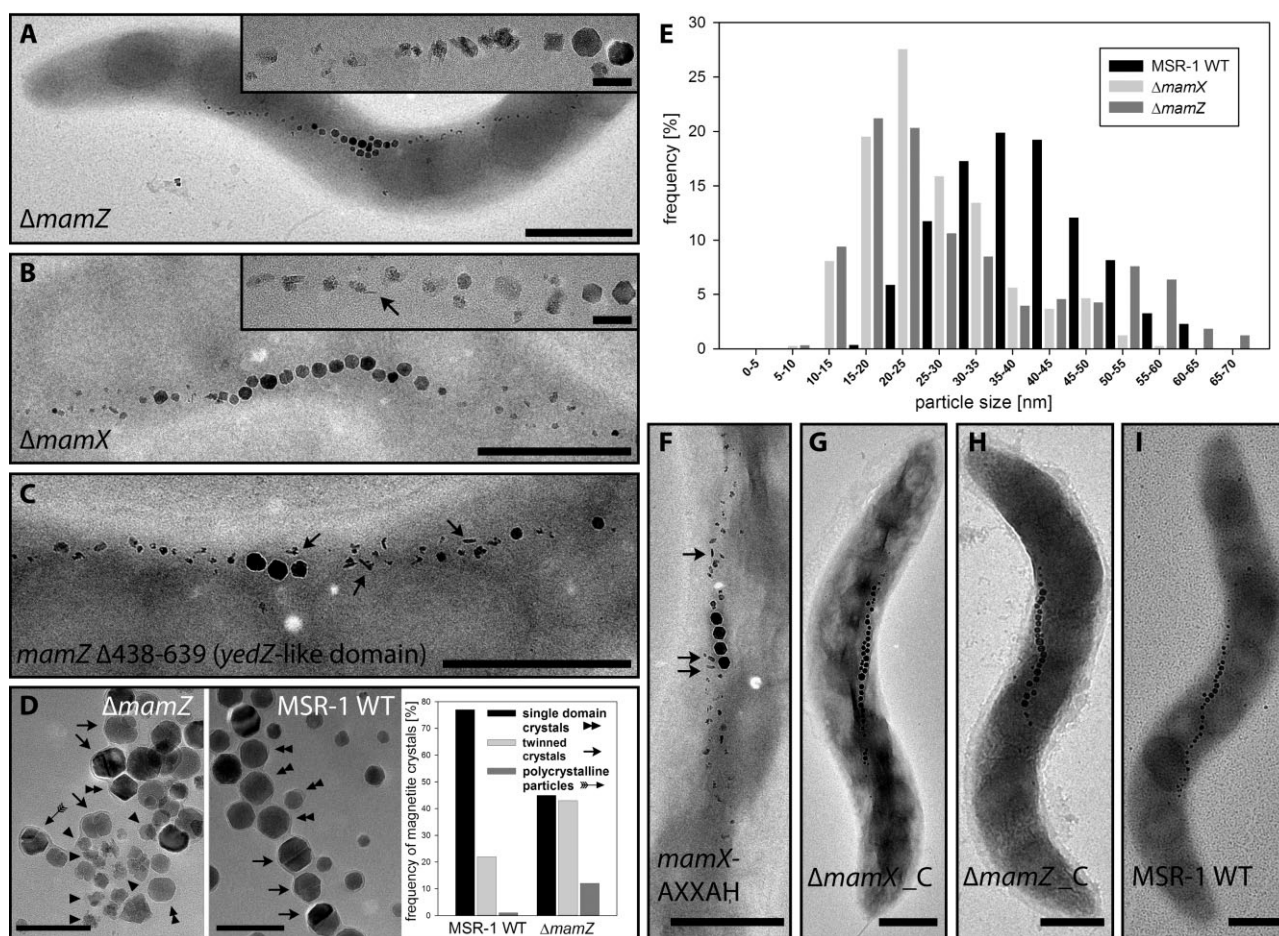


Fig. 2. Effects of *mamZ* and *mamX* deletion and domain substitutions on magnetite biomineralization. TEM micrographs and statistical analysis of magnetosome size and shape from different MSR mutant strains.

A and B. Representative $\Delta mamZ$ cell (A) and $\Delta mamX$ cell (B). Subsets represent a high-magnification detail of the end of the magnetosome chain. Arrow indicates needle-like crystal.

C. Deletion of *yedZ*-like (ferric reductase) domain of *mamZ*. Arrows indicate needle-like crystals.

D. TEM micrographs of isolated magnetosome particles from $\Delta mamZ$ and MSR-1 WT. Arrowhead: poorly crystalline flake-like particle, double arrowhead: regular crystals, black arrows: twinned crystals, feathered arrow: polycrystalline particle. Graph: Proportions of regular, twinned and polycrystalline particles in WT ($n = 218$) and $\Delta mamZ$ ($n = 233$) cells.

E. Crystal size distribution of WT ($n = 307$), $\Delta mamX$ ($n = 410$) and $\Delta mamZ$ ($n = 330$).

F. Micrograph of MSR-1 *mamX* magnetochrome ($2 \times CXXCH \rightarrow AXXAH$) substitution mutant. Arrows indicate needle-like crystals.

G. Representative $\Delta mamX$ cell trans-complemented with pOR098.

H. Representative $\Delta mamZ$ cell trans-complemented with pOR031.

I. Representative MSR-1 WT cell.

Scale bars: 500 nm (whole cells) and 100 nm [subsets and (D)].

the nucleation of even regular crystals is disturbed at an early stage in the mutants.

Cryo-electron tomography (CET) of both mutants showed that the shape and size of empty and partially filled magnetosome membrane vesicles were unaffected. As in the WT, vesicles were found in close proximity to the inner cell membrane (Fig. 4Aii, Biii, Cii, Ciii) and associated closely with the cytoskeletal magnetosome filament (Fig. 4Bi). Both regular particles and flakes were surrounded by WT-like vesicles (Fig. 4A–C). However, multiple nucleation sites were sometimes observed in the flake-containing vesicles (Fig. 4Biii).

EGFP fused to the C-terminus of the magnetosome marker protein MamC (Lang and Schüler, 2008) localized as a filamentous structure at midcell in the WT as well in $\Delta mamX$ and $\Delta mamZ$. The extension of the fluorescent signal correlated with the length of the particle chains (regular crystals + flakes) (Fig. 4D and E) typically observed by TEM. This again indicates that the MM-specific localization of magnetosome-associated proteins is not affected for both regular and flake-like particles in $\Delta mamX$ and $\Delta mamZ$.

Synthesis of WT-like magnetosome crystals and chains could be restored by expressing WT *mamX* and *mamZ*

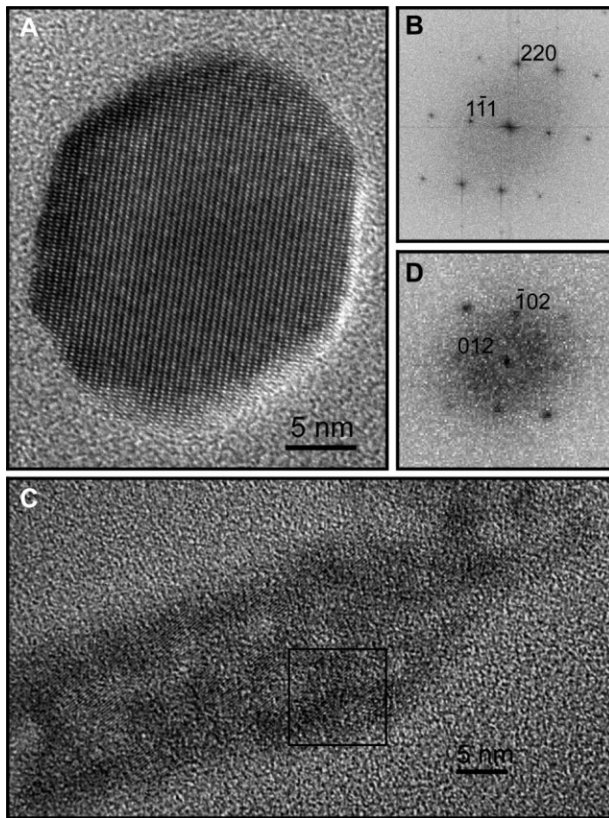


Fig. 3. HRTEM images of regular and flake-like particles from $\Delta mamX$ and $\Delta mamZ$. A. HRTEM image of a regular magnetite particle from $\Delta mamX$. B. Fourier transform (FT) of the image in (A), indexed according to the magnetite structure, and indicating that the crystal is viewed along the [112] crystallographic direction. C. HRTEM image of a needle-shaped, flake-like particle from the $\Delta mamZ$ mutant. D. FT of the boxed area in (C), indicating that the enclosed region is haematite, viewed along the [2–21] crystallographic zone axis.

alleles in their respective deletion backgrounds from plasmids (pOR98 and 031) under control of the native P_{mamXY} (Fig. 2G and H), demonstrating that the observed similar phenotypes were due to the absence of the targeted genes rather than polar effects of the deletions. Notably, even slight modifications of the C-terminus of MamX, such as the fusion of peptides or proteins (mCherry, a 6 \times -His tag or even two additional amino acids) abolished the ability to complement the $\Delta mamX$ mutant (data not shown), indicating a stringent requirement for domain conservation.

Dynamics of biomineralization in $\Delta mamX$ and $\Delta mamZ$ mutants

As mutant cells cultivated under standard conditions always exhibited two clearly distinct types of particles, we determined whether the haematite containing flakes

are intermediates that can be eventually converted into regular magnetite crystals, or if the fate of individual particles is predetermined at an early stage of biomineralization. To investigate the time-course of flake formation in the mutants, we performed iron induction experiments. Strains were passaged in low-iron medium until they were non-magnetic ($C_{mag} = 0$). Magnetite formation was then induced by transferring cells back to iron-sufficient

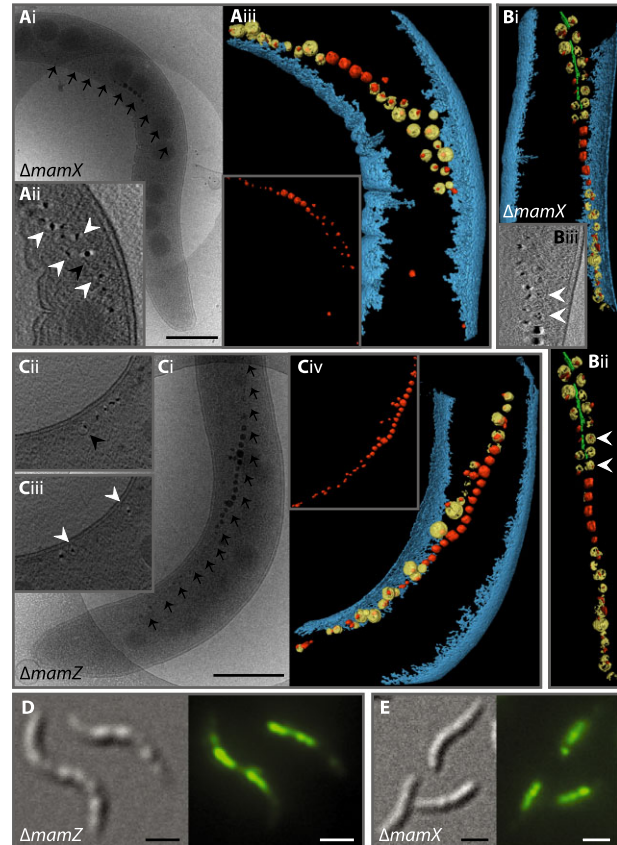


Fig. 4. CET and fluorescence microscopy (MamC-EGFP) of MSR $\Delta mamX$ and $\Delta mamZ$

A. $\Delta mamX$ cryo-TEM micrograph, the magnetosome chain is indicated by arrows. (Aii) Section of tomogram shows that flakes (white arrowheads) and small regular magnetosomes (black arrowhead) are both surrounded by a magnetosome membrane. (Aiii) Segmented tomogram, the subset shows magnetosome particles only. B. Segmented tomograms of a $\Delta mamX$ cell and (Bii) its magnetosome chain. (Biii) Section of tomogram, white arrowheads indicate vesicles with more than one nucleating particle. C. $\Delta mamZ$ cryo-TEM micrograph, the magnetosome chain is indicated by arrows. (Cii) and (Ciii) Sections of tomogram show detached (black arrowhead) and CM-attached magnetosome vesicles (white arrowheads). (Civ) Segmented tomogram, the subset shows magnetosome particles only. Outer and inner cell membranes are segmented blue, vesicles yellow, magnetite crystals red and the magnetosome filament green. Scale bars: 500 nm (TEM). D and E. DIC and fluorescence images of $\Delta mamZ$ (D) and $\Delta mamX$ (E) expressing MamC-GFP. Scale bars: 1 μ m (fluorescence microscopy).

medium (50 μ M ferric citrate) as previously described (Faivre *et al.*, 2008; Scheffel *et al.*, 2008). The WT started to form magnetite crystals (as indicated by an increase in C_{mag} after 2 h) and after 4 h had almost completely restored its C_{mag} to normal levels, whereas both mutants showed a substantial delay in regaining magnetic properties, as indicated by a slower recovery of the C_{mag} (Fig. 5). As seen in the WT, magnetosome particles were emerging from different positions along the entire length of the ΔmamZ mutant cells without any consistent pattern. Although flakes were dominating at the beginning of the experiments, at later stages more and larger regular crystals were appearing and, similar to the WT, chains were formed with regular crystals at mid-chain, flanked by flake-like particles, thereby restoring the regular phenotype of the mutants as observed under continuous standard growth conditions (Fig. 5). TEM revealed that the ΔmamZ cells contained already many flakes and a few small, but regularly shaped particles 4 h after iron induction. However, the C_{mag} of the mutant was only marginally increased, indicating that flakes and small crystals did not contribute much to the cellular magnetic response (Fig. 5). At later stages, the ratio of mature crystals to flakes increased steadily in the ΔmamZ mutant, reflected also by an increasing C_{mag} (Fig. 5). However, even after 7 h, the C_{mag} was still lower than usually observed for ΔmamZ cultures continually grown under iron-replete conditions.

After iron induction, the ΔmamX mutant showed a very similar pattern with respect to the different stages of biomineralization. However, magnetic response and particle formation re-evolved faster, although still slower than in the WT (Fig. 5). During the entire experiment, we never observed gradual intermediates between flake-like particles and regular magnetosomes, but particles always had distinct appearances that could be assigned to either the 'flake' or 'regular' type with respect to shape, size and crystallinity (Fig. 5).

We also studied magnetosome formation in division-inhibited cells treated with cephalixin. By inhibiting the cell division protein FtsI, cephalixin blocks final septation and separation of the daughter cells while the cells still constrict at stalled division sites, leading to highly elongated filaments that are equivalent to several consecutive generations (Katzmann *et al.*, 2011). Similar to the WT, 12–16 h after cephalixin treatment both ΔmamX (Fig. S4) and ΔmamZ (not shown) mutants displayed separate multiple magnetosome chains at distinct stalled division sites. As in untreated cells, the central parts of chains consisted of regular crystals flanked by flakes at their ends. Between these chains, scattered and apparently immature particles were frequently found, which could be identified either as irregularly shaped flakes or as small but regularly shaped crystals (Fig. S4). Larger regular crystals

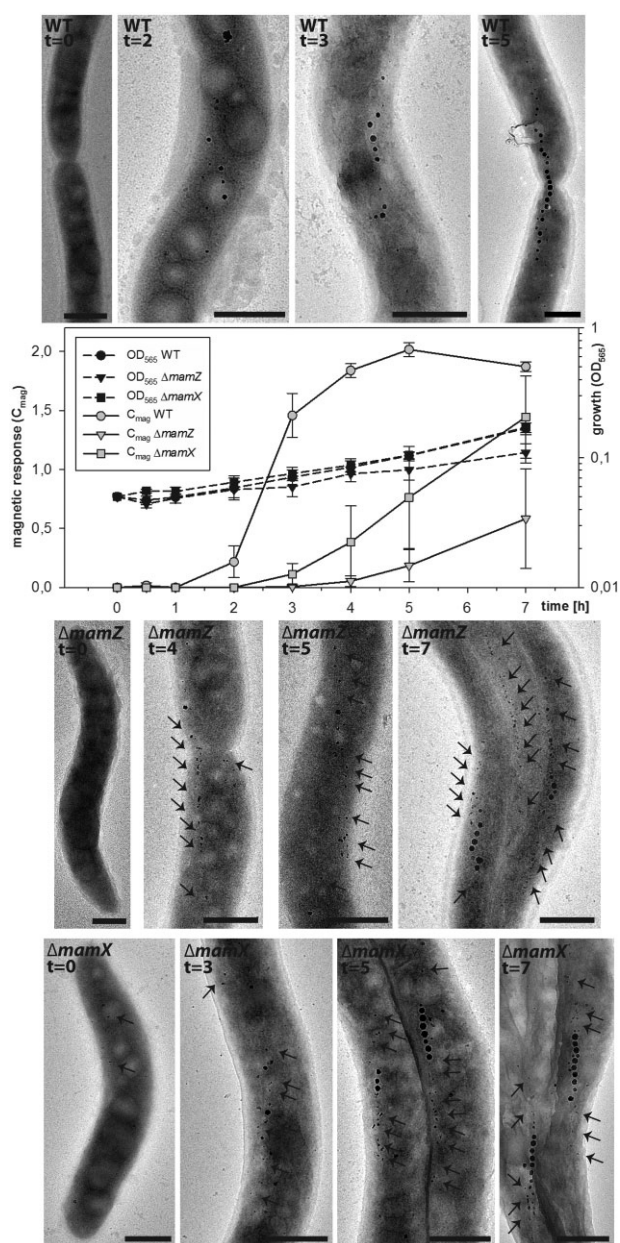


Fig. 5. Development of magnetosome particles after iron-induction shows delay of biomineralization in ΔmamX and ΔmamZ . Growth and C_{mag} of WT, ΔmamX and ΔmamZ after transfer of iron-starved, non-magnetic cultures into iron-repleted FSM medium. TEM micrographs represent different stages of magnetosome formation in all strains followed over the time of the experiment. Arrows indicate the position of single or concatenated flakes. Scale bars: 500 nm.

were usually found in the magnetosome chains but also scattered within the cells (Fig. S4). Small regular crystals and flakes thus coexisted throughout all stages of magnetosome development. Combined with the absence of transient crystallization phases this observation therefore indicates that crystal fate is already determined at an early

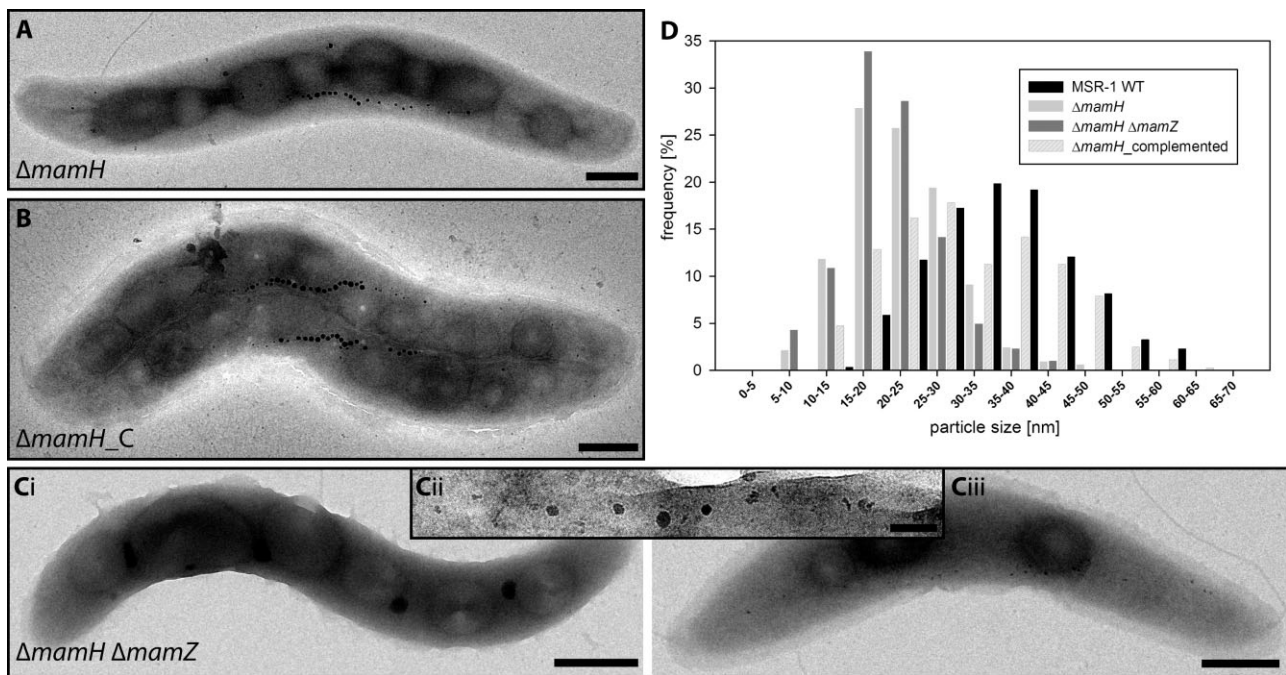


Fig. 6. Effects of *mamH* deletion and *mamH mamZ* co-deletion for magnetite biomineralization. TEM micrographs and statistical analysis of magnetosome sizes from different MSR mutant strains. A. Representative $\Delta mamH$ cell. B. Representative $\Delta mamH$ cell trans-complemented with pOR101. C. Magnetosome particles of various cells of $\Delta mamHZ$. While some cells (Ci) contained no particles, most other cells contained both very small regular crystals and flake-like particles. Scale bars: 500 nm (whole cells) and 100 nm (detail). D. Magnetosome size distribution of MSR-1 ($n = 307$), $\Delta mamH$ mutant ($n = 330$), $\Delta mamHZ$ mutant ($n = 304$) and trans-complemented $\Delta mamH$ mutant (+ pOR101) ($n = 444$).

stage of nucleation, before particles mature and develop to their full size.

Double deletions of mamH and mamZ have an additive effect on biomineralization, whereas single mamH deletion only affects magnetosome number and size

MamZ is predicted to have 18 transmembrane domains (TMD) and a unique domain architecture with a MFS transporter domain fused to a putative ferric reductase-like transmembrane component (PFAM: ferric_reduct, in the following referred to as ferric reductase domain) (Fig. 1C) (Richter *et al.*, 2007). The N-terminal MFS transporter domain of MamZ shows 64% similarity to MamH, another magnetosome protein of MSR-1. MamH is encoded by the first gene of the *mamAB* operon and was also predicted to be an MFS transporter (Schübbe *et al.*, 2003; Richter *et al.*, 2007), suggesting a related function in biomineralization. MFS family members typically are characterized by a 12-fold TMD topology (Reddy *et al.*, 2012) with a long cytoplasmic loop between TMD 6 and 7, features also shared by MamZ and MamH (Fig. 1C and D). To investigate a potential functional rela-

tionship of MamZ and MamH, we constructed markerless in-frame deletions, in which *mamH* was excised alone or in combination with *mamZ*. Deletion of *mamH* alone resulted in a decrease of magnetosome number and size. Whereas the WT had 31.4 ± 5.7 magnetosomes per cell with a mean size of 39.2 ± 9.3 nm under standard conditions, $\Delta mamH$ only exhibited 21.3 ± 7.8 magnetosomes per cell with a size of 22.2 ± 7.0 nm (Fig. 6D). The C_{mag} of $\Delta mamH$ was only slightly decreased (83% of WT). All magnetosomes of $\Delta mamH$ had a cubo-octahedral shape and despite their smaller size appeared WT-like (Fig. 6A). Deletion of *mamH* in the $\Delta mamZ$ background had considerably stronger effects: the C_{mag} of this mutant was significantly decreased ($21 \pm 7\%$ of WT) and only very few or no regular crystals were detectable in the cells (Fig. 6C). Most of the observed particles resembled the poorly crystalline flakes of $\Delta mamX$ or $\Delta mamZ$ cells. Transcomplementation of $\Delta mamH$ by expressing the WT gene under control of the P_{mamDC} promoter (pOR101) partially restored the synthesis of larger crystals (31.0 ± 10.7 nm), although not fully back to WT level, as frequently observed in MSR-1 for genes expressed from medium-copy plasmids (Uebe *et al.*, 2011) (Fig. 6B and D).

The YedZ-like domain of MamZ is essential for protein function

MamZ is one of the very few MFS members with fusions to other functional domains (Reddy *et al.*, 2012). The predicted ferric reductase domain of MamZ shows highest similarity to the haem B binding membrane protein YedZ, which is found in various bacteria (Brokx *et al.*, 2005; von Rozycki *et al.*, 2005). From 2700 predicted hybrid proteins with conserved ferric reductase domains deposited in the PFAM database, 57% are fused to a FAD-binding domain and/or a NAD-binding domain, 37% have YedZ-like architecture, whereas no other protein besides MamZ shows fusion to a MFS domain (Von Rozycki *et al.*, 2005). As the YedZ-like domain in MamZ, YedZ from *Escherichia coli* has six TMD and resides in the cytoplasmic membrane. In a complex with the periplasmic molybdopterin binding subunit YedY, YedZ forms an oxidoreductase for diverse sulphoxide compounds (Loschi *et al.*, 2004). YedZ orthologues from bacteria contain the conserved putative haem B-coordinating residues His-91, His-151 and His-164 (Brokx *et al.*, 2005), a feature also shared by the YedZ-like domain of MamZ. To study the role of the C-terminal YedZ-like ferric reductase domain in MamZ function, we deleted this domain by removing a large internal region in MamZ, starting 39 bp downstream of the last codon of the putative 12th trans membrane domain and upstream of the last 12 bp (genotype: *mamZ* Δ 438–639). Expression of the truncated MamZ protein on isolated magnetosomes was confirmed by mass spectrometry. Deletion of the YedZ-like domain alone phenocopied the deletion of the entire *mamZ* gene, i.e. both mutants produced regular magnetosome crystals flanked by the same flake-like particles (Fig. 2C). This demonstrates that the YedZ-like domain has a crucial role for the function of the entire protein in magnetosome biomineralization. In the magnetospirilla AMB-1 and MSR-1 a genuine *yedZ* gene is located elsewhere in the genome in addition to *mamZ*, forming an operon together with *yedY*. To analyse if the YedZ-like domain of MamZ functionally interacts with the genuine YedY protein in magnetosome formation, we constructed a YedY deletion mutant in MSR-1, which however, showed WT-like magnetosomes and magnetosome organization but no biomineralization defect (Fig. S5). We therefore exclude a functional connection of MamZ and YedY in magnetosome formation of MSR-1.

Absence of nitrate further impairs biomineralization in Δ *mamX* and Δ *mamZ*

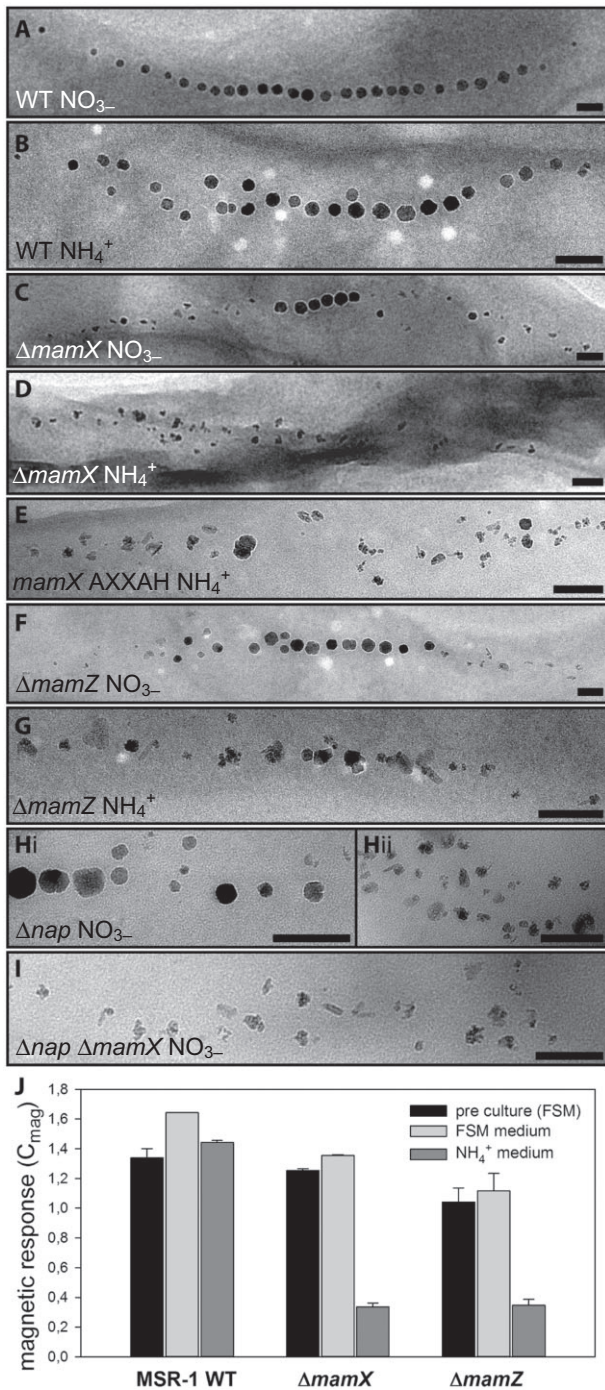
Previous work suggested a role of nitrate reduction in redox control for magnetite biomineralization. Poorly crystalline magnetosome particles somewhat resembling those of Δ *mamX* and Δ *mamZ* were biomineralized in MSR-1 cells deficient in nitrate reductase (Δ *nap*) (Li *et al.*,

2012). This observation prompted us to investigate a potential link between MamX and MamZ functions, redox control and nitrate reduction. Neither increased concentrations (up to 500 μ M), nor the redox state of iron supplied in the medium (either all-ferrous or all-ferric), or growing the cells in the entire absence of oxygen had a pronounced effect on biomineralization in the mutants. Cultivation of Δ *mamX* and Δ *mamZ* in ammonium medium, where NO_3^- (4 mM) was substituted by equimolar amounts of NH_4^+ , however, resulted in a strong exacerbation of the phenotype: both Δ *mamX* and Δ *mamZ* showed an even stronger C_{mag} reduction when grown under micro-oxic conditions and in the absence of nitrate (Fig. 7J), whereas WT cells were unaffected under these conditions (Li *et al.*, 2012; Fig. 7A and B). Likewise, the number of regular crystals decreased and flakes prevailed. Only 27% of Δ *mamX* cells and 34% of Δ *mamZ* cells ($n = 100$) had one to three apparently regular crystals, whereas all other particles were flakes (Fig. 7C–D and F–G). Increasing nitrate concentrations (0–4 mM) gradually restored C_{mag} and increased the number of regular crystals in Δ *mamX* cultures (Fig. S6). Addition of 1 mM nitrite to ammonium medium did not restore the ability to form abundant regular magnetite crystals, although all nitrite became consumed by the culture (Fig. S6).

To further analyse a possible relation of biomineralization defects to denitrification we deleted *mamX* in a genetic background in which the entire operon (*nap*) encoding the periplasmic nitrate reductase was deleted. Δ *nap* predominantly produces irregularly shaped particles, although some cells also form regular magnetite crystals (Li *et al.*, 2012; Fig. 7H). The Δ *nap* Δ *mamX* double mutant grown in FSM medium, however, was even more severely impaired in biomineralization and resembled Δ *mamX* grown in the absence of nitrate with almost only flake-like particles and a C_{mag} of only 0.11 (Δ *mamX*: 1.17; Δ *nap*: 0.42). This demonstrates that deletion of *mamX* in the Δ *nap* background further reduces the magnetite formation ability and indicates an independence of both functions.

Substitution of a putative paired CXXCH ('magnetochrome') motif in MamX abolishes its function

In search for possible redox-active domains, we identified a characteristic paired CXXCH motif in MamX (aa 65–69 and 104–108) (Fig. 1B), which is known to mediate covalent haem binding in c-type cytochromes (Bowman and Bren, 2008) and was recently described as a haem c bound 'magnetochrome domain' in MamE of AMB-1 and MamP of the magnetotactic spirillum QH-2 (Siponen *et al.*, 2012). In order to elucidate the relevance of the putative magnetochrome domain for MamX function, we exchanged both CXXCH sites to AXXAH by introducing



four single aa substitutions into the chromosomal *mamX* gene. Although we failed to directly detect the mutated protein in isolated magnetosome samples by mass spectrometry, evidence from other studies suggest that this specific aa substitution does generally not affect protein stability (Tomlinson and Ferguson, 2000; Quinlan *et al.*, 2011). The resulting *mamX* AXXAH double exchange mutant exhibited the same phenotype as $\Delta mamX$

Fig. 7. Effect of media composition on magnetosome particle morphology in MSR-1 WT, $\Delta mamX$, $\Delta mamZ$ and $\Delta mamX$ AXXAH. Magnetosome phenotype of Δnap and $\Delta nap \Delta mamX$. TEM micrographs of MSR strains cultivated in FSM (NO₃⁻) and ammonium medium (NH₄⁺).

A and B. Magnetosome particles of WT cultivated in (A) FSM or (B) NH₄⁺ medium.

C–E. Magnetosome particles of $\Delta mamX$ cultivated in (C) FSM or (D) NH₄⁺ medium and (E) *mamX* AXXAH cultivated in NH₄⁺ medium.

F and G. Magnetosome particles of $\Delta mamZ$ cultivated in (F) FSM or (G) NH₄⁺ medium.

H. Phenotypic variations of magnetosome particles from different cells of Δnap cultivated in FSM medium.

I. Magnetosome particles of $\Delta nap \Delta mamX$ cultivated in FSM medium.

Scale bars: 100 nm.

J. C_{mag} values of WT, $\Delta mamX$ and $\Delta mamZ$ cultivated in FSM or NH₄⁺ medium.

(Fig. 2F): as in $\Delta mamX$, under microoxic conditions and in the presence of nitrate, the C_{mag} (1.24 ± 0.03) of the *mamX* AXXAH mutant was approximately 15% lower than WT C_{mag} (1.46 ± 0.03) and further decreased to 0.29 ± 0.03 when the cells were grown in ammonium medium. These results were further confirmed by TEM, which revealed an identical phenotype as in $\Delta mamX$, i.e. the production of regular crystals and flakes in FSM medium and prevalence of flakes in the absence of nitrate (Fig. 7E). Although we cannot entirely preclude effects of altered expression levels, this indicates that inactivation of the putative haem *c* binding sites is already sufficient to completely abolish MamX function and phenocopies loss of the entire protein.

Discussion

In this study we showed that the *mamX*, *mamZ* and *mamH* genes play a key role in magnetite biomineralization in MSR-1. In $\Delta mamX$ and $\Delta mamZ$, two distinct types of particles were found to coexist within the same cells: besides regularly sized and shaped, but predominantly twinned magnetite crystals, small and amorphous or poorly crystalline, flake-like particles were present. We never observed intermediate sizes and shapes that would possibly represent gradual transitions between regular and flake-like particles. In division-inhibited and iron-induced $\Delta mamX$ and $\Delta mamZ$ cells both regular crystals and flakes were developing simultaneously at different locations, but became recruited into magnetosome chains, indicating that a transformation of flakes into regular crystals at a later stage is rather unlikely. Although the flake-like particles appeared to be poorly crystalline and to consist of several grains, crystalline islands were present in many of them. Several of the crystalline parts in flake-like particles could be imaged in near crystallographic zone-axis orientations, i.e. Fourier transforms of their HRTEM images contained a

two-dimensional periodic pattern of intensity maxima. In all cases the d-spacings derived from these maxima and the angles between reciprocal lattice rows were consistent with the structure of the non-magnetic iron oxide haematite (α -Fe₂O₃). The presence of haematite in the flake-like particles was also confirmed by several HRTEM images. Haematite particles were previously observed in cells of MSR-1 as the result of a single amino acid substitution in the putative magnetosomal iron transporter MamM (Uebe *et al.*, 2011), and it was speculated that the formation of haematite was favoured over magnetite by disturbance of magnetosomal pH, or ferric to ferrous iron ratios and concentrations (Jolivet *et al.*, 1992; Faivre *et al.*, 2004). Alternatively, haematite might result from chemical transformation of amorphous ferric hydroxide initially present in flakes, either within living cells or during the subsequent specimen preparation and storage. Despite previous speculation that magnetosomal magnetite may directly evolve from haematite precursors (Staniland *et al.*, 2007), this would require the dissolution of haematite and subsequent recrystallization as magnetite (Behrends and Van Cappellen, 2007), which is unlikely to occur in the magnetosome vesicles. We therefore conclude that the fate of developing crystals must already be predetermined at a very early stage of mineralization, consistent with the existence of an 'activation' mechanism or 'checkpoint' for magnetite synthesis as suggested previously (Komeili *et al.*, 2004; Komeili, 2011; Quinlan *et al.*, 2011), which commits nascent crystals to develop into either one or the other mineral.

Although both types of particles aligned in a linear fashion, larger regular and ferrimagnetic magnetite crystals were found tightly spaced at mid-chain, while presumably non-magnetic flakes were located at the ends. This observation provides further indications that magnetic interaction of magnetosomes is necessary for their concatenation and positioning within chains, but not for linear organization *per se* which relies on the action of biological structures (Katzmann *et al.*, 2011; Klumpp and Faivre, 2012).

MamZ and MamH are putative iron transporters and MamZ is involved in redox control for magnetosome formation

MamZ contains a conserved ferric reductase transmembrane component of the YedZ-type, which is assumed to bind haem B and therefore might be involved in electron shuttling and redox reactions (Brokx *et al.*, 2005). In *E. coli* YedZ interacts with the molybdopterin-binding subunit YedY to form a putative oxidoreductase complex (Loschi *et al.*, 2004; Brokx *et al.*, 2005; Kappler, 2011). However, MamZ function in MSR-1 does not require interaction with the genuine YedY, since our deletion of YedY

had no effect on magnetite biomineralization. In addition, MamZ contains a MFS transporter domain and represents the only known example in which this domain is fused to a ferric reductase domain (von Rozycki *et al.*, 2005; Reddy *et al.*, 2012). The MFS domain of MamZ also shares high identity with MamH, which indicated a functional relationship of both proteins. Despite the similarities between MamZ and MamH, we failed to swap the YedZ-like domain of MamZ to full-length MamH, as the resulting chimeric protein was non-functional and unable to complement either Δ *mamH* or Δ *mamZ* (data not shown). We demonstrated, however, that deletion of *mamH* resulted in a slightly reduced C_{mag} in MSR-1 caused by a somewhat reduced size and number of magnetosomes, as it was also already described for the same mutant in the related strain AMB-1 (Murat *et al.*, 2010). However, whereas single deletions of either *mamZ* or *mamH* were still able to synthesize larger and regular magnetite crystals, double deletion of *mamZ* and *mamH* had a more severe effect, as magnetite biomineralization was substantially reduced in Δ *mamHZ*, and only few cells produced regular crystals at all. We therefore conclude that both proteins have partially redundant functions, whereas the presence of at least one of those MFS homologues is necessary for the synthesis of regular magnetite crystals.

For many MFS members the substrate which they transport is still unknown (Saier *et al.*, 1999; Reddy *et al.*, 2012), and the distinct branching of MamH and MamZ within the family tree (von Rozycki *et al.*, 2005; Richter *et al.*, 2007) prohibits reliable similarity-based predictions. It nevertheless was shown that distant MFS members from fungi and pathogenic bacteria indeed transport iron chelates (Lesuisse *et al.*, 1998; Chatfield *et al.*, 2012), and based on its unique combination of a putative ferric reductase with a MFS transporter domain, MamZ was hypothesized to be an iron transporter (Von Rozycki *et al.*, 2005; Reddy *et al.*, 2012). It is therefore tempting to speculate that the magnetosome-associated MamH and MamZ are as well involved in magnetosomal iron transport, but might have functions slightly distinct from the CDF proteins MamM and MamB, which were already implicated in magnetosomal iron accumulation (Uebe *et al.*, 2011). For example, instead of divalent ferrous iron, the common substrate of CDF transporters, MamZ might mediate transport of ferric iron, as suggested by the presence of a putative iron reductase component and transporter domain combined in a single protein. Our observation that deletions of the ferric reductase domain alone already abolished protein function would be consistent with this assumption. Despite repeated attempts we failed to detect any iron transport or iron reductase activity upon MamZ expression in *E. coli in vitro* or *in vivo* (data not shown). Therefore, future work has to directly prove the predicted functions of MamZ and MamH in reduction and transport of iron.

MamX is a putative magnetochrome protein involved in redox control of magnetite biomineralization

We identified a putative haem *c* binding (paired CXXCH) motif in MamX, which shares the characteristics of similar domains recently identified in other magnetosome proteins (MamPTE) which because of their exclusive occurrence in MTB and their ability to bind haem *c* were designated 'magnetochromes' (Siponen *et al.*, 2012). Magnetochromes are cytochrome *c*-like proteins and are assumed to regulate redox conditions for magnetosome formation (Siponen *et al.*, 2012). MamX_{MSR-1} and its homologues from AMB-1 and *Magnetospirillum magnetotacticum* (MS-1) are highly conserved, whereas MamX_{MC-1} contains an additional putative paired CXXCH haem-binding motif and has a larger size (345 aa, 55% similarity to MamX_{MSR-1}). MamX_{MV-1} is shorter (110 aa, 61% similarity to MamX_{MSR-1}), but also contains the characteristic paired CXXCH motif. Our deletion of either full-length *mamX* or the substitution of its paired CXXCH motif impaired magnetite biomineralization in MSR-1. This suggests that MamX is a redox-active protein, and its putative magnetochrome domains are essential for its function. In a previous study the magnetosome protein MamE of AMB-1 was also implicated in magnetite crystal maturation, a function which was associated with its magnetochrome domains (Quinlan *et al.*, 2011), and deletion of *mamP* and *mamT* led to the formation of irregular particles in the same organism (Murat *et al.*, 2010).

MamX thus is likely involved in redox control for the synthesis of the mixed-valence iron oxide Fe₃O₄ under oxidant-limiting conditions, i.e. at low oxygen and nitrate concentrations. Likewise, a role in iron reduction was already demonstrated for several *c*-type cytochromes from dissimilatory ferric iron reducers (Shi *et al.*, 2012). Intriguingly, effects of deletions of *mamZ* and *mamX* could be partially rescued by nitrate, whereas only relatively minor effects of nitrate were detected for the WT. Nitrate reductase activity was recently implicated in poisoning redox conditions for magnetosome formation. Deletion of the *nap* operon encoding a periplasmic nitrate reductase led to the formation of smaller and irregular magnetosome particles in MSR-1, somewhat reminiscent of the flakes produced in Δ *mamX* and Δ *mamZ*, and it was concluded that, independent of its function as a respiratory nitrate reductase, the protein is involved in magnetosomal redox control (Li *et al.*, 2012). The strong impairment of biomineralization in Δ *mamX* and Δ *mamZ* in the absence of nitrate might therefore hint towards a direct functional connection with nitrate reductase activity, and it was hypothesized by Siponen *et al.* that NapC, a CymA-like multihaem cytochrome encoded by the *nap* operon may transfer electrons from the quinone pool to magnetochrome-containing proteins (Siponen *et al.*, 2012). However, the additive effect on

magnetite synthesis upon our co-deletion of *mamX* and *nap* seems to argue for functional independence and redundancy of MamX and Nap in redox control, rather than a direct link of both pathways.

MamXZH may form an iron oxidoreductase and transport complex

Deletion mutants of the syntenic and overlapping *mamX* and *mamZ* genes resulted in nearly identical phenotypes under all tested conditions, which were strongly reminiscent of the deletion of the entire *mamXY* operon (Lohße *et al.*, 2011). Furthermore, co-deletion of *mamZ* and *mamH* led to severe impairments in magnetosome formation and indicated a partly redundant function of both MFS transporters. While *mamY*, the first gene of the *mamXY* operon, is not likely involved in biomineralization (Tanaka *et al.*, 2010), deletion of *ftsZm*, the last operonal gene encoding a truncated FtsZ protein was previously found to have a similar effect on magnetite synthesis (Ding *et al.*, 2010). We therefore conclude that MamX, MamZ together with MamH act on the same stage of magnetite biomineralization and postulate a hypothetical model of interaction. Based on experimental findings (Grünberg *et al.*, 2004; Tanaka *et al.*, 2006; Lohße *et al.*, 2011) and predictions, MamX, MamZ and MamH are associated with the magnetosome membrane, where they are likely to interact directly or indirectly. MamX and MamZ may then form a complex for the reduction of ferric iron and its concomitant transport by MamZ and MamH. The close interaction of MamXZH might be facilitated by further scaffolding factors, such as for instance FtsZm, which is encoded within the same operon as MamX and MamZ and a member of the tubulin-like FtsZ family known to serve as an interaction hub for multi-protein assembly forming the divisome complex (Goley *et al.*, 2011). This model provides several predictions which can be experimentally tested in future work, such as the haem association of MamX and MamZ, direct interaction of MamXZH and FtsZm to form a common complex and iron transport as well as oxidoreductase activity of MamXZ. In conclusion, our study has uncovered key functions of three major magnetosome proteins in magnetite synthesis, which requires proper redox control by pathways that are partially redundant, and interlinked with cellular metabolism.

Experimental procedures

Bioinformatics and sequence analysis

Protein sequences, primary structures and predicted localizations were analysed with BLAST (<http://blast.ncbi.nlm.nih.gov/>), SMART (Letunic *et al.*, 2004) and CELLO (Yu *et al.*, 2004) algorithms. For comparative protein sequence analyses, CLUSTALΩ (Sievers *et al.*, 2011) was used. Protein topologies

were modelled with the TMHMM algorithm (Krogh *et al.*, 2001) and visualized with TMRPres2D (<http://bioinformatics.biol.uoa.gr/TMRPres2D/>). The annotation of *mamZ* in MSR-1 was corrected by comparing and analysing the annotation and conserved genomic context in MSR-1, AMB-1 and MS-1 (Fig. S1).

Bacterial strains, plasmids, culture conditions and magnetosome isolation

Bacterial strains and plasmids used in this study are listed in Tables S1 and S2. *E. coli* strains were cultivated in lysogeny broth (LB) medium. When necessary, kanamycin (km) was added to 25 µg ml⁻¹. *E. coli* BW29427 cultures were supported with 1 mM DL-α, ε-diaminopimelic acid (DAP). Media were solidified by addition of 1.5% (w/v) agar. Unless otherwise stated, *M. gryphiswaldense* cultures were grown at 30°C under microoxic conditions (1% O₂) in modified flask standard medium (FSM) (Heyen and Schüler, 2003) or in ammonium medium where 4 mM nitrate is equimolarly substituted by ammonium. When appropriate, km was added to 5 µg ml⁻¹. For cultivation experiments in ammonium medium, cells from FSM pre-cultures were passaged at least three times before samples were taken. Optical density (OD) and magnetic response (C_{mag}) of exponentially growing cultures were measured photometrically at 565 nm as described previously (Schüler *et al.*, 1995).

For iron induction experiments, *M. gryphiswaldense* strains were cultivated in low-iron medium (LIM), supplemented with 10 µM 2,2'-dipyridyl (Faivre *et al.*, 2008; Uebe *et al.*, 2011) under microoxic conditions until no magnetic response was detectable. Cultures were then washed with FSM medium and inoculated into gas-flushed 250 ml bottles with 100 ml FSM medium to an initial OD₅₆₅ of 0.025 and further cultivated under standard conditions. Samples were taken after 0, 0.5, 1, 2, 3, 4, 5 and 7 h for C_{mag} determination and TEM analysis.

For cephalixin inhibition experiments, overnight cultures of *M. gryphiswaldense* strains were 1:10 diluted and further cultivated for 12–16 h under microoxic conditions in the presence of 10 µg ml⁻¹ cephalixin (Katzmann *et al.*, 2011).

Magnetosome isolation was performed using a magnetized separation column and essentially as previously described (Grünberg *et al.*, 2004; Uebe *et al.*, 2011).

Molecular and genetic techniques

Oligonucleotides (Table S3) were purchased from Sigma-Aldrich. Plasmids were constructed by standard recombinant techniques using enzymes from Thermo Scientific and Agilent Technologies. Sequencing was accomplished using BigDye terminator v3.1 chemistry on an ABI 3700 capillary sequencer (Applied Biosystems). Plasmid and Oligonucleotide constructions were performed using Vector NTI (Invitrogen).

Generation of mutant strains

Deletion of *mamX* and *mamZ* was accomplished by a modified cre-lox-based method essentially as described (Ullrich and Schüler, 2010; Lohße *et al.*, 2011). Therefore, flanking sections were amplified using primer pairs oOR006/007

(upstream) and oOR008/009 (downstream) for *mamX* deletion and oOR036/037 (upstream) and oOR038/043 (downstream) for *mamZ* deletion respectively. The flanking sections were cloned into pAL01 and pAL02/2 or the derivative pOR012, resulting in plasmids pOR003/004 for *mamX* and pOR008/013 for *mamZ* deletion. The target genes and the integrated plasmids were excised from the genome by expressing Cre recombinase from pLJY087. Deletion of *mamH*, *yedY* and *mamZ* Δ438–639 as well as site-directed mutagenesis in *mamX* was accomplished by a two step homologous recombination technique essentially as described (Schultheiss *et al.*, 2004; Scheffel *et al.*, 2008). For plasmid constructions, 750 bp–1000 bp regions flanking the target genes were amplified, directly fused in a second PCR and cloned into pOR025. For *mamH* deletion plasmid pOR026 was created by amplifying and cloning the flanking regions using primers oOR045/46/47/48. The constructs for deletion of *mamZ* Δ438–639 and *yedY* were amplified using primers oOR115/116/117/118 and pOR231/232/233/234 respectively and cloned to yield pOR056 and pOR109. For site-directed mutagenesis in *mamX*, the target gene sequence was amplified using primers oOR110/210 and subsequently cloned into pJET 1.2, followed by PCR mediated base pair substitution using primer pairs oOR187/188 and oOR189/190. The resulting sequence was cloned into pOR025 to yield pOR093. All plasmid integrations and specific gene deletions were verified by PCR and by sequencing of the amplification products.

Construction of plasmids for expression and complementation studies

For expression studies, the *mamXY* promoter was amplified and cloned into the medium copy number plasmid pBBR1MCS-2 using primers oOR087 and oOR088, yielding plasmid pOR028. *egfp* was cloned into pOR028 using primers oOR112 and 113, yielding plasmid pOR053. P_{*mamXY*} was exchanged by the intergenic region in between *mamY* and *mamX* (P_{*mamX*}), using primers oOR152/072, yielding plasmid pOR054. To gain the promoter-less control pOR069, we removed P_{*mamXY*} in pOR028 by NdeI/Asel restriction and subsequent religation. For construction of an IPTG inducible plasmid, we amplified *egfp* with primers oOR113/113 and cloned it into the pBBR1MCS-2 derivative pFM210, harbouring a *lac* promoter/operator and the repressor gene *lacI* to yield pOR070. The compatible oligonucleotides oOR106/107, which together form the short *mamDC* promoter with an optimized RBS (C. Lang *et al.*, unpublished), were used to exchange the P_{*mamXY*} promoter in pOR053 to yield pOR071. To replace the reporter EGFP by Gusa, the *gusA* gene was amplified with primers oOR217/218 and cloned into pOR053, pOR070 and pOR071 to yield plasmids pOR102, pOR105 and pOR106.

For complementation studies, *mamY* and *mamX* were cloned into pOR028 using primers oOR089/90 and OR091/194 respectively to gain pOR029 and pOR098. *mamH* was amplified using primers oOR221/223 and cloned into pOR071 to yield pOR101.

Fluorescence microscopy

For fluorescence microscopy, 7 µl samples of *M. gryphiswaldense* overnight cultures containing plasmids pOR053

(P_{mamX} -*egfp*), 54 (P_{mamX} '-*egfp*), 69 (promoter-less *egfp*), 71 (P_{mamDC} -*egfp*) and pCL6 (P_{mamDC} -*mamC*-*egfp*) were immobilized on 1% (w/v) agarose pads. The samples were imaged with an Olympus BX81 microscope equipped with a 100× UPLSAPO100XO objective and an Orca-ER camera (Hamamatsu) and appropriate filter sets. Images were recorded at 500 ms exposure time and eventually processed (brightness and contrast adjustments) using Olympus Xcellence software. For promoter activity assays, pOR071 served as positive and the pOR069 as negative control.

Transmission electron microscopy (TEM) and high-resolution TEM (HRTEM)

For conventional TEM analysis, unstained formaldehyde-fixed cells were absorbed on carbon coated copper grids. Bright-field TEM was performed on a FEI Tecnai F20 or a FEI CM200 transmission electron microscope using an accelerating voltage of 200 kV or 160 kV respectively. Images were captured with an Eagle 4k CCD camera using EMMenu 4.0 (Tietz) and FEI software. For data analysis the software ImageJ was used.

HRTEM was performed using a JEOL 3010 microscope, operated at 297 kV and equipped with a Gatan Imaging Filter (GIF) for the acquisition of electron energy-loss spectra and energy-filtered compositional maps. For TEM data processing and interpretation the DigitalMicrograph and SingleCrystal software were used.

Cryo-electron tomography (CET)

Droplets (5 μ l) of MSR-1 culture and 5 μ l of 10–15 nm colloidal gold clusters were added on glow-discharged Quantifoil holey carbon copper grids, blotted and embedded in vitreous ice by plunge freezing into liquid ethane (< -170°C). For cryo-electron tomography, a FEI Tecnai F30 Polara transmission electron microscope equipped with a 300 kV field emission gun, Gatan GIF 2002 Post-Column Energy Filters and a 2 K Multiscan CCD Camera was used. Data collection was performed at 300 kV, with the energy filter operated in the zero-loss mode (slit width of 20 eV). Tilt series were acquired using Serial EM and FEI software. The specimen was tilted about one axis with 1.5° increments over a typical total angular range of $\pm 65^\circ$. To minimize the electron dose applied to the ice-embedded specimen, data were recorded under low-dose conditions. The total dose accumulated during the tilt series was kept below 150 e \AA^{-2} . To account for the increased specimen thickness at high tilt angles, the exposure time was multiplied by a factor of $1/\cos \alpha$. Images were recorded at nominal -6 μ m or -8 μ m defocus. The object pixel size was 0.805 at 27 500× magnification.

CET data analysis

Three-dimensional reconstructions from tilt series were performed with the weighted back-projection method using the TOM toolbox (Nickell *et al.*, 2005). Visualizations of the tomograms were done with Amira software on two times binned volumes.

Acknowledgements

We thank Günter Pfeifer and Emanuel Katzmann for help with TEM and CET. This project was funded by the Deutsche Forschungsgemeinschaft (Schu 1080/12-1 and 13-1) and the European Union (Bio2Man4MRI).

References

- Behrends, T., and Van Cappellen, P. (2007) Transformation of hematite into magnetite during dissimilatory iron reduction – conditions and mechanisms. *Geomicrobiol J* **24**: 403–416.
- Bowman, S.E.J., and Bren, K.L. (2008) The chemistry and biochemistry of heme c: functional bases for covalent attachment. *Nat Prod Rep* **25**: 1118–1130.
- Brox, S.J., Rothery, R.A., Zhang, G., Ng, D.P., and Weiner, J.H. (2005) Characterization of an *Escherichia coli* sulfite oxidase homologue reveals the role of a conserved active site cysteine in assembly and function. *Biochemistry* **44**: 10339–10348.
- Chatfield, C.H., Mulhern, B.J., Viswanathan, V.K., and Cianciotto, N.P. (2012) The major facilitator superfamily-type protein LbtC promotes the utilization of the legiobactin siderophore by *Legionella pneumophila*. *Microbiology* **158**: 721–735.
- Ding, Y., Li, J., Liu, J., Yang, J., Jiang, W., Tian, J., *et al.* (2010) Deletion of the *ftsZ*-like gene results in the production of superparamagnetic magnetite magnetosomes in *Magnetospirillum gryphiswaldense*. *J Bacteriol* **192**: 1097–1105.
- Draper, O., Byrne, M.E., Li, Z., Keyhani, S., Barrozo, J.C., Jensen, G., *et al.* (2011) MamK, a bacterial actin, forms dynamic filaments *in vivo* that are regulated by the acidic proteins MamJ and LimJ. *Mol Microbiol* **82**: 342–354.
- Faivre, D., and Schüler, D. (2008) Magnetotactic bacteria and magnetosomes. *Chem Rev* **108**: 4875–4898.
- Faivre, D., Agrinier, P., Menguy, N., Zuddas, P., Pachana, K., Gloter, A., *et al.* (2004) Mineralogical and isotopic properties of inorganic nanocrystalline magnetites. *Geochim Cosmochim Acta* **68**: 4395–4403.
- Faivre, D., Böttger, L.H., Matzanke, B.F., and Schüler, D. (2007) Intracellular magnetite biomineralization in bacteria proceeds by a distinct pathway involving membrane-bound ferritin and an iron(II) species. *Angew Chem Int Ed Engl* **46**: 8495–8499.
- Faivre, D., Menguy, N., Pósfai, M., and Schüler, D. (2008) Environmental parameters affect the physical properties of fast-growing magnetosomes. *Am Mineral* **93**: 463–469.
- Fischer, A., Schmitz, M., Aichmayer, B., Fratzl, P., and Faivre, D. (2011) Structural purity of magnetite nanoparticles in magnetotactic bacteria. *J R Soc Interface* **8**: 1011–1018.
- Goley, E.D., Yeh, Y.-C., Hong, S.-H., Fero, M.J., Abeliuk, E., McAdams, H.H., *et al.* (2011) Assembly of the Caulobacter cell division machine. *Mol Microbiol* **80**: 1680–1698.
- Grünberg, K., Müller, E.-C., Otto, A., Reszka, R., Linder, D., Kube, M., *et al.* (2004) Biochemical and proteomic analysis of the magnetosome membrane in *Magnetospirillum gryphiswaldense*. *Appl Environ Microbiol* **70**: 1040–1050.
- Heyen, U., and Schüler, D. (2003) Growth and magnetosome formation by microaerophilic *Magnetospirillum* strains in an oxygen-controlled fermentor. *Appl Microbiol Biotechnol* **61**: 536–544.

- Jogler, C., and Schüler, D. (2007) Genetic analysis of magnetosome biomineralization. In *Magnetoreception and Magnetosomes in Bacteria*. Schüler, D. (ed.). Berlin, Heidelberg: Springer, pp. 133–161.
- Jogler, C., and Schüler, D. (2009) Genomics, genetics, and cell biology of magnetosome formation. *Annu Rev Microbiol* **63**: 501–521.
- Jolivet, J.P., Belleville, P., Tronc, E., and Livage, J. (1992) Influence of Fe(II) on the formation of the spinel iron oxide in alkaline medium. *Clays Clay Miner* **40**: 531–539.
- Kappler, U. (2011) Bacterial sulfite-oxidizing enzymes. *Biochim Biophys Acta* **1807**: 1–10.
- Katzmann, E., Scheffel, A., Gruska, M., Plitzko, J.M., and Schüler, D. (2010) Loss of the actin-like protein MamK has pleiotropic effects on magnetosome formation and chain assembly in *Magnetospirillum gryphiswaldense*. *Mol Microbiol* **77**: 208–224.
- Katzmann, E., Müller, F.D., Lang, C., Messerer, M., Winklhofer, M., Plitzko, J.M., et al. (2011) Magnetosome chains are recruited to cellular division sites and split by asymmetric septation. *Mol Microbiol* **82**: 1316–1329.
- Klumpp, S., and Faivre, D. (2012) Interplay of magnetic interactions and active movements in the formation of magnetosome chains. *PLoS ONE* **7**: e33562.
- Komeili, A. (2011) Molecular mechanisms of compartmentalization and biomineralization in magnetotactic bacteria. *FEMS Microbiol Rev* **36**: 232–255.
- Komeili, A., Vali, H., Beveridge, T.J., and Newman, D.K. (2004) Magnetosome vesicles are present before magnetite formation, and MamA is required for their activation. *Proc Natl Acad Sci USA* **101**: 3839–3844.
- Komeili, A., Li, Z., Newman, D.K., and Jensen, G.J. (2006) Magnetosomes are cell membrane invaginations organized by the actin-like protein MamK. *Science* **311**: 242–245.
- Krogh, A., Larsson, B., Von Heijne, G., and Sonnhammer, E.L. (2001) Predicting transmembrane protein topology with a hidden Markov model: application to complete genomes. *J Mol Biol* **305**: 567–580.
- Lang, C., and Schüler, D. (2008) Expression of green fluorescent protein fused to magnetosome proteins in microaerophilic magnetotactic bacteria. *Appl Environ Microbiol* **74**: 4944–4953.
- Lesuisse, E., Simon-Casteras, M., and Labbe, P. (1998) Siderophore-mediated iron uptake in *Saccharomyces cerevisiae*: the SIT1 gene encodes a ferrioxamine B permease that belongs to the major facilitator superfamily. *Microbiology* **144**: 3455–3462.
- Letunic, I., Copley, R.R., Schmidt, S., Ciccarelli, F.D., Doerks, T., Schultz, J., et al. (2004) SMART 4.0: towards genomic data integration. *Nucleic Acids Res* **32**: D142–D144.
- Li, Y., Katzmann, E., Borg, S., and Schüler, D. (2012) The periplasmic nitrate reductase Nap is required for anaerobic growth and involved in redox control of magnetite biomineralization in *Magnetospirillum gryphiswaldense*. *J Bacteriol* **194**: 4847–4856.
- Lohße, A., Ullrich, S., Katzmann, E., Borg, S., Wanner, G., Richter, M., et al. (2011) Functional analysis of the magnetosome island in *Magnetospirillum gryphiswaldense*: the *mamAB* operon is sufficient for magnetite biomineralization. *PLoS ONE* **6**: e25561.
- Loschi, L., Brox, S.J., Hills, T.L., Zhang, G., Bertero, M.G., Lovering, A.L., et al. (2004) Structural and biochemical identification of a novel bacterial oxidoreductase. *J Biol Chem* **279**: 50391–50400.
- Murat, D., Quinlan, A., Vali, H., and Komeili, A. (2010) Comprehensive genetic dissection of the magnetosome gene island reveals the step-wise assembly of a prokaryotic organelle. *Proc Natl Acad Sci USA* **107**: 5593–5598.
- Murat, D., Falahati, V., Bertinetti, L., Csencsits, R., Körnig, A., Downing, K., et al. (2012) The magnetosome membrane protein, MmsF, is a major regulator of magnetite biomineralization in *Magnetospirillum magneticum* AMB-1. *Mol Microbiol* **85**: 684–699.
- Nickell, S., Förster, F., Linaroudis, A., Net, W.D., Beck, F., Hegerl, R., et al. (2005) TOM software toolbox: acquisition and analysis for electron tomography. *J Struct Biol* **149**: 227–234.
- Quinlan, A., Murat, D., Vali, H., and Komeili, A. (2011) The HtrA/DegP family protease MamE is a bifunctional protein with roles in magnetosome protein localization and magnetite biomineralization. *Mol Microbiol* **80**: 1075–1087.
- Reddy, V.S., Shlykov, M.A., Castillo, R., Sun, E.I., and Saier, M.H. (2012) The Major Facilitator Superfamily (MFS) Revisited. *FEBS J* **279**: 2022–2035.
- Richter, M., Kube, M., Bazylinski, D.A., Lombardot, T., Glöckner, F.O., Reinhardt, R., et al. (2007) Comparative genome analysis of four magnetotactic bacteria reveals a complex set of group-specific genes implicated in magnetosome biomineralization and function. *J Bacteriol* **189**: 4899–4910.
- Rong, C., Zhang, C., Zhang, Y., Qi, L., Yang, J., Guan, G., et al. (2012) FeoB2 functions in magnetosome formation and oxidative stress protection in *Magnetospirillum gryphiswaldense* strain MSR-1. *J Bacteriol* **194**: 3972–3976.
- Saier, M.H., Beatty, J.T., Goffeau, A., Harley, K.T., Heijne, W.H.M., Huang, S., et al. (1999) The major facilitator superfamily. *J Mol Microbiol Biotechnol* **1**: 257–279.
- Scheffel, A., Gruska, M., Faivre, D., Linaroudis, A., Plitzko, J.M., and Schüler, D. (2006) An acidic protein aligns magnetosomes along a filamentous structure in magnetotactic bacteria. *Nature* **440**: 110–114.
- Scheffel, A., Gärdes, A., Grünberg, K., Wanner, G., and Schüler, D. (2008) The major magnetosome proteins MamGFDC are not essential for magnetite biomineralization in *Magnetospirillum gryphiswaldense* but regulate the size of magnetosome crystals. *J Bacteriol* **190**: 377–386.
- Schübbe, S., Kube, M., Scheffel, A., Wawer, C., Heyen, U., Meyerdierks, A., et al. (2003) Characterization of a spontaneous nonmagnetic mutant of *Magnetospirillum gryphiswaldense* reveals a large deletion comprising a putative magnetosome island. *J Bacteriol* **185**: 5779–5790.
- Schüler, D., Uhl, R., and Bäuerlein, E. (1995) A simple light scattering method to assay magnetism in *Magnetospirillum gryphiswaldense*. *FEMS Microbiol Lett* **132**: 139–145.
- Schultheiss, D., Kube, M., and Schüler, D. (2004) Inactivation of the flagellin gene *flaA* in *Magnetospirillum gryphiswaldense* results in nonmagnetotactic mutants lacking flagellar filaments. *Appl Environ Microbiol* **70**: 3624–3631.
- Shi, L., Rosso, K.M., Clarke, T.A., Richardson, D.J., Zachara, J.M., and Fredrickson, J.K. (2012) Molecular underpinnings of Fe(III) oxide reduction by *Shewanella oneidensis* MR-1. *Front Microbiol* **3**: 50.

- Sievers, F., Wilm, A., Dineen, D., Gibson, T.J., Karplus, K., Li, W., *et al.* (2011) Fast, scalable generation of high-quality protein multiple sequence alignments using Clustal Omega. *Mol Syst Biol* **7**: 539.
- Siponen, M.I., Adryanczyk, G., Ginet, N., Arnoux, P., and Pignol, D. (2012) Magnetochrome: a c-type cytochrome domain specific to magnetotactic bacteria. *Biochem Soc Trans* **40**: 1319–1323.
- Staniland, S., Ward, B., Harrison, A., Van der Laan, G., and Telling, N. (2007) Rapid magnetosome formation shown by real-time x-ray magnetic circular dichroism. *Proc Natl Acad Sci USA* **104**: 19524–19528.
- Tanaka, M., Okamura, Y., Arakaki, A., Tanaka, T., Takeyama, H., and Matsunaga, T. (2006) Origin of magnetosome membrane: proteomic analysis of magnetosome membrane and comparison with cytoplasmic membrane. *Proteomics* **6**: 5234–5247.
- Tanaka, M., Arakaki, A., and Matsunaga, T. (2010) Identification and functional characterization of liposome tubulation protein from magnetotactic bacteria. *Mol Microbiol* **76**: 480–488.
- Tanaka, M., Mazuyama, E., Arakaki, A., and Matsunaga, T. (2011) MMS6 protein regulates crystal morphology during nano-sized magnetite biomineralization *in vivo*. *J Biol Chem* **286**: 6386–6392.
- Tomlinson, E.J., and Ferguson, S.J. (2000) Loss of either of the two heme-binding cysteines from a class I c-type cytochrome has a surprisingly small effect on physicochemical properties. *J Biol Chem* **275**: 32530–32534.
- Uebe, R., Voigt, B., Schweder, T., Albrecht, D., Katzmann, E., Lang, C., *et al.* (2010) Deletion of a fur-like gene affects iron homeostasis and magnetosome formation in *Magnetospirillum gryphiswaldense*. *J Bacteriol* **192**: 4192–4204.
- Uebe, R., Junge, K., Henn, V., Poxleitner, G., Katzmann, E., Plitzko, J.M., *et al.* (2011) The cation diffusion facilitator proteins MamB and MamM of *Magnetospirillum gryphiswaldense* have distinct and complex functions, and are involved in magnetite biomineralization and magnetosome membrane assembly. *Mol Microbiol* **84**: 818–835.
- Ullrich, S., and Schüler, D. (2010) Cre-lox-based method for generation of large deletions within the genomic magnetosome island of *Magnetospirillum gryphiswaldense*. *Appl Environ Microbiol* **76**: 2439–2444.
- Ullrich, S., Kube, M., Schübbe, S., Reinhardt, R., and Schüler, D. (2005) A hypervariable 130-kilobase genomic region of *Magnetospirillum gryphiswaldense* comprises a magnetosome island which undergoes frequent rearrangements during stationary growth. *J Bacteriol* **187**: 7176–7184.
- Von Rozycki, T., Yen, M.-R., Lende, E.E., and Saier, M.H. (2005) The YedZ family: possible heme binding proteins that can be fused to transporters and electron carriers. *J Mol Microbiol Biotechnol* **8**: 129–140.
- Yang, W., Li, R., Peng, T., Zhang, Y., Jiang, W., Li, Y., *et al.* (2010) *mamO* and *mamE* genes are essential for magnetosome crystal biomineralization in *Magnetospirillum gryphiswaldense* MSR-1. *Res Microbiol* **161**: 701–705.
- Yu, C.-S., Lin, C.-J., and Hwang, J.-K. (2004) Predicting subcellular localization of proteins for Gram-negative bacteria by support vector machines based on n-peptide compositions. *Protein Sci* **13**: 1402–1406.

Supporting information

Additional supporting information may be found in the online version of this article at the publisher's web-site.

Publication B: Supplementary Information

The magnetosome proteins MamX, MamZ, and MamH are involved in redox control of magnetite biomineralization in *Magnetospirillum gryphiswaldense*

Supplementary experimental procedures

GusA activity assay

Overnight cultures of *M. gryphiswaldense* strains harboring plasmids pOR102 (P_{mamXY} -*gusA*), pOR105 (P_{lac} -*egfp*, no IPTG added – negative control) or pOR106 (P_{mamDC} -*egfp*, positive control) were harvested, resuspended in 2-3 mL phosphate-buffered saline (PBS) (pH = 7,4; 4°C) and subsequently disrupted by sonication. After pelleting cell debris, the total protein concentration in the soluble protein fraction was measured using Pierce BCA Protein Assay Kit (Thermo Scientific). β -Glucuronidase activity was determined at 37°C as described by (Wilson et al., 1992). Units were expressed as nmol product formed per minute per milligram protein. The values reported were averaged by using three independent cultures.

Supplementary figures:

```

MamZ_MSR-1      VPCVTTISTACGLMLEAWMPK-SGKPKSTGTPADFAPTQWNIIYLLMTVGSLSVAALSISI
MamZ_AMB-1      APCATITSTAFGRMREAWMPRNAEAPAKGTTADDFAPTQWNIIYLLMTVGALMAALSISI
MamZ_MS-1       APCATITSTAFGRMREAWMPRNAEAPAKGTTAADFAPTQWNIIYLLMTVGALMAALSISI
MamZ_MC-1       -----MLALRSRFRTEHILYMLSVMSTLAIALAVGV
MamZ_MV-1       -----MNEYVIEHWRWNALYLLLATSSVIMTLTVGM
MamH_MSR-1      -----MEPGRSEVEGHQRNALYLLSALCMVFMTLVVAI
                                     . : * : * . : : * : : :

```

Fig. S1. Correction of mispredicted N-Terminus of MamZ_{MSR-1}. Alignment of N-terminal MamZ sequences from MSR-1, AMB-1, MS-1, MC-1, MV-1 and MamH from MSR-1. The annotated start is marked in bold letter. MamZ from AMB-1 and MS-1 are shown with putative aa encoded by preceding codons (italic). MamZ in MSR-1 was annotated with a longer, nonconserved N-terminus as compared to other homologs. There are two conserved methionine, which might represent the genuine protein start (white triangles). Analog to MamZ_{AMB-1} and MamZ_{MS-1}, we define the second conserved M, as most probable start codon in MamZ_{MSR-1}. The black triangle indicates the beginning of highly conserved region in MamZ_{MSR-1}, MamZ_{AMB-1} and MamZ_{MS-1}.

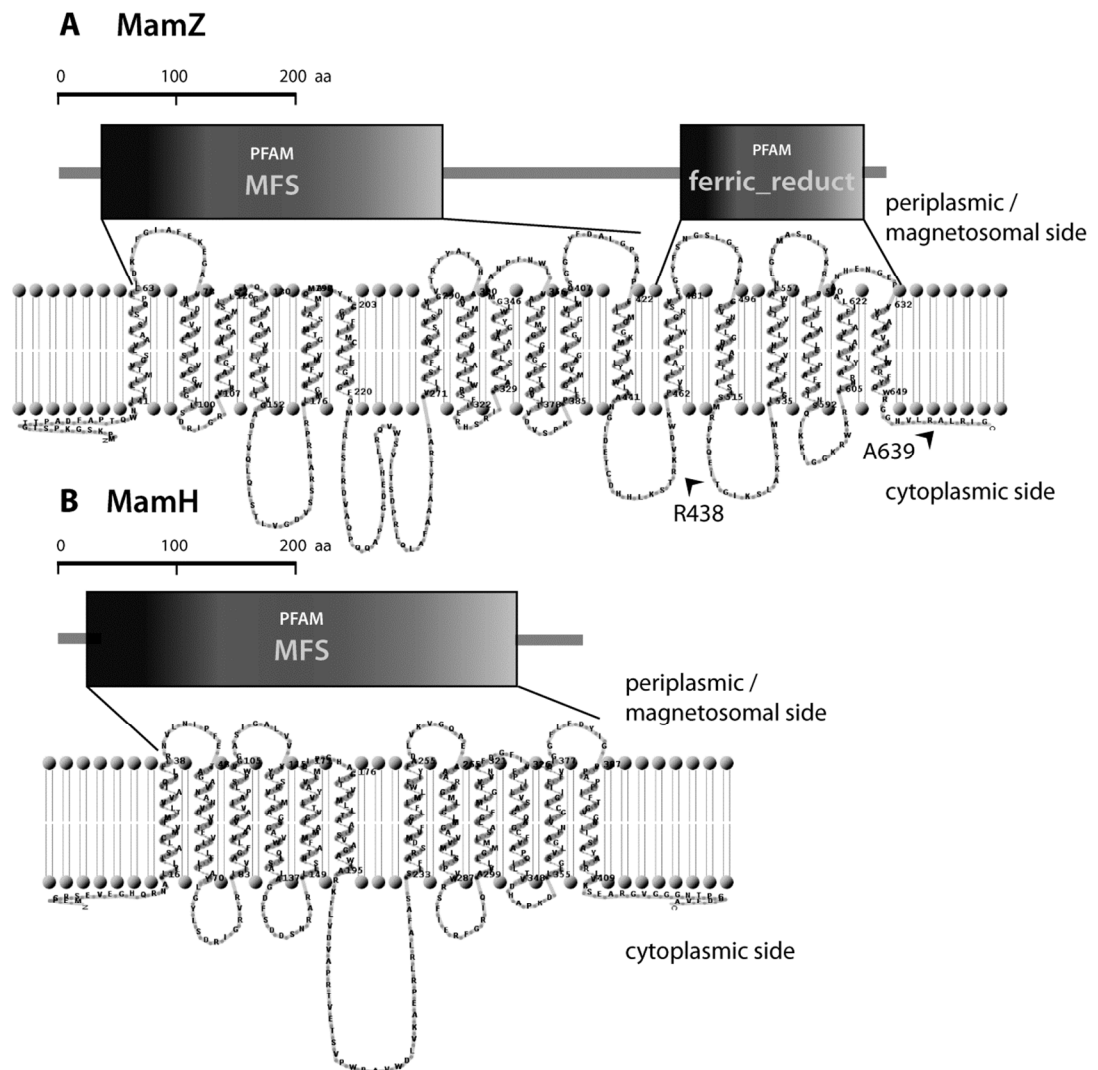


Fig. S2. Predicted domain structure and membrane topology of MamZ and MamH. A. Predicted domain structure of MamZ. The protein consists of a C-terminal MFS domain, comprising the first 12 TMD and an N-terminal ferric reductase-like transmembrane component, comprising the last 6 TMD. Marked R438 and A639 residues represent the predicted boundaries of the ferric reductase domain. B. Predicted domain structure of MamH.

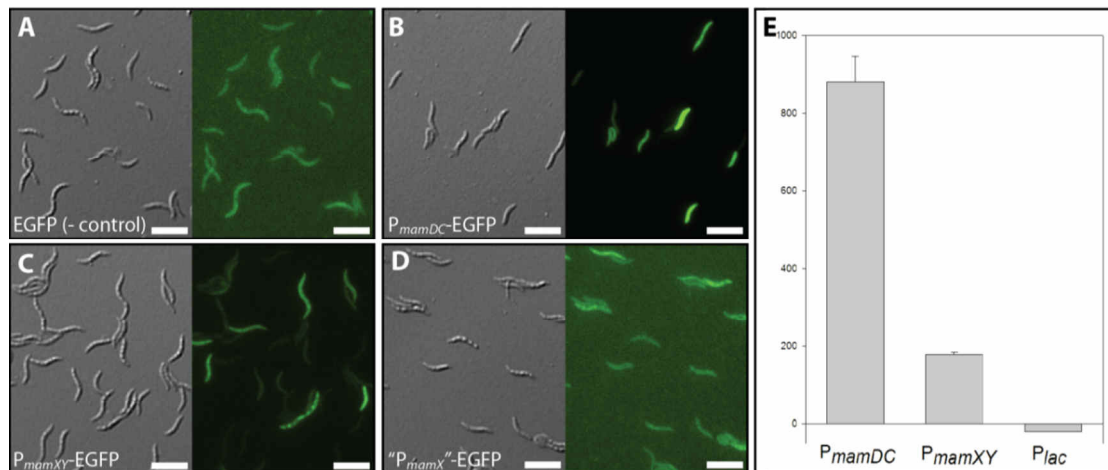


Fig. S3. Comparison of expression strengths of P_{mamDC}, P_{mamXY} and "P_{mamX}" and P_{lac} promoters: Fluorescence micrographs and GusA activity assays of MSR-1 strains expressing transcriptional *egfp/gusA* fusions.

A. *egfp* w/o promoter (negative control).

B. P_{mamDC}-*egfp*.

C. P_{mamXY}-*egfp*.

D. "P_{mamX}"-*egfp* (intergenic region between *mamX* and *mamY*).

Scale bars: 5 μm.

E. GusA activity assay with P_{mamDC}-*gusA*, P_{mamXY}-*gusA* and P_{lac}-*gusA* in FSM medium. Units are given as nmol product formed per minute per mg protein.

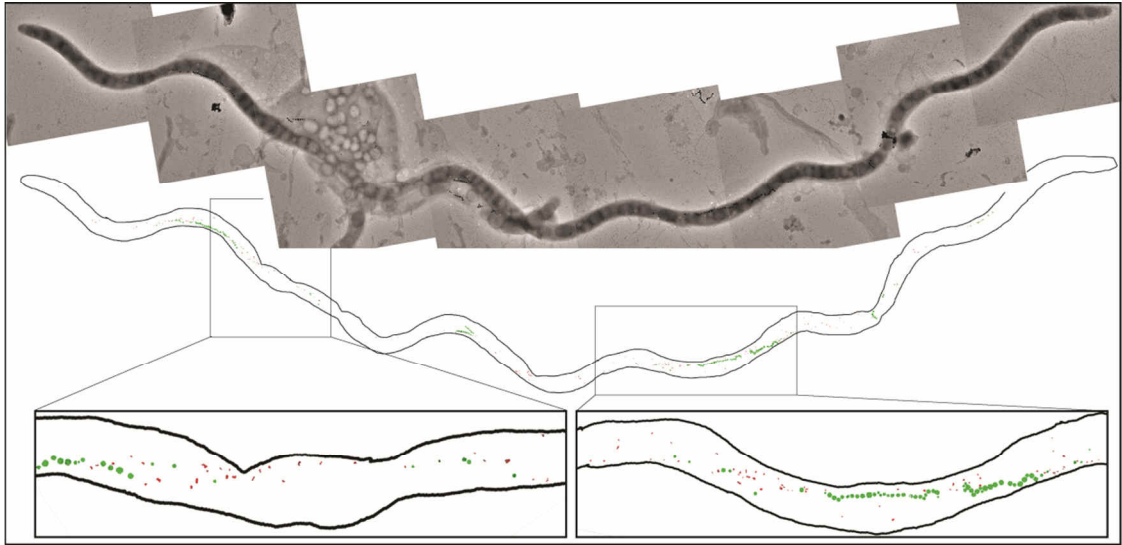


Fig. S4. Merged TEM micrographs of a representative cephalexin-inhibited $\Delta mamX$ cell 12 h after cephalexin addition and the corresponding segmentation with details. Regularly-shaped (cubo-octahedral) WT-like crystals (green) and flake-like particles (red) develop independently.

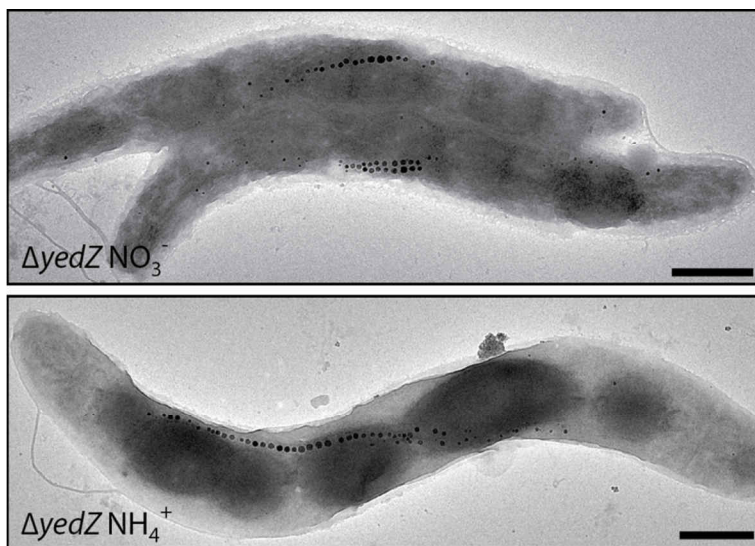


Fig. S5. *yedY* deletion has no effect for magnetite biomineralization, either in the presence or absence of nitrate. TEM micrographs of representative cells.

A. $\Delta yedY$ grown in nitrate containing FSM medium.

B. $\Delta yedY$ grown in ammonium medium.

Scale bars: 500 nm.

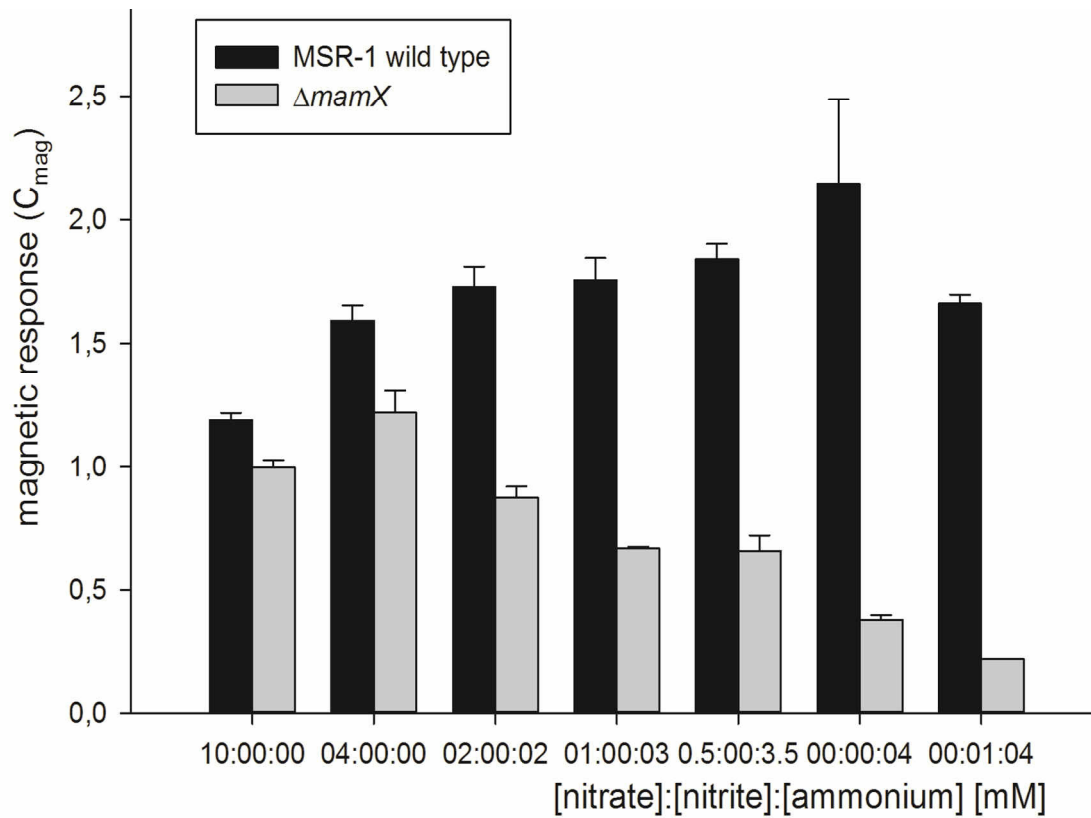


Fig. S6. Addition of nitrate can partly rescue $\Delta mamX$ phenotype, whereas addition of nitrite has no effect. C_{mag} values of MSR-1 WT and $\Delta mamX$ grown in media with different nitrate, nitrite and ammonium compositions.

Supplementary Tables

Table S1: Bacterial strains

Strain	genotype	Reference
<i>Magnetospirillum gryphiswaldense</i> (MSR-1)		
MSR-1 R3/S1	wildtype, Rif ^R , Sm ^R	[54]
MSR-1 R3/S1 Δnap	Δnap	[75]
OR003	$\Delta mamX$	This study
OR004	$\Delta mamZ$	This study
OR005	$\Delta mamH$	This study
OR006	$\Delta mamH \Delta mamZ$	This study
OR014	<i>mamX</i> C65,86,104,107A	This study
OR016	<i>mamZ</i> Δ 438-639	This study
OR017	$\Delta yedY$	This study
OR018	$\Delta nap \Delta mamX$	This study
<i>Escherichia coli</i>		
DH5 α	F' Φ 80d <i>lacZ</i> Δ M15(<i>lacZYA-argF</i>)U169 <i>deoR recA1 endA1 hsdR17</i> (rk-, mk+) <i>phoA supE44</i> λ - <i>thi-1 gyrA96 relA1</i>	Invitrogen
BW29427	<i>thrB1004 pro thi rpsL hsdS lacZ</i> Δ M15 <i>RP4-1360</i> Δ (<i>araBAD</i>)567 Δ <i>dapA1341</i> ::[<i>erm pir</i> (wt)]	K.A. Datsenko and B.L. Wanner, unpublished

Table S2: Plasmids

Plasmid	Purpose / relevant characteristics	Reference or source
pAL01	pK19mobGII derivative, Km ^H , <i>lox71</i>	Lohße et al., 2011
pAL02/2	pT18mob2 derivative, Gm ^H , <i>lox66</i>	Lohße et al., 2011
pBBR1 MCS-2	Replicative backbone vector, <i>mob</i> , Km ^H	Kovach et al., 1995
pCL6	<i>P_{mamDC}-mamC-egfp</i> , pBBR1MCS-2 derivative, Km ^H	Lang and Schüler, 2008
pFM210	pBBR1MCS-2 derivative, Km ^H , <i>P_{lac}</i> , <i>lacI</i> ,	F. Müller, <i>unpublished</i>
pJET1.2	General cloning vector, Ap ^R , T7-promoter, EC471R, <i>P_{lac}-UV5</i>	Thermo Scientific
pOR003	<i>mamX</i> deletion, pAL01 derivative, Km ^R , <i>lox71</i>	This study
pOR004	<i>mamX</i> deletion, pAL02/2 derivative, Km ^R , <i>lox66</i>	This study
pOR008	<i>mamZ</i> deletion, pAL01 derivative, Km ^R , <i>lox71</i>	This study
pOR012	pAL02/2 derivative, Km ^H , <i>lox66</i> , terminator	This study
pOR013	<i>mamZ</i> deletion, pAL02/2 derivative, Km ^H , <i>lox66</i> , terminator	This study
pOR025	pK19mobGII derivative, Km ^R	This study
pOR026	<i>mamH</i> deletion, pK19mobGII derivative, Km ^R	This study
pOR028	<i>P_{mamXY}</i> , pBBR1MCS-2 derivative, Km ^R	This study
pOR031	<i>P_{mamXY}-mamZ</i> , pBBR1MCS-2 derivative, Km ^H	This study
pOR053	<i>P_{mamXY}-egfp</i> , pBBR1MCS-2 derivative, Km ^H	This study
pOR054	<i>P_{mamX}-egfp</i> , pBBR1MCS-2 derivative, Km ^H	This study
pOR056	<i>mamZ</i> 438-639 deletion, pK19mobGII derivative, Km ^H	This study
pOR069	promoterless <i>oegfp</i> , pBBR1MCS-2 derivative, Km ^H	This study
pOR070	<i>P_{lac}-egfp</i> , pFM210 derivative, Km ^H , <i>lacI</i>	This study
pOR071	<i>P_{mamDC}-egfp</i> , pBBR1MCS-2 derivative, Km ^H	This study
pOR093	<i>mamX</i> CXXCH (65,104)->AXXAH, pK19mobGII derivative, Km ^R	This study
pOR098	<i>P_{mamXY}-mamX</i> , pBBR1MCS-2 derivative, Km ^R	This study
pOR101	<i>P_{mamDC}-mamH</i> , pBBR1MCS-2 derivative, Km ^H	This study
pOR102	<i>P_{mamXY}-gusA</i> , pBBR1MCS-2 derivative, Km ^H	This study
pOR105	<i>P_{lac}-gusA</i> , pFM210 derivative, Km ^H , <i>lacI</i>	This study
pOR106	<i>P_{mamDC}-gusA</i> , pBBR1MCS-2 derivative, Km ^H	This study
pOR109	<i>yedY</i> deletion, pK19mobGII derivative, Km ^H	This study

Table S3: Oligonucleotide primers

Restriction sites are underlined

Oligo-nucleotide	Sequence (5' – 3')	application
oOR006	GCCGGAATT <u>C</u> CCGCGAGTAGTAACGTCTACGGC	mamX_upstream_fw
oOR007	TAAT <u>G</u> CGGCCGCGAGTTGCGACTGTGGTCAAAGTGG	mamX_upstream_rw
oOR008	ATTAGGATCCTGGATTACGCCATGAGCGTC	mamX_downstream_fw
oOR009	GACTAAGCTTGCCCAATAGCGGTTGACG	mamX_downstream_fw
oOR036	CGCGGAATT <u>C</u> GACGATTAACGGAGGAGCCC	mamZ_upstream_fw
oOR037	AATT <u>G</u> CGGCCGCTTACCGCTCTTCGGCATCC	mamZ_upstream_rw
oOR038	CTGAGGTACCCTGCGAATCGGCTAAATGG	mamZ_downstream_fw
oOR043	AGCT <u>G</u> CTAGCGATCCCGTCGAGCATGTAGG	mamZ_downstream_rw
oOR045	GACT <u>G</u> TCGACAGCCAGCGATTCAAGCTCG	mamH_upstream_fw
oOR046	CGCTAGGCCACTTCGTCATCTGATCTGCCAGGTTCCATTCC	mamH_upstream_rw
oOR047	GGAATGGAACCTGGCAGATCAGATGACGAAGTGGCCTAGCG	mamH_downstream_fw
oOR048	GCGTGAATTCTTATCCAGTGCGAAAAGGC	mamH_downstream_rw
oOR125	ATTAGGATCCGCGACCCTAATGATCTGGTCC	PmamX_fw
oOR072	CTGACATATGAGTTCGACTGTGGTCAAAGTGG	PmamX_rw
oOR087	ATTAGGATCCGGCAGCCTCATTTAAACATTGAGG	PmamY_fw
oOR088	TTACAAGCTTCATATGGGCTGCTCCCGTGGTGG	PmamY_rw
oOR091	ACTCCATATGAACACCAAAGCCGTTGC	mamX_fw
oOR194	AGTCCTCGAGTTACCGCTCTTCGGCATCCAC	mamX_rw
oOR093	ACTCCATATGCCCTGCGTGACGACC	mamZ_fw
oOR094	AGTCCTCGAGTTAGCTAGCGCCGATTTCGCAGGGCG	mamZ_rw
oOR106	CTAGACTTTTTCGCTTTACTAGCTTTAGTTCTCCAATAAATTCCTG CGAAGCTTAGGAGATCAGCA	PmamDC_ins_1
oOR107	TATGCTGATCTCCTAAGCTTCGCAGGGAATTTATTGGAGAACTAAGA GCTAGTAAAGCGAAAAAGT	PmamDC_ins_2
oOR112	TACGCATATGGTGTGCAAGGGCGAGG	oegfp_fw
oOR113	CCATCTCGAGTCACTTATACAGCTCGTCCATGCC	oegfp_rw
oOR123	CACTGCAGGCGCTGTCCATCTCTATCCAGC	mamZ_trunc_upstream_fw
oOR116	CCATTTAGCCGATTTCGCAGGGTGGATTTAAGGTGGTGATCG	mamZ_trunc_upstream_rw
oOR117	CGATCACCACTTAAATCCACCCTGCGAATCGGCTAAATGG	mamZ_trunc_downstream_fw
oOR124	TCACTAGTCGCCGATGCTTGATTCTTCC	mamZ_trunc_downstream_rw
oOR110	GACTCTGCAGCTATTTTCGCGGGTACAAGAACG	mamX_ins_fw
oOR210	ACGGACTAGTGAACACCAAATTTCCCATCAGGC	mamX_ins_rw
oOR187	GAAGATGGTCGCCTCCAGCGCCCATATCGTCACC	mamX_AXXAH_1_fw
oOR188	TCGCGGCCATCGCGATGGG	mamX_AXXAH_1_fw
oOR189	CGAGAAGATGGCCGCCAGTGCCACACCATCG	mamX_AXXAH_2_fw
oOR190	CGTCCATCCACATGCGGCGCC	mamX_AXXAH_2_fw
oOR217	TTACCATATGATGTTACGTCCTGTAGAAACCCC	gusA_fw
oOR218	CTAGCTCGAGTCATTGTTTGCCTCCCTGC	gusA_rw
oOR221	TTACCATATGATGGAACCTGGCAGATCAGAAG	mamH_fw
oOR223	ACTCATGCATCTAGGCCACTTCGTCATCCC	mamH_rw
oOR231	GACACTGCAGGGGATGAAGCTGAACCACACC	yedY_upstream_fw
oOR249	GCATCAGTAATTGACCCGCAAATCGCGGATCAGCATGGCTTGG	yedY_upstream_rw
oOR250	CCAAGCCATGCTGATCCGCGATTTCGCGGTCAATTAAGTATGC	yedY_downstream_fw
oOR251	ACTCACTAGTTCGAAATCCCTCCACATCTTGG	yedY_downstream_rw

Supplementary references

- Kovach, M.E., Elzer, P.H., Hill, D.S., Robertson, G.T., Farris, M.A., Roop, R.M., et al. (1995) Four new derivatives of the broad-host-range cloning vector pBBR1MCS, carrying different antibiotic-resistance cassettes. *Gene* 166: 175–176.
- Lang, C. and Schüler, D. (2008) Expression of green fluorescent protein fused to magnetosome proteins in microaerophilic magnetotactic bacteria. *Appl Environ Microbiol* 74: 4944–53.
- Li, Y., Katzmann, E., Borg, S., and Schüler, D. (2012) The Periplasmic Nitrate Reductase Nap Is Required for Anaerobic Growth and Involved in Redox Control of Magnetite Biomineralization in *Magnetospirillum gryphiswaldense*. *J Bacteriol* 194: 4847–56.
- Lohße, A., Ullrich, S., Katzmann, E., Borg, S., Wanner, G., Richter, M., et al. (2011) Functional Analysis of the Magnetosome Island in *Magnetospirillum gryphiswaldense*: The mamAB Operon Is Sufficient for Magnetite Biomineralization. *PLoS one* 6: e25561.
- Schultheiss, D. and Schüler, D. (2003) Development of a genetic system for *Magnetospirillum gryphiswaldense*. *Arch Microbiol* 179: 89–94.
- Wilson, K.J., Hughes, S.G., and Jefferson R. A. (1992) The *Escherichia coli* gus operon: induction and expression of the gus operon in *E. coli* and the occurrence and use of GUS in other bacteria. In, Gallagher, S.R. (ed), GUS protocols. Using the GUS gene as reporter of gene expression. Academic Press Inc., San Diego, pp. 7–22.

4.3 Manuscript C:

Genetic and ultrastructural analysis reveals the key players and initial steps of bacterial magnetosome membrane biogenesis

Oliver Raschdorf^{1,2}, Yvonne Forstner¹, Isabel Kolinko¹, René Uebe^{1,3},
Jürgen M. Pitzko² and Dirk Schüler^{1,3}

Affiliations:

1: Ludwig Maximilian University Munich, Department of Microbiology

2: Max-Planck-Institute of Biochemistry, Department of Molecular Structural
Biology

3: University of Bayreuth, Department of Microbiology

In preparation

Updated version of manuscript, 23 March 2016

Abstract

Magnetosomes of magnetotactic bacteria contain well-ordered nanocrystals for magnetic navigation and have recently emerged as the most sophisticated model system to study the formation of membrane bounded organelles in prokaryotes. Magnetosome biosynthesis is thought to begin with the formation of a dedicated compartment, the magnetosome membrane (MM), in which the biosynthesis of a magnetic mineral is strictly controlled. While the biomineralization of magnetosomes and their subsequent assembly into linear chains recently have become increasingly well studied, the molecular mechanisms and early stages involved in MM formation remained poorly understood.

In the Alphaproteobacterium *Magnetospirillum gryphiswaldense*, approximately 30 genes were found to control magnetosome biosynthesis. By cryo-electron tomography of several key mutant strains we identified the gene complement controlling MM formation in this model organism. Whereas the putative magnetosomal iron transporter MamB was most crucial for the process and caused the most severe MM phenotype upon elimination, MamM, MamQ and MamL were also required for the formation of wild-type-like MMs. However, only a subset of seven genes (*mamLQBIEMO*) combined within a synthetic operon was sufficient to restore the formation of intracellular membranes in the absence of other genes from the key *mamAB* operon. Tracking of de novo magnetosome membrane formation by genetic induction revealed that magnetosomes originate from random locations before alignment into coherent chains. Our results indicate that no single factor is essential for MM formation, which instead is orchestrated by the cumulative and rather unspecific action of several magnetosome proteins.

Introduction

Although many prokaryotes are currently known to form intracytoplasmic membranes (ICM), the underlying mechanisms of ICM formation are still widely unexplored [1,2]. One of the most sophisticated model systems to study the biogenesis of prokaryotic ICM and organelles are bacterial magnetosomes, which are nanometer-sized particles of a magnetic mineral bounded by a distinct membrane [3,4]. In the freshwater Alphaproteobacterium *Magnetospirillum gryphiswaldense* (MSR-1), biosynthesis of magnetosomes was dissected into distinct steps. First, by invagination from the cytoplasmic membrane (CM) the magnetosome membrane (MM) forms a confined compartment. Next, supersaturating amounts of iron are transported into the MM which provides a controlled environment for the nucleation and maturation of well-ordered cuboctahedral crystals of magnetite. Eventually, individual magnetosome particles become concatenated and aligned into a linear chain along a dedicated cytoskeletal structure to most efficiently serve as sensor for the Earth's weak magnetic field [5-8]. While the biomineralization of magnetite crystals is increasingly well understood, much less is known about the genetic determinants and mechanisms which control the formation of the MM. In MSR-1 the MM was found to contain a set of specific proteins [9,10] which are assumed to control magnetosome biosynthesis and are encoded by several gene clusters of a compact genomic magnetosome island (MAI) [11-13]. Previous studies of MSR-1 suggested that only 6 (*mamB*, *mamM*, *mamE*, *mamO*, *mamQ*, and *mamL*) of the ~30 known MAI genes are individually essential for the biomineralization of at least rudimentary iron-oxide particles as revealed by conventional TEM. MamQ belongs to the widespread LemA protein family [10], but magnetobacterial MamQ is the only member that could be linked to a known cellular process [14]. MamL is a small, MTB-specific hypothetical membrane protein without any known functional domains [15]. The paralogous MamB and MamM proteins belong to the cation diffusion facilitator family and are assumed to transport ferrous iron into the magnetosome lumen. Both proteins form homo- and heterodimers and MamB becomes destabilized in the absence of MamM [8]. It was further suggested that the C-terminal tetratricopeptide repeat domain of MamB interacts with the PDZ domain of MamE [8]. MamE and MamO are putative membrane-integral serine proteases of the HtrA/DegP family and important for magnetite maturation *in vivo* [16]. It was

suggested that MamE functions in magnetosome protein sorting, and by its protease activity provides a “checkpoint” control for magnetite maturation [16].

While deletion of *mamB* in MSR-1 reportedly also eliminated the formation of MMs, Δ *mamM*, Δ *mamE* and Δ *mamO* strains continued to form empty MM vesicles devoid of electron dense crystals [8,17]. In the related *Magnetospirillum magneticum* (AMB-1) in addition single deletions of *mamL*, *mamQ* and *mamI* (encoding a small MTB-specific protein of unknown function) were reported to completely eliminate MM formation, while deletion of *mamN* (encoding a putative proton exporter) caused the formation of empty MMs [18]. However, the effects on MM formation have not been studied in Δ *mamQ*, Δ *mamN*, Δ *mamI* and Δ *mamL* mutant strains of MSR-1, and thus the full complement of genes and their specific functions controlling MM formation in MTB has remained unknown. In addition, it is not clear whether MM formation proceeds in a stepwise manner, and if so, whether intermediate MM states of invagination exist, and how magnetosome proteins become organized prior and during MM formation. It is further still disputed whether the invaginated MMs remain permanently connected with the CM, eventually become pinched off to form free magnetosome vesicles, or if different MTB use different mechanisms [19].

In this study, we thoroughly characterized magnetosome membranes in MSR-1 wild type and several mutant strains. Cryo-electron tomography (CET) revealed previously unknown details of MM structure, including the presence of novel atypical membrane vesicles, putatively representing defective or immature MM states. We systematically assessed the gene complement controlling MM formation and discovered that MamB is the most crucial protein for MM formation. While the combined expression of all identified genes affecting MM formation (*mamLMQB*) failed to restore MM formation, an extended subset of genes (*mamLQBIEMO*) from the large *mamAB* operon combined in a synthetic expression cassette was sufficient to induce the formation of intracellular membranes in the presence the auxiliary *mms6*, *mamGFDC* and *mamXY* operons. Furthermore, we developed a system to trigger synchronous MM biogenesis by induced expression of the *mamB* gene, which enabled us to dynamically track *de novo* magnetosome formation by time-lapse fluorescence microscopy and CET. This revealed that magnetosomes originate at unspecific cellular locations and that MM invagination proceeds rapidly without any

detectable intermediary membrane deformation stages. Overall, MM formation involves a larger number of partially redundant protein functions, but is less specifically controlled than vesicle formation in eukaryotes.

Results

Structural characteristics of magnetosome membranes

To analyze the size, position and structure of regular MMs from the MSR-1 wild type, we imaged intact cells by CET (Fig 1). When cultivated under standard microoxic conditions, sizes of intracellular MMs ranged from 23 to 68 nm (mean 46 nm) (Fig 1, Fig 2). Partially empty MMs of similar but more variable size were also observed in aerobically cultivated non-magnetic wild type cells (Fig 1C and Fig 2), showing that MM formation is not suppressed by conditions known to inhibit biomineralization of magnetite [20]. MMs were always found in close proximity to the cytoplasmic membrane (CM) (Fig 1B). Although the missing wedge problem of tomography allows unambiguous interpretation only in a limited area of the cell, some MMs clearly appeared as vesicles that are disconnected from the CM (S1 Video and S1 Fig). Other MMs were continuous with the CM by a protruding neck with a length of around 6-10 nm, mouthing into the periplasm by a seemingly unobstructed annulus (Fig 1Bii), whose diameter of around 5-8 nm should allow the diffusion of small molecules or even proteins between the periplasm and the MM lumen. To explore this idea, we created a strain in which enhanced green fluorescent protein (EGFP, estimated size 2.4 x 4.2 nm [21]) was directed to the periplasm by fusing the protein to a twin arginine transporter (TAT)-export signal peptide (RR) derived from a putative hydrogenase subunit of MSR-1. As indicated by an even fluorescence signal in the cell periphery, RR-EGFP was transported into the periplasmic space (S2 Fig). However, we found no enrichment of RR-EGFP at positions of the magnetosome chain and failed to detect EGFP in immunoblots of MM proteins from purified magnetosome particles (S2 Fig B+C). Similar results were obtained when cells were cultivated in the presence of the soluble, but CM-impermeable dye 5(6)-Carboxyfluorescein (376 Da) which failed to become entrapped in regions of putative magnetosome locations (S2 Fig D).

Identification of the gene complement controlling magnetosome membrane formation

We assessed the roles of all suspected candidate genes by thorough CET analysis of the respective mutant strains. Both $\Delta mamN$ and $\Delta mamI$ of MSR exhibited MM vesicles with a similar size, shape and chain-like alignment at midcell like in the wild

type (Fig 2, Fig 3A+B and S1 Table). Some, but not all vesicles contained electron dense particles as were already detected previously by TEM [15] (Fig 3A+B). In a recent study, $\Delta mamL$ cells grown under standard conditions appeared devoid of crystalline particles, but occasionally contained few tiny conspicuous electron-dense structures that were difficult to discern by conventional TEM of dried cells [15] (see S3 Fig). Indeed, careful examination by CET clearly revealed the presence of less abundant and small MM vesicles in more than half of the analyzed $\Delta mamL$ cells, occasionally also aligned in a chain and associated with the magnetosome filament (Fig 2, Fig 3C and S1 Table). Although cells displayed no detectable magnetic response (C_{mag}), some vesicles contained tiny (<10 nm) electron-dense particles. If grown at lower temperatures known to enhance magnetite biomineralization [20], a weak magnetic response of $\Delta mamL$ cells became detectable (C_{mag} of 0.08 at 15°C) and cells indeed formed larger [mean: 17.2 ± 5.4 nm] and presumably more [14.2 ± 6.7] magnetite particles, now also clearly visible in dried cells observed by conventional bright field TEM (S3 Fig).

The unexpected detection of MMs and magnetite particles in the absence of *mamL* prompted us to closer assess the function of the protein, and in particular its C-terminal domain that contains nine conspicuous basic amino acid residues that were previously implicated in MM formation [7,22]. Partial replacements by similar neutral amino acids only caused mild magnetite biomineralization defects, while neutralization of all nine residues ($MamL_{all\ neutral}$) copied the severe biomineralization phenotype of the $\Delta mamL$ mutant (Fig 4B). Nevertheless, $MamL_{all\ neutral}$ -EGFP and all other GFP fused mutant versions of MamL partially localized in linear chains or aligned patches at midcell, similar to $MamL_{wild\ type}$ -EGFP, suggesting that the positively charged C-terminal residues are not essential for MM-tubulation or -interaction but rather participate in a process related to magnetite maturation (Fig 4B, see S1 Text for details).

Interestingly, in tomograms of $\Delta mamL$ we noticed vesicular structures that coexisted with smaller wild type-like vesicles but were entirely devoid of electron dense particles and had a distinct, almost uniformly dense appearance, in contrast to the light lumen enclosed by an electron-denser membrane in wild type-like vesicles (Fig 3C). However, their alignment with the linear magnetosome chain suggested that they are related to magnetosome vesicles (Fig 3C). To distinguish them from regular MM vesicles, we termed these novel structures “dense magnetosome

membrane-like structures” (DMMs). Similar DMMs were even more abundant in tomograms of $\Delta mamQ$: While approximately 25% of the analyzed cells were devoid of any vesicular structures in tomograms, we occasionally also detected in some cells isolated empty vesicles of rather wild type-like MM appearance (Fig 3Ei). However, large quantities (up to 50) of small, closely spaced and magnetosome filament-associated DMMs were present in 7 of the 16 analyzed cells (Fig 3E, Fig 2 and S1 Table). Interestingly, we also imaged nascent DMM structures apparently connected to the CM (Fig 3Eii). This, together with their association with the magnetosome filament and their compact chain alignment, strongly suggests that these structures represent aberrant states of the MM. To gain a better understanding about the function of MamQ, we N-terminally labeled the protein with fluorescent EGFP and mCherry. The fusion proteins mainly localized in distinct but highly mobile patches in the CM and in immunoblots showed lower abundance in purified magnetosomes. Additionally, amino acid substitution of five conserved and putative surface exposed aromatic or acidic residues that might possibly be involved in protein-protein interactions, inactivated MamQ function in terms of magnetite formation (see S2 Text, S5 Fig and S6 Fig for more details). These results might hint towards a role of MamQ in organizing other proteins within the CM.

Another pair of candidate genes implicated in magnetosome formation are *mamM* and *mamB* [8,18]. Again and as in $\Delta mamQ$, we found 6 out of 16 analyzed cryo-electron tomograms of $\Delta mamM$ cells to contain small abundant filament-attached DMMs, while also sometimes a few scattered wild type-like empty MM vesicles were observed (Fig 3F, Fig 2 and S1 Table). In stark contrast, $\Delta mamB$ cells were devoid of WT-like vesicles, and only 5 of the 18 analyzed $\Delta mamB$ cells exhibited few isolated structures, resembling aberrant DMMs, but often lacking the characteristic association with the magnetosome filament and never aligned in coherent chains, as seen in $\Delta mamQ$ and $\Delta mamM$ (Fig 3D and S1 Table). Thus, deletion of *mamB* caused the most severe MM phenotype of all tested candidate genes.

The magnetosome marker MamI-GFP shows chain-like localization in $\Delta mamL$, $\Delta mamQ$, $\Delta mamM$, but not in $\Delta mamB$

Next, we were interested how the variable impairments of MM formation in the mutant strains affected the localization of other magnetosome proteins. To this end,

we expressed a MamI-EGFP fusion as MM marker [16,18,23] in $\Delta mamL$, $\Delta mamQ$, $\Delta mamB$, $\Delta mamM$, as well as in wild type and MSR-1B (a spontaneous mutant lacking all magnetosome-related MAI genes except the auxiliary *mamXY* operon [24]). In contrast to the confined linear chain signal prevailing in the wild type (Fig 4A), localization of the MamI-GFP signal was drastically altered in MSR-1B: the fluorescence was homogeneously distributed over the CM in most cells, indicating that MamI-GFP entirely lost specific localization in the absence of MM and most other magnetosome proteins (Fig 4A). In $\Delta mamB$, no linear chain localization was visible as expected due to the absence of MM vesicle chains in this strain. However, MamI-GFP was predominantly localized in patches in the membrane or in a single spot at midcell, suggesting that the presence of other magnetosome proteins already caused MamI-GFP to accumulate in distinct foci (Fig 4A). In contrast, when expressed in $\Delta mamM$, $\Delta mamQ$, and $\Delta mamL$ backgrounds, MamI-GFP localized as linear signals of short to intermediate length in approximately 48%, 18%, and 14% of the analyzed cells, respectively, while other cells showed fluorescent patches in the CM and single strong foci (Fig 4A). The partially linear MamI-GFP fluorescence is thus consistent with the chain-organized MMs or DMMs also observed by CET in some cells of these strains, indicating that MamI is present in both types of membranes and further corroborates that DMMs are indeed magnetosome-like structures.

Co-expression of mamLQBIEMO restores internal membrane formation, but not magnetite biosynthesis in the absence of other mamAB operon genes

We found that MamL, MamQ, MamM and particularly MamB are the only proteins that play important roles in the formation of regular MMs. To test whether these genes are altogether also sufficient for MM formation in the absence of other magnetosome genes, we constructed artificial operons, first combining the native *mamAB* promoter with *mamL*, *mamQ*, *mamR*, *mamB*, and in a second version adding *mamM*. The small *mamR* gene was conveniently retained between *mamQ* and *mamB* to maintain the native gene order. While both constructs upon chromosomal integration restored magnetic responses in the single gene deletion strains $\Delta mamL$, $\Delta mamQ$, $\Delta mamB$ and $\Delta mamM$, respectively, expression in MSR-1B did neither restore biomineralization of particles nor MMs as assayed by TEM and CET. A third construct (pBAM-minMAI) comprised two fully synthetic expression cassettes with

the entire complement of genes individually found to be essential for magnetite biomineralization in MSR-1 [15] and each controlled by an independent copy of the P_{mamAB} promoter ($P_{mamAB-mamLQB}$ and $P_{mamAB-mamIEMO}$). Chromosomal integration and expression of the construct in $\Delta mamQ$ and $\Delta mamM$ backgrounds partly restored the magnetic orientation of the strains (>60% wild type C_{mag}), but not in MSR-1B or $\Delta mamAB$. However, while expression in MSR-1B also did not notably induce internal membrane formation (rare vesicular structures were detected), empty membrane vesicles became clearly visible in $\Delta mamAB$ cells expressing the construct (Fig 5): 11 of 15 analyzed tomograms contained at least 2-3, but up to 14 vesicular structures that were on average larger (62 ± 21 nm, up to 105 nm) than MMs of the wild type. Besides their unspecific localization along the cell body, we sometimes detected these membrane structures accumulated in close proximity to cell poles, an atypical position for magnetosomes (Fig 5G). Notably, four of all detected vesicles did contain very tiny (5-10 nm) electron dense particles of unknown identity (Fig 5C and F). Other structures in the cells were reminiscent of DMMs (Fig 5A). For comparison, similar single vesicular structures were only observed in 2 out of 11 analyzed cells of the $\Delta mamAB$ parent strain. These results indicate that the *mamLQBIEMO* genes alone are insufficient to restore magnetite biomineralization, but sufficient to induce the formation of intracellular membranes in the presence of the auxiliary *mms6*, *mamGFDC* and *mamXY* operons.

Induction of MamB expression reveals dynamics of de novo magnetosome membrane formation

All experiments described so far only yielded a static view on MM biogenesis. To resolve the spatiotemporal dynamics of magnetosome *de novo* formation, we designed an inducible genetic system that allowed the tuned expression of key magnetosome genes (see Materials and Methods). We first tested induction of MamL expression from the *lac* promoter in a $\Delta mamL$ background. As expected, this restored magnetosome formation back to wild type levels within several hours and also the proper localization of the previously mislocalized magnetosome marker protein MamC-EGFP (S7 Fig and S8 Fig). However, as noted during the course of this study, the presence of previously undetected MM vesicles and magnetite crystals in $\Delta mamL$ rendered this strain inappropriate to analyze *de novo* MM formation. We therefore engineered an analogous strain for the genetic induction of *mamB*

(MamB_{ind}), which had emerged as the most important gene for MM formation in this study. In the absence of IPTG, no MamB expression was detectable in MamB_{ind} by immunoblots, verifying its desired tight repression (Fig 6Aii). However, 1 hour after IPTG addition, MamB expression became apparent and its levels further increased gradually over approximately the next 10 hours, after which MamB levels remained constant (Fig 6Aii). Yet, a magnetic response (C_{mag}) of the cells became detectable only 5 hours post induction, but further steadily increased until the end of the experiment (Fig 6Ai). The cells were devoid of any electron-dense particles before induction, but few isolated and several concatenated magnetite particles with an average diameter of around 11 nm became discernable by TEM within few cells already after 2 hours (Fig 6Aiii). The crystal size was further increased 3 hours after induction, and cells on average contained 5 (up to 20) magnetite particles, while only very few cells remained completely devoid of crystals (Fig 6Ai+iii). Whenever multiple particles were visible, they predominantly already assembled as a loosely spaced chain at midcell (Fig 6Aiii), even when still in their superparamagnetic size range below 15-20 nm [25]. Although after 14 hours the cells on average contained still fewer (14, max. 33) and smaller (around 22 nm) magnetosomes than wild type cells (Fig 6Ai+iii), the slow *de novo* development of chain-aligned magnetosomes thus rendered the strain particularly useful for resolving the dynamics of MM formation over time. We pursued this in the next experiment in which cells were plunge-frozen and analyzed by CET at distinct time points after induction: Wild-type like MM vesicles were absent from the non-induced strain, but single crystal containing MM vesicles became visible at least 2 hours post induction (Fig 6Bi+ii), along with magnetosome filament-associated DMMs. 3 hours post induction, the numbers of MM vesicles had increased and few crystal-containing, filament-associated and loosely aligned MMs became visible both at the inner and outer curvature of the helical cells. They were mostly found in the recorded areas close to the division site, sometimes adjacent or in several 100 nm distance from each other. Furthermore, both closely chain-aligned DMMs and independent single crystal-containing magnetosomes were found within the same cells (Fig 6Biii-v). 4 hours post induction, two cells exhibited small and occasionally multiple linear magnetosome assemblies (up to three vesicles) with immature crystals (Fig 6Bviii). One cell contained both DMMs and wild type-like MM vesicles associated with the same visible section of the magnetosome filament (Fig 6Bvi), while another cell

contained >10 chain-aligned DMMs. Altogether, the CET results suggested that wild-type MM formation after induction of *mamB* expression proceeded slowly and gradually, rather than by the simultaneous formation of large numbers of MMs. Notably, despite very careful examination, we failed to identify any structures resembling intermediate stages of early MM development (e.g. crystal bearing membrane transformation stages other than spherical invaginations) in any of the 23 analyzed tomograms from any time point (1, 2, 3 or 4 hours post induction). This indicates that if such intermediary structures exist at all, they must likely be very transient and differentiate into spherical MM before biomineralization is initiated. Because of the low time resolution of CET sampling, we also attempted to track magnetosome formation in living cells by time-lapse fluorescence microscopy in a strain in which an inducible MamB was fused to EGFP (MamB-EGFP_{ind.}) This fusion was previously demonstrated to become recruited into the MM [8] and shows a linear localization within cells that form magnetosome chains (see S6 Fig A). As MamB_{ind.}, MamB-EGFP_{ind.} also developed magnetosomes after induction, as determined by a C_{mag} of approximately 0.3 after over-night induction with IPTG. Using an improved protocol (see Material and Methods), cells could be imaged for more than 24 hours and for at least up to 6 consecutive divisions in a single experiment (S9 Fig, S9 Video and S10 Video). Faint fluorescence signals became visible approximately 1 hour post induction. In dividing cells, the fluorescence intensity then steadily increased over approximately the next 10 hours (\cong 2-3 divisions). During the first hours, the signal was mainly localized in multiple punctuate foci at unspecific positions within the cells, but in few frames was predominantly accumulated at midcell (Fig 6C). Approximately 8 to 9 hours post induction, the fluorescence signal developed into a linear localization at or close to midcell, co-existing with single foci at unspecific positions (Fig 6C). This linear localization then persisted, became elongated and segregated in many of the dividing cells, and could even be observed in some cells after the GFP signal gradually began to fade after 14-15 hours (\cong 3-4 divisions) post induction (Fig 6C, S9 Fig). In corroboration of the CET results, our observations indicate that newly synthesized MamB-GFP first becomes clustered all over the cell body into distinct foci at the CM, from which MM formation is then orchestrated. The fluorescent foci most likely represent MamB-GFP enriched magnetosome protein clusters or single

magnetosomes, which then become recruited into coherent magnetosome chains over time.

Discussion

MamB is the most important determinant, but not sufficient for magnetosome membrane formation

Previously, various proteins (MamB, I, L, Q, Y) were assumed to be essential for MM formation and/or to actively participate in membrane remodeling [18,19,26,27]. However, we found that *mamI* is not required for the formation of wild type-like MMs in MSR-1. Contrary to previous assumptions, also single deletions of *mamQ* and *mamL* continued to form MMs or similar aberrant structures. While the requirement of *mamM* for MM formation was already questioned [8], its deletion also caused the formation of aberrant internal membranes. Most unexpectedly, we found no single candidate protein to be undoubtedly essential for MM formation, since even in the Δ *mamB* mutant strain, which exhibited the most severe MM phenotype, a background of low abundant aberrant membrane structures could be detected in few cells by careful CET analysis. However, since loss of MamB abrogated the formation of abundant concatenated internal membranes, it emerged as the most important factor for MM biogenesis.

The severe impairments in magnetite crystallization in the absence of MamL suggest that besides its participation in MM formation, this protein is primarily involved in the maturation of magnetite crystals, consistent with its universal presence in all magnetite-producing MTB, but absence from greigite producers [28]. The positively charged carboxy-terminus of MamL seems to be highly important for this function. MamL could either act directly on magnetite biosynthesis, or alternatively might be involved in the organization and recruitment of other magnetite maturation proteins, as suggested by the variable degrees of MamI-GFP and MamC-GFP mislocalization in Δ *mamL*, and the magnetosome recruitment of the MamC-GFP upon re-induction of MamL expression.

While fluorescent fusions of other analyzed Mam proteins predominantly localized to the MM, mCherry-MamQ, was mainly localized in the CM. The putative surface exposed, highly conserved acidic and aromatic amino acid residues that we found to be important for the function of MamQ might be involved in direct electrostatic or stacking interactions with other magnetosome proteins. Thereby, MamQ might participate in magnetosome formation by acting as a hub in the CM for the early organization of magnetosome proteins prior to membrane invagination.

Expression of *mamB* together with all other genes (*mamQ*, *L* and *M*) affecting MM formation in our study was not sufficient to restore MM biogenesis in absence of the other 21 genes from the *mamAB*, *mms6* and *mamGFDC* operons. Only co-expression of the synthetic *mamLQBIEMO* construct in a Δ *mamAB* strain restored the formation of few intracellular membranes reminiscent of MMs. However, as indicated by the lack of similarly abundant structures upon expression in the MSR-1B background, intracellular membrane formation was supported by the presence of additional genes from the *mms6*, *mamGFDC* and *mamXY* operons. This is unexpected, since deletion of these operons, alone or in combination, did not affect MM formation in previous studies, and the *mamAB* operon alone was sufficient to sustain rudimentary magnetosome formation in both MSR-1 and AMB-1 [29,30]. Altogether, this suggests that some or most MM proteins have unspecific (i.e. apart from their specific functions e.g. in magnetite biomineralization) and cumulative functions in MM biogenesis, and factors outside the *mamAB* operon might be required for MM formation depending on genetic context.

Our results are in clear contrast to observations in AMB-1, where *mamI*, *-L*, *-Q* and *mamB* were found to be essential for MM formation, as assayed by cryo-ultramicrotomy/TEM [18]. However, similar to our findings, the combined expression of *mamILBQ* in this strain also proved insufficient to restore MM formation in the absence of other *mamAB* operon genes [18]. Despite the high conservation of their major MAI genes, and apart from the possibility that rudimentary MM-structures might have escaped detection due to technical differences in the other study, these findings hint towards discrepancies in the magnetosome formation processes between the two closely related organisms.

Aberrant DMMs are putative precursors of regular magnetosome membranes

Empty and smaller magnetosome-like vesicles with electron-dense lumen (DMMs) became abundant upon re-induction of MM biogenesis and often outnumbered wild type-like MMs. DMMs were also found in high numbers in cells of Δ *mamM* and Δ *mamQ* and represent a previously unidentified, but distinct intracellular structure. Their association with the magnetosome filament, their apparent origin by invagination from the cytoplasmic membrane and the partial linear co-localization of the magnetosome marker MamI-GFP in mutants exhibiting chains of DMMs

suggests that these structures in fact represent immature or defective MMs. The formation of DMMs could be explained by two different scenarios: i) They might just represent aberrant invaginations that are smaller due to the lower incorporated amounts of proteins, possibly caused either by the absence of early landmark proteins such MamQ and MamM, or following the artificially slow re-induction of a single key protein. ii) DMMs might be precursors that accumulate due to delayed MM biosynthesis (upon *mamB* induction) but eventually will convert into regular MMs, or became stalled at early stages in the mutants. The absence of early key proteins might prevent hierarchical recruitment of additional proteins downstream and thus, inhibit further development. If DMMs represent intermediate stages of MM biogenesis, they should transiently also occur in wild type cells. Indeed, conspicuous structures coexisting with regular magnetosomes in some cells (e.g. see [S1 Video](#), ends of chain [right] and close to regular magnetosomes [left]) might be identical to DMMs.

Dynamics of magnetosome membrane formation

Since their first visualization, it has remained unclear whether MMs remain permanently continuous with the cytoplasmic membrane (CM) from which they originate, or if they become eventually pinched off, thus developing into vesicles discontinuous with the CM [5,6]. In contrast to a previous study of AMB-1 in which the vast majority of MM appeared connected to the CM [6], we here identified MMs that although still in close vicinity, were clearly discontinuous with the CM, thus confirming previous observations from MSR-1 [31,32]. Similarly, a recent CET study of the magnetotactic Alphaproteobacterium *Magnetovibrio blakemorii* also failed to reveal connections of MMs with the cytoplasmic membrane [33]. Although the lumen of invaginating MMs, i. e. those in *statu nascendi*, might transiently form a continuum with the periplasm, our results suggest that the molecular exchange between the two compartments is tightly regulated or obstructed by a physical barrier.

Synchronous genetic induction enabled us to track *de novo* magnetosome biogenesis with unprecedented time resolution by electron and live-cell fluorescence microscopy. Soon after induction, MamB-GFP formed patches at the CM and later linear signals within the cells. The early punctuate fluorescent signals might

represent local protein clusters in the CM, or early magnetosomes. This coincided with the appearance of single nascent magnetosomes in tomograms. As already speculated from previous iron-induction experiments [5], magnetosomes therefore do not originate only from specific locations within the cell, but appear along the entire length, before they are concatenated into closely spaced chains. Single nascent magnetite-containing magnetosomes were often already attached to the MamK magnetosome filament, indicating that the cytoskeletal structure becomes connected with the newly developing MM immediately, or even plays an assisting role in orchestrating of early magnetosome formation. Later, when magnetite crystals were still in the superparamagnetic size range, crystal-containing MMs in tomograms were still found isolated or in very short chains at different positions within dividing cells. According to results from TEM and fluorescent microscopy, magnetosomes then became organized in dense chains at mid-cell, presumably by the action of the magnetosome filament.

In a very recent study published during revision of this manuscript, MM formation was genetically induced via the *mamQ* gene in the related AMB-1 [34]. The results of this study also suggested that the machinery required for magnetosome membranes formation is distributed at multiple site throughout the cytoplasmic membrane. Nascent magnetosome membranes became first organized into linear, but discontinuous long-range aligned assemblies, after which the gaps between adjacent magnetosomes were closed by a mechanism dependent on the MamK magnetosome filament [34].

Magnetosome membrane biogenesis is multi-determined but not specifically controlled

As shown by several studies, the lack of certain magnetosome proteins can affect the proper localization of others. For instance, MamC mislocalized upon deletion of *mamQ*, *mamA*, *mamM* [8,15], and, as presented here, also *mamL*. Similarly, MamA, MamI and MamC mislocalized upon deletion of *mamE* [16,18], which indicates a hierarchical recruitment of proteins to the MM. Based on our and previous findings, we delineate a hypothetical model for MM biogenesis: The analyzed key proteins MamB, MamM, MamQ and MamL mark the beginning of a recruitment cascade and are required to position a network of additional magnetosome proteins, including

MamI, MamE and MamO (Fig 7). In turn, recruitment of further magnetosome proteins and oligomerization into high molecular weight complexes may introduce curvature into the cytoplasmic membrane (Fig 7), as was already previously speculated by Nudelman *et al.* [35]. This could be similar to ICM formation in *Rhodobacter sphaeroides* where simulations predicted that regular insertion of the curved multi-protein RC-LH1-PufX photosynthetic “core” complex and arrays of LH2 complexes into a model membrane can cause membrane curvature, tubulation and invagination [36,37]. Similarly, the compact assembly of magnetosome proteins in a pre-complex within the CM might lead to membrane invagination. In fact, previous studies with bacteria that naturally lack ICM structures (such as *E. coli*) already suggested that the formation of internal membranes can be induced by the overexpression of unspecific membrane proteins [38,39].

In eukaryotes, the formation of membrane vesicles is mediated by specific proteins that either form coats, scaffolds or insert into the membrane to create local curvature [40-43]. However, homologs of well-studied factors controlling vesicle formation in eukaryotes are absent from MTB and prokaryotes. Our findings suggest that MM formation is not accomplished by the specific function of individual proteins, but proceeds by the combined action of the membrane-integral core factors MamLQBIEMO and several other magnetosome proteins, that are not all individually essential for the formation of wildtype-like MMs. Thus, the mechanisms of internal membrane formation in bacteria appear to be less specifically controlled than in eukaryotic cells. In summary, we present the so far most comprehensive ultrastructural analysis of the complex magnetosome organelle and identify the genetic determinants involved in the initial steps of its biogenesis. Understanding the assembly of magnetosomes provides the conceptual framework for investigating the biogenesis of other bacterial organelles and for constructing synthetic organelles for bioengineering applications [44].

Figures

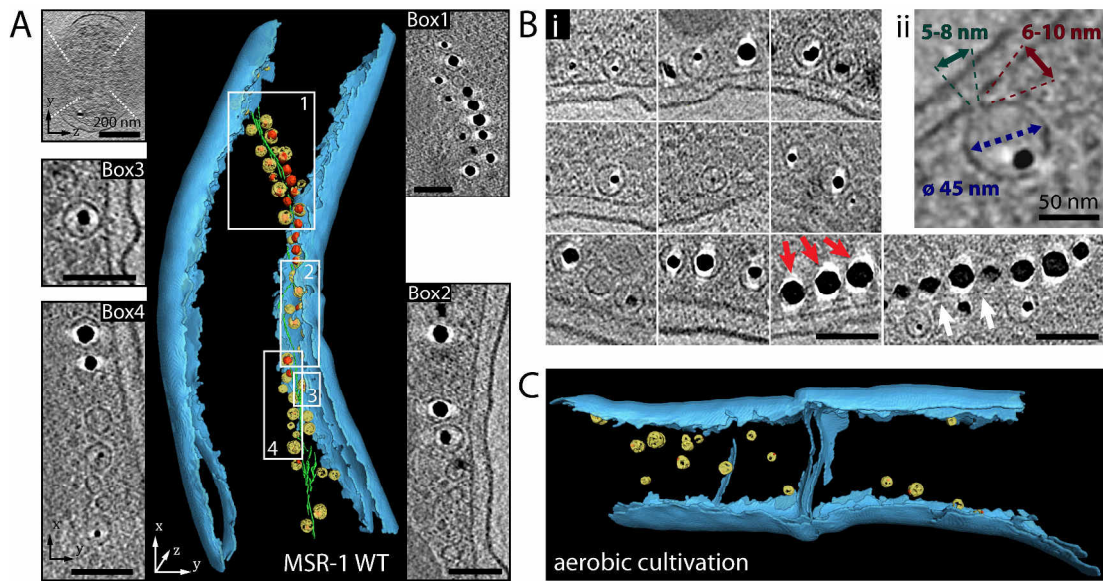


Figure 1: Ultrastructural analysis of magnetosome membranes from wild type.

A): Segmented cryo-electron tomogram of cell with selected details from x-y slices of tomographic reconstruction (Box 1-4) and a y-z slice, illustrating information loss by the missing wedge. The outer and cytoplasmic membrane (CM) are depicted in blue, magnetosome membranes (MMs) in yellow, magnetite crystals in red and the magnetosome filament in green. Scale bars in boxes: 100 nm.

(B): Panel with details from x-y slices of tomographic reconstructions of MSR-1 wild type cells, showing MMs that contain magnetite crystals of different sizes. The magnetosome filament is indicated by white arrows. The halo visible around magnetite crystals (red arrow shows examples) is caused by missing wedge effects and might obscure MM identification. (Bii): Section of x-y slice from tomogram showing MM that is continuous with CM and contains a small crystal. Numbers in graph represent average value for all measured MM diameters (blue) ($n = 289$), approximate values for the annulus diameter to the periplasmic space of continuous MMs (green) and approximate values for the length of the protruding neck between the CM and MM (red). Scale bars: 100 nm.

(C): Segmented cryo-electron tomogram of aerobically cultivated cell that contains MMs (some with small crystal). Full tomogram is shown in S2 Video..

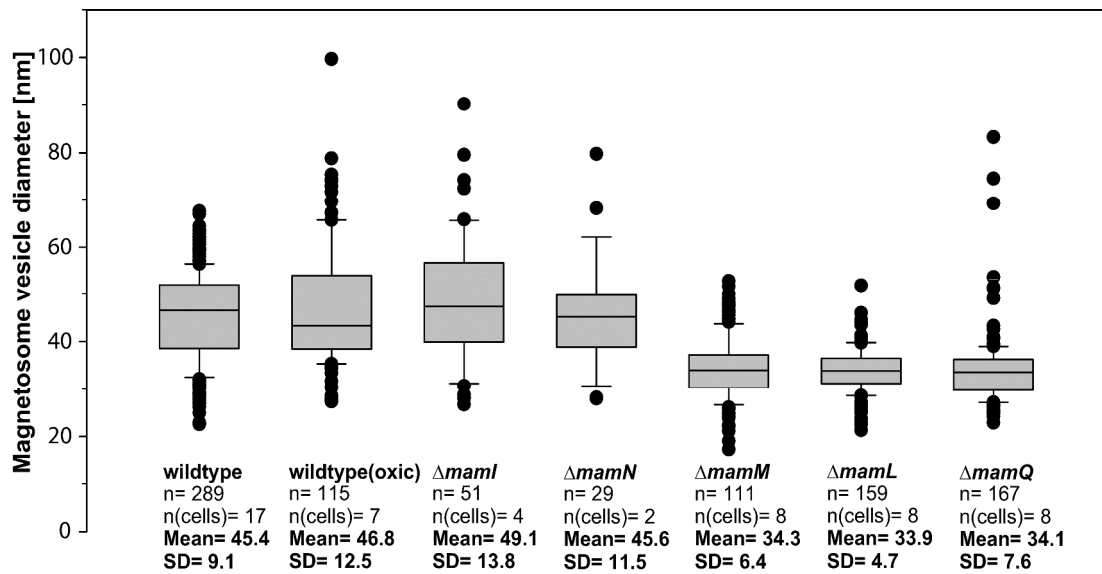


Figure 2: Diameters of magnetosome membranes and similar structures from wild type and several mutant strains.

Diameters of magnetosome membranes (MMs) or dense MM-like structures were measured from cryo-electron tomograms. Box plots are indicating 10th and 90th percentiles (whiskers), 25th and 75th percentiles (box), median and outliers. The number of measured membranes [n] and analyzed cells [n(cells)] are indicated. The mean value and the standard deviation (SD) of the diameters are given for each strain.

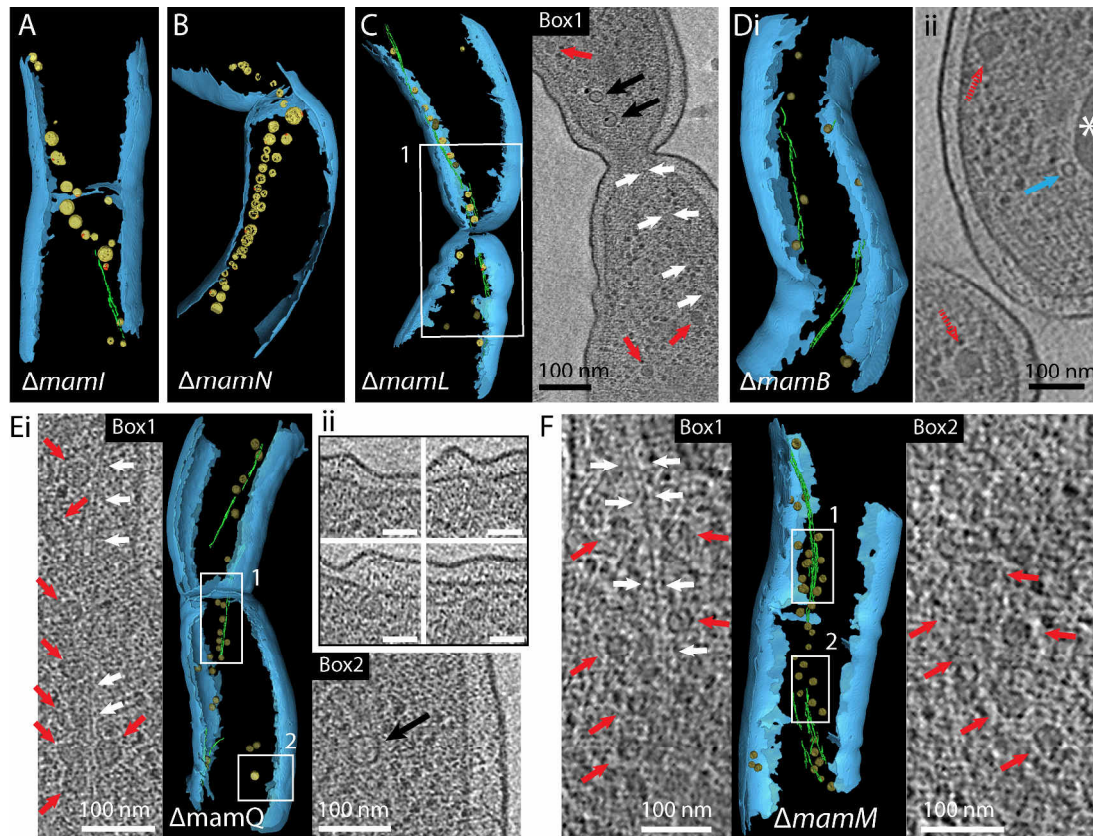


Figure 3: Cryo-electron tomograms of different MSR-1 mutant strains.

Segmented tomograms show representative phenotypes of mutants (compare with [Table S1](#)). The inner and outer membrane of the cells are depicted in blue, wild type-like magnetosome membranes (MMs) in yellow [black arrow in x-y slices], iron-minerals in red and the magnetosome filament in green [white arrow in x-y slices]. Distinguishable dense magnetosome membrane-like structures (DMMs) are depicted in dark yellow [red arrows in x-y slices], emphasizing the differential appearance in contrast to wild type-like MMs. Full tomograms are shown in S3-S8 Videos.

(A): $\Delta mamI$ cell containing wild type-like MMs that partially enclose mineral particles.

(B): $\Delta mamN$ cell containing a dense chain of empty and partially magnetite-filled wild type-like MMs.

(C): $\Delta mamL$ cell with x-y slice detail (Box 1), showing small wild type-like MMs, partially containing crystals, and potential DMMs.

(Di): $\Delta mamB$ cell displaying some putative isolated DMMs. (Dii): x-y slice detail of another tomogram shows putative DMMs (dashed red arrows) and a “mini-inclusion” structure (blue arrow) occasionally seen also in tomograms of the wild type and several other mutants. Asterisks marks polyhydroxyalkanoate inclusion that also occurred in all other analyzed strains.

(Ei): $\Delta mamQ$ cell with two x-y slice details (Box 1 and Box 2). Box 1 shows filament-attached DMMs, Box 2 shows putative wild-type like MM. (Eii): x-y slice sections of another tomogram show four putative DMMs of which some appear continuous with the cytoplasmic membrane. Scale bars: 50 nm

(F): $\Delta mamM$ cell with two x-y slice details (Box 1 and Box 2) showing filament attached DMMs.

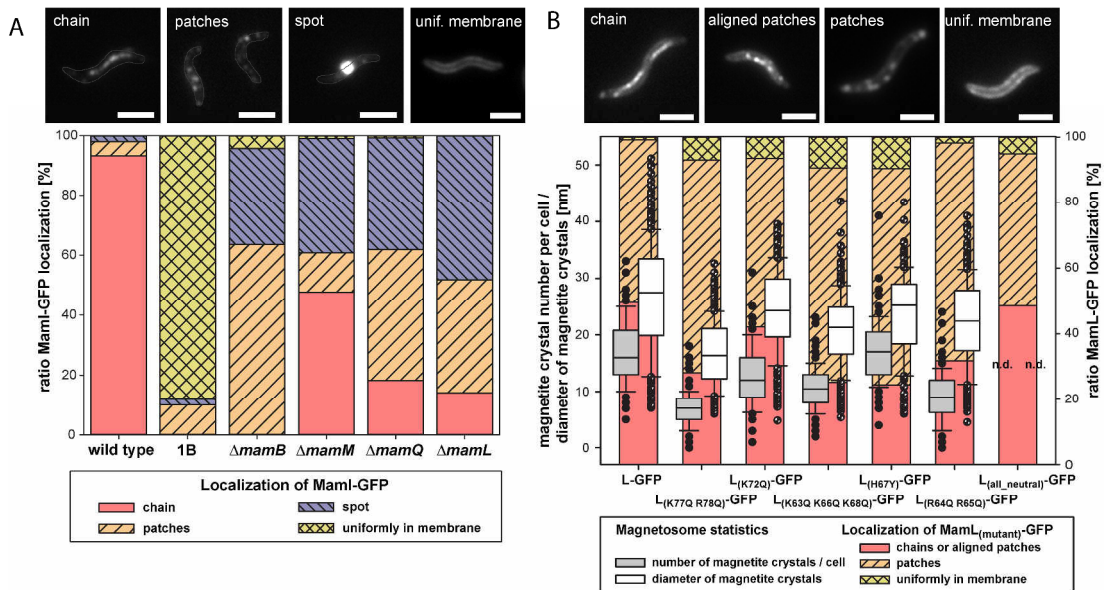


Figure 4: Localization of MamI-GFP in several mutants and complementation/localization assay of mutated MamL-GFP.

(A) Statistical analysis of localization of plasmid expressed $P_{mamDC45}\text{-mamI}\text{-egfp}$ in MSR-1, MSR 1B, $\Delta mamB$, $\Delta mamM$, $\Delta mamQ$ and $\Delta mamL$. The localization patterns in individual cells were grouped into four different classes (examples are indicated; boundary of cells is outlined). More than 100 cells were analyzed for each strain. Scale bars: 2 μm .

(B) Effects of exchange of basic amino acid residues in the C-terminus of MamL, fused to EGFP by an alpha-helical linker. Statistical analysis of magnetite crystal number/cell (grey) and magnetite crystal sizes (white) of MSR $\Delta mamL$ complemented with transposon-integrated $P_{mamDC45}\text{-mamL}\text{-egfp}$, $P_{mamDC45}\text{-mamL}_{K77Q-R78Q}\text{-egfp}$, $P_{mamDC45}\text{-mamL}_{K72Q}\text{-egfp}$, $P_{mamDC45}\text{-mamL}_{K63Q-K66Q-K68Q}\text{-egfp}$, $P_{mamDC45}\text{-mamL}_{H67Y}\text{-egfp}$, $P_{mamDC45}\text{-mamL}_{R64Q-R65Q}\text{-egfp}$ and $P_{mamDC45}\text{-mamL}_{all\ neutral}\text{-egfp}$. Box plots are indicating 10th and 90th percentiles (whiskers), 25th and 75th percentiles (box), median and outliers. Over 100 cells and 200 magnetosomes were analyzed for each strain. For statistical analysis of MamL_(mutant)-EGFP localization (colorful bars in background), fluorescence patterns were grouped into three classes (examples are indicated; chain and aligned patches are visualized as one class). Scale bars: 2 μm

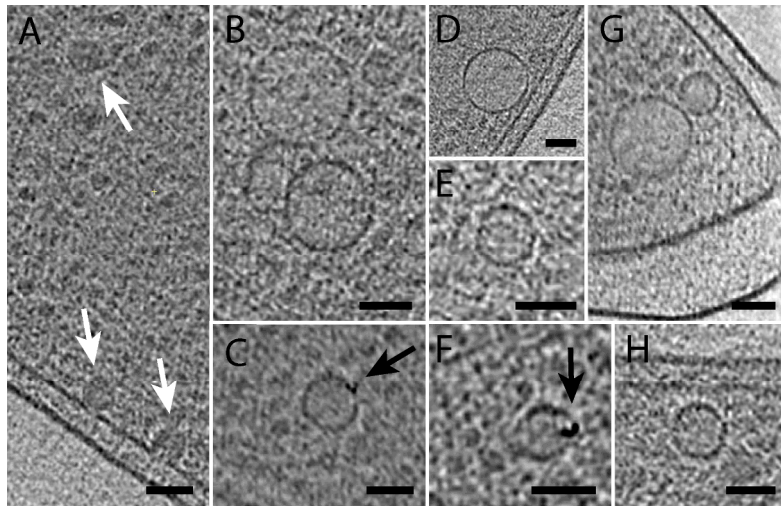


Figure 5: Internal membranes formed by expression of *mamQLBMEIO* in Δ *mamAB*

x-y slices from cryo-electron tomograms, showing typical magnetosome-vesicle like internal membrane structures in Δ *mamAB* P*mamAB*-*mamLQB*-P*mamAB*-*mamIEMO*. Image A shows structures reminiscent of dense magnetosome membrane-like structures (white arrows). Images B, D, and G show internal membranes that are larger than regular magnetosome membranes. Images in C and F show conspicuous electron dense inclusions within the vesicles (black arrow). Scale bars: 50 nm.

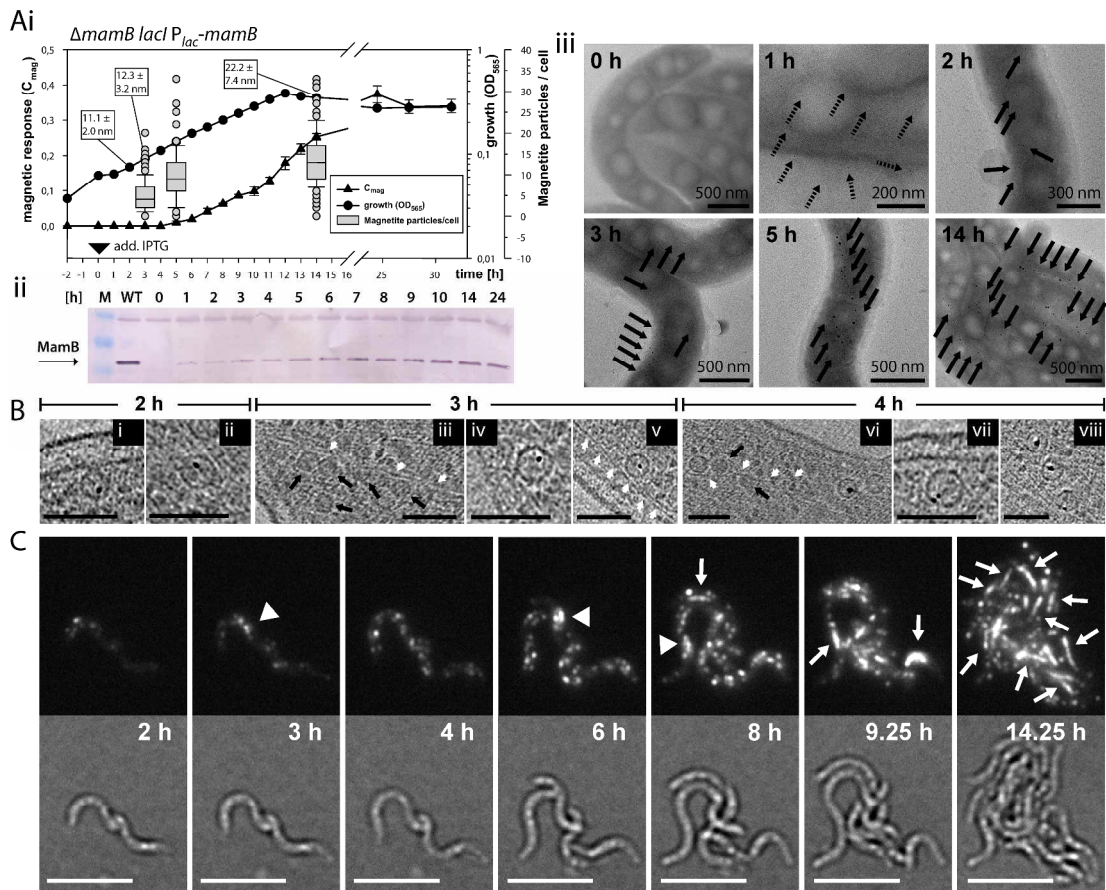


Figure 6: Induction of *mamB* and *mamB*-GFP expression enables *de novo* magnetosome formation.

(Ai): Progression of growth (OD_{565} [circles]) and magnetic response (C_{mag} [triangles]) over time after induction of *mamB* expression with 2 mM IPTG in strain $MamB_{ind}$. IPTG was added at time point 0 (black triangle). TEM micrographs of formaldehyde-fixed cells were utilized to determine the number of magnetite particles per cell (box plots) and average magnetite particle diameter (white boxes) at certain time points. (Aii): Western blot with immune-detection against MamB after SDS-PAGE with whole cell samples from experiment (i) taken at certain time points. The cell density of the samples was normalized based on OD_{565} . (Aiii): Examples of TEM micrographs of formaldehyde-fixed cells obtained at different time points of experiment (i). Black arrows indicate the positions of single or multiple magnetite crystals (tiny particles after one hour of induction might stem from background). (B): Details of x-y slices from cryo-electron tomograms acquired with $MamB_{ind}$ cells, plunge-frozen at a various time points after induction with 2 mM IPTG in a separate experiment. (i) and (ii): Details from two cells 2 hours post induction. (iii-v): Details from one cell 3 hours post induction. (v-viii): Details from two cells 4 hours post induction. Putative DMMs are indicated by black arrows, the magnetosome filament by white arrows. Scale bars: 100 nm.

(C): 24 hours time-lapse live-cell fluorescent microscopy of induced $MamB$ -EGFP_{ind} strain. Cells were grown at 30°C on sealed 1% agarose pads containing modified FSM medium and 3 mM IPTG. Fluorescence and corresponding bright field images from various indicated time points after induction are shown. White arrowheads indicate accumulation of fluorescent patches at midcell, while white arrows indicate linear fluorescence signals within cells. Scale bar: 2 μ m

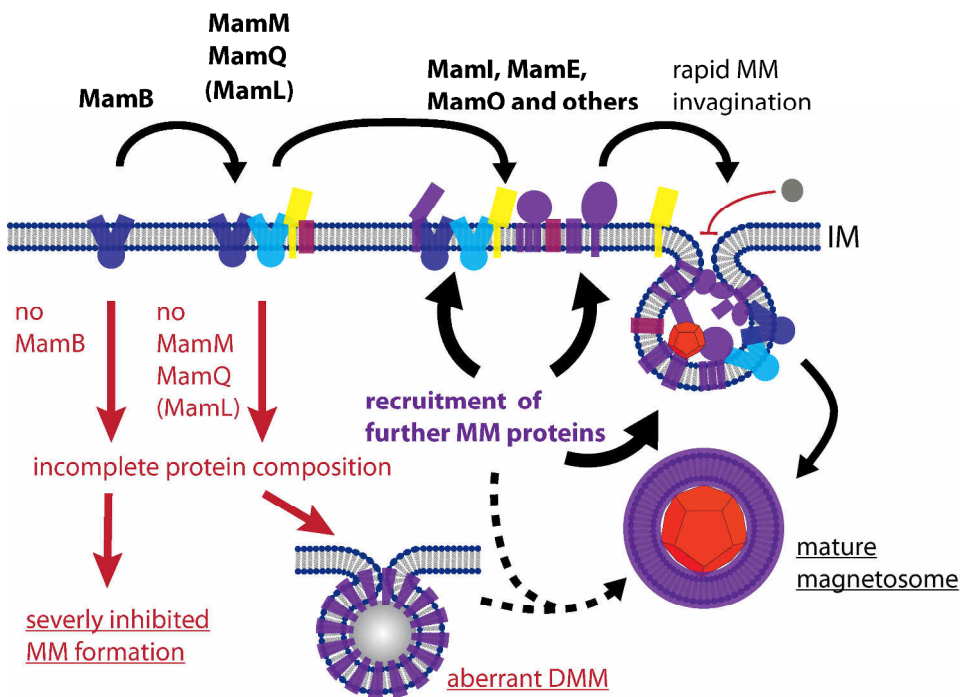


Fig 7. Hypothetical model for magnetosome membrane formation.

The model suggests that magnetosome membrane proteins (colorful shapes) are recruited to certain sites of the cytoplasmic membrane in a hierarchical manner, with the key proteins MamB, MamM, MamQ and MamL (labeled in shades of blue, yellow and red) acting as nucleating factors, which is followed by recruitment of MamI, MamE, MamO and other magnetosome proteins. Since MamB was found most important for magnetosome membrane (MM) formation, it might act as the initial landmark protein to prime complex formation at certain sites within the cytoplasmic membrane. After a critical size and composition of the multi-protein assembly is reached, the formed lipid-protein complex induces rapid invagination to form the magnetosome lumen. Diffusion from the periplasm into this lumen is blocked. Later, several further magnetosome proteins might become recruited into the MM, which eventually becomes detached to form magnetosome vesicles. The absence of MamB strongly inhibits MM formation, while the absence of either MamM, MamQ or MamL might cause a disturbed protein composition, which leads to the formation of aberrant dense magnetosome membrane-like structures (DMMs) that lack magnetite crystals or blocks magnetosome formation at an immature state.

Experimental procedures

Bacterial strains, plasmids, culture conditions and C_{mag} measurement

Bacterial strains and plasmids used in this study are listed in **S2 Table** and **S3 Table**. *E. coli* strains were cultivated in lysogeny broth (LB) medium. When necessary, kanamycin (km) was added to 25 $\mu\text{g mL}^{-1}$. *E. coli* BW29427 and WM3064 cultures were supported with 1 mM DL- α,ϵ -diaminopimelic acid (DAP). Media were solidified by addition of 1.5% (w/v) agar. Unless otherwise stated, *M. gryphiswaldense* cultures were grown at 30°C under microoxic conditions (1% O₂) in modified flask standard medium (FSM) [45]. When appropriate, km was added to 5 $\mu\text{g mL}^{-1}$. Optical density (OD) and magnetic response (C_{mag}) of exponentially growing cultures were measured photometrically at 565 nm as described previously [46]. Conjugation of plasmids were performed essentially as described earlier [47,48]. For Tn7 transposon containing plasmids, a triparental mating conjugation was applied using *E. coli* WM3064 strains harboring the respective plasmid and pT18mob2PmamDC-TnsADas helper plasmid for transposase expression. In-frame markerless chromosomal gene fusions were created as earlier described [49].

Molecular and genetic techniques

Oligonucleotides (**S4 Table**) were purchased from Sigma-Aldrich. Plasmids (**S3 Table**) were constructed by standard recombinant techniques using enzymes from Life Technologies and Agilent Technologies (see **S1 Supplemental experimental procedures**) and confirmed by sequencing. Sequencing was accomplished using BigDye terminator v3.1 chemistry on an ABI 3700 capillary sequencer (Applied Biosystems).

Induction experiments

Strains for *mamL*, *mamB* and *mamB-GFP* induction were created by site-specific, Tn7 transposon-mediated chromosomal integration of P_{lac} controlled genes from plasmids pOR118, pOR160 and pOR169, respectively (see **S1 Supplemental experimental procedures**). For gene induction experiments, MSR-1 strains were passaged in sealed 1% oxygen gas-flushed 500 mL or 1L bottles with 100-300 mL FSM medium containing 8 mM NaNO₃. A 30°C overnight culture was inoculated into a fresh bottle with starting OD₅₆₅ of 0.02 to 0.05 ($t = -2$ h) and cultivated under mild shaking at 30°C. 2 h after inoculation, gene expression was induced by addition

of 2 mM IPTG ($t = 0$). 2 mL samples were taken at certain time points and immediately fixed with formaldehyde for TEM analysis and OD_{565} and C_{mag} determination. For protein expression analysis, 10 mL culture samples were immediately pelleted at 4°C and stored on ice. Samples were resuspended in ice-cold Tris-HCl buffer (pH 7.4) to a final OD_{565} of 10 and frozen at -20°C. SDS-PAGE and Western blot were performed as previously described [8]. Prior to SDS-PAGE, samples were supplemented with electrophoresis sample buffer and incubated at 60°C for 10 minutes. For cryo-electron tomography preparations, a separate induction experiment was analogously conducted and cell samples were plunge frozen on Quantifoil holey carbon molybdenum grids as previously described [50]. Less than 10 minutes passed in between sampling and plunge-freezing.

Fluorescence microscopy and time lapse microscopy experiments

For epi-fluorescence microscopy, 3 μ l samples of *M. gryphiswaldense* over-night cultures were immobilized on 1% (w/v) agarose pads with FSM medium salts. The samples were imaged with an Olympus BX81 microscope equipped with a 100 \times UPLSAPO100XO 1.4NA objective and an Orca-ER camera (Hamamatsu) and appropriate filter sets using Olympus Xcellence software. Alternatively, a DeltaVision Elite microscope (GE Healthcare), equipped with InsightSSI Illumination System, 100 \times Super-Plan-Apo 1.4NA objective, and a CoolSnap HQ2 CCD camera was used. Here, image acquisition was performed with SoftWoRx Suite 2.0. All samples were recorded in Z-stacks with 300-1000 ms exposure time per image. Images were processed with ImageJ 1.48s (<http://imagej.nih.gov/ij/>) using Fiji package (<http://fiji.sc/>).

For time lapse microscopy with $\Delta mamB$ P_{lac} *mamB-egfp*, an exponential growing culture was induced with 2 mM IPTG. A 3 μ l sample was immobilized on 1% (w/v) agarose pads containing all FSM medium components, but reduced peptone (1 g/L) and increased NaNO₃ (8 mM) concentrations and additional 3 mM IPTG. The pad was overlaid with a coverslip and sealed with hot liquid paraffin under constant 1% O₂/99% N₂ gas stream. The sample was transferred to 30°C preheated DeltaVision Elite microscope and imaged for 24 hours in 15 minute intervals (bright field and GFP fluorescence with 500 ms 32% exposure power using 475/28 nm excitation and 525/50 nm emission filter). Imaging started approximately 15 min post induction (this time point is referred as 0). Focus was maintained using implemented laser-

based hardware autofocus. Lateral shifts were corrected with ImageJ 1.48s, using StackReg plugin of Fiji package (<http://bigwww.epfl.ch/thevenaz/stackreg/>).

Transmission electron microscopy

For conventional TEM analysis, unstained and formaldehyde-fixed (0.075% w/v) cells were absorbed on carbon coated copper grids. Bright field TEM was performed on a FEI CM200 transmission electron microscope using an accelerating voltage of 160 kV. Images were captured with an Eagle 4k CCD camera using EMMenu 4.0 (Tietz). For data analysis and measurements, the software ImageJ 1.48s was used.

Cryo-electron tomography, tomogram reconstruction and analysis

Sample preparation and data acquisition were essentially performed as previously described [50]. A 300 kV FEI Tecnai F30 Polara, equipped with Gatan Post-Column Energy Filter and either 2 x 2 k Multiscan CCD Camera (Gatan) or 3838 x 3710 Direct Detector Device (DDD) K2 summit (Gatan) operated in counting and dose-fractionation mode was used for imaging. Images were recorded at nominal -5 μm to -8 μm defocus. The object pixel size was either 0.81, 0.71 (CCD) or 0.52 nm (DDD). Prior to microscopy, samples were plunge-frozen on holey carbon molybdenum grids. Increased blotting times often caused slight flattening of the cells.

Three-dimensional reconstructions from tilt series were performed with the weighted back-projection method using the TOM toolbox [51], creating 2-times binned volumes. For alignment purposes prior to reconstruction, automated fiducial tracking was frequently performed using eTomo (IMOD 4.7) [52].

Vesicle diameters were measured with ImageJ 1.48s. Segmentation of tomograms was performed using Amira software version 5.6.0 (FEI). Cell membranes were beforehand automatically segmented using TomoSegMemTV [53].

Further experimental procedures are found in **S1 Supplemental experimental procedures**

Acknowledgement

We thank Günter Pfeifer and Emanuel Katzmann for support with CET.

Experimental work was supported by Daniel Richter, Yihe Xu, Simrika Thapa, Verena Henn, Anna Lohße and Yingjie Li. Marc Bramkamp and Natalie Zeytuni are acknowledged for their helpful discussion.

References

1. Diekmann Y, Pereira-Leal JB. Evolution of intracellular compartmentalization. *Biochem J*. 2013;449: 319–331. doi:10.1042/BJ20120957
2. Stolz JF. Bacterial Intracellular Membranes. *Encycl Life Sci*. 2007; doi:10.1002/9780470015902.a0000303.pub2
3. Balkwill DL, Maratea D, Blakemore RP. Ultrastructure of a magnetotactic spirillum. *J Bacteriol*. 1980;141: 1399–1408.
4. Gorby YA, Beveridge TJ, Blakemore RP. Characterization of the bacterial magnetosome membrane. *J Bacteriol*. 1988;170: 834–41.
5. Scheffel A, Gruska M, Faivre D, Linaroudis A, Graumann PL, Plitzko JM, et al. An acidic protein aligns magnetosomes along a filamentous structure in magnetotactic bacteria. *Nature*. 2006;440: 110–4. doi:10.1038/nature04382
6. Komeili A, Li Z, Newman DK, Jensen GJ. Magnetosomes are cell membrane invaginations organized by the actin-like protein MamK. *Science*. 2006;311: 242–245. doi:10.1126/science.1123231
7. Greene SE, Komeili A. Biogenesis and subcellular organization of the magnetosome organelles of magnetotactic bacteria. *Curr Opin Cell Biol*. 2012;24: 490–495. doi:10.1016/j.ceb.2012.05.008
8. Uebe R, Junge K, Henn V, Poxleitner G, Katzmann E, Plitzko JM, et al. The cation diffusion facilitator proteins MamB and MamM of *Magnetospirillum gryphiswaldense* have distinct and complex functions, and are involved in magnetite biomineralization and magnetosome membrane assembly. *Mol Microbiol*. 2011;84: 818–835. doi:10.1111/j.1365-2958.2011.07863.x
9. Grünberg K, Müller E-C, Otto A, Reszka R, Linder D, Kube M, et al. Biochemical and Proteomic Analysis of the Magnetosome Membrane in *Magnetospirillum gryphiswaldense*. *Appl Environ Microbiol*. 2004;70: 1040–1050. doi:10.1128/AEM.70.2.1040-1050.2004
10. Grünberg K, Wawer C, Tebo BM, Schüler D. A Large Gene Cluster Encoding Several Magnetosome Proteins Is Conserved in Different Species of Magnetotactic Bacteria. *Appl Environ Microbiol*. 2001;67: 4573–4582. doi:10.1128/AEM.67.10.4573-4582.2001
11. Ullrich S, Kube M, Schübbe S, Reinhardt R, Schüler D. A Hypervariable 130-Kilobase Genomic Region of *Magnetospirillum gryphiswaldense* Comprises a Magnetosome Island Which Undergoes Frequent Rearrangements during Stationary Growth. *J Bacteriol*. 2005;187: 7176–7184. doi:10.1128/JB.187.21.7176

12. Richter M, Kube M, Bazylinski DA, Lombardot T, Glöckner FO, Reinhardt R, et al. Comparative genome analysis of four magnetotactic bacteria reveals a complex set of group-specific genes implicated in magnetosome biomineralization and function. *J Bacteriol.* 2007;189: 4899–910. doi:10.1128/JB.00119-07
13. Lefèvre CT, Wu L-F. Evolution of the bacterial organelle responsible for magnetotaxis. *Trends Microbiol.* 2013; 1–10. doi:10.1016/j.tim.2013.07.005
14. Schüler D. Molecular analysis of a subcellular compartment: The magnetosome membrane in *Magnetospirillum gryphiswaldense*. *Arch Microbiol.* 2004;181: 1–7. doi:10.1007/s00203-003-0631-7
15. Lohße A, Borg S, Raschdorf O, Kolinko I, Tompa É, Pósfai M, et al. Genetic dissection of the mamAB and mms6 operons reveals a gene set essential for magnetosome biogenesis in *magnetospirillum gryphiswaldense*. *J Bacteriol.* 2014;196: 2658–2669. doi:10.1128/JB.01716-14
16. Quinlan A, Murat D, Vali H, Komeili A. The HtrA/DegP family protease MamE is a bifunctional protein with roles in magnetosome protein localization and magnetite biomineralization. *Mol Microbiol.* 2011;80: 1075–1087. doi:10.1111/j.1365-2958.2011.07631.x
17. Yang W, Li R, Peng T, Zhang Y, Jiang W, Li Y, et al. mamO and mamE genes are essential for magnetosome crystal biomineralization in *Magnetospirillum gryphiswaldense* MSR-1. *Res Microbiol.* 2010;161: 701–5. doi:10.1016/j.resmic.2010.07.002
18. Murat D, Quinlan A, Vali H, Komeili A. Comprehensive genetic dissection of the magnetosome gene island reveals the step-wise assembly of a prokaryotic organelle. *Proc Natl Acad Sci U S A.* 2010;107: 5593–5598. doi:10.1073/pnas.0914439107
19. Lower BH, Bazylinski DA. The bacterial magnetosome: a unique prokaryotic organelle. *J Mol Microbiol Biotechnol.* 2013;23: 63–80. doi:10.1159/000346543
20. Katzmann E, Eibauer M, Lin W, Pan Y, Plitzko JM, Schüler D. Analysis of magnetosome chains in magnetotactic bacteria by magnetic measurements and automated image analysis of electron micrographs. *Appl Environ Microbiol.* 2013;79: 7755–62. doi:10.1128/AEM.02143-13
21. Ormö M, Cubitt AB, Kallio K, Gross LA, Tsien RY, Remington SJ. Crystal structure of the *Aequorea victoria* green fluorescent protein. *Science.* 1996;273: 1392–1395. doi:10.1126/science.273.5280.1392

22. Murat D, Byrne M, Komeili A. Cell biology of prokaryotic organelles. *Cold Spring Harb Perspect Biol.* 2010;2: a000422. doi:10.1101/cshperspect.a000422
23. Draper O, Byrne ME, Li Z, Keyhani S, Barrozo JC, Jensen G, et al. MamK, a bacterial actin, forms dynamic filaments in vivo that are regulated by the acidic proteins MamJ and LimJ. *Mol Microbiol.* 2011;82: 342–354. doi:10.1111/j.1365-2958.2011.07815.x
24. Schübbe S, Kube M, Scheffel A, Wawer C, Heyen U, Meyerdierks A, et al. Characterization of a Spontaneous Nonmagnetic Mutant of *Magnetospirillum gryphiswaldense* Reveals a Large Deletion Comprising a Putative Magnetosome Island. *J Bacteriol.* 2003;185: 5779–5790. doi:10.1128/JB.185.19.5779-5790.2003
25. Muxworthy AR, Williams W. Critical superparamagnetic/single-domain grain sizes in interacting magnetite particles: implications for magnetosome crystals. *J R Soc Interface.* 2009;6: 1207–1212. doi:10.1098/rsif.2008.0462
26. Komeili A. Molecular Mechanisms of Compartmentalization and Biomineralization in Magnetotactic Bacteria. *FEMS Microbiol Rev.* 2012;36: 232–255. doi:10.1111/j.1574-6976.2011.00315.x
27. Tanaka M, Arakaki A, Matsunaga T. Identification and functional characterization of liposome tubulation protein from magnetotactic bacteria. *Mol Microbiol.* 2010;76: 480–8. doi:10.1111/j.1365-2958.2010.07117.x
28. Lefèvre CT, Trubitsyn D, Abreu F, Kolinko S, Jogler C, de Almeida LGP, et al. Comparative Genomic Analysis of Magnetotactic Bacteria from the Deltaproteobacteria Provides New Insights into Magnetite and Greigite Magnetosome Genes Required for Magnetotaxis. *Environ Microbiol.* 2013;15: 2712–2735. doi:10.1111/1462-2920.12128
29. Lohße A, Ullrich S, Katzmann E, Borg S, Wanner G, Richter M, et al. Functional Analysis of the Magnetosome Island in *Magnetospirillum gryphiswaldense*: The mamAB Operon Is Sufficient for Magnetite Biomineralization. Battista JR, editor. *PLoS One.* 2011;6: e25561. doi:10.1371/journal.pone.0025561
30. Murat D, Falahati V, Bertinetti L, Csencsits R, Körnig A, Downing K, et al. The magnetosome membrane protein, MmsF, is a major regulator of magnetite biomineralization in *Magnetospirillum magneticum* AMB-1. *Mol Microbiol.* 2012;85: 684–699. doi:10.1111/j.1365-2958.2012.08132.x
31. Katzmann E, Scheffel A, Gruska M, Plitzko JM, Schüler D. Loss of the actin-like protein MamK has pleiotropic effects on magnetosome formation and chain assembly in *Magnetospirillum gryphiswaldense*. *Mol Microbiol.* 2010;77: 208–224. doi:10.1111/j.1365-2958.2010.07202.x

32. Katzmann E, Müller FD, Lang C, Messerer M, Winklhofer M, Plitzko JM, et al. Magnetosome chains are recruited to cellular division sites and split by asymmetric septation. *Mol Microbiol.* 2011;82: 1316–1329. doi:10.1111/j.1365-2958.2011.07874.x
33. Abreu F, Sousa AA, Aronova MA, Kim Y, Cox D, Leapman RD, et al. Cryo-electron tomography of the magnetotactic vibrio *Magnetovibrio blakemorei*: Insights into the biomineralization of prismatic magnetosomes. *J Struct Biol.* 2013;181: 162–168. doi:10.1016/j.jsb.2012.12.002
34. Cornejo E, Subramanian P, Li Z, Jensen GJ. Dynamic Remodeling of the Magnetosome Membrane Is Triggered by the Initiation of Biomineralization. 2016;7: 1–9. doi:10.1128/mBio.01898-15.Editor
35. Nudelman H, Zarivach R. Structure prediction of magnetosome-associated proteins. *Front Microbiol.* 2014;5: 1–17. doi:10.3389/fmicb.2014.00009
36. Qian P, Bullough PA, Hunter CN. Three-dimensional reconstruction of a membrane-bending complex: the RC-LH1-PufX core dimer of *Rhodobacter sphaeroides*. *J Biol Chem.* 2008;283: 14002–11. doi:10.1074/jbc.M800625200
37. Hsin J, Gumbart J, Trabuco LG, Villa E, Qian P, Hunter CN, et al. Protein-induced membrane curvature investigated through molecular dynamics flexible fitting. *Biophys J.* 2009;97: 321–9. doi:10.1016/j.bpj.2009.04.031
38. Arechaga I, Miroux B, Karrasch S, Huijbregts R, De Kruijff B, Runswick MJ, et al. Characterisation of new intracellular membranes in *Escherichia coli* accompanying large scale over-production of the b subunit of F1F₀ ATP synthase. *FEBS Lett.* 2000;482: 215–219. doi:10.1016/S0014-5793(00)02054-8
39. Eriksson HM, Wessman P, Ge C, Edwards K, Wieslander A. Massive formation of intracellular membrane vesicles in *Escherichia coli* by a monotopic membrane-bound lipid glycosyltransferase. *J Biol Chem.* 2009;284: 33904–14. doi:10.1074/jbc.M109.021618
40. McMahon HT, Gallop JL. Membrane curvature and mechanisms of dynamic cell membrane remodelling. *Nature.* 2005;438: 590–596. doi:10.1038/nature04396
41. Kirchhausen T. Bending membranes. *Nat Cell Biol.* 2012;14: 906–908.
42. Ariotti N, Rae J, Leneva N, Ferguson C, Loo D, Okano S, et al. Molecular Characterization of Caveolin-Induced Membrane Curvature. *J Biol Chem.* 2015; 1–26. doi:10.1074/jbc.M115.644336
43. Zimmerberg J, Kozlov MM. How proteins produce cellular membrane curvature. *Nat Rev Mol Cell Biol.* 2006;7: 9–19. doi:10.1038/nrm1784

44. Chen AH, Silver PA. Designing biological compartmentalization. *Trends Cell Biol.* 2012;22: 662–670. doi:10.1016/j.tcb.2012.07.002
45. Heyen U, Schüler D. Growth and magnetosome formation by microaerophilic *Magnetospirillum* strains in an oxygen-controlled fermentor. *Appl Microbiol Biotechnol.* 2003;61: 536–44. doi:10.1007/s00253-002-1219-x
46. Schüler D, Uhl R, Bäuerlein E. A simple light scattering method to assay magnetism in *Magnetospirillum gryphiswaldense*. *FEMS Microbiol Lett.* 1995;132: 139–145. doi:10.1016/0378-1097(95)00300-T
47. Schultheiss D, Schüler D. Development of a genetic system for *Magnetospirillum gryphiswaldense*. *Arch Microbiol.* 2003;179: 89–94. doi:10.1007/s00203-002-0498-z
48. Ullrich S, Schüler D. Cre-lox-based method for generation of large deletions within the genomic magnetosome island of *Magnetospirillum gryphiswaldense*. *Appl Environ Microbiol.* 2010;76: 2439–44. doi:10.1128/AEM.02805-09
49. Raschdorf O, Plitzko JM, Schüler D, Müller FD. A tailored galK counterselection system for efficient markerless gene deletion and chromosomal tagging in *Magnetospirillum gryphiswaldense*. *Appl Environ Microbiol.* 2014;80: 4323–4330. doi:10.1128/AEM.00588-14
50. Raschdorf O, Müller FD, Pósfai M, Plitzko JM, Schüler D. The magnetosome proteins MamX, MamZ, and MamH are involved in redox control of magnetite biomineralization in *Magnetospirillum gryphiswaldense*. *Mol Microbiol.* 2013;89: 872–886. doi:10.1111/mmi.12317
51. Nickell S, Förster F, Linaroudis A, Net W Del, Beck F, Hegerl R, et al. TOM software toolbox: acquisition and analysis for electron tomography. *J Struct Biol.* 2005;149: 227–34. doi:10.1016/j.jsb.2004.10.006
52. Kremer JR, Mastronarde DN, McIntosh JR. Computer visualization of three-dimensional image data using IMOD. *J Struct Biol.* 1996;116: 71–6. doi:10.1006/jsbi.1996.0013
53. Martinez-Sanchez A, Garcia I, Asano S, Lucic V, Fernandez J-J. Robust membrane detection based on tensor voting for electron tomography. *J Struct Biol.* 2014;186: 49–61. doi:10.1016/j.jsb.2014.02.015

Manuscript C: Supplementary Information

Genetic and ultrastructural analysis reveals the key players and initial steps of bacterial magnetosome membrane biogenesis

S1 Text. Amino acid substitutions within MamL

MamL contains nine basic and potentially positively charged (including histidine) amino acid residues close to or at its very C-terminus. The C-terminal accumulation of basic residues is a conserved feature in MamL and MamL-like homologs from other MTB (S4 Fig). In order to analyze if these residues play a role for protein localization or magnetite biomineralization, we expressed a MamL-EGFP fusion in $\Delta mamL$ and also substituted the positively charged residues in MamL-EGFP to six different combinations to structurally similar but neutral amino acids [(a) K77Q R78Q; (b) K72Q; (c) K63Q K66Q K68Q; (d) H67Y; (e) R64Q R65Q; (f) all nine point mutations combined (MamL_{all neutral})]. Complementation with wild type MamL-EGFP rescued 62% and 66% of wild type magnetosome number and diameter respectively, while expression of MamL_{all neutral}-EGFP did not enhance particle formation at 30°C and thus phenocopied the $\Delta mamL$ mutant. All other point mutants caused a slight or intermediate decrease in magnetite crystal number and size as compared to the *mamL-egfp* control (Fig 4B). MamL-EGFP localized in (short) linear fluorescent signals in 50% of the analyzed cells, indicating an at least partial magnetosome localization of the fusion protein (Fig 4B). In the single amino acid substituted MamL-GFP strains, also 25% to 42% of the cells showed a linear localization pattern (Fig 4B). While not restoring biomineralization, MamL_{all neutral}-GFP surprisingly localized in a chain-like pattern in 48% of the cells as well (Fig 4B), suggesting that the positively charged C-terminal residues are not involved in MM-tubulation or -interaction but rather participate in a function related to magnetite maturation.

S2 Text. Amino acid substitutions within MamQ

MamQ shows homology to the widespread, but so far non-characterized LemA protein family of which another homolog (63% similarity, LemA_{MSR} [MGR_0326 or MGMSRv2_3349]) is encoded outside the MAI of MSR-1. We deleted *lemA_{MSR-1}* and could not find an aberrant magnetosome phenotype, indicating that the gene is irrelevant for magnetosome formation. LemA from *Thermotoga maritima* is the only homolog of MamQ (46% similarity) with an experimentally determined crystal structure. The soluble part of the protein (PDB ID 2ETD) shows a 4-helix bundle which is attached to a predicted transmembrane helix. LemA_{MSR}/LemA_{T.maritima} and MamQ_{MSR} differ mainly in their N-terminal regions and a MamQ specific stretch

within the predicted helix bundles (S5 Fig). Based on the crystal structure of LemA_{T.maritima}, we obtain a structural MamQ_{MSR} model and identified several conserved residues [E111; E179, Y181, Y241, F242] shared by all analyzed MamQ and LemA homologs and which are putatively exposed on the surface in loop regions of the helix bundle or on a flexible C-terminal region (S5 Fig and S6 Fig). To analyze their role for the *in vivo* function of the protein, we substituted the mentioned residues by allelic replacement in 5 different combinations to neutral amino acids [1: Y241A F242A; 2: E179A; 3: Y181A; 4: E111A; 5: E179A Y181A E111A] in *mamQ::egfp-mamQ*. Expression of the mutated *egfp-mamQ* versions was indicated by a weak fluorescence signal in patches along the cytoplasmic membrane (S6 Fig). However, none of the mutants showed a restoration of regular magnetosome formation as analyzed by a C_{mag} of 0 and no detectable magnetite crystals by conventional TEM, in contrast to an almost wild type-like C_{mag} (1.75) of the non-mutated *egfp-mamQ* complementation strain. These results indicate the importance of these putatively surface-exposed conserved residues for the function of MamQ.

Supplementary tables and figures

S1 Table: Summary of phenotypes obtained by analyzing cryo-electron tomography data of different MSR-1 mutant cells. MM: magnetosome membrane, DMM: dense magnetosome membrane-like structure

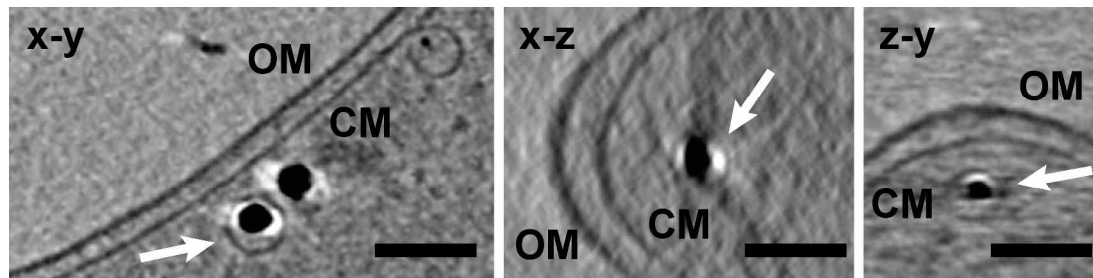
Strain	Total # of analyzed cells	# cells with chain of wild type-like MMs	# cells with dense chains of DMMs	# cells with single vesicular structures (DMMs or wild type-like)	# cells without vesicles
<i>ΔmamI</i>	6	4			2
<i>ΔmamN</i>	5	4			1
<i>ΔmamL</i>	18	5*		8	5
<i>ΔmamQ</i>	16		7**	5***	4
<i>ΔmamB</i>	18			5****	13
<i>ΔmamM</i>	16		6**	7***	3

* putative DMMs occasionally seen

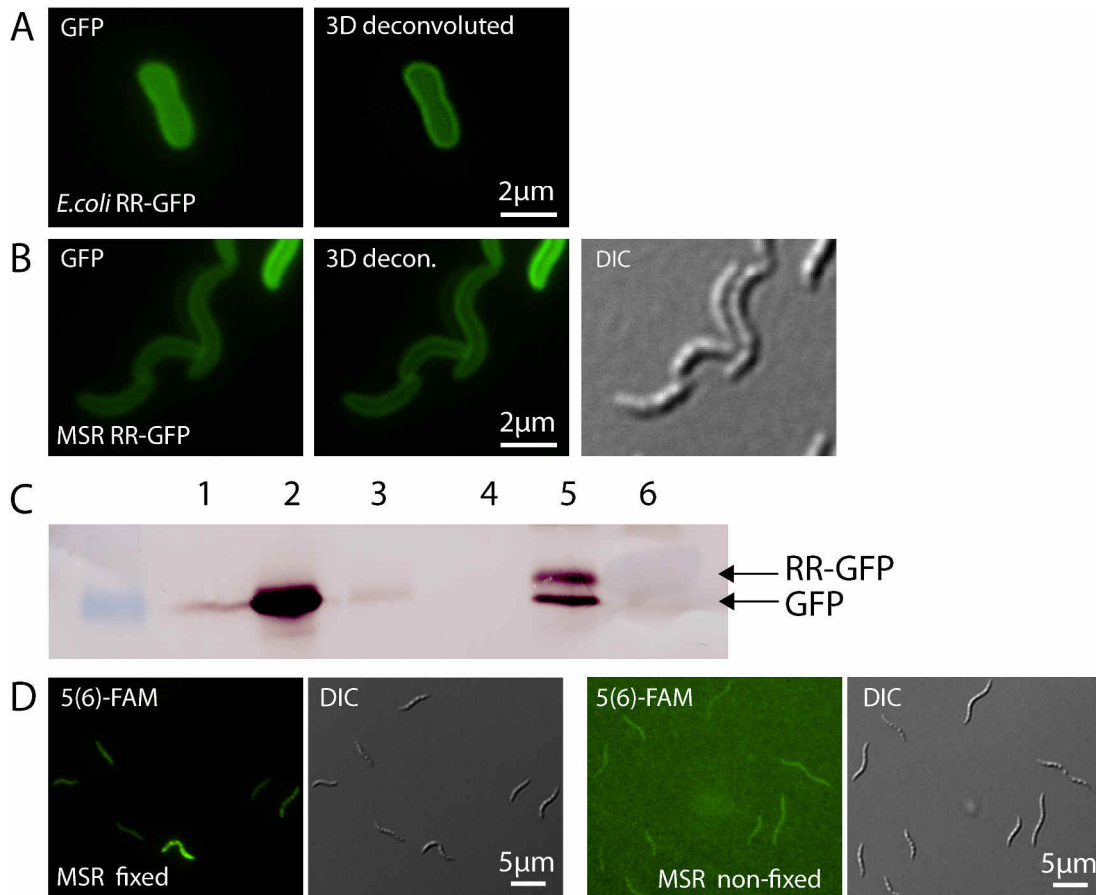
** wildtype-like MMs occasionally seen

*** DMMs predominant

**** putative DMMs only

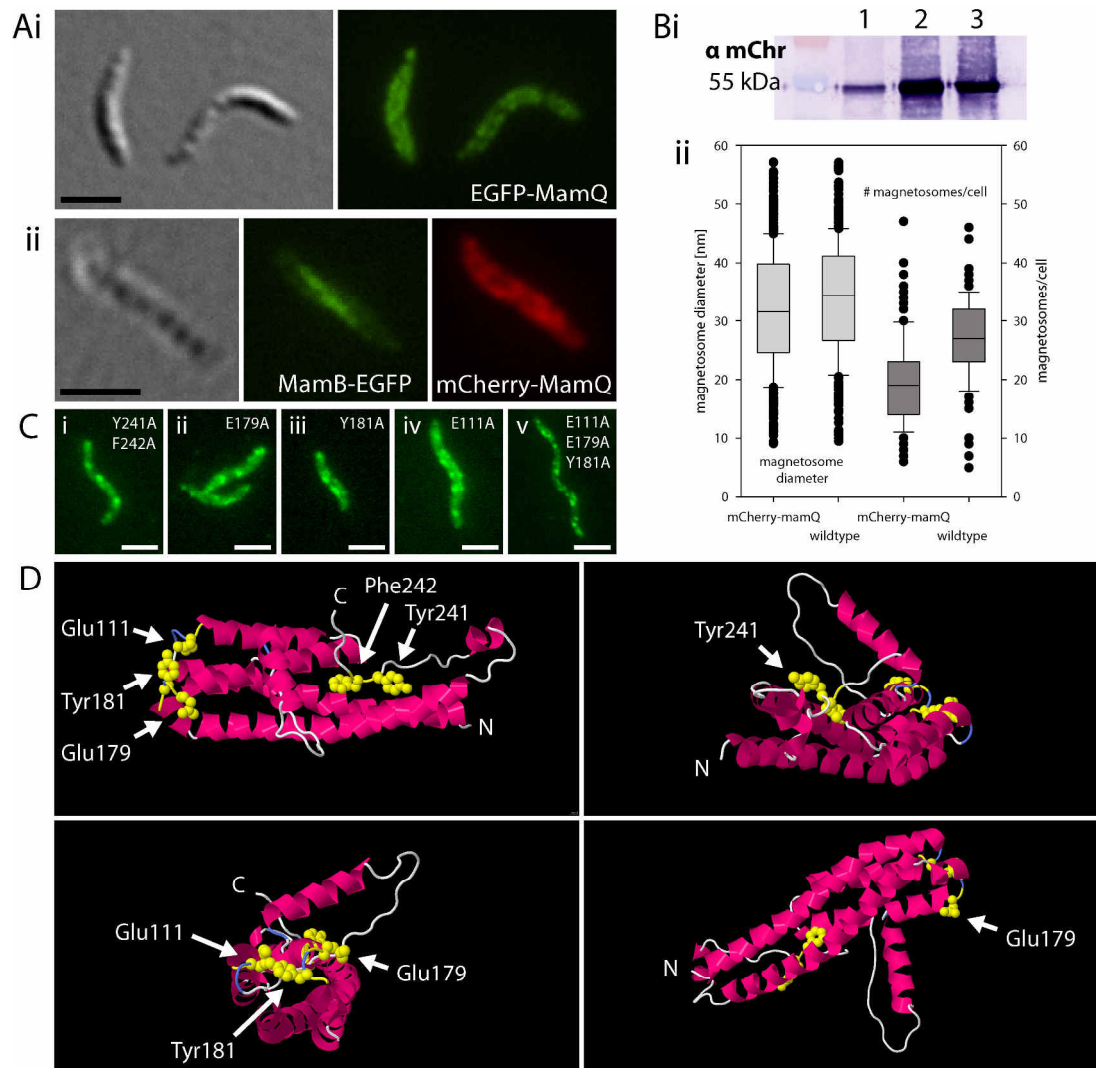


S1 Figure: Visualization of a magnetosome membrane vesicle clearly detached from the cytoplasmic membrane. Image slices (x-y; x-z; z-y) from cryo-electron tomogram of MSR-1 wildtype. The same magnetite-containing magnetosome membrane vesicle is indicated in all three image slices by white arrows. The vesicle resides within some distance and is clearly disconnected from the cytoplasmic membrane (CM). Outer membrane (OM) is indicated. Scale bar: 100 nm.



S2 Figure. Periplasmic GFP and 5(6) Carboxyfluorescein do not become entrapped in magnetosome membrane compartments.

The Twin Arginine Translocation (TAT) signal peptide (RR) of MSR-1 protein MGR0500 was fused to EGFP and the construct expressed in *E. coli* strain BW29427 and MSR-1. Fluorescent micrographs show that the modified EGFP was efficiently translocated into the periplasmic space of (A) *E. coli* and (B) MSR-1. No linear signal was detected within MSR-1, indicating lack of diffusion and entrapment of the protein in the MM. Left: green channel, middle: 3D-deconvoluted representation, right (in B): DIC channel. (C): Western blot with purified and protein concentration normalized fractions from MSR expressing EGFP (lanes 1-3) or RR-EGFP (lanes 4-6). MM protein fraction (lane 1 and 4), total soluble protein fraction (lane 2 and 5) and total cellular membrane protein fraction (lane 3 and 6). Immunodetection was performed with GFP Antibody. Arrows indicate a putative signal for GFP and RR-GFP. The RR-signal cleavage after translocation of the protein to the periplasm can be observed in the blot. (D): Assay to determine 5(6) Carboxyfluorescein (FAM)-diffusion into MM. MSR-1 was cultivated over-night in FSM medium supplemented with 1 mM 5(6) FAM. Cells were either 3x washed in 1 volume of PBS or previously chemically fixed by addition of 0.075% formaldehyde and 5 mg/mL BSA for 15 min before washing. Left micrographs shows fixed cells that are fluorescent, indicating enclosure of 5(6) FAM, right micrograph shows unfixed cells that are non-fluorescent



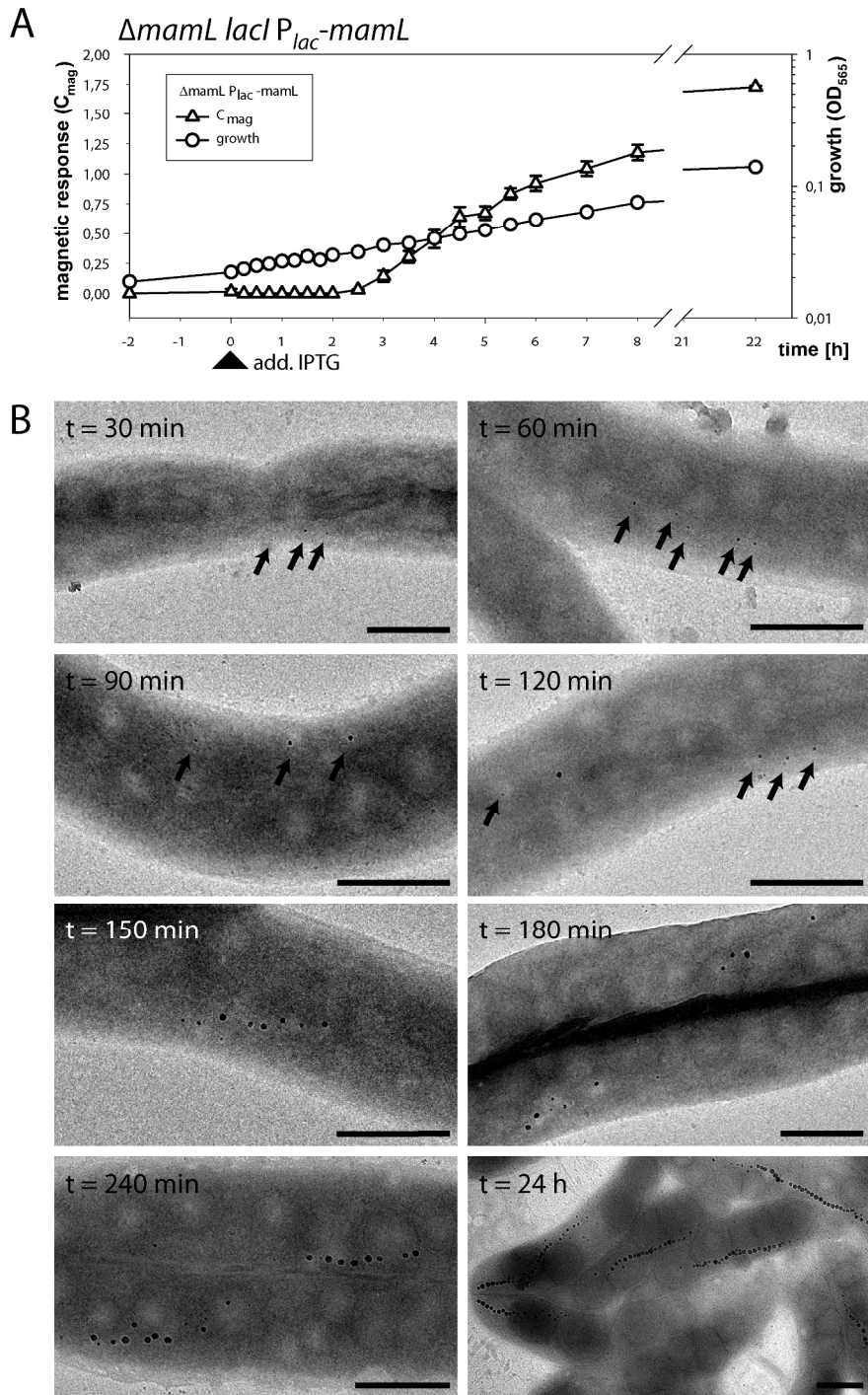
S6 Figure. Predicted structure of MamQ and localization of fluorescently labeled protein

(A): Representative fluorescence micrographs of MSR-1 cells (Ai): overexpressing $P_{mamDC45}$ -*mamQ*-*egfp* and (Aii): expressing chromosomal in-frame allelic replacements of *mamB*::*mamB*-GFP and *mamQ*::*mCherry*-*mamQ*. From left to right: DIC channel, green fluorescent channel, red fluorescent channel. Scale bars: 2 μ m

(Bi): Western blot with separated and concentration-normalized fractions obtained from *mamQ*::*mCherry*-*mamQ* cell lysate. Total soluble protein fraction (lane 1), total non-magnetic membrane protein fraction (lane 2) and magnetosome membrane protein fraction (lane 3). Primary immuno-detection was performed with mCherry antibody.

(Bii): Statistical analysis of magnetosome diameter (left) and magnetosome number (right) of *mamQ*::*mCherry*-*mamQ* and wild type. Box plots are indicating 10th and 90th percentiles (whiskers), 25th and 75th percentiles (box), median and outliers. Over 500 magnetosomes and 100 cells were analyzed, each. (C): Fluorescence micrographs of non-magnetic MSR-1 cells expressing in-frame chromosomal replacements of (i) *mamQ*::*egfp*-*mamQ*_{Y241A F242A}, (ii) *mamQ*::*egfp*-*mamQ*_{E179A}, (iii) *mamQ*::*egfp*-*mamQ*_{Y181A}, (iv) *mamQ*::*egfp*-*mamQ*_{E111A} and (v) *mamQ*::*egfp*-*mamQ*_{E111A E179A Y181A}. Scale bars: 2 μ m. (vi) shows x-y slice from cryo-electron tomogram of *mamQ*::*egfp*-*mamQ*_{E179A} containing putative magnetosome membrane vesicle with enclosed tiny magnetite crystal.

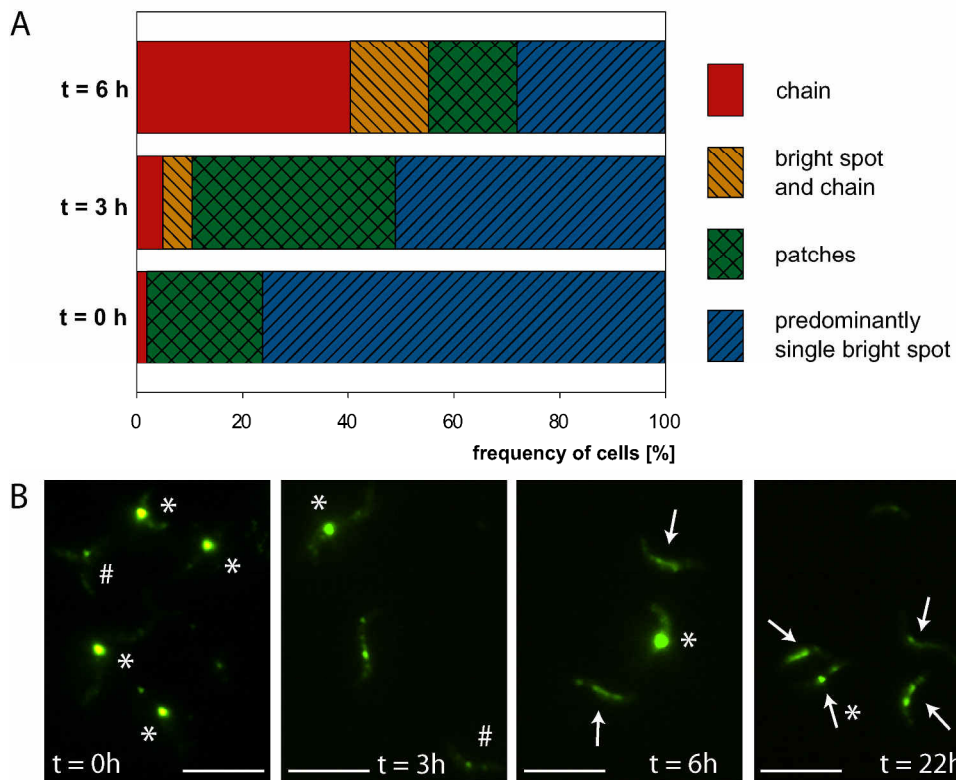
(D): Different views on the model of MamQ_{MSR-1} tertiary structure. The protein structure of the soluble part of MamQ (using amino acids 70 – 246) was modelled with SWISS-MODEL and the experimentally determined 2.28 Å resolved crystal structure of LemA_{*T.maritima*} [PDB ID 2ETD] as template (GMQE = 0.30, QMEAN = -6.80). Only the backbone of the structure is visualized. Putative alpha-helical regions are depicted in purple, the side chains of the mutated amino acids in this study are depicted in yellow, represented in stick and ball model and indicated by an arrow if visible in the view. They are either localized in predicted loop or flexible regions. If visible, also the N and C-termini of the modeled protein structure are indicated. The predicted trans-membrane domain of MamQ continues at the indicated N-terminus.



S7 Figure. Induction of *mamL* expression increases magnetosome size and C_{mag} to wild type-like levels. Induction of *mamL* expression in $\Delta mamL$ P_{lac} $-mamL$. In the absence of the inducer IPTG, the strain failed to exhibit a magnetic response ($C_{mag} = 0$) when cultivated at 30°C. Upon addition of IPTG, a gradual restoration of C_{mag} and magnetosome size and number was detected and wild type-like levels were reached after over-night incubation.

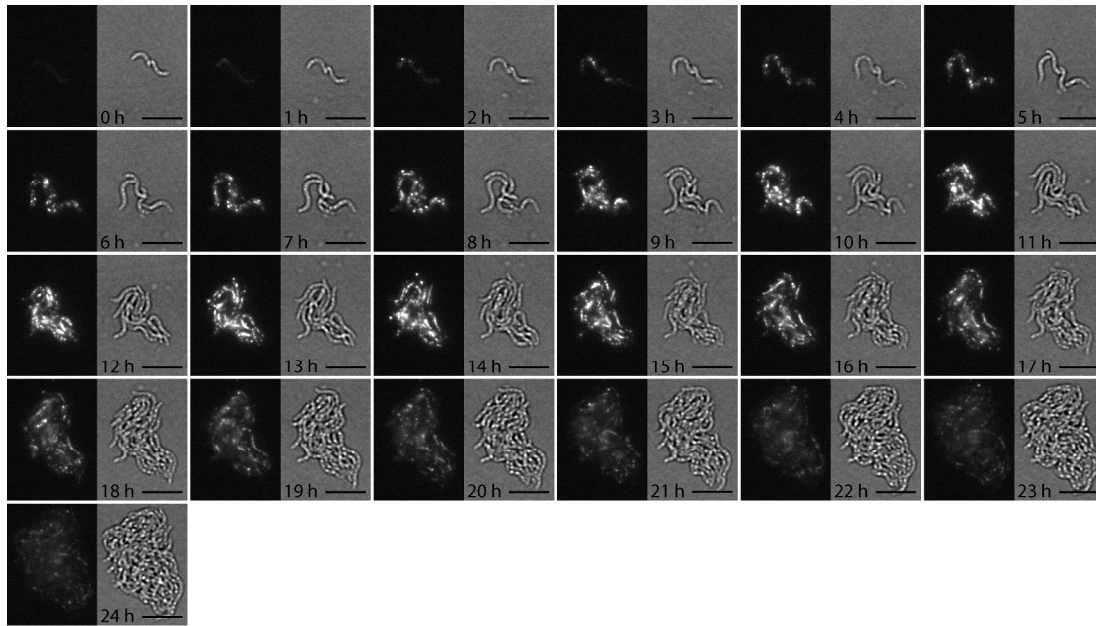
(A): Progression of growth (OD_{565} , circles) and magnetic response (C_{mag} , triangles) over time after induction of *mamL* expression with 2mM IPTG in $\Delta mamL$ P_{lac} $-mamL$. IPTG was added at time point 0 (black triangle).

(B) TEM micrographs showing magnetite crystal morphology in cell from experiment (A) at several distinct time points after induction of gene expression. Arrows indicate the positions of tiny magnetite crystals, while bigger crystals are not labeled. Scale bars: 500 nm



S8 Figure. Effects on MamC-EGFP localization after induction of *mamL* expression.

The magnetosome marker protein MamC-EGFP was constitutively co-expressed (in-frame allelic replacement) during induction of *mamL* expression in $\Delta mamL mamC-egfp P_{lac}-mamL$. The localization gradually developed from a bright punctuate to a predominant linear signal in the first six hours after start of induction. Samples were taken 0, 3, 6 and 22 hours after 2mM IPTG induction. (A): Statistical analysis of MamC-EGFP localization 0, 3 and 6 hours after induction. Fluorescent signals in around 200 cells were analyzed for each time point and classified into different localization patterns which are exemplified in representative micrographs of different time points in (B): Single bright spots (asterisk), bright spot and chain (asterisk + arrow), patches (hash) and chains (arrow). Scale bar: 5 μ m



S9 Figure. Time-lapse live-cell fluorescent microscopy of $\Delta mamB P_{lac-mamB-egfp}$.

More detailed representation of Figure 6C. The strain was induced with 2 mM IPTG, transferred to 1% agarose pads containing modified FSM medium and 3 mM IPTG, sealed and incubated at 30°C. Images were acquired every 15 min. The depicted micrographs were acquired in 1 h intervals. Bright field and fluorescence channels are shown. Scale bar: 2 μ m

S1 Video. Cryo-electron tomogram of MSR-1 wildtype cell. Tilt images were obtained with direct detector camera, original image pixel size: 0.52 nm

S2 Video. Cryo-electron tomogram of MSR-1 wildtype cell cultivated under non-standard conditions with vigorous shaking at atmospheric oxygen concentrations. Tilt images were obtained with CCD camera, original image pixel size: 0.81 nm. Partially segmented (outer and inner membranes: blue, magnetosome membrane: yellow, iron mineral particles: red)

S3 Video. Cryo-electron tomogram of $\Delta mamI$ cell. Tilt images were obtained with CCD camera, original image pixel size: 0.81 nm. Partially segmented (outer and inner membranes: blue, magnetosome filament: green, magnetosome membrane: yellow, iron mineral particles: red)

S4 Video. Cryo-electron tomogram of $\Delta mamN$ cell. Tilt images were obtained with CCD camera, original image pixel size: 0.81 nm. Partially segmented (outer and inner membranes: blue, magnetosome filament: green, magnetosome membrane: yellow, magnetite crystals: red)

S5 Video. Cryo-electron tomogram of $\Delta mamL$ cell. Tilt images were obtained with direct detector camera, original image pixel size: 0.52 nm. Partially segmented (outer and inner membranes: blue, magnetosome filament: green, magnetosome membrane: yellow, dense magnetosome membrane-like structures: dark yellow, magnetite crystals: red)

S6 Video. Cryo-electron tomogram of MSR-1 $\Delta mamB$ cell. Tilt images were obtained with CCD camera, original image pixel size: 0.71 nm. Partially segmented (outer and inner membranes: blue, magnetosome filament: green, potential dense magnetosome membrane-like structures: dark yellow)

S7 Video. Cryo-electron tomogram of $\Delta mamQ$ cell. Tilt images were obtained with direct detector camera, original image pixel size: 0.52 nm. Partially segmented (outer and inner membranes: blue, magnetosome filament: green, magnetosome membrane: yellow, dense magnetosome membrane-like structures: dark yellow)

S8 Video. Cryo-electron tomogram of MSR-1 $\Delta mamM$ cell. Tilt images were obtained with CCD camera, original image pixel size: 0.71 nm. Partially segmented (outer and inner membranes: blue, magnetosome filament: green, magnetosome membrane: yellow, dense magnetosome membrane-like structures: dark yellow)

S9 Video. Time-lapse live-cell fluorescent microscopy with several cells of $\Delta mamB P_{lac}-mamB-egfp$. The strain was induced with 2 mM IPTG, transferred to 1% agarose pads containing modified FSM medium and 3 mM IPTG, sealed and incubated at 30°C. Frames were acquired in 15 min intervals. Fluorescence channel is shown.

S10 Video. Time-lapse live-cell fluorescent microscopy of $\Delta mamB P_{lac}-mamB-egfp$ (detail of S9 Video, source of Fig 6 and S9 Fig). Fluorescence channel is shown.

S1 Supplementary experimental procedures

Plasmid construction

Plasmids for fluorescent magnetosome protein fusions

By integrating oligonucleotides oOR164 and 165, coding for a stable 25 aa alpha-helical linker region [LA(EAAAK)₄AAA] (HL) [1], upstream or downstream of MSR-1-optimized *egfp* [2] into the pBBR1MCS2 derivative pOR071, we developed a platform for N- or C- terminal EGFP fusions under control of the strong $P_{mamDC45}$ promoter. The genes *mamI* (C-terminal fusion, primers: oOR155 and 170), *mamL* (C-terminal fusion; neutrally point mutated to remove internal *NdeI* restriction site, primers: oOR157 and 171) and *mamQ* (N-terminal fusion; neutrally point mutated to remove internal *NdeI* restriction site, primers: oOR180 and 181) were amplified from genomic MSR-1 DNA and cloned into this platform to create plasmids pOR075, pOR077 and pOR086. For stable genomic integrations, we additionally cloned the P_{mamDC} *egfp*-HL-*mamQ* and P_{mamDC} *mamL*-HL-*egfp* expression cassettes in between the Tn5 ends of pBAM-1 by restriction digestion to create pOR150 and pOR151. By subcloning of P_{mamDC} *mamL*-HL-*egfp* and PCR-based site directed PCR mutagenesis before re-integration into pOR151, we created pBAM-based plasmids pOR163-167 for point mutation analysis. For construction of pOR168, harboring P_{mamDC} *mamL*_[all neutral]-HL-*egfp*, the point mutated *mamL* gene was fully synthesized (ATG:biosynthetics GmbH, Germany) and cloned into pOR151.

The plasmids for genomic in-frame integration of *egfp-mamQ* were created by amplifying and fusing DNA fragments upstream of *mamQ*, and *egfp*-HL-*mamQ* (primers: oOR264-267) and by cloning them into pORFM galK [3] to create pYF001. An analogous procedure was used to create pORFM B-GFP. Point mutations in *egfp*-HL-*mamQ* in plasmids pYF003-007 were introduced by subcloning and site directed PCR mutagenesis (primers: oOR296-305). By overlap extension PCR cloning [4] from pYF001, *egfp* in *egfp*-HL-*mamQ* was replaced by *mCherry* to create pYF002 (primers: oOR278 and 279).

Integrative plasmids for expression of artificial mam operons

Plasmids for the expression of *mamLQRB* (pOR140) and *mamLMQRB* (pOR155) were constructed by amplification of *mamL* from pOR077 using primer pair

oOR171/359 and amplification of *mamQRB* from genomic MSR-1 DNA using primer pair oOR360/361, followed by fusion and cloning of both fragments into a pBAM-1 derived vector. The P_{mamDC} promoter in the plasmid was exchanged by P_{mamAB} , (oligonucleotides oOR357/358) creating pOR140. *mamLM* was amplified using oOR171/375 and cloned into pOR140 to replace *mamL*, creating pOR155. For generation of a minimal magnetosome gene cluster, two artificially arranged operons were designed and synthesized (ATG:biosynthetics GmbH). The two building blocks comprised the genes (i) *mamL*, *mamB*, *mamQ* and (ii) *mamI*, *mamE*, *mamM*, *mamO*. Both operons were put under transcriptional control of the *mamAB* promoter (P_{mamAB}). Artificial Shine Dalgarno sequences with free accessibility on the messenger RNA were designed according to different computational models [5-7]. The coding sequences were not further optimized except for removal of disruptive endonuclease restriction sites. To allow the future complete de-assembly, recovery as well as recycling of all genes, individual coding sequences were each separated by an ABM (AscI-BssHII-MauBI) restriction site. The artificial expression cassettes were cloned in between the Tn5 ends of pBAM-1 to create pBAM_minMAI.

Integrative plasmids for induction of magnetosome gene expression

The following system was designed for the induction of single magnetosome gene expression in the respective gene-deletion background strain. To ensure reliably inducible, but tightly controlled expression, we used the *lac* promoter - *lacI* repressor system, which was shown to be functional in MSR-1 [8,9] and combined it with a chromosomally integrative vector. To avoid potential undesired expression upon random genomic insertion, we utilized the site-specific Tn7 transposon system [10], which integrated specifically and reliably into a genomic region around the *glmS* gene in MSR-1. The MSR-adapted Tn7 transposable pre-plasmid for magnetosome protein induction (pT18-Tn7T-Km) was created as following: A minimized pT18mob2 vector backbone was amplified using primers pT18mob2+Tet_for_NotI and pT18mob2_rev_NcoI, digested and ligated with a mini-Tn7 fragment that was amplified from plasmid pUC18R6K-mini-Tn7T-Km using primers Tn7Km_for and Tn7Km_rev. The MSR-adapted transposase-encoding helper plasmid pT18mob2PmamDC-TnsAD was obtained by digestion of the transposase (TnsA) containing fragment from pTns2 and cloning into pT18mob2 vector. A P_{mamDC} -TnsA fragment was created by two-step fusion-PCR using primer pairs TnsA for/rev and

PmamDCrev/PmamDC96 and subsequently cloned into the vector to replace P_{lac} -TnsA. Plasmids for induction of *mamL*, *mamB* and *mamB-egfp* expression were constructed by first amplifying the genes, using primer pairs oOR171/282, oOR386/387 for *mamL* and *mamB*, respectively and cloning them into pFM211 [8]. *mamB* and HL-*egfp* were amplified using primer pairs oOR420/421 and oOR422/423 and fused in a two-step PCR. The created plasmids were named pOR117, pOR158 and pOR169. The constructs, containing P_{lac} -*mamL/mamB/mamB-GFP* and *lacI* were cloned in between the Tn7 ends Tn7L and Tn7R in pT18-Tn7T-Km to create pOR118, pOR160 and pOR171, respectively. Plasmid transfer into MSR-1 was mediated by triparental mating.

Cell fractionation, SDS-gel electrophoresis and immunological detection

Cellular fractionation of MSR-1 and magnetosome purification were performed essentially as previously described using a magnetized separation column [11,12]. SDS-PAGE was performed as previously described [12]. Protein concentrations were determined using BCA-Protein Micro assay (Pierce) and normalized fraction samples (approx. 2 μ g protein) were supplemented with electrophoresis buffer and heated to 95°C for 5 min. These samples or whole cell samples from the induction experiment, respectively, were subjected to 12% polyacrylamide gels. For western blot analysis, proteins were electro-blotted on PVDF membranes. Immunological protein detection was performed as described [12]. In this study, Anti-MamB [12] and Anti-RFP [5F8] (ChromoTek GmbH, Martinsried, Germany) were used as primary antibodies.

Periplasmic diffusion experiments

In search for a suitable export signal for the twin-arginine translocon, we examined the genomes of *Escherichia coli* and MSR-1 for suitable candidates. We found TorA from *E. coli* and NapA and the Ni,Fe-hydrogenase I small subunit MGR_0500 from MSR-1 as suitable candidates. Extend of the export signals (RR) was analyzed by the TatP prediction server (<http://www.cbs.dtu.dk/services/TatP/>). We amplified the respective DNA sequences from genomic DNA and fused them with *egfp*. Expressed from pBBR plasmids and the P_{lac}/P_{mamDC} promoter, all RR-GFP versions were partially transported into the periplasmic space of *E. coli* and MSR-1. Highest fluorescence in the periplasmic space of MSR-1 was obtained with the RR-signal from MGR_0500, which was utilized for final fluorescence microscopy and western-

blot experiments. The utilized plasmid pOR082 was created by cloning RR (MGR0500)-*egfp* (Fusion PCR using primer oOR113/134 and oOR130/146) into pOR071. For experiments with 5(6) Carboxyfluorescein (FAM), MSR-1 wild type cells were incubated overnight with FSM medium containing 1 mM (5)6 FAM. The cells showed normal growth. Cell were harvested by centrifugation and either 3x washed in 1 volume of PBS or previously chemically fixed by addition of 0.075% formaldehyde and 5 mg/mL BSA for 15 min before washing in order to entrap the molecule within the cells (control). Cells were prepared on agarose slices for fluorescence microscopy.

Bioinformatic tools

The protein structure of MamQ was modelled with SWISS-MODEL [13] using amino acids 70-246 on Template 2ETD (PDB ID) and displayed with Jmol 3.7 (<http://www.jmol.org/>). Proteins were analyzed using SMART [14] and the NCBI database (<http://www.ncbi.nlm.nih.gov/>). Sequence alignments were performed with clustalΩ (<http://www.ebi.ac.uk/Tools/msa/clustalo/>).

S2 Table: Bacterial strains used in this study

Strains and plasmids	Description	Source
MSR strains		
MSR-1 R3/S1	wildtype and mother strain of deletion mutants	[15]
$\Delta mamAB$	Cre/lox deletion	[16]
1B	Spontaneous partial MAI deletion mutant, including deletion of <i>mamAB</i> , <i>mms6</i> , and <i>mamGFDC</i> operons (non-magnetic)	[17]
$\Delta mamI$	Markerless in-frame deletion	[18]
$\Delta mamN$	Markerless in-frame deletion	[18]
$\Delta mamQ$	Markerless in-frame deletion	[18]
$\Delta mamL$	Markerless in-frame deletion	[18]
$\Delta mamB$	Cre/lox deletion	[12]
$\Delta mamM$	Cre/lox deletion	[12]
$\Delta mamL$ P _{lac-mamL} , <i>lacI</i> (MamL _{ind})	Tn7 transposon integrated (pOR118)	this study
$\Delta mamB$ P _{lac-mamB} , <i>lacI</i> (MamB _{ind})	Tn7 transposon integrated (pOR158)	this study
$\Delta mamB$ P _{lac-mamB-egfp} , <i>lacI</i> (MamB-EGFP _{ind})	Tn7 transposon integrated (pOR169)	this study
<i>mamQ::mCherry:mamQ</i>	Allelic replacement (pYF002)	this study
<i>mamQ::egfp-mamQ</i>	Allelic replacement (pYF001)	this study
<i>mamQ::egfp-mamQ</i> _[Y242A F242A]	Allelic replacement (pYF003)	this study
<i>mamQ::egfp-mamQ</i> _[E179A]	Allelic replacement (pYF004)	this study
<i>mamQ::egfp-mamQ</i> _[Y181A]	Allelic replacement (pYF005)	this study
<i>mamQ::egfp-mamQ</i> _[E111A]	Allelic replacement (pYF006)	this study
<i>mamQ::egfp-mamQ</i> _[E179A Y181A E111A]	Allelic replacement (pYF007)	this study
$\Delta mamQ$ P _{mamDC-egfp-mamQ}	Tn5 transposon integrated	this study
<i>mamQ::mCherry-mamQ</i> <i>mamB::mamB:egfp</i>	Allelic replacements (pORFM B-GFP, pYF002)	this study
$\Delta mamL$ P _{mamDC-mamL-egfp}	Tn5 transposon integrated (pOR151)	this study
$\Delta mamL$ P _{mamDC-mamL} _{[K77Q R78Q]-egfp}	Tn5 transposon integrated (pOR163)	this study
$\Delta mamL$ P _{mamDC-mamL} _{[K72Q]-egfp}	Tn5 transposon integrated (pOR164)	this study
$\Delta mamL$ P _{mamDC-mamL} _{[K63Q]-egfp}	Tn5 transposon integrated (pOR165)	this study
$\Delta mamL$ P _{mamDC-mamL} _{[K63Q K66Q K68Q]-egfp}	Tn5 transposon integrated (pOR166)	this study
$\Delta mamL$ P _{mamDC-mamL} _{[R64Q R65Q]-egfp}	Tn5 transposon integrated (pOR167)	this study
$\Delta mamL$ P _{mamDC-mamL} _{[all neutral]-egfp}	Tn5 transposon integrated (pOR168)	this study
$\Delta mamAB$ P _{mamAB-mamLQRB}	Tn5 transposon integrated (pOR140)	this study
1B P _{mamAB-mamLQRB}	Tn5 transposon integrated (pOR140)	this study
1B P _{mamAB-mamLMQRB}	Tn5 transposon integrated (pOR155)	this study

$\Delta mamL$ P _{mamAB-mamLMQRB}	Tn5 transposon integrated (pOR155)	this study
$\Delta mamQ$ P _{mamAB-mamLMQRB}	Tn5 transposon integrated (pOR155)	this study
$\Delta mamB$ P _{mamAB-mamLMQRB}	Tn5 transposon integrated (pOR155)	this study
$\Delta mamM$ P _{mamAB-mamLMQRB}	Tn5 transposon integrated (pOR155)	this study
$\Delta mamAB$ P _{mamAB-mamLQB-} P _{mamAB-mamIEMO}	Tn5 transposon integrated (pBAM_minMAI)	this study
1B P _{mamAB-mamLQB-} P _{mamAB-mamIEMO}	Tn5 transposon integrated (pBAM_minMAI)	this study
$\Delta mamQ$ P _{mamAB-mamLQB-} P _{mamAB-mamIEMO}	Tn5 transposon integrated (pBAM_minMAI)	this study
$\Delta mamM$ P _{mamAB-mamLQB-} P _{mamAB-mamIEMO}	Tn5 transposon integrated (pBAM_minMAI)	this study
<i>E. coli</i> strains		this study
BW29427	<i>thrB1004 pro thi rpsL hsdS</i> <i>lacZDM15 RP4-</i> <i>1360D(araBAD)567DdapA</i>	Datsenko & Wanner, unpublished
DH5a	<i>1341::[erm pir(WT)]trahsdR17</i> <i>recA1-endA1gyrA96thi-1relA1</i>	Invitrogen
S17-1 λ pir	RPA-2, Tc::Mu-Km::Tn7 (λ pir)	[19]
WM3064	<i>thrB1004 pro thi rpsL hsdS</i> <i>lacZDM15 RP4-1360D(araBAD)</i> <i>567DdapA::[erm pir]</i>	W. Metcalf, unpublished

S3 Table: Plasmids used in this study

Plasmids	Notable features / Description	Source
pJet1.2	Ap ^r , <i>eco47IR</i> , <i>rep</i> (pMB-1)	Life Technologies
pBAM1	<i>oriR6K</i> , Km ^r , Ap ^r , <i>tnpA</i> , Tn5 transposition platform	[20]
pBBR1MCS2	Mobilizable broad-host-range vector, Km ^r	[21]
pT18mob2	Mobilizable broad-host-range vector, Tet ^r	[22]
pUC18R6K-mini-Tn7T-Km	Mini-Tn7 transposable plasmid, Km ^r	[23]
pTns2	helper plasmid for Tn7 transposase expression, Tet ^r	[23]
pT18-Tn7T-Km	MSR adapted plasmid with mini-Tn7 transposition platform, Km ^r	this study
pT18mob2PmamDC-TnsAD	MSR adapted helper plasmid for Tn7 transposase expression, Tet ^r	this study
pORFM GalK	Vector for genomic in-frame modifications, Km ^r	[3]
pORFM blu	Vector for genomic in-frame modifications, Km ^r	[3]
pFM211	pBBR1 P _{lac} - <i>ftsZm-mCherry</i> , <i>egfp-mamK</i> , <i>lacI</i> , Km ^r	[8]
pOR071	pBBR1 P _{mamDC} - <i>egfp</i> , Km ^r	[24]
pOR075	pBBR1 P _{mamDC} - <i>mamI-egfp</i> , Km ^r	this study
pOR077	pBBR1 P _{mamDC} - <i>mamL-egfp</i> , Km ^r	this study
pOR082	pBBR1 P _{mamDC} -RR(mgr_0500)- <i>egfp</i>	this study
pOR086	pBBR1 P _{mamDC} - <i>egfp-mamQ</i> , Km ^r	this study
pOR117	pBBR1 P _{lac} - <i>mamL</i> , <i>lacI</i> , Km ^r	this study
pOR118	pT18-Tn7T-Km P _{lac} - <i>mamL</i> , <i>lacI</i> , Km ^r	this study
pOR140	pBAM P _{mamAB} - <i>mamLQRB</i> , Km ^r	this study
pOR150	pBAM P _{mamDC} - <i>egfp-mamQ</i> , Km ^r	this study
pOR151	pBAM P _{mamDC} - <i>mamL-egfp</i> , Km ^r	this study
pOR155	pBAM P _{mamAB} - <i>mamLMQRB</i> , Km ^r	this study
pOR158	pBBR1 P _{lac} - <i>mamB</i> , <i>lacI</i> , Km ^r	this study
pOR160	pT18-Tn7T-Km P _{lac} - <i>mamB</i> , <i>lacI</i> , Km ^r	this study
pOR163	pBAM P _{mamDC} - <i>mamL</i> _[K77Q R78Q] - <i>egfp</i> , Km ^r	this study
pOR164	pBAM P _{mamDC} - <i>mamL</i> _[K72Q] - <i>egfp</i> , Km ^r	this study
pOR165	pBAM P _{mamDC} - <i>mamL</i> _[K63Q K66Q K68Q] - <i>egfp</i> , Km ^r	this study
pOR166	pBAM P _{mamDC} - <i>mamL</i> _[H67Y] - <i>egfp</i> , Km ^r	this study
pOR167	pBAM P _{mamDC} - <i>mamL</i> _[R64Q R65Q] - <i>egfp</i> , Km ^r	this study
pOR168	pBAM P _{mamDC} - <i>mamL</i> _[K63Q R64Q R65Q K66Q H67Y K68Q K72Q K77Q R78Q (all neutral)] - <i>egfp</i> , Km ^r	this study
pOR169	pT18-Tn7T-Km P _{lac} - <i>mamB-egfp</i> , <i>lacI</i> , Km ^r	this study

pYF001	pORFM derivate, for chromosomal <i>eGFP-mamQ</i> in-frame fusion, Km ^r	this study
pYF002	pORFM derivate, for chromosomal <i>mCherry-mamQ</i> in-frame fusion, Km ^r	this study
pYF003	pORFM derivate, for chromosomal <i>eGFP-mamQ</i> _[Y242A F242A] in-frame fusion, Km ^r	this study
pYF004	pORFM derivate, for chromosomal <i>eGFP-mamQ</i> _[E179A] in-frame fusion, Km ^r	this study
pYF005	pORFM derivate, for chromosomal <i>eGFP-mamQ</i> _[Y181A] in-frame fusion, Km ^r	this study
pYF006	pORFM derivate, for chromosomal <i>eGFP-mamQ</i> _[E111A] in-frame fusion, Km ^r	this study
pYF007	pORFM derivate, for chromosomal <i>eGFP-mamQ</i> _[E179A Y181A E111A] in-frame fusion, Km ^r	this study
pORFM B-GFP	pORFM derivate, for chromosomal <i>mamB-GFP</i> in frame-fusion, Km ^r	this study
pA0-mamX-Tn5	Fully synthetic plasmid, P _{mamAB-mamLBQ} P _{mamAB-mamIEMO} , Km ^r	this study
pBAM_minMAI	pBAM P _{mamAB-mamLBQ} P _{mamAB-mamIEMO} , Km ^r	this study

S4 Table: Oligonucleotides used in this study

Identifier	Description/Name	Sequence
oOR113	oegfp_rw	<u>CCATCTCGAGTCACTTATACAGCTCGTCCATGCC</u>
oOR134	oegfp_fw	<u>ATTAGGATCCGTGTCTCGAAGGGCGAGGAAGT</u>
oOR130	MGR0500_TAT_fw	<u>ACTGCATATGTACGACGACAGCGCCG</u>
oOR146	MGR0500_TAT_rev	<u>TCTAGGATCCGATGGCGGGCGGCGATCTG</u>
		<u>TACTCGAGGCTAGCCTGGCCGAAGCCGCGGCCAAGGAGGC</u>
	Oligo for Helix	<u>CGCCGCGAAGGAAGCCGCGGCCAAGGAGGCCGCGCGAA</u>
oOR164	linker_fw	<u>GGCCGCGGCCGTGCACGGTACCTA</u>
		<u>TAGGTACCGTGCACGGCCGCGCCTTCGCGGCGGCCTCCTT</u>
	Oligo for Helix	<u>GGCCGCGGCTTCCTTCGCGGCGGCCTCCTTGGCCGCGGCTT</u>
oOR165	linker_rev	<u>CGGCCAGGCTAGCCTCGAGTA</u>
	oegfp_fw (ApaLI, MfeI)	<u>TACTGTGCACATGGTGTCTCGAAGGGCGAGG</u>
	oegfp_rw (ApaLI, MfeI)	<u>TAGTCAATTGTCACTTATACAGCTCGTCCATGCC</u>
oOR112	o_egfp_fw	<u>TACGCATATGGTGTCTCGAAGGGCGAGG</u>
oOR169	oegfp_wo stop_rev	<u>ATCACTCGAGCTTATACAGCTCGTCCATGCC</u>
oOR170	mamI_fw	<u>GATACATATGCCAAGCGTGATTTTCGG</u>

oOR155	mamI_rev	<u>ATACGCTAGCACCATCGATGTTAGGGTCTGAGTTC</u>
oOR171	mamL_fw	<u>AGCTCATATGGTAAGAGTGATCGGATCGTTGG</u>
oOR157	mamL_rev	<u>TGTGGCTAGCGCGCTTAATGACGATGTTTTTCCC</u>
oOR158	mamL-NdeI fw	<u>CCCGATTTGGGCCACTGATAATGC</u>
oOR159	mamL-NdeI rev	<u>TTTCCACCATGTGGGCGTTGG</u>
oOR181	mamQ_fw	<u>ACTCCATATGGTGCACGCAGTAAGCGATGCGGACG</u>
oOR182	mamQ_rev	<u>ACTCATGCATTACAGCTAGCATTCTTGGATTCTGCGAATGG</u>
oOR199	mamQ-NdeI fw	<u>CCTACAAGCACATGATGACCTCG</u>
oOR200	mamQ-NdeI rev	<u>TATCCGCCGACTGAACGG</u>
oOR264	mamQ-down_fw	<u>TAGAGTCGACCCGATTGCCATCCGGTAGG</u>
oOR265	mamQ-down_rev	<u>CCTCGCCCTTCGACACCATATCCGCCTCGTTGCTATCGTC</u> <u>GACGATAGCAACGAGGCGGATATGGTGTCTGAAGGGCGAG</u>
oOR266	GFP_fw	<u>G</u>
oOR267	mamQ_rev_stopp	<u>ACTCACTAGTTCAATTCTTGGATTCTGCGAATGG</u>
oOR278	mcherry_mamQ_fw (overlap extension)	<u>TGAGATGACGATAGCAACGAGGCGGATATGGTGAGCAAGG</u> <u>GCGAGG</u> <u>CGGCTTCGGCCAGGCTAGCCTCGAGCTTGTACAGCTCGTCC</u>
oOR279	mcherry_mamQ_rev	<u>ATGCC</u>
oOR282	mamL_rev	<u>CTAGCTCGAGTCAGCGCTTAATGACGATGTTTTTCC</u>
oOR283	Plac_Tn7_fw	<u>GACTAAGCTTCGTTGGCCGATTCATTAATGC</u>
oOR284	Plac_Tn7_rev	<u>TAGAGAGCTCGGAACAAAAGCTGGGTACCC</u>
oOR290	mamQ_up_fw	<u>CTGAGTCGACCCACGTGATAAATTAGCCAGAGCC</u>
oOR291	mamQ_up_rev	<u>CATAGCTAGCCCGCCTTTCCGATCAATTCC</u>
oOR296	Q_TyrPhe_AlaAla forw	<u>TGGAGGCTGCCACGAAAAGC</u>
oOR297	Q_TyrPhe_AlaAla rev	<u>CGCGCTTGAACCCGGTG</u>
oOR298	Q_Glu112_Ala fw	<u>CCATTGTCGCGCAGTATCCC</u>
oOR299	Q_Glu112_Ala rev	<u>CCATCAGCCGCCCCAGC</u>
oOR300	Q_Tyr114_Ala fw	<u>CGAGCAGGCTCCCACCG</u>
oOR301	Q_Tyr114_Ala rev	<u>ACAATGGCCATCAGCCGC</u>
oOR302	Q_Glu44_Ala fw	<u>CCGCTTTGGCGCACTCCATC</u>
oOR303	Q_Glu44_Ala rev	<u>CATGATTCAGCGTCAACTTGACC</u>
oOR304	Q_GluTyr_AlaAla fw	<u>CATTGTCGCGCAGGCTCCCACC</u>
oOR305	Q_GluTyr_AlaAla rev	<u>GCCATCAGCCGCCCCAGC</u> <u>CTAGAttatggcttgtaaccgacctcgattcgttgctatagtcctgccaattggagtggaatt</u>
oOR357	PmamAB_fw	<u>gtgacgCA</u>
oOR358	PmamAB_rev	<u>TATGcgtcacaattcacctccaattcgacggactatagcaacgaatcgaggtcggttgacaa</u>

		<u>gccataaT</u>
oOR359	mamL_rev	<u>AGTAGCTAGCTCAGCGCTTAATGACGATGTTTTTCC</u>
oOR360	mamQ_5UTR_fw	<u>AGTAGCTAGCGATGTAGAAGGTCTCATTGAGATGACG</u>
oOR361	mamB_rev	<u>ACTCATGCATTTCAGACCCGGACCGTCACG</u>
oOR375	MamM_rev	<u>AGTAGCTAGCCTAGTTATCCACCTTGGACAGCATGAC</u>
oOR386	mamB_fw	<u>ACTGCATATGAAGTTCGAAAATTGCAGAGACTGC</u>
oOR387	mamB_rev	<u>ATCACTCGAGTCAGACCCGGACCGTCACG</u>
	mamL_K5R5-	
oOR396	QQ_GFP_fw	<u>CATCGTCATTTCAGCAAGCTAGCCTGGC</u>
	mamL_K5R5-	
oOR397b	QQ_rev	<u>TTTTTCCCAGGCAGTTTATGCTTGC</u>
oOR398	mamL_K4-Q_fw	<u>CTGCCTGGGCAGAACATCGTC</u>
oOR399	mamL_K4-Q_rev	<u>TTTATGCTTGCGCCGTTTCATAAC</u>
	mamL_K1K2K3-	
oOR400	QQQ_fw	<u>GCGCCAGCATCAACTGCCTG</u>
	mamL_K1K2K3-	
oOR401	QQQ_rev	<u>CGTTGCATAACATTCGCAAACAC</u>
oOR402	mamL_H3-Y_fw	<u>GGCGCAAGTATAAACTGCCTGG</u>
oOR403	mamL_H3-Y_rev	<u>GTTTCATAACATTCGCAAACACCAAC</u>
oOR404	mamL_R3R4-QQ_fw	<u>ATGTTATGAAACAGCAGAAGCATAAACTGC</u>
	mamL_R3R4-	
oOR405	QQ_rev	<u>TCGCAAACACCAACACAATCC</u>
oOR420	mamB_fw	<u>ACTGCATATGAAGTTCGAAAATTGCAGAGACTG</u>
oOR421	mamB_rev	<u>GCTAGCGACCCGGACCGTCACGG</u>
oOR422	Helix-oegfp_fw	<u>GCTAGCCTGGCCGAAGCC</u>
oOR423	Helix-oegfp_rev	<u>TGCGGTGCGACTCACTTATACAGCTCGTCCATGCC</u>
oOR435	MluI_ins_fw	<u>CTAGACCTAACGCGTAATCGAGCT</u>
oOR436	MluI_ins_rev	<u>CGATTACGCGTTAGGT</u>
	pT18mob2+Tet_for_	<u>CATGGCGGCCGCAGTCATAGTTGCACTTTATCA</u>
	NotI	
	pT18mob2_rev_NcoI	<u>CATCCCATGGCCAGTCGGGAAACCTGTCTGT</u>
	Tn7Km_for	<u>CAGCCGCGTAACCTGGCAAA</u>
	Tn7Km_rev	<u>CAGTGAGCGAGGAAGCGGAA</u>
	TnsA for	<u>ACACTTGCCGGAGATCAGATGGCTAAAGCAAACCTCTT</u>
	TnsA rev	<u>TTAATTTGCCACATAGCG</u>
	PmamDCrev	<u>AAGAGTTTGCTTTAGCATGCTGATCTCCGGCAAGTGTATG</u>
	PmamDC96	<u>CTTTTTCGCTTACTAGCTC</u>
	mamB(wt)_KpnI_for	<u>CGGCGGTACCATGAAGTTCGAAAATTGC</u>
	HL3-oeGFP-	<u>TGACGGTCCGGGTCTGGTGCTAGCCTGGCCGAAGCC</u>
	mamBC-term_for	

HL3-oeGFP- mamBC-term_rev	<u>GAGCTCGGCTTCCATGTCGGCAGA</u>
mamBC- termoeGFP_rev	<u>GCGGCTTCGGCCAGGACCCGGACCGTCACGGC</u>
oeGFP_Bdo_for	<u>agctgtataagtgaTCAGGAGAGGGGAATCATGGAC</u>
oeGFP_Bdo_rev	<u>TTCCCCTCTCCTGATCACTTATACAGCTCGTCC</u>

Supplemental references

1. Arai R, Ueda H, Kitayama A, Kamiya N, Nagamune T. Design of the linkers which effectively separate domains of a bifunctional fusion protein. *Protein Eng.* 2001;14: 529–32.
2. Borg S, Hofmann J, Pollithy A, Lang C, Schüler D. New Vectors for Chromosomal Integration Enable High-Level Constitutive or Inducible Magnetosome Expression of Fusion Proteins in *Magnetospirillum gryphiswaldense*. *Appl Environ Microbiol.* 2014;80: 2609–16. doi:10.1128/AEM.00192-14
3. Raschdorf O, Plitzko JM, Schüler D, Müller FD. A tailored galK counterselection system for efficient markerless gene deletion and chromosomal tagging in *Magnetospirillum gryphiswaldense*. *Appl Environ Microbiol.* 2014;80: 4323–4330. doi:10.1128/AEM.00588-14
4. Bryksin A V, Matsumura I. Overlap extension PCR cloning: a simple and reliable way to create recombinant plasmids. *Biotechniques.* 2010;48: 463–5. doi:10.2144/000113418
5. Salis HM, Mirsky EA, Voigt CA. Automated design of synthetic ribosome binding sites to control protein expression. *Nat Biotechnol.* 2009;27: 946–950. Available: <http://dx.doi.org/10.1038/nbt.1568>
6. Andronescu M, Condon A, Hoos HH, Mathews DH, Murphy KP. Computational approaches for RNA energy parameter estimation. *RNA.* 2010;16: 2304–2318. doi:10.1261/rna.1950510
7. Mathews DH. Using an RNA secondary structure partition function to determine confidence in base pairs predicted by free energy minimization. *RNA. United States;* 2004;10: 1178–1190. doi:10.1261/rna.7650904
8. Müller FD, Raschdorf O, Nudelman H, Messerer M, Katzmann E, Plitzko JM, et al. The FtsZ-Like Protein FtsZm of *Magnetospirillum gryphiswaldense* Likely Interacts with Its Generic Homolog and Is Required for Biomineralization under Nitrate Deprivation. *J Bacteriol.* 2014;196: 650–9. doi:10.1128/JB.00804-13

9. Lang C, Pollithy A, Schüler D. Identification of promoters for efficient gene expression in *Magnetospirillum gryphiswaldense*. *Appl Environ Microbiol.* 2009;75: 4206–10. doi:10.1128/AEM.02906-08
10. Lambertsen L, Sternberg C, Molin S. Mini-Tn7 transposons for site-specific tagging of bacteria with fluorescent proteins. *Environ Microbiol.* 2004;6: 726–732. doi:10.1111/j.1462-2920.2004.00605.x
11. Grünberg K, Müller E-C, Otto A, Reszka R, Linder D, Kube M, et al. Biochemical and Proteomic Analysis of the Magnetosome Membrane in *Magnetospirillum gryphiswaldense*. *Appl Environ Microbiol.* 2004;70: 1040–1050. doi:10.1128/AEM.70.2.1040-1050.2004
12. Uebe R, Junge K, Henn V, Poxleitner G, Katzmann E, Plitzko JM, et al. The cation diffusion facilitator proteins MamB and MamM of *Magnetospirillum gryphiswaldense* have distinct and complex functions, and are involved in magnetite biomineralization and magnetosome membrane assembly. *Mol Microbiol.* 2011;84: 818–835. doi:10.1111/j.1365-2958.2011.07863.x
13. Biasini M, Bienert S, Waterhouse A, Arnold K, Studer G, Schmidt T, et al. SWISS-MODEL: Modelling protein tertiary and quaternary structure using evolutionary information. *Nucleic Acids Res.* 2014;42: 252–258. doi:10.1093/nar/gku340
14. Letunic I, Copley RR, Schmidt S, Ciccarelli FD, Doerks T, Schultz J, et al. SMART 4.0: towards genomic data integration. *Nucleic Acids Res.* 2004;32: D142–4. doi:10.1093/nar/gkh088
15. Schultheiss D, Schüler D. Development of a genetic system for *Magnetospirillum gryphiswaldense*. *Arch Microbiol.* 2003;179: 89–94. doi:10.1007/s00203-002-0498-z
16. Ullrich S, Schüler D. Cre-lox-based method for generation of large deletions within the genomic magnetosome island of *Magnetospirillum gryphiswaldense*. *Appl Environ Microbiol.* 2010;76: 2439–44. doi:10.1128/AEM.02805-09
17. Schübbe S, Kube M, Scheffel A, Wawer C, Heyen U, Meyerdierks A, et al. Characterization of a Spontaneous Nonmagnetic Mutant of *Magnetospirillum gryphiswaldense* Reveals a Large Deletion Comprising a Putative Magnetosome Island. *J Bacteriol.* 2003;185: 5779–5790. doi:10.1128/JB.185.19.5779-5790.2003
18. Lohße A, Borg S, Raschdorf O, Kolinko I, Tompa É, Pósfai M, et al. Genetic dissection of the mamAB and mms6 operons reveals a gene set essential for magnetosome biogenesis in *magnetospirillum gryphiswaldense*. *J Bacteriol.* 2014;196: 2658–2669. doi:10.1128/JB.01716-14

19. Simon R, Priefer U, Pühler A. A Broad Host Range Mobilization System for In Vivo Genetic Engineering: Transposon Mutagenesis in Gram Negative Bacteria. *Nat Biotechnol.* 1983;1: 784–791. doi:10.1038/nbt1183-784
20. Martínez-García E, Calles B, Arévalo-Rodríguez M, de Lorenzo V. pBAM1: an all-synthetic genetic tool for analysis and construction of complex bacterial phenotypes. *BMC Microbiol.* BioMed Central Ltd; 2011;11: 38. doi:10.1186/1471-2180-11-38
21. Kovach ME, Elzer PH, Hill DS, Robertson GT, Farris MA, Roop RM, et al. Four new derivatives of the broad-host-range cloning vector pBBR1MCS, carrying different antibiotic-resistance cassettes. *Gene.* 1995;166: 175–176. doi:10.1016/0378-1119(95)00584-1
22. Kirchner O, Tauch A. Tools for genetic engineering in the amino acid-producing bacterium *Corynebacterium glutamicum*. *J Biotechnol.* Netherlands; 2003;104: 287–299.
23. Choi K-H, Gaynor JB, White KG, Lopez C, Bosio CM, Karkhoff-Schweizer RR, et al. A Tn7-based broad-range bacterial cloning and expression system. *Nat Methods.* 2005;2: 443–448. doi:10.1038/nmeth765
24. Raschdorf O, Müller FD, Pósfai M, Plitzko JM, Schüler D. The magnetosome proteins MamX, MamZ, and MamH are involved in redox control of magnetite biomineralization in *Magnetospirillum gryphiswaldense*. *Mol Microbiol.* 2013;89: 872–886. doi:10.1111/mmi.12317

4.4 Manuscript D:

Semi-quantitative analysis of the integral magnetosome membrane sub-proteome

Oliver Raschdorf¹, Florian Bonn², Natalie Zeytuni³, Raz Zariwach³, Dörte
Becher² and Dirk Schüler^{1,4}

Affiliations:

1: Ludwig Maximilian University Munich, Department of Microbiology

2: Ernst Moritz Arndt University of Greifswald, Department of Microbiology

3: Ben-Gurion University of the Negev, Beer-Sheva, Macromolecular
Crystallography

4: University of Bayreuth, Department of Microbiology

In preparation

Updated version of manuscript, 23 March 2016

Abstract

Magnetosomes are membranous organelles that contain crystals of magnetic minerals and enable magnetotactic bacteria to orientate in magnetic fields. The enveloping magnetosome membrane is highly enriched with a subset of specific proteins that are encoded within a confined genomic island. However, along with proteins that have a determinable influence on magnetosome biosynthesis, proteomic studies repetitively revealed the presence of numerous other and partially highly abundant proteins within the magnetosome fraction, which could not yet clearly be discriminated as contaminants or genuine integral magnetosome membrane proteins.

In order to clearly identify all proteins from the magnetotactic Alphaproteobacterium *Magnetospirillum gryphiswaldense* that are specifically targeted to the magnetosome membrane and to estimate their abundance, we measured, analyzed and compared the protein composition of several cellular fractions by semi-quantitative mass spectrometry. Although spectra from over 1000 proteins were found within the magnetosome fraction, our comparative approach could exclude most of them as contaminants. We found that almost all specifically magnetosome membrane-integral proteins belong to the well-defined subgroup of previously identified magnetosome-associated proteins, indicating that the protein composition of the compartment is strongly controlled. Furthermore, the correlation of our semi-quantitative proteome data with recently published quantitative western blot and cryo-electron tomography results revealed that the magnetosome membrane is tightly packed with transmembrane domains of integral proteins, indicating a very high protein composition of the membrane. Our findings will help to further define the structure of the organelle and contribute to the elucidation of the processes involved in biogenesis of magnetosomes.

Introduction

Magnetotactic bacteria (MTB) are capable of magnetic navigation by means of intracellular, membrane-bounded magnetic crystals, called magnetosomes. These organelles are associated with a cytoskeletal structure, the magnetosome filament, and are arranged into chains along the cellular long-axis. Biochemical analysis of purified magnetosomes of the magnetotactic Alphaproteobacterium *Magnetospirillum gryphiswaldense* (MSR-1) revealed the presence of specific integral or associated magnetosome membrane proteins. Reverse genetic approaches and comparative genomic analysis subsequently led to the detection of the corresponding genes, which were termed *mam* (magnetosome membrane) and *mms* (magnetosome membrane specific) [1-3]. These genes are organized within four operons of a hypervariable genomic magnetosome island (MAI), namely *mamABop* (17 genes), *mamGFDCop* (4 genes), *mms6op* (4 genes) and *mamXYop* (4 genes) [3-5]. Additionally, other single or small-operon encoded genes of the MAI were implicated in magnetosome formation (*mamF2*, *mamD2*, *feoAB1*, *mamW*) [3, R. Uebe, unpublished]. According to the current models, all aspects of magnetosome biogenesis are controlled by the MAI-encoded Mam and Mms proteins [4,6-9]. However, a multitude of other non MAI-encoded proteins was found to co-purify with the magnetosome membrane [2,5,10] and so far it was not clear if these proteins are either functional integral constituents of the native magnetosome membrane, associated soluble proteins or cellular contaminants adsorbed during the isolation process. Although the magnetosome membrane proteome was already compared to other sub-proteomes of the outer/inner membrane and soluble protein fraction in different studies, this issue is not yet resolved [5,8]. Additionally, the relative abundances of the genuine (*bona fide*) magnetosome membrane proteins were so far not elucidated, which prevented the estimation of the protein composition of this organelle.

To reveal the core membrane-integral magnetosome sub-proteome and to estimate the relative abundances of the individual proteins, we executed a comparative, semi-quantitative mass spectrometry analysis with purified magnetosomes and several cellular fractions. Our results indicated that most of the previously found non-MAI encoded proteins within the magnetosome membrane fraction are likely contaminants. We could confirm the highly specific enrichment of several Mam and

Mms proteins, including proteins that were only recently suggested to be involved in magnetosome formation. Furthermore, we found few putative novel *bona fide* magnetosome membrane proteins, of which one (MGR_4114) is encoded within the MAI. Correlation of our semi-quantitative proteomic data with recently published quantitative western blot data allowed us to roughly estimate the absolute copy numbers of *bona fide* magnetosome membrane proteins within the organelle. Using the predicted topology of these proteins, we could further estimate the membrane coverage of integral proteins, which hints towards a very crowded protein organization within the magnetosome membrane. In summary, our data revealed the likely protein composition of the complex magnetosome membrane and will contribute to uncover the processes involved in biogenesis of this sophisticated bacterial organelle.

Experimental Procedures

Cultivation and cell harvesting of *M. gryphiswaldense*, C_{mag} determinations

Bacterial strains and plasmids used in this study are listed in Table S2 and S3. *E. coli* strains were cultivated in lysogeny broth (LB) medium. When necessary, kanamycin (Km) was added to 25 $\mu\text{g mL}^{-1}$. *E. coli* BW29427 and WM3064 cultures were supported with 1 mM DL- α,ϵ -diaminopimelic acid. Media were solidified by addition of 1.5% (w/v) agar. *M. gryphiswaldense* cultures were grown at 30°C in modified flask standard medium (FSM) [11]. When appropriate, Km was added to 5 $\mu\text{g mL}^{-1}$. Optical density (OD) and magnetic response (C_{mag}) of exponentially growing cultures were measured photometrically at 565 nm as described previously [12]. Conjugation of plasmids were performed essentially as described earlier [13,14].

Cellular fractionation and purification

Cultivation and all further fractionation steps were performed in independent triplicates. *M. gryphiswaldense* was cultivated and scaled up to 5 L culture in closed 5 L-Schott bottles (air in headspace) over-night and harvested by centrifugation (10,000 g, 15 min, 4°C). The cell pellets were washed in buffer containing 20 mM HEPES (pH 7.4), 5 mM EDTA and frozen at -20°C. All further steps were carried out at 4°C. The cell pellets obtained from cell harvesting were resuspended in buffer containing 50 mM HEPES (pH 7.4), 1 mM EDTA and complete protease inhibitor (Roche, Germany) and lysed by a high-pressure cell disruption system. Cellular storage PHB granules were removed by centrifugation (210 g, 10 min 4°C) of the lysate. The lysate was applied on MACS cell separation column type CS (Miltenyi Biotec, Germany), magnetized with two neodymium iron boron cube magnets (gravity flow). The flow-through was applied for a second time on column and then collected as **total nonmagnetic lysate (non-mag)**. The fraction bound to the separation column was washed with each 50 mL extraction buffer (10 mM HEPES (pH 7.4), 1 mM EDTA, 0.1 mM PMSF), 2x with salt buffer (10 mM HEPES (pH 7.4), 1 mM EDTA, 200 mM NaCl, 0.1 mM PMSF) and again extraction buffer by gravity flow. The magnets were removed; the magnetic fraction eluted from column with approx. 10 mL H₂O and supplemented to final HEPES (pH 7.4), EDTA and PMSF concentrations of extraction buffer. An ultracentrifugation tube was filled with

60% (w/w) sucrose (in extraction buffer) and overlaid with magnetic fraction. After ultracentrifugation (100,000 g, 1.5 h), pellet was resuspended in 2 mL extraction buffer as **magnetically separated magnetosome fraction (mag)**.

The total nonmagnetic cellular lysate was centrifuged for 1 h at 100,000g and the membrane pellet resuspended (central small white PHB pellet was omitted) and incubated in carbonate buffer (200 mM Na₂CO₃, 10 mM EDTA, 1 mM PMSF, pH 11.0) for 30 min under mild shaking. After centrifugation for 1 h at 100,000 g, the pellet was resuspended in high-salt buffer (20 mM TRIS, 1 M NaCl, 10 mM EDTA, 1 mM PMSF, pH 7.5) and incubated under mild shaking for 30 min. After centrifugation for 1 h at 100,000 g, the pellet was resuspended in 50 mM TEAB (pH 7.8) and immediately pelleted for 1 h at 100,000 g. The pellet formed the total **nonmagnetic membrane fraction (mem)**.

The magnetically separated magnetosomes were centrifuged for 30 min at 100 000 g and the pellet resuspended in carbonate buffer. Subsequent purification was performed as described for the membrane fraction, only 30 min centrifugation runs between washes. The resulting pellet formed the **ultra-purified magnetosome (mag.pur)** fraction (Figure 1).

SDS-PAGE, tryptic digestion and mass spectroscopy analysis

All triplicate fractions were treated independently. For sodium dodecyl sulfate polyacrylamide gel electrophoresis (SDS-PAGE), all liquid samples were supplemented and all pelleted samples were dissolved in/with 2x SDS sample buffer and heated at 60°C for 5 min. Appropriate amounts of samples were determined empirically (Fig S 1). Electrophoresis of the protein samples was performed on 12% polyacrylamide gels. Staining, in gel tryptic digestion and LC-MS/MS was performed according to [15] with minor modifications. In brief, the in-gel digested peptides were separated with an easy nLC 2 (Thermo Fisher Scientific, MA, USA) column and analyzed with an LTQ Orbitrap Velos (Thermo Fisher Scientific). The 20 most intense precursor ions of each full scan were selected for collision induced dissociation fragmentation. A list of all open reading frames (ORFs) from the draft genome sequence of *M. gryphiswaldense* [3], was used as target database, supplemented with entries of recently assigned ORFs. The resulting output files were compiled with Scaffold 4 (Proteome Software, OR, USA). Proteins were only considered as identified if at least two unique peptides, matching solid quality criteria

($\Delta cN > 0.1$ and $XCorr > 2.2$; 3.3; 3.7 for doubly, triply, or higher charged peptides) have been assigned, resulting in a false positive rate below 0.2% on protein level.

Proteinase K membrane shaving

If not otherwise noted, all steps were carried out at 4°C. A 1 mL batch of magnetically separated magnetosomes was centrifuged for 30 min at 100,000 g. The pellet was resuspended in carbonate buffer and incubated for 1 h under mild shaking. Urea was added to final concentration of 8 M. For protein reduction, tris(2-carboxyethyl)phosphine hydrochloride was added to final concentration of 5 mM and sample incubated for 45 min at 60°C. Alkylation was performed by addition of 10 mM iodoacetamide and incubation for 15 min at room temperature in the dark. Proteinase K solution (3 μ L/mL) was added and sample proteolytically digested for 15 h at 37°C under mild shaking. Samples were supplemented with 5% acetonitril, cooled down on ice and centrifuged for 1 h at 100,000 g. Supernatant was removed and pellet overlaid with 50mM TEAB solution before centrifugation for 1 h at 100,000 g. Resulting pellet was frozen at -70°C. Pellet was resuspended in 180 μ L of digestion buffer (50 mM TEAB, pH 7.8, 0.5 % RapiGest (Waters, MA, USA)) and incubated for 30 min at 30°C under mild shaking. 6 μ g of Chymotrypsin and 10 mM $CaCl_2$ were added and solubilized sample digested for 7 h at 30°C with mild shaking. HCl was added to final concentration of 250 mM and sample incubated at 37°C for 45 min to precipitate detergent. Sample was repetitively centrifuged for 12 min at 20,000 g, until no magnetosome and membrane pellet was visible any more. Sample was injected into LC-MS/MS and analyzed as described in [16].

Data analysis

All calculations described in the main text were performed in Microsoft Excel. To develop our working model, we made the following assumptions:

- (1) The **semi-quantitative relative abundance** of a single protein can be estimated by dividing the number of assigned spectra to this protein by the predicted molecular weight (MW) of the protein and the total number of spectra measured from one complete 2D gel lane. This ratio allows a size-independent comparison of protein abundance over several fractions. Semi-quantitative abundance (A_N) of protein N is defined by

$$A_N = \frac{SpC_N}{(\sum_{i=1}^n SpC_i)} \times MW_N$$

whereas

N is the protein index

SpC is the number of unique peptide spectra matching the protein

MW is the molecular weight of the protein

n is the total number of proteins identified in the screen of a single sample

For further calculations, the A_N of all detected proteins was individually calculated for all samples and averaged for the three replicate fractions.

(2) A ***bona fide* integral magnetosome membrane protein** has to fulfill the following conditions:

a. It is a membrane protein. Determined by:

$A_{\text{mem(N)}}/A_{\text{non-mag(N)}} \geq 1$ (the protein is relatively more enriched in the membrane fraction than in the total non-magnetic lysate)

b. It is highly enriched in the magnetosome membrane as compared to the total membrane fraction of the cell. Determined by:

$A_{\text{mag(N)}}/A_{\text{mem(N)}} > 1 > f$ (the protein is comparatively more [or by the factor of 'f' much more] enriched in the magnetosome than in the non-magnetic membrane fraction)

c. Its relative enrichment has to increase when the magnetosomes are subjected to more stringent washing that removes associated proteins and contaminations. Determined by:

$A_{\text{mag.pur(N)}}/A_{\text{mag(N)}} \geq 1$ (after additional stringent washing, the protein is comparatively more enriched in the magnetosomes than before)

d. optional: it is highly abundant in the magnetosome membrane.

Determined by:

$A_{\text{mag.pur(N)}}/A_{\text{mag.pur(MamC)}} > t$ (the semi-quantitative abundance of the protein has to at least meet threshold 't', when compared to a known highly abundant magnetosome protein, here MamC)

Calculations for magnetosome protein abundance and surface coverage model

Based on quantitative western blots with MamC-GFP labeled magnetosomes and the correlation with iron content, a conservatively estimated number of approximately 100 molecules (estimated range: 80 - 260) of MamC were suggested for an average-sized magnetosome [17]. By calculating the $A_{\text{mag,pur(N)}}/A_{\text{mag,pur(MamC)}}$ value for every protein of interested, we estimated its abundance in relation to MamC and calculated the likely copy number of the proteins in an average magnetosome by assuming a MamC copy number of 100. For calculation of the transmembrane domain (TMD) coverage of the magnetosome membrane, we made the following assumption: i) A simple transmembrane helix (TMH), perpendicularly inserted into the lipid bilayer, has a cross-section diameter of at least 1.1 nm [18]. This is a very conservative assumption, since contributing large amino acid residues and different insertion angles might increase the cross-section diameter ii) TMHs are surrounded by boundary lipids that interact with the hydrophobic protein domain. The major phospholipids in *M. gryphiswaldense* and its magnetosomes are phosphatidylethanolamin (PE) and phosphatidylglycerol (PG) [2], the lipid head cross-section area and the diameter of dilauroyl-PE and dilauroyl-PG are 0.39 nm^2 (0.70 nm) and 0.43 nm^2 (0.74 nm), respectively [19]. On average, the diameter of a lipid head group in the magnetosome membrane can therefore be estimated to be 0.72 nm. Hence, an annular boundary lipid shell would increase the diameter of an embedded TMH to 2.5 and 4.0 nm for one and two rings of boundary lipids, respectively. iii) TMHs of multi-membrane spanning proteins are more packed and without internal lipid boundary layers. According to Jacobson *et al.*, a diameter of 2.4 nm can be assumed for the whole TMD of a tetraspan-protein, and a diameter of 3.2 nm for a heptaspan-protein, excluding boundary lipids [18]. We interpolated these values for magnetosome membrane proteins that exhibit 1 to 18 predicted TMH [20] by power regression. The average diameter of a magnetosome vesicle from *M. gryphiswaldense* is 45.5 nm [O. Raschdorf, unpublished]; the spherical surface area therefore can be calculated to be approx. 6450 nm^2 . Taking into account the number of predicted TMHs and the here estimated absolute copy numbers of *bona fide* magnetosome proteins, we calculated the integral protein occupancy of the membrane (surface) for both the scenarios that all TMH are isolated and that TMHs of a single protein form a packed TMD.

Molecular and genetic techniques

Oligonucleotides were purchased from Sigma-Aldrich (Germany). Plasmids were constructed by standard recombinant techniques using enzymes from Thermo Fisher Scientific and Agilent Technologies (CA, USA) and confirmed using BigDye terminator v3.1 chemistry on an ABI 3700 capillary sequencer (Thermo Fisher Scientific). All plasmids used in this study are listed in suppl. Table S 1

Plasmids pOR129 and pOR156 for markerless in-frame deletion of MGR_3691 and the MGR_4114 operon, respectively, were created by PCR amplification and fusion of approximately 750 bp regions up- and downstream of the target sequences and cloning into pORFM.. Genes were deleted as described in [21].

Magnetosome proteins were C- or N-terminally fused to EGFP and (over)expressed under control of the strong $P_{mamDC45}$ [17] promoter either from replicative plasmids or by transposon mediated random integration in the genome. In all cases, the two fusion proteins were separated by a 25 amino acid alpha-helical linker region [LA(EAAAK)₄AAA] (HL) [22]. Alternatively, in-frame genomic fusions were constructed. Replicative plasmids pOR079, pOR089 and pOR099 were constructed by replacing *mamI* in pOR075 by PCR-amplified *mamW*, *mamR* or *mms6* sequences, respectively, using restriction digestion. Similarly, pOR085, pOR087, pOR088, were constructed by replacing *mamQ* in pOR086 by *mmsF*, *mamR* and *mamE* sequences, respectively. The P_{mamDC} -*mamE*-HL-*egfp* sequence from pOR088 was further cloned into the transposable plasmid pBAM-1 by restriction digestion, creating pOR148. A chromosomal *mamA*-GFP fusion was generated as described in [21], using plasmid pOR068. The plasmid was created by exchanging flanking regions of *mamC* in pFM236, by approximately 750 bp homologous flanking regions of *mamA* using restriction digestion. All primers used for PCR amplifications are found in suppl. Table S 2.

Microscopy methods

For fluorescence microscopy, 3 μ l samples of *M. gryphiswaldense* over-night cultures were immobilized on 1% (w/v) agarose pads with FSM medium salts. The samples were imaged with an BX81 microscope (Olympus, Japan) equipped with a 100 \times UPLSAPO100XO 1.4NA objective and an Orca-ER camera (Hamamatsu, Japan) and appropriate filter sets using Olympus Xcellence software.

Results and Discussion

Based on pre-experiments, the four following different cellular fractions from *M. gryphiswaldense* were prepared for comparative mass spectroscopy analysis: (1) **Magnetically separated magnetosomes (mag)**, following standard isolation protocols, (2) **ultra-purified magnetosomes (mag.pur)**, additionally washed in high-salt and alkaline carbonate buffer, (3) total **non-magnetic lysate (non-mag)** after magnetic column separation, (4) total enriched **non-magnetic membrane fraction (mem)**, washed in high-salt and alkaline carbonate buffer (Figure 1). Analysis of the mass spectroscopy data in total showed 2237 unique proteins in all fractions and replicates meeting our filter criteria, which would account for approximately 53% off all predicted open reading frames (ORFs) of *M. gryphiswaldense* [23]. 1135 proteins were detected in magnetically separated magnetosomes, 1027 proteins in the ultra-purified magnetosome fraction, 2031 proteins in the total non-magnetic fraction and 1305 proteins in the enriched non-magnetic membrane fraction. Peptides of two reverse decoy proteins were found in the database, but omitted from further analysis.

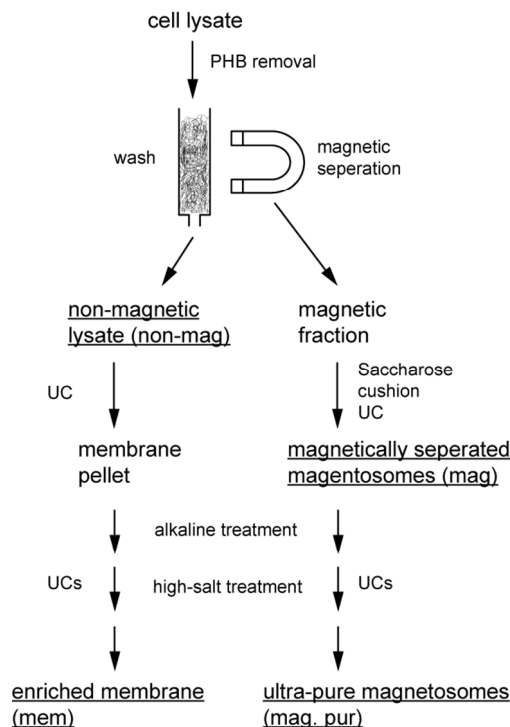


Figure 1: Workflow for fractionation of magnetically separated magnetosomes, ultra-purified magnetosomes, non-magnetic cell lysate and enriched non-magnetic membrane fraction. UC: Ultracentrifugation

Evaluating parameters to identify the integral magnetosome membrane sub proteome

By comparing the semi-quantitative, relative abundance A of proteins within the four fractions, we developed a working model to identify highly and specifically enriched (*bona fide*) integral magnetosome membrane proteins from contaminants. To fulfill our criteria, the protein had to be (A) a membrane protein (determined by $A_{\text{mem}}/A_{\text{non-mag}}$ -ratio), (B) strongly enriched in the magnetosome membrane compared to the non-magnetic membrane fraction (determined by $A_{\text{mag}}/A_{\text{mem}}$ -ratio) and (C) would not become depleted from the magnetosome by stringent washing (determined by $A_{\text{mag.pur}}/A_{\text{mag}}$ -ratio). For more information, see data analysis section in experimental procedures.

In total, only 81 proteins (of which 23 were Mam and Mms annotated) were assigned as *bona fide* integral magnetosome membrane proteins if the parameters of our model were set to $A_{\text{mem}}/A_{\text{non-mag}} \geq 1$, $A_{\text{mag}}/A_{\text{mem}} > 1$ and $A_{\text{mag.pur}}/A_{\text{mag}} \geq 1$; (Table 1). All criteria contributed to the exclusion of proteins of the list of *bona fide* magnetosome proteins, i.e. without taking into account every term, the number of assigned magnetosome proteins, especially those that are not encoded by the *mam* and *mms* operons, was unreasonably high (suppl. Table S 3). On the other hand, when $A_{\text{mem}}/A_{\text{non-mag}}$ and $A_{\text{mag.pur}}/A_{\text{mag}}$ were set above the value of ≥ 1 , e.g. to ≥ 3 and ≥ 2 , respectively, the number of assigned proteins and especially of *mam* and *mms* encoded proteins highly decreased, indicating that the two terms should not exceed ≥ 1 . (suppl. Table S 3)

Genuine magnetosome proteins should be highly enriched in the magnetosome membrane. Accordingly, the total number of assigned proteins further decreased when the $A_{\text{mag}}/A_{\text{mem}}$ coefficient was set more stringently, while the number of assigned Mam/Mms magnetosome membrane proteins only decreased by a number of two when $A_{\text{mag}}/A_{\text{mem}}$ was changed from > 1 to > 4 (Table 1), indicating that the more stringent conditions are still sufficient to select for confirmed magnetosome membrane proteins. Therefore parameter sets of $A_{\text{mem}}/A_{\text{non-mag}} \geq 1$, $A_{\text{mag}}/A_{\text{mem}} \geq 4$ and $A_{\text{mag.pur}}/A_{\text{mag}} \geq 1$ seemed to be ideal to predict the most likely *bona fide* magnetosome proteins.

Table 1: Number of assigned *bona fide* magnetosome proteins is highly influenced by all discrimination parameters

Parameters	$A_{\text{mem}}/A_{\text{non-mag}} \geq$	1	1	1	1	1	1
	$A_{\text{mag}}/A_{\text{mem}} >$	1	2	3	4	5	6
	$A_{\text{mag.pur}}/A_{\text{mag}} \geq$	1	1	1	1	1	1
Total # of assigned proteins ^A		81	35	33	30	30	26
# assigned predicted MMP ^B		23	21	21	21	21	17
# non-assigned predicted MMP ^C		9	11	11	11	11	15
# assigned predicted non-MMP ^D		58	14	12	9	9	9

^A total number of proteins that meet the applied parameter filter set (= assigned)

^B number of assigned proteins that are predicted magnetosome membrane proteins (MMPs)

[encoded in *mam* or *mms* operons (including *mamW*, *mamF2*, *mamD2* and *ftsZm*)]

^C number of proteins that are predicted MMPs, but do not meet parameter criteria

^D number of assigned proteins that are not predicted MMPs

By comparing the semi-quantitative abundance of individual proteins within the ultra-purified magnetosome fraction, the number of *bona fide* magnetosome proteins might be further refined. MamC was previously suggested to be the most abundant protein in the magnetosome membrane [1,24]. An $A_{\text{mag.pur(N)}}/A_{\text{mag.pur(MamC)}}$ -threshold of 0.01 would indicate that for 100 estimated copies of MamC, at least one copy of the protein of interest N has to be present in the magnetosome membrane. The effect of supplementing the aforementioned conditions by the filter $A_{\text{mag.pur(N)}}/A_{\text{mag.pur(MamC)}} > t$ (t of 0.1, 0.01 or 0.001) to eliminate low abundant proteins is visualized in suppl. Table S 4.

A threshold t of 0.1 further reduced the number of predicted non-magnetosome membrane proteins by 38 for $A_{\text{mem}}/A_{\text{non-mag}} \geq 1$, $A_{\text{mag}}/A_{\text{mem}} \geq 1$, $A_{\text{mag.pur}}/A_{\text{mag}} \geq 1$ and by 4 for the more restrictive $A_{\text{mem}}/A_{\text{non-mag}} \geq 1$, $A_{\text{mag}}/A_{\text{mem}} \geq 4$, $A_{\text{mag.pur}}/A_{\text{mag}} \geq 1$, while being alone not sufficient for adequate filtering (suppl. Table S 4). In combination with the parameters $A_{\text{mem}}/A_{\text{non-mag}} \geq 0$, $A_{\text{mag}}/A_{\text{mem}} \geq 4$, $A_{\text{mag.pur}}/A_{\text{mag}} \geq 1$, a $A_{\text{mag.pur}}/A_{\text{mag.pur(MamC)}}$ threshold t of 0.01 determined only 30 genuine magnetosome membrane proteins, of which 22 were predicted Mam/Mms proteins. These values are comparable to the effects of $A_{\text{mem}}/A_{\text{non-mag}} \geq 1$, $A_{\text{mag}}/A_{\text{mem}} \geq 4$, $A_{\text{mag.pur}}/A_{\text{mag}} \geq 1$ without MamC abundance threshold and particular interesting as an alternative

because the $A_{\text{mem}}/A_{\text{non-mag}}$ coefficient could potentially also exclude proteins that are so highly affine to the magnetosome membrane that they are completely undetectable in the nonmagnetic membrane fraction.

The genuine magnetosome membrane proteome is mainly composed of Mam and Mms proteins

In the following, the proteins that were identified as genuine integral magnetosome membrane proteins for different applied parameter sets are presented and discussed: With the exception of MamL, all other Mam and Mms proteins were identified in our proteomic data, including the recently identified MamF2 and MamD2 as well as MamX and MamI, which were never found in previous proteomic studies [8]. MamL is very small (approx. 9 kDa) protein, that contains two predicted hydrophobic transmembrane domains and only two tryptic peptides that are in the theoretically detectable mass range. Although expressed and at least partially targeted to the magnetosome membrane, as seen in studies with MamL-GFP protein fusions [7], the protein was never found in a proteomic analysis. It therefore stands in contrast to equally small proteins like MamR (approx. 8 kDa) and MamI (approx. 7 kDa), which were confidently identified in this study and in the case of MamI also comprise two predicted trans-membrane domains, but more theoretical tryptic peptides. The general absence of MamL from the data is an indication that some proteins might be underrepresented.

With the stringent parameters of $A_{\text{mem}}/A_{\text{non-mag}} \geq 1$, $A_{\text{mag}}/A_{\text{mem}} \geq 4$, $A_{\text{mag.pur}}/A_{\text{mag}} \geq 1$, the 21 assigned and also predicted *bona fide* integral magnetosome membrane proteins were: MamE, MamD, Mms6, MamO, MamM, MamC, MamB, MamY, MamP, MamF2, MmsF, MamF, MamS, MamH, MamT, MamZ, MamI, MamN, MamW, MamX and MamG. The two proteins MamQ and Mms48 (MGR_4070) succeeded $A_{\text{mem}}/A_{\text{non-mag}} \geq 1$ and $A_{\text{mag.pur}}/A_{\text{mag}} \geq 1$, but only showed an $A_{\text{mag}}/A_{\text{mem}}$ value of 2.0 or 1.6 respectively. With a less stringent interpretation of the parameters the proteins therefore would also be assigned as *bona fide* magnetosome proteins. It is possible that both proteins are genuine magnetosome membrane proteins that are similarly abundant in the cytoplasmic membrane; however, with an $A_{\text{mag.pur}}/A_{\text{mag.pur(MamC)}}$ value of 0.01, the abundance of Mms48 in the magnetosome membrane fraction is very low. Fluorescently labeled MamQ also was already

reported to be mainly localized within the cytoplasmic membrane [O. Raschdorf, unpublished].

In addition to the undetectable MamL protein, several other Mam/Mms proteins did not meet the criteria for *bona fide* magnetosome membrane proteins. MamA, for example, failed twice: Although its calculated $A_{\text{mag}}/A_{\text{mem}}$ value of 51.2 was the second highest in the whole experiment, it did not fulfill the membrane protein threshold ($A_{\text{mem}}/A_{\text{non-mag}} = 0.6$) and could also be efficiently washed off from the magnetosome membrane in the purification process ($A_{\text{mag.pur}}/A_{\text{mag}} = 0.3$). It is well-established that the protein only associates to the magnetosome surface and is not integral part of its membrane, but becomes easily washed off with alkaline treatment [25-27]. The results therefore are in good agreement with published data and consequently another proof for the effectiveness of the selected parameter model. MamJ was excluded for the same reasons, however shows less clear parameters ($A_{\text{mem}}/A_{\text{non-mag}}$ and $A_{\text{mag.pur}}/A_{\text{mag}} = 0.9$). Since it also does not contain predictable transmembrane domains, MamJ is most likely strongly magnetosome membrane associated, but not integral. The actin-like MamK protein was excluded since it was more abundant in the non-magnetic membrane than the magnetosome membrane and the total non-magnetic lysate. The latter indicates that polymerized, high molecular weight MamK is either pelleted with the membrane fraction, or is bound to the cytoplasmic membrane. Although, MamD2 (like MamF2) was highly enriched in the magnetosome membrane, the protein could not meet the criteria because it was washed off from ultra-purified magnetosomes ($A_{\text{mag.pur}}/A_{\text{mag}} = 0.6$). The protein comprises two predicted transmembrane domains, but is poorly studied so far. The relevance of this finding therefore remains unclear, but might indicate that the protein is not an integral magnetosome membrane protein.

MamR is an 8 kDa protein without any predicted transmembrane domain. It was virtually exclusively found in the magnetosome fraction, and could not be washed off. With a $A_{\text{mag.pur}}(\text{MamR})/A_{\text{mag.pur}}(\text{MamC})$ value of 0.2, it was additionally highly abundant in and therefore seems to be strongly magnetosome associated. Since it was undetectable in the membrane and almost undetectable in the soluble protein fraction, MamR is an ambiguous case but formally had to be excluded. Although mostly no integral component, the proteins seems strongly magnetosome associated. Similar to Mms48, Mms36 was excluded because of its low $A_{\text{mag}}/A_{\text{mem}}$ value of 1.0. Additionally, both proteins show a very low semi-quantitative abundance in the

magnetosomes. Hence, Mms48 and Mms36, that were found to have a minor role in magnetite formation [9], rather play an active role in the cytoplasmic membrane. FtsZm by far failed all criteria and was almost non-detectable in magnetosomes. It is therefore also most likely active in another cellular compartment, presumably the cytoplasm. Finally, the predicted soluble MamU also failed all criteria and therefore is most likely not magnetosome associated. The MAI-encoded [R. Uebe, unpublished] iron transporter FeoAB1 was recently implicated in magnetite formation [28]. While FeoA1 was not found in our screen, FeoB1 was present with the same abundance in magnetosome and non-magnetic membrane fraction ($A_{\text{mag}}/A_{\text{mem}} = 1.0$, $A_{\text{mem}}/A_{\text{non-mag}} = 2.7$, $A_{\text{mag.pur}}/A_{\text{mag}} = 1.2$), and therefore not found to be magnetosome membrane specific.

We fluorescently labeled some of the Mam and Mms proteins which localization was not yet assessed by fluorescence microscopy in *M. gryphiswaldense*, in order to corroborate parts of the findings of the magnetosome proteome analysis. GFP-labeled Mms6 and MmsF predominantly showed a strong linear fluorescent signal within the cells, resembling the organization of the magnetosome chain and indicating a strong enrichment in the magnetosome membrane (Figure 2A+B) as seen in our proteomic analysis. GFP-MamE also showed an signal accumulation at midcell, however with higher cellular background (Figure 2C) Since MamW is only conserved in *Magnetospirilla* species, not organized in one of the four major operons of the MAI and deletion did not show any phenotype [7,8], its participation in magnetosome formation was yet not proved. The linear signal of the MamW-GFP fusion (Figure 2F) however corroborated our proteomic results and further suggests that MamW is a specifically magnetosome associated protein. MamR and MamA GFP-fusions also showed a weak linear localization signal within the cell, along with a high cytoplasmic background (Figure 2D+E). These results corroborate the finding that both proteins were not assigned as *bona fide* integral magnetosome membrane proteins in this study, but were still found highly enriched in the magnetosome fraction, indicating strong magnetosome association.

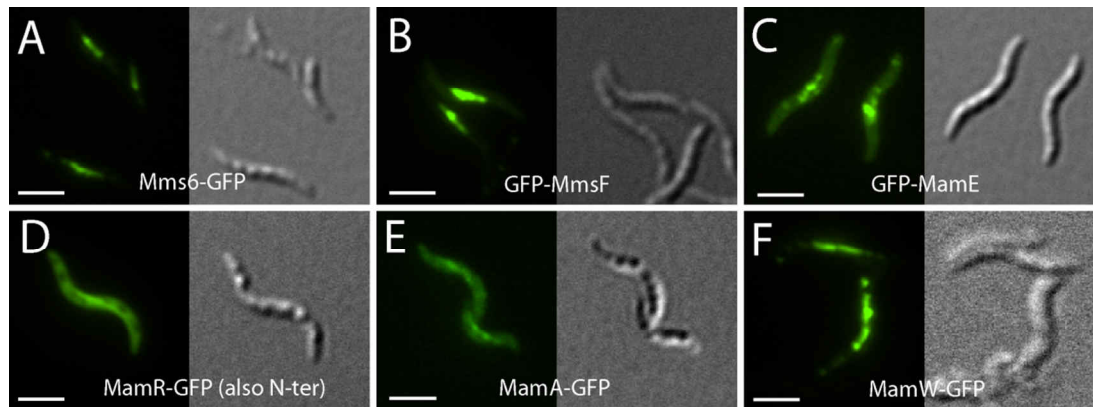


Figure 2: Cellular localization of six Mam/Mms proteins in *M. gryphiswaldense*. All proteins were C- or N-terminally fused to EGFP and expressed in the wild type. A 30 amino acid alpha-helical linker (HL) was placed in between the fusion proteins. A) C-terminal P_{mamDC} -*mms6*-HL-*egfp* construct, expressed from plasmid. B) N-terminal P_{mamDC} -*mmsF*-HL-*egfp* construct, expressed from plasmid. C) N-terminal P_{mamDC} -*mamE*-HL-*egfp* construct, expressed from ectopic chromosomal locus. D) C-terminal P_{mamDC} -*mamR*-HL-*egfp* construct, expressed from plasmid. N-terminal fusion exhibited comparable localization pattern. E) C-terminal *mamA*-HL-*egfp* construct, expressed from native chromosomal locus (in-frame gene fusion) F) C-terminal P_{mamDC} -*mamW*-HL-*egfp* construct, expressed from plasmid. Fluorescence (left) and corresponding differential interference contrast (right) images are shown. Scale bar: 2 μ m

With over 1000 proteins found in the magnetosome fraction, it is highly likely that most of them must be contaminations. Comparable to previous proteomic studies, predicted outer membrane proteins and ATPase subunits were among the highest abundant proteins in the magnetosome membrane fraction [1,2,5] (Table 2). However, the proteins did not meet the stringently applied filter criteria, showing that highly abundant proteins in the magnetosome fraction can be contaminants. Other proteins are not predicted to be magnetosome associated (non Mam/Mms), but met the filter criteria or were highly enriched in the magnetosome membrane. As can be seen in Table 1 and Table 3, this only accounts for few proteins. Only one of those proteins, the small (7 kDa) hypothetical transmembrane MGR_4114 protein, is encoded within the magnetosomeisland and there part of a four genes comprising operon. The operon also encodes for two additional hypothetical proteins and one protein with similarities to ParA/MinD-like ATPases. Although MGR_4114 might be a *bona fide* magnetosome protein, deletion of the encoding operon did not cause a notable magnetosome phenotype (data not shown). Interestingly, MGR_3691 (also known as MM22 [2]) was the most highly magnetosome enriched protein identified in our screen ($A_{mag}/A_{mem} = 64.8$), but not assigned *bona fide* integral magnetosome

protein, as it became washed off in ultra-purified magnetosomes and did not complete the integral membrane protein threshold ($A_{\text{mag.pur}}/A_{\text{mag}} = 0.5$, $A_{\text{mem}}/A_{\text{non-mag}} = 0.5$). However, deletion of the gene did also not notably lead to a magnetosome related phenotype (data not shown), again indicating that it has no important function in magnetosome formation. Among the most highly abundant proteins, the previously identified Mms16 (MGR_0659) was also identified, but not assigned *bona fide* magnetosome protein (Table 2) due to an $A_{\text{mem}}/A_{\text{non-mag}}$ value of 0.6 and an $A_{\text{mag}}/A_{\text{mem}}$ value of 2.4. The protein was previously connected with magnetosome formation [29], but later in fact shown to represent a phasin that functions in PHB metabolism of *M. gryphiswaldense* [30]. Therefore, also this contamination was successfully uncovered in our approach. While three of the other magnetosome assigned non-magnetosome predicted proteins showed a $A_{\text{mag.pur(MamR)}}/A_{\text{mag.pur(MamC)}}$ below 0.01 (Table 2), five further proteins exhibited a value between 0.01 and 0.02. These are the hypothetical proteins MGR_2833, MGR_0916 and MGR_2730 as well as the histidine kinase MGR_0622 and the *ccb3*-type cytochrome oxidase maturation protein MGR_2552 (Table 2). Since their abundance in the magnetosome membrane is very low and currently no functional connection to magnetosome formation could be drawn for those proteins, it is highly likely that they represent false positive hits.

Table 2: Top20-abundant and all assigned *bona fide* magnetosome proteins

<i>Bona fide?</i>	$A_{\text{mag,pur}}/A_{\text{mag,pur(MamC)}}/[\# \text{ copies}]$	Rank ($A_{\text{mag,pur}}$)	Set parameters: $A_{\text{mem}}/A_{\text{non-mag}} \geq 1$, $A_{\text{mag}}/A_{\text{mem}} > 4$, $A_{\text{mag,pur}}/A_{\text{mag}} \geq 1$
yes	1.21 [121]	1	Mms6 (13 kDa)
yes	1.00 [100]	2	MamC (12 kDa)
yes	0.51 [51]	3	MamD (30 kDa)
	0.48	4	YajC preprotein translocase subunit (13 kDa)
yes	0.31 [31]	5	MamF2 (12 kDa)
yes	0.31 [31]	6	MamE (78 kDa)
	0.26	7	MGR_0659 (Mms16) (16 kDa)
yes	0.25 [25]	8	MmsF (14 kDa)
	0.24	9	MGR_3650 Outer membrane protein (porin) (41 kDa)
yes	0.23 [23]	10	MamB (32 kDa)
yes	0.21 [21]	11	MamM (34 kDa)
yes	0.21 [21]	12	MamF (12 kDa)
	0.20	13	MamR (8 kDa)
	0.18	14	AtpF ATP synthase B chain precursor (19 kDa)
	0.18	15	MGR_1798 Outer membrane protein (17 kDa)
	0.17	16	MamA (24 kDa)
yes	0.17 [17]	17	MamY (41 kDa)
yes	0.14 [14]	18	MamO (65 kDa)
	0.13	19	AtpG ATP synthase B' chain (18 kDa)
	0.13	20	MamJ (44 kDa)
yes	0.11 [11]	24	MamP (28 kDa)
yes	0.10 [10]	25	MamT (19 kDa)
yes	0.09 [9]	28	MamS (19 kDa)
yes	0.06 [6]	36	MamG (8 kDa)
yes	0.06 [6]	40	MamI (8 kDa)
yes	0.05 [5]	43	MamW (15 kDa)
yes	0.05 [5]	47	MGR_4114 hypothetical protein (7kDa)
yes	0.04 [4]	58	MamH (46 kDa)
yes	0.04 [4]	60	MamN (46 kDa)
yes	0.02 [2]	95	MGR_0622 ATP-binding region, Histidine kinase (50 kDa)
yes	0.02 [2]	100	MGR_2552 Cytochrome oxidase maturation cbb3-type (7kDa)
yes	0.02 [2]	102	MGR_2833 Protein of unknown function (26 kDa)
yes	0.02 [2]	111	MamX (28 kDa)
yes	0.02 [2]	127	MamZ (72 kDa)
yes	0.01 [1]	187	MGR_2730 conserved hypothetical protein (20 kDa)
yes	0.01 [1]	226	MGR_0916 conserved hypothetical protein (9 kDa)
yes	0.00 [0]	444	MGR_0581 conserved hypothetical protein (10 kDa)
yes	0.00 [0]	535	MGR_2491 hypothetical protein (8 kDa)
yes	0.00 [0]	1040	MGR_3321 two-comp. sensor histidine kinase (47 kDa)

Table 3 shows additional proteins that might be *bona fide* magnetosome membrane proteins, identified using less stringent filter conditions ($A_{\text{mem}}/A_{\text{non-mag}} \geq 1$, $A_{\text{mag}}/A_{\text{mem}} \geq 1$, $A_{\text{mag.pur}}/A_{\text{mag}} \geq 1$), but with a predicted abundance of at least two protein copies per magnetosome ($A_{\text{mag.pur(N)}}/A_{\text{mag.pur(MamC)}} \geq 0.02$). Besides MamQ, these proteins are putative translocases, peptidases, hypothetical proteins, acyl- or glycosyl-transferases. However, only MamQ shows a reasonably high $A_{\text{mag}}/A_{\text{mem}}$ enrichment coefficient and also $A_{\text{mag.pur}}/A_{\text{mag.pur(MamC)}}$ abundance. Similarly, ignoring the $A_{\text{mag}}/A_{\text{mem}}$ threshold, only MamR and a putative phasin could be additionally assigned with high $A_{\text{mag.pur}}/A_{\text{mag.pur(MamC)}}$ abundance.

Except few candidate proteins, of with one showed higher confidence (MGR_4114), it therefore appears that only previously predicted magnetosome membrane proteins are part of the specific integral magnetosome membrane sub-proteome.

Table 3: Additional putative genuine magnetosome membrane proteins. Proteins here are only listed if not already mentioned in Table 2.

$A_{\text{mem}}/$ $A_{\text{non-mag}}$	$A_{\text{mag}}/$ A_{mem}	$A_{\text{mag.pur}}/$ A_{mag}	$A_{\text{mag.pur}}/$ $A_{\text{mag.pur(MamC)}}$	Rank ($A_{\text{mag.pur}}$)	Set parameters: $A_{\text{mem}}/A_{\text{non-mag}} \geq 1$, $A_{\text{mag}}/A_{\text{mem}} > 1$, $A_{\text{mag.pur}}/A_{\text{mag}} \geq 1$, $A_{\text{mag.pur(N)}}/A_{\text{mag.pur(MamC)}} \geq 0.02$
4.3	2.0	1.3	0.07	32	MamQ (30 kDa)
3.4	1.3	1.5	0.07	34	MGR_3120 Bacterial sec-independent translocation protein mttA/Hcf106 (8 kDa)
2.9	1.3	1.3	0.07	35	MGR_1712 translocase, subunit Tim44 (26 kDa)
1.2	1.4	1.0	0.05	46	MGR_0255 conserved hypothetical protein (11 kDa)
5.0	3.7	1.3	0.03	66	MGR_1199 Peptidase M48, Ste24p (33 kDa)
1.1	1.2	1.2	0.02	87	MGR_4238 regulatory protein (22 kDa)
3.9	1.1	1.1	0.02	93	MGR_0007 glycosyl transferase, group 2 family (27 kDa)
6.6	1.3	1.9	0.02	114	MGR_0417 serine O-acetyltransferase (27 kDa)
4.3	1.9	1.1	0.02	129	MGR_3354 phos.lipid/glycerol acyltransferase (30 kDa)
$A_{\text{mem}}/$ $A_{\text{non-mag}}$	$A_{\text{mag}}/$ A_{mem}	$A_{\text{mag.pur}}/$ A_{mag}	$A_{\text{mag.pur}}/$ $A_{\text{mag.pur(MamC)}}$	Rank ($A_{\text{mag.pur}}$)	Set parameters: $A_{\text{mem}}/A_{\text{non-mag}} \geq -1$, $A_{\text{mag}}/A_{\text{mem}} > 4$, $A_{\text{mag.pur}}/A_{\text{mag}} \geq 1$, $A_{\text{mag.pur(N)}}/A_{\text{mag.pur(MamC)}} > 0.01$
0.0	∞	1.1	0.20	13	MamR (8 kDa)
0.4	6.5	1.5	0.10	27	MGR_2633 Phasin (12 kDa)
0.1	6.8	1.2	0.02	116	MGR_2416 cytochrome c (12 kDa)
0.8	5.0	1.1	0.01	142	MGR_1351 CreA (17 kDa)

Proteinase K-shaved magnetosome membranes are most highly enriched with Mam/Mms protein fragments

To gain additional information about the integral magnetosome membrane proteome, we proceeded with a Proteinase K membrane shaving assay with isolated magnetosomes. Proteinase K treatment ideally cleaves off and digests all external protein domains, while buried transmembrane and membrane enclosed domains stay intact. Mass spectroscopy analysis of shaved magnetosomes membranes assigned peptide spectra to 61 proteins (suppl. Table S 5). Although we found previously undetected peptides derived from predicted hydrophobic transmembrane helices of Mam and Mms proteins, most assigned spectra were from predicted soluble protein domains. However, among the 20 proteins with the highest exclusive un-normalized peptide spectra counts (SpC), 15 were Mam and Mms proteins (suppl. Table S 5). While 19 % of all spectra were assigned to the magnetosome protein MamO, the top-10 proteins with highest SpC already covered 75 % of all spectra (top-20 – 89%). Besides MamS and MamP, all identified *bona fide* Mam and Mms magnetosome membrane proteins (according to Table 2) were also detected in the membrane shaving assay, however with highly variable SpC. Additionally, MamJ, MamA and MamD2 were also identified with comparably low SpC (suppl. Table S 5). Although with low SpC, only MGR_2730 and the MAI-encoded MGR_4114 were identified from the list of non-Mam/Mms, but assigned *bona fide* magnetosome proteins (Table 2). As in whole magnetosomes, MGR_3691 was again identified with a high SpC (suppl. Table S 5), emphasizing its role as a candidate magnetosome membrane protein. 6 proteins previously not found in all analyzed fractions had assigned peptide spectra, of which MGR_1410, a predicted ammonia permease, had the highest SpC. Notably, also FeoB1 was detected with intermediary SpC. Most other identified proteins, usually with a comparably low SpC, were components of transporters or of redox pathways and other proteins of the energy-metabolism. The results from the Proteinase K membrane shaving assay again suggest that magnetosome membranes are specifically enriched mainly with Mam and Mms proteins.

Predictions of protein abundancies suggest that the magnetosome membrane is densely packed with integral proteins.

Recently, based on quantitative western blots with MamC-GFP labeled magnetosomes and the correlation with iron content, a conservatively estimated number of approximately 100 molecules (estimated range: 80 - 260) of MamC was suggested for an average sized magnetosome [17]. Based on this number and the calculated $A_{\text{mag.pur(N)}}/A_{\text{mag.pur(MamC)}}$ -values, we estimated the copy numbers of all other integral *bona fide* magnetosome proteins for an average wild type magnetosome (Table 3).

The average diameter of magnetosome vesicles from *M. gryphiswaldense* is 45.5 nm [O. Raschdorf, unpublished]; the spherical surface area can therefore be calculated to be approx. 6450 nm². Taking into account the number of predicted transmembrane alpha helices and the here estimated absolute copy numbers of *bona fide* magnetosome proteins, the integral protein occupancy of the membrane (surface) can be calculated (see experimental procedures for details). Several theoretical considerations have to be taken into account: i) A simple, perpendicular transmembrane helix (TMH) has a cross-section diameter of at least 1.1 nm [18]. ii) TMHs are surrounded by one or two layers of boundary lipids that interact with the hydrophobic protein domain. The major phospholipids in *M. gryphiswaldense* and its magnetosomes are phosphatidylethanolamin (PE) and phosphatidylglycerol (PG), the cross-section surface and the diameter of dilauroyl-PE and dilauroyl-PG are 0.39 nm² (0.70 nm) and 0.43 nm² (0.74 nm), respectively. On average, the diameter of one lipid can therefore be assumed to be 0.72 nm. Hence, an annular boundary lipid shell would increase the diameter of an embedded TMH to 2.5 and 4.0 nm for one and two boundary lipid layers, respectively. iii) TMHs of multi-membrane spanning proteins are more packed and without internal lipid boundary layers. According to Jacobson *et al.*, a diameter of 2.4 nm can be assumed for the whole transmembrane domain (TMD) of a tetraspan-protein, and a diameter of 3.2 nm for a heptaspan-protein, excluding boundary lipids [18]. We interpolated these values for magnetosome membrane proteins that exhibit 1 to 18 transmembrane domains and calculated the average TMH-coverage of the magnetosome membrane for different assumptions (Table 4). Only *bona fide mam* and *mms* proteins were taken into account, since the

copy numbers of other potential integral magnetosome membrane proteins are negligible.

Table 4: Coverage of the magnetosome membrane surface by transmembrane domains of integral magnetosome proteins

Integral magnetosome membrane coverage by TMDs^A	All TMHs^B are isolated from each other	TMHs of individual proteins are tightly packed
No boundary lipid	18 %	20 %
One boundary lipid	97 %	63 %
Two boundary lipids	238 %	132 %

A: Transmembrane domain

B: Transmembrane helix

According to this data, TMD from magnetosome proteins already cover 18-20% of the magnetosome surface, independent on any boundary lipids. If one ring of boundary lipid is added, this number increases to 62-97% and further to impossible 131-238% if a second ring of boundary lipids is included. This indicates that TMHs of all proteins seem to be in close contact to each other and in most cases can be only surrounded by one layer of boundary lipids. Therefore, the magnetosome membrane seems to be very rigid and tightly packed with trans-membrane proteins and only contains a smaller number of “free” lipids. For comparison, the hepta-spanning archaeal Bacteriorhodopsin is one of the most tightly clustered transmembrane proteins and might be present in up to 600.000 molecules on a surface of 15 μm^2 [31]. Assuming a trimer configuration of the molecule with an approximate TMD-diameter of 5.2 nm [PDB] (including 3 enclosed lipids), this would indicate a total membrane coverage of 28%, which is somewhat higher but in the same range as our conservatively estimated coverage of the magnetosome membrane.

In summary, our proteomic data and modelling estimated the composition of the integral magnetosome membrane proteome of MSR-1. Although the prediction of relative protein abundancies from label-free mass spectroscopy data is error-prone and might lead to under- or overestimations for individual proteins, the cautious interpretation of our data allowed us to coarsely estimate the protein composition and

coverage of the magnetosome membrane in a novel approach. Absolute quantifications of other individual magnetosomes membrane proteins in the future will contribute to confirm and further refine our model, which will be the basis for more precise determination of the structure of this unique bacterial organelle. By directly comparing protein abundancies of magnetosomes purified from single magnetosome gene deletion mutants with those of the wild type, our approach could be utilized to systematically assay the interdependency on protein localization to the organelle. This might proof as a powerful tool to further investigate the complex interaction-network of magnetosome proteins. Finally, our prediction of a crowded protein composition within the membrane of the organelle also might substantially contribute to the elucidation of the processes involved in biogenesis of magnetosomes.

References

1. Grünberg K, Wawer C, Tebo BM, Schüler D. A Large Gene Cluster Encoding Several Magnetosome Proteins Is Conserved in Different Species of Magnetotactic Bacteria. *Appl Environ Microbiol.* 2001;67: 4573–4582. doi:10.1128/AEM.67.10.4573-4582.2001
2. Grünberg K, Müller E-C, Otto A, Reszka R, Linder D, Kube M, et al. Biochemical and Proteomic Analysis of the Magnetosome Membrane in *Magnetospirillum gryphiswaldense*. *Appl Environ Microbiol.* 2004;70: 1040–1050. doi:10.1128/AEM.70.2.1040-1050.2004
3. Richter M, Kube M, Bazylinski DA, Lombardot T, Glöckner FO, Reinhardt R, et al. Comparative genome analysis of four magnetotactic bacteria reveals a complex set of group-specific genes implicated in magnetosome biomineralization and function. *J Bacteriol.* 2007;189: 4899–910. doi:10.1128/JB.00119-07
4. Ullrich S, Kube M, Schübbe S, Reinhardt R, Schüler D. A Hypervariable 130-Kilobase Genomic Region of *Magnetospirillum gryphiswaldense* Comprises a Magnetosome Island Which Undergoes Frequent Rearrangements during Stationary Growth. *J Bacteriol.* 2005;187: 7176–7184. doi:10.1128/JB.187.21.7176
5. Tanaka M, Okamura Y, Arakaki A, Tanaka T, Takeyama H, Matsunaga T. Origin of magnetosome membrane: proteomic analysis of magnetosome membrane and comparison with cytoplasmic membrane. *Proteomics.* 2006;6: 5234–47. doi:10.1002/pmic.200500887
6. Schübbe S, Kube M, Scheffel A, Wawer C, Heyen U, Meyerdierks A, et al. Characterization of a Spontaneous Nonmagnetic Mutant of *Magnetospirillum gryphiswaldense* Reveals a Large Deletion Comprising a Putative Magnetosome Island. *J Bacteriol.* 2003;185: 5779–5790. doi:10.1128/JB.185.19.5779-5790.2003
7. Murat D, Quinlan A, Vali H, Komeili A. Comprehensive genetic dissection of the magnetosome gene island reveals the step-wise assembly of a prokaryotic organelle. *Proc Natl Acad Sci U S A.* 2010;107: 5593–5598. doi:10.1073/pnas.0914439107
8. Lohße A, Ullrich S, Katzmann E, Borg S, Wanner G, Richter M, et al. Functional Analysis of the Magnetosome Island in *Magnetospirillum gryphiswaldense*: The *mamAB* Operon Is Sufficient for Magnetite Biomineralization. Battista JR, editor. *PLoS One.* 2011;6: e25561. doi:10.1371/journal.pone.0025561
9. Lohße A, Borg S, Raschdorf O, Kolinko I, Tompa É, Pósfai M, et al. Genetic dissection of the *mamAB* and *mms6* operons reveals a gene set essential for magnetosome biogenesis in *magnetospirillum gryphiswaldense*. *J Bacteriol.* 2014;196: 2658–2669. doi:10.1128/JB.01716-14

10. Matsunaga T, Nemoto M, Arakaki A, Tanaka M. Proteomic analysis of irregular, bullet-shaped magnetosomes in the sulphate-reducing magnetotactic bacterium *Desulfovibrio magneticus* RS-1. *Proteomics*. 2009;9: 3341–3352. doi:10.1002/pmic.200800881
11. Heyen U, Schüler D. Growth and magnetosome formation by microaerophilic *Magnetospirillum* strains in an oxygen-controlled fermentor. *Appl Microbiol Biotechnol*. 2003;61: 536–44. doi:10.1007/s00253-002-1219-x
12. Schüler D, Uhl R, Bäuerlein E. A simple light scattering method to assay magnetism in *Magnetospirillum gryphiswaldense*. *FEMS Microbiol Lett*. 1995;132: 139–145. doi:10.1016/0378-1097(95)00300-T
13. Schultheiss D, Schüler D. Development of a genetic system for *Magnetospirillum gryphiswaldense*. *Arch Microbiol*. 2003;179: 89–94. doi:10.1007/s00203-002-0498-z
14. Ullrich S, Schüler D. Cre-lox-based method for generation of large deletions within the genomic magnetosome island of *Magnetospirillum gryphiswaldense*. *Appl Environ Microbiol*. 2010;76: 2439–44. doi:10.1128/AEM.02805-09
15. Bonn F, Bartel J, Büttner K, Hecker M, Otto A, Becher D. Picking vanished proteins from the void: How to collect and ship/share extremely dilute proteins in a reproducible and highly efficient manner. *Anal Chem*. 2014;86: 7421–7427. doi:10.1021/ac501189j
16. Wolff S, Hahne H, Hecker M, Becher D. Complementary analysis of the vegetative membrane proteome of the human pathogen *Staphylococcus aureus*. *Mol Cell Proteomics*. 2008;7: 1460–8. doi:10.1074/mcp.M700554-MCP200
17. Borg S, Hofmann J, Pollithy A, Lang C, Schüler D. New Vectors for Chromosomal Integration Enable High-Level Constitutive or Inducible Magnetosome Expression of Fusion Proteins in *Magnetospirillum gryphiswaldense*. *Appl Environ Microbiol*. 2014;80: 2609–16. doi:10.1128/AEM.00192-14
18. Jacobson K, Mouritsen OG, Anderson RGW. Lipid rafts: at a crossroad between cell biology and physics. *Nat Cell Biol*. 2007;9: 7–14. doi:10.1038/ncb0107-7
19. Gunstone FD, Harwood JL, Padley FB. *The Lipid Handbook*. second edi. London: Chapman & Hall/CRC; 1994.
20. Nudelman H, Zarivach R. Structure prediction of magnetosome-associated proteins. *Front Microbiol*. 2014;5: 1–17. doi:10.3389/fmicb.2014.00009
21. Raschdorf O, Plitzko JM, Schüler D, Müller FD. A tailored galK counterselection system for efficient markerless gene deletion and chromosomal tagging in *Magnetospirillum gryphiswaldense*. *Appl Environ Microbiol*. 2014;80: 4323–4330. doi:10.1128/AEM.00588-14

22. Arai R, Ueda H, Kitayama A, Kamiya N, Nagamune T. Design of the linkers which effectively separate domains of a bifunctional fusion protein. *Protein Eng.* 2001;14: 529–32.
23. Wang X, Wang Q, Zhang W, Wang Y, Li L, Wen T, et al. Complete Genome Sequence of *Magnetospirillum gryphiswaldense*. *Genome Announc.* 2014;2: 2–3. doi:10.1128/genomeA.00171-14.
24. Scheffel A, Gärdes A, Grünberg K, Wanner G, Schüler D. The major magnetosome proteins MamGFDC are not essential for magnetite biomineralization in *Magnetospirillum gryphiswaldense* but regulate the size of magnetosome crystals. *J Bacteriol.* 2008;190: 377–86. doi:10.1128/JB.01371-07
25. Taoka A, Asada R, Sasaki H, Anzawa K, Wu L-F, Fukumori Y. Spatial localizations of Mam22 and Mam12 in the magnetosomes of *Magnetospirillum magnetotacticum*. *J Bacteriol.* 2006;188: 3805–12. doi:10.1128/JB.00020-06
26. Zeytuni N, Ozyamak E, Harush K Ben, Davidov G, Levin M, Gat Y, et al. Self-recognition mechanism of MamA, a magnetosome-associated TPR-containing protein, promotes complex assembly. *Proc Natl Acad Sci U S A.* 2011; doi:10.1073/pnas.1103367108
27. Yamamoto D, Taoka A, Uchihashi T, Sasaki H, Watanabe H, Ando T, et al. Visualization and structural analysis of the bacterial magnetic organelle magnetosome using atomic force microscopy. *Proc Natl Acad Sci U S A.* 2010;107: 9382–7. doi:10.1073/pnas.1001870107
28. Rong C, Zhang C, Zhang Y, Qi L, Yang J, Guan G, et al. FeoB2 Functions in Magnetosome Formation and Oxidative Stress Protection in *Magnetospirillum gryphiswaldense* Strain MSR-1. *J Bacteriol.* 2012;194: 3972–6. doi:10.1128/JB.00382-12
29. Okamura Y, Takeyama H, Matsunaga T. A Magnetosome-specific GTPase from the Magnetic Bacterium *Magnetospirillum magneticum* AMB-1. *J Biol Chem.* 2001;276: 48183–48188. doi:10.1074/jbc.M106408200
30. Schultheiss D, Handrick R, Jendrossek D, Hanzlik M, Schüler D. The Presumptive Magnetosome Protein Mms16 Is a Poly(3-Hydroxybutyrate) Granule-Bound Protein (Phasin) in *Magnetospirillum gryphiswaldense*. *J Bacteriol.* 2005;187: 2416–2425. doi:10.1128/JB.187.7.2416
31. del Rosario RCH, Oppawsky C, Tittor J, Oesterhelt D. Modeling the membrane potential generation of bacteriorhodopsin. *Math Biosci. Elsevier Inc.*; 2010;225: 68–80. doi:10.1016/j.mbs.2010.02.002

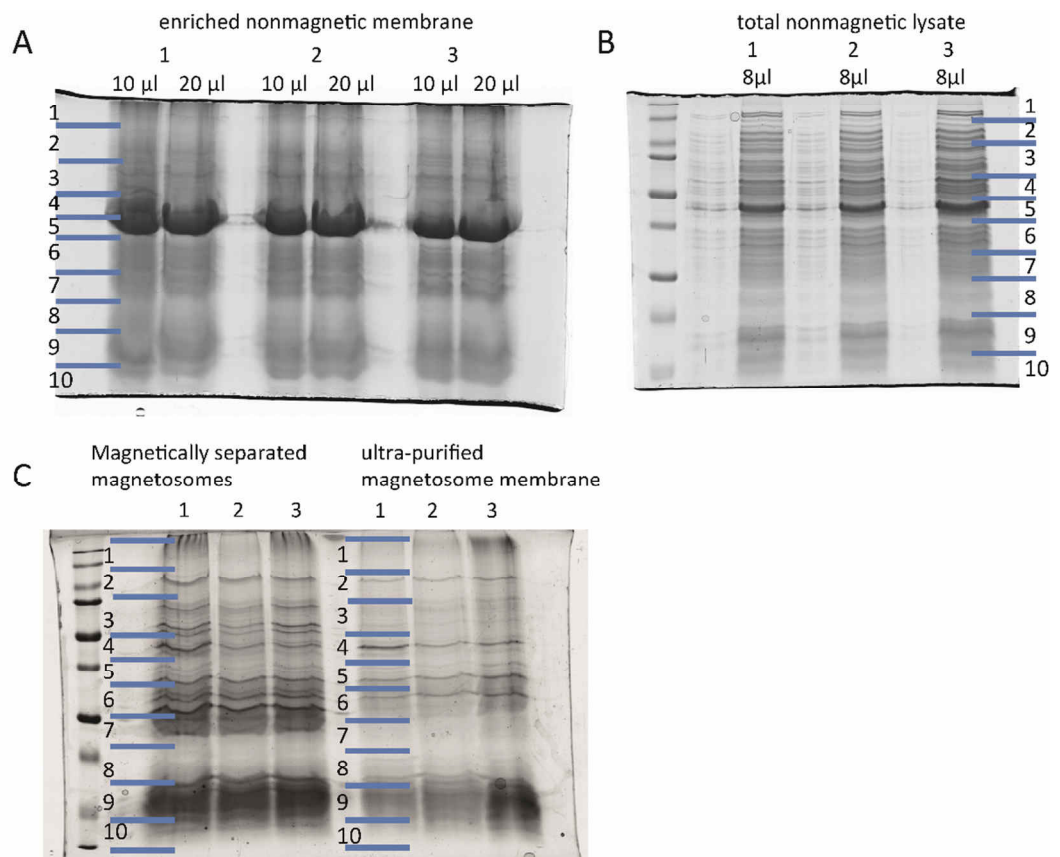
Supporting information

Fig S 1: 2D SDS-PAGE of fractions employed for mass spectrometry analysis: The individual gel pieces, cut and subjected to in-gel trypsin digestion, are indicated. 10 μ l lane was utilized for enriched non-magnetic fraction.

suppl. Table S 1: Strains and plasmids used in this study

Strains and plasmids	Description	References
MSR strains		
MSR-1 R3/S1	Wildtype and mother strain of deletion mutants	[1]
Δ mgr_3691 (MM22)	Markeless mgr_3691 deletion mutant (pOR129)	this study
Δ mgr_4114_op	Markeless mgr_4114 operon deletion mutant (pOR156)	this study
<i>mamA::mamA-egfp</i>	Allelic replacement (pOR068)	this study
MSR P_{mamDC} - <i>mamE-egfp</i>	Tn5 transposon integrated (pOR148)	this study
<i>E. coli</i> strains		
BW29427	<i>thrB1004 pro thi rpsL hsdS lacZDM15 RP4-1360D(araBAD)567DdapA</i>	Datsenko & Wanner, unpublished
DH5a	<i>1341::[erm pir(WT)]trahsdR17 recA1-endA1gyrA96thi-1relA1</i>	Thermo Fisher Scientific
Plasmids		
pBBR1MCS2	Mobilizable broad-host-range vector, Km ^r	[2]
pORFM GalK	Vector for genomic in-frame deletions/integration, Km ^r galK tetR mobRK2	[3]
pFM236	pORFM derivate, for chromosomal <i>mamC-egfp</i> in-frame fusion, Km ^r	[3]
pBAM1	<i>oriR6K</i> , Km ^r , ap ^r , Tn5 transposition platform	[4]
pOR068	pORFM derivate, for chromosomal <i>mamA-egfp</i> in-frame fusion, Km ^r	this study
pOR079	pBBR1 P_{mamDC} - <i>mamW-HL-egfp</i> , Km ^r	this study
pOR085	pBBR1 P_{mamDC} - <i>egfp-HL-mmsF</i> , Km ^r	this study
pOR087	pBBR1 P_{mamDC} - <i>egfp-HL-mamR</i> , Km ^r	this study
pOR088	pBBR1 P_{mamDC} - <i>egfp-HL-mamE</i> , Km ^r	this study
pOR090	pBBR1 P_{mamDC} - <i>mamR-HL-egfp</i> , Km ^r	this study
pOR099	pBBR1 P_{mamDC} - <i>mms6-HL-egfp</i> , Km ^r	this study
pOR129	pORFM derivate, for mgr_3691 deletion, Km ^r	this study
pOR148	pBAM P_{mamDC} - <i>egfp-HL-mamE</i> , Km ^r	this study
pOR156	pORFM derivate, for mgr_4114 deletion, Km ^r	this study

suppl. Table S 2: Oligonucleotides used in this study

Oligo-nucleotide	Description	Sequence
oOR141	mamA_up_for	<u>GACTGTGACGCCATTGGCAGGGCATGG</u>
oOR142	mamA_up_rev	<u>CTGAGGTACCGACGGCCGAACGTTTCATCG</u>
oOR143	mamA_down_for	<u>GCTAGAATTCGCAGTCGATGTAGAAGGTCTCATTG</u>
oOR144	mamA_down_rev	<u>TCACGCTAGCACATCGGCACCCGAATGC</u>
oOR162	mamW for	<u>ATTGCATATGCTAACTGCGATCATTGCC</u>
oOR163	mamW rev	<u>ATAGGCTAGCGAGTCCAGGCGATTGCTTCC</u>
oOR179	mmsF for	<u>TACTGTGCACAAGAAGTTCGAAGTGCAGCGACG</u>
oOR180	mmsF rev	<u>ATCTATGCATTCAGATCCGGTCCGGCCACC</u>
oOR183	mamR_N_C_for	<u>ACTCCATATGGTGCACACCTTTGTTTCAGGGCGCCATG</u> <u>G</u>
oOR184	mamR_N_C_rev	<u>ACTCATGCATTCAGCTAGCTCGGTTTCATGTATTCCAC</u> <u>AAGATTGG</u>
oOR185	mamE_N_C_for	<u>ACTCCATATGGTGCACACCATGTTCAATGGTGATGTG</u> <u>G</u>
oOR186	mamE_N_C_rev	<u>ACTCATGCATTCAGCTAGCAAGAACAATCCAGAACT</u> <u>CTTGGC</u>
oOR219	mms6_for	<u>TTCACATATGATGGTTTGCCCCCTGGG</u>
oOR220	mms6_rev	<u>ATAGGCTAGCGGACAGCGGTCGCGC</u>
oOR332	mm22_down_for	<u>TAGAGTCGACACACCTGTATACCCGGCAGATGG</u> <u>GGAGGAATATCATGGCCGCGGCGCACTGATCGGCTG</u> <u>GTTC</u>
oOR333	mm22_down_rev	<u>GAACCAGCCGATCAGTGCGCCGCGGCCATGATATTC</u> <u>CTCC</u>
oOR334	mm22_up_for	<u>ACTCACTAGTGCAGTTCGCCTCGATTTTCG</u>
oOR335	mm22_up_rev	<u>ACTCACTAGTGCAGTTCGCCTCGATTTTCG</u>
oOR380	mgr4114_up_for	<u>GACTACTGCAGATAGATACCTCATGCCATTGTTCG</u> <u>GCACCGAACGGAAGTGAACCCGTATCCGCCTGTTCT</u> <u>TTCAGG</u>
oOR381	mgr4114_up_rev	<u>CCTGAAAGAACAGGCGGATACGGGTTCACTTCCGTT</u> <u>CGGTGC</u>
oOR382	mgr4114_down_for	<u>CGGTGC</u>
oOR383	mgr4114_down_rev	<u>ACTCACTAGTTCACGCCGTTAATCAGCCG</u>

suppl. Table S 3. Number of assigned *bona fide* magnetosome proteins under different parameter conditions

Parameters	$A_{\text{mem}}/A_{\text{non-mag}} \geq$	1	0	1	1	0	3	1
	$A_{\text{mag}}/A_{\text{mem}} >$	1	1	0	1	1	1	1
	$A_{\text{mag.pur}}/A_{\text{mag}} \geq$	1	1	1	0	0	1	2
Total # of assigned proteins ^A		81	151	557	155	651	58	9
# assigned predicted MMP ^B		23	24	24	24	27	16	1
# non-assigned predicted MMP ^C		9	8	8	8	5	16	31
# assigned predicted non-MMP ^D		58	127	533	131	624	42	8

^A total number of proteins that meet the applied parameter filter set (= assigned)

^B number of assigned proteins that are predicted magnetosome membrane proteins (MMPs) [encoded in *mam* or *mms* operons (including *mamW*, *mamF2*, *mamD2* and *ftsZm*)]

^C number of proteins that are predicted MMPs, but do not meet parameter criteria

^D number of assigned proteins that are not predicted MMPs

suppl. Table S 4: Introduction of semi-quantitative MamC abundance threshold

Parameters	$A_{\text{mem}}/A_{\text{non-mag}} \geq$	1	1	1	1	0	0
	$A_{\text{mag}}/A_{\text{mem}} >$	1	1	1	4	4	0
	$A_{\text{mag.pur}}/A_{\text{mag}} \geq$	1	1	1	1	1	0
	$A_{\text{mag.pur}}/A_{\text{mag.pur(MamC)}} >$	0.1	0.01	0.001	0.1	0.01	0.01
Total # of assigned proteins ^A		13	43	76	26	30	205
# assigned predicted MMP ^B		13	23	23	21	22	28
# non-assigned predicted MMP ^C		19	9	9	11	10	4
# assigned predicted non-MMP ^D		0	20	53	5	8	177

suppl. Table S 5: Proteins with identified peptides from shaving assay. Bona fide magnetosome proteins from semi-quantitative analysis are labeled in light gray, proteins only found in membrane shaving preparation in dark grey (not found n.f.)

Bona fide?	Rank	Protein	MW	SpC
yes	1	MamO	65 kDa	918
yes	2	MamB	32 kDa	560
yes	3	MamF	12 kDa	374
yes	4	MamC	12 kDa	328
no	5	MGR_3691 conserved hypothetical membrane	20 kDa	323
yes	6	MamT	19 kDa	320
yes	7	MamZ	72 kDa	210
yes	8	MamF2	12 kDa	202
yes	9	MamE	78 kDa	194
yes	10	MamM	34 kDa	168
yes	11	MamH	46 kDa	127
yes	12	MamD	30 kDa	85
no	13	FixN Cytochrome CBB3 subunit 1	60 kDa	79
no	14	FeoB1	76 kDa	76
yes	15	MmsF	14 kDa	62
n.f.	16	MGR_1410 Ammonia permease	43 kDa	60
yes	17	MamN	46 kDa	58
yes	18	MamY	41 kDa	56
yes	19	MamI	8 kDa	55
no	20	ActP Cation/acetate symporter	59 kDa	41
no	21	MGR_1081 Rh-like protein/ammonium transporter	15 kDa	35
no	22	NuoH NADH:ubiquinone oxidoreductase subunit 1	38 kDa	35
no	23	AtpE ATP synthase C chain	7 kDa	32
n.f.	24	MGR_3690 membrane protein	7 kDa	32
no	25	NorB Nitric-oxide reductase subunit B	50 kDa	30
no	26	HppA pyrophosphate-energized proton pump	71 kDa	30
no	27	FixO Cytochrome C oxidase, mono-heme subunit	27 kDa	26
no	28	MGR_3632 ubiquinone/menaquinone biosynthesis	32 kDa	22
no	29	MGR_1236 apocytochrome b	48 kDa	21
no	30	MGR_3499 conserved hypothetical membrane	12 kDa	21
no	31	NorC Nitric-oxide reductase subunit	16 kDa	19
no	32	fixP Cytochrome c oxidase cbb3-type, subunit III	32 kDa	16
no	33	MGR_1855 Outer membrane protein and related peptidoglycan-associated (lipo)proteins	34 kDa	15
n.f.	34	MGR_1656 ABC-type nitrate/sulfonate/bicarbonate transport system, permease component	19 kDa	14
yes	35	MGR_4114 hypothetical protein	7 kDa	13
n.f.	36	MGR_4271 Membrane transport family protein	33 kDa	13
no	37	MamA	24 kDa	12
yes	38	Mms6	13 kDa	10
yes	39	MamD2	19 kDa	10

no	40	MGR_2609 NADH dehydrogenase subunit 2	51 kDa	8
no	41	MGR_1348 ADP-heptose:LPS heptosyltransferase	41 kDa	7
no	42	MGR_2607 NADH-plastoquinone oxidoreductase, chain 5	70 kDa	7
no	43	MamJ	44 kDa	7
no	44	SecF Protein export membrane protein	34 kDa	7
no	45	FixI E1-E2 type cation ATPase FixI	85 kDa	7
no	46	MGR_1854 CDP-diacylglycerol--serine O-	31 kDa	6
no	47	MGR_3263 60 kDa inner membrane insertion protein	64 kDa	6
no	48	MGR_0760 multidrug resistance protein	110	5
yes	49	MGR_2730 conserved hypothetical protein	20 kDa	5
n.f.	50	MGR_4264 membrane protein	11 kDa	5
n.f.	51	MGR_3103 NnrS family protein	42 kDa	4
yes	52	MamX	28 kDa	4
no	53	MGR_1141 conserved hypothetical protein	57 kDa	4
no	54	MGR_1156 conserved hypothetical protein	44 kDa	4
yes	55	MamW	15 kDa	3
no	56	MGR_4265 Sodium:solute symporter family protein	59 kDa	3
no	57	MGR_3445 Outer membrane protein and related peptidoglycan-associated (lipo)proteins	19 kDa	3
no	58	NapC Denitrification system tetra-heme	26 kDa	2
yes	59	MamG	8 kDa	2
no	60	MGR_3631 methyltransferase Fe-S oxidoreductase	24 kDa	2
no	61	MGR_1590 conserved hypothetical membrane	29 kDa	2

Acknowledgement

I would like to sincerely thank Prof. Dirk Schüler for giving me the opportunity to work on the highly interesting projects of this thesis and for the successful years of magnetosome research we jointly conducted in his lab. The freedom I received for my research was inspiring and I am very grateful that I was allowed and supported to finish my work in Munich.

Many thanks also to the other examiners of this thesis for their interest in my work. I would like to specially thank Prof. Marc Bramkamp and Prof. Thomas Ott for being part of my thesis advisory committee over the last four years and for helpful discussions in the course of this project.

Marc Bramkamp is additionally warmly thanked not only for providing me laboratory and office space for more than a year, but also for welcoming me into his research group as if I were his own student.

Prof. Jürgen Plitzko is highly acknowledged for giving me the opportunity to work in the department of Prof. Wolfgang Baumeister at the Max Planck Institute of Biochemistry and for his technical support with microscopy, whenever it was needed. Special thanks in this sense also to Dr. Emanuel Katzmann for teaching me the basics of electron microscopy and tomography.

Moreover, I would like to acknowledge Prof. Dörte Becher, Dr. Florian Bonn, Prof. Raz Zarivach, Dr. Natalie Zeytuni and Prof. Mihály Pósfai for our successful collaborations and helpful discussions that positively influenced my thesis. Most sincere thanks go to my students Yvonne Forstner, Daniel Richter, Simrika Thapa and Yihe Xu for their strong motivation and the scientific effort they put into this work.

Unfortunately, space is too limited to acknowledge all the other great colleagues that I met over the past years in the Magnetolab, the Baumeister department, the Bramkamp group and all over the campus. It was a great pleasure to work with you all and I would like to thank you for the great atmosphere you created in and outside the lab. I hope you know that I mean you! You are awesome! Thank you!

Last, but definitely not least, I would like to thank my family, friends and my darling Prachi for all their support, patience and for making me aware of the good life I have outside the lab. You are very important.

